Universidad de Oviedo
Universidá d'Uviéu
University of Oviedo

Departamento de Ingeniería Eléctrica, Electrónica,
de Computadores y Sistemas

Doctoral Thesis

Design of wireless systems exploiting advanced positioning techniques: RFID applications and freehand electromagnetic characterization

Guillermo Álvarez Narciandi

Advisors: Marcos R. Pino and Jaime Laviada

Programa de Doctorado en Tecnologías de la Información y
Comunicaciones en Redes Móviles

2021

Directors:
Dr. Marcos Rodríguez Pino, Universidad de Oviedo
Dr. Jaime Laviada Martínez, Universidad de Oviedo

Preliminary examiners:
Dr. Baolong Wu, Hunan University (China)
Dr. Miguel Caro Cuenca, The Netherlands Organisation for applied scientific research (TNO)

Examining board:
Prof. Cyril Luxey, University Nice-Sophia Antipolis
Dr. Jorge Teniente Vallinas, Universidad Pública de Navarra
Dr. Rafael González Ayestarán, Universidad de Oviedo
Dr. Susana Loredo Rodríguez, Universidad de Oviedo
Dr. Ana Arboleya Arboleya, Universidad Rey Juan Carlos

A los que me habéis impulsado y ayudado a crecer como persona.

Agradecimientos

Como colofón al trabajo realizado durante estos años, quiero expresar mi más profundo agradecimiento a aquellas personas que me han acompañado, no solo durante esta etapa, sino a lo largo de mi vida.

En primer lugar, como no puede ser de otra forma, quiero agradecer su apoyo a mis directores de tesis. Marcos, gracias por respaldar este proyecto y por tus consejos. Jaime, te considero mi mentor en el ámbito de la investigación. No he escogido esta palabra a la ligera, pues creo que debo ensalzar tu implicación y apoyo, que me han demostrado que no solo eres un gran investigador, sino una gran persona. Durante estos años he intentado aprender lo máximo posible de tu forma de trabajar, rigurosa y concienzuda.

En segundo lugar, quiero dar las gracias a Fernando y a Yuri, que allá en 2013 me ofrecieron empezar a colaborar con el Área de Teoría de la Señal y Comunicaciones, con los que continúo trabajando activamente y que desde entonces me han ayudado en múltiples ocasiones. También quiero expresar mi agradecimiento al resto de personas del Área, en especial a mis compañeros del *Taburdiu*. Carlos, Cebrián, René, *Putty*, no solo habéis estado siempre dispuestos a echar una mano, sino que sin vosotros muchas tardes hubieran sido mucho más aburridas. Ana, Miguel, Dani, Leti, Álvaro, Borja, hemos compartido largos ratos de esparcimiento sin los que el trabajo hubiera sido mucho más monótono.

I would also like to thank Prof. Paolo Nepa, Andrea Michele, Andrea Motroni, Alice Buffi and my colleagues from the lab for welcoming me in Pisa. It has been a pleasure to work with you. I would also like to thank Prof. Guillaume Ducournau for giving me the opportunity of collaborating with him during my stay in Lille.

Quiero dar las gracias a mis amigos, porque, aunque sigamos caminos distintos, vuestro apoyo es constante.

También quiero expresar mi agradecimiento a mi familia, en especial a mis padres. Sin vuestro cariño y dedicación hoy sería una persona muy diferente.

Mamá, estoy seguro de que estarías muy orgullosa de mí. Gracias por tu fuerza y optimismo. Gracias por intentar enseñarme a ver siempre el lado positivo de las cosas y de las personas. Papá, gracias por tu paciencia, por tu cariño, por ser mi apoyo constante. No puedo pensar en mejores padres ni en una mejor educación.

Por último, quiero expresar mi agradecimiento a María, mi compañera de viaje, con la que he recorrido medio mundo. Has sido un apoyo constante y no entendería los últimos años de mi vida sin ti.

Resumen

Esta Tesis Doctoral se centra en el desarrollo de sistemas de seguimiento y posicionamiento avanzados basados en el uso de señales electromagnéticas emitidas por sensores o dispositivos de propósito general, así como en el desarrollo de aplicaciones electromagnéticas avanzadas apoyadas en dichos sistemas de posicionamiento. En concreto, en la primera parte de esta Tesis se explota la tecnología de identificación por radiofrecuencia (RFID) para el desarrollo de sistemas que permiten estimar la posición y orientación de objetos equipados con etiquetas RFID, así como de realizar su seguimiento. Por otro lado, en la segunda parte de la Tesis se emplean sistemas de posicionamiento externos como base para el desarrollo de sistemas versátiles para aplicaciones de inspección no destructiva y caracterización de antenas. En consecuencia, la Tesis Doctoral se ha estructurado en tres capítulos principales, además de un primer capítulo en el que se revisa el estado del arte y de un capítulo final que recoge las conclusiones y las líneas futuras de trabajo.

De este modo, el segundo de los capítulos está dedicado al desarrollo de dos sistemas que hacen uso de la tecnología RFID para la automatización de procesos logísticos. El primero de dichos sistemas permite la estimación de la orientación de mercancías empleando una agrupación de etiquetas RFID pasivas. El segundo de los sistemas proporciona una solución económica, cuyo despliegue es rápido y sencillo, para monitorizar el tránsito de mercancías en puntos de control. En concreto, este sistema utiliza un conjunto de etiquetas RFID pasivas, dispuestas en forma de rejilla sobre el suelo del punto de control a monitorizar, y una única antena conectada a un lector RFID.

El siguiente capítulo recoge el desarrollo de un sistema manual para la generación de imagen electromagnética de interés en el ámbito de la inspección no destructiva y en aplicaciones de seguridad. Dicho sistema se basa en el uso de un módulo de radar integrado en un chip que se desplaza de forma manual describiendo una trayectoria arbitraria sobre la zona bajo investigación. Además, la posición y orientación del módulo radar es monitorizada a lo largo

de su trayectoria de manera que las señales radar adquiridas son combinadas de forma coherente mediante técnicas de radar de apertura sintética (SAR), lo que permite generar imágenes de alta resolución en tiempo real. En concreto, el sistema propuesto fue validado en primer lugar usando una configuración cuasi-monoestática y, posteriormente, su funcionamiento fue evaluado empleando una arquitectura Multiple-Input Multiple-Output (MIMO). Asimismo, se ha desarrollado de forma satisfactoria un método de calibración que permite reducir los errores de posicionamiento.

Finalmente, el cuarto capítulo resume el desarrollo de un sistema manual para el diagnóstico y caracterización de antenas. El sistema se basa en la adquisición de medidas del campo radiado por la antena bajo medida (AUT) empleando una antena sonda que se desplaza de forma manual frente a la apertura de la misma. De forma análoga al sistema de generación de imagen electromagnética, se realiza un seguimiento de la posición y orientación de la antena sonda, de manera que es posible combinar las distintas medidas de campo radiado para calcular una distribución de corrientes equivalentes en la apertura de la antena bajo medida y, en última instancia, determinar su diagrama de radiación en campo lejano. En primer lugar, el sistema propuesto fue implementado considerando la adquisición tanto de la amplitud como de la fase del campo radiado por la AUT y, posteriormente, empleando únicamente información de amplitud. El sistema desarrollado es de gran interés en distintas aplicaciones como para la caracterización rápida de antenas en condiciones de laboratorio o para la medida de antenas ya desplegadas y en condiciones operativas o de antenas embarcadas. Asimismo, cabe destacar que el sistema propuesto se ha validado en un rango de frecuencias notablemente amplio, desde banda X hasta frecuencias submilimétricas, lo que le confiere una gran versatilidad y constituye una característica muy ventajosa del mismo, especialmente en el contexto actual, en el que se está desarrollando un gran número de aplicaciones que hacen uso de estas bandas de frecuencia (como por ejemplo para comunicaciones de alta capacidad).

Conclusiones

Esta tesis, presentada como compendio de publicaciones, se basa fundamentalmente en el trabajo desarrollado en las publicaciones [**I**]-[**V**], que se resumen en el presente documento. En primer lugar, en el capítulo 1 se presenta una revisión del estado del arte relacionado con los sistemas diseñados. El capítulo 2 describe los sistemas desarrollados basados en el uso de tecnología RFID y su validación. El capítulo 3 recoge el diseño y validación de un sistema manual para la generación de imagen electromagnética y, por último, el capítulo 4 presenta un sistema manual para el diagnóstico y caracterización de antenas.

El primero de los sistemas desarrollados basado en tecnología RFID permite la estimación de la orientación de objetos mediante una agrupación de etiquetas RFID [xviii], [xvii], [**II**]. En concreto, el sistema propuesto emplea la fase de las señales dispersadas por las etiquetas RFID del array [**I**], cuya dirección de llegada al mismo se estima mediante el algoritmo Multiple Signal Classification (MUSIC) y, posteriormente, se calcula la orientación del objeto etiquetado. Aquí cabe destacar la importancia de la geometría de la agrupación de etiquetas. En particular, el uso de una agrupación lineal con etiquetas RFID separadas de manera uniforme (ULA) permite realizar estimaciones en azimuth, mientras que el uso de una agrupación circular con etiquetas distribuidas de forma angularmente uniforme (UCA) permite tanto estimaciones de azimuth como de elevación. En esta tesis se han considerando las dos alternativas, habiéndose realizado un estudio del impacto en la precisión del sistema de imperfecciones en la geometría de la agrupación de etiquetas y una validación experimental en ambos casos. Los resultados obtenidos muestran que el sistema permite estimar con precisión la orientación de objetos en un amplio margen angular. El sistema propuesto, que permite mejorar el nivel de automatización de procesos logísticos, también puede usarse para obtener información de posicionamiento [xvi].

El segundo de los sistemas basados en el uso de etiquetas RFID permite la monitorización del tránsito de mercancías en puntos de control [xi], [**III**].

Este sistema se basa en el uso de un conjunto de etiquetas RFID pasivas de referencia, dispuestas en forma de rejilla, que se colocan en el suelo de la zona a monitorizar y una única antena conectada a un lector RFID. En este caso, la estimación de la dirección de movimiento de las mercancías se realiza en base al efecto sombra que tiene lugar cuando la carretilla o máquina elevadora que las transporta bloquea las etiquetas de referencia. Dicha sombra se cuantifica en términos de etiquetas no leídas durante una ventana temporal y en términos de una reducción del número de lecturas de una etiqueta. La determinación de la dirección de movimiento de las mercancías se realiza en base a la información anterior, que se emplea como atributos de entrada de una red neuronal. El sistema propuesto fue validado mediante una campaña de medidas realizada en las instalaciones de la Universidad de Pisa. Entre las ventajas del sistema cabe destacar su robustez y la sencillez del equipo necesario, lo que hace que el sistema sea económico y fácil de desplegar.

Por otro lado, el sistema manual de generación de imagen electromagnética [v], [**IV**] constituye el primer sistema capaz de generar imágenes electromagnéticas aplicando técnicas de radar de apertura sintética empleando las medidas adquiridas durante un escaneo manual en 3D con un dispositivo de bolsillo. En concreto, el sistema utiliza un módulo de radar integrado en chip a frecuencias milimétricas que se desplaza sobre el área a inspeccionar. Durante el escaneo del área a inspeccionar se realiza el seguimiento de la posición y orientación del módulo radar, de forma que es posible generar imágenes de alta resolución en tiempo real. Las imágenes obtenidas se muestran al operador del sistema a medida que se realizan más adquisiciones radar, lo que permite adaptar el escáner del área a inspeccionar de acuerdo a las mismas. El sistema propuesto fue validado en primera instancia empleando una configuración cuasi-monoestática, habiéndose obtenido buenos resultados. Posteriormente, el sistema se extendió a una configuración MIMO, consiguiéndose una mejora en la velocidad de escaneo y en la calidad de las imágenes obtenidas. Asimismo, se ha propuesto un método de calibración para reducir errores de posicionamiento, lo que redunda en una mayor calidad de las imágenes obtenidas.

Por último, el sistema manual para el diagnóstico y caracterización de antenas se basa en la adquisición del campo radiado por la antena bajo medida mediante el uso de una antena sonda que es desplazada manualmente frente a la apertura de la misma. La posición y orientación de la antena sonda se monitoriza de forma que es posible combinar las distintas medidas del campo radiado para estimar una distribución de corrientes equivalentes en la apertura

de la antena bajo medida y, posteriormente, calcular su diagrama de radiación en campo lejano resolviendo las integrales de radiación correspondientes. Inicialmente, el sistema propuesto fue implementado considerando la adquisición tanto de la amplitud como de la fase del campo radiado [x], [ix], [**V**]. Posteriormente, el sistema fue adaptado para emplear únicamente medidas de amplitud del campo radiado, lo que conlleva una simplificación del equipo necesario para la adquisición del campo radiado y evita la necesidad de una referencia de fase [iv]. En concreto, el uso exclusivo de información de amplitud permite realizar el diagnóstico y la caracterización de antenas en condiciones operativas, reducir el coste del sistema y extender la frecuencia máxima de operación del mismo, que se ha validado hasta frecuencias submilimétricas. Debido a su versatilidad, el sistema propuesto es de gran interés en múltiples aplicaciones como la evaluación rápida de antenas en laboratorio o la caracterización de antenas desplegadas o embebidas en otros dispositivos.

Abstract

This dissertation focuses on the development of advanced positioning and tracking systems using electromagnetic signals emitted by sensors or general purpose devices, as well as on the design of systems for advanced electromagnetic applications built on positioning systems. In particular, under the common nexus of positioning techniques, the first part of this thesis leverages Radio Frequency IDentification (RFID) technology for the localization, attitude determination and tracking of tagged objects. On the other hand, the second part of this dissertation exploits state-of-the-art external positioning systems to develop flexible measurement systems for Non-Destructive Evaluation (NDE) and antenna characterization. In addition to the first chapter describing the state of the art and the last chapter, where the conclusions and the future lines of work are drawn, the dissertation is structured in three main chapters.

Thus, the second chapter is devoted to the development of two advanced RFID systems aiming to optimize the automation of logistic processes. The first system was designed for the estimation of the attitude of tagged goods using an array of passive RFID tags. The second system provides a cost-effective and easy-to-deploy solution to monitor the transit of goods at checkpoints. In particular, this system employs a reference grid of RFID tags deployed on the floor of the checkpoint being controlled and a single antenna connected to a RFID reader.

The next chapter is devoted to the development of a handheld imaging system, which can be of great interest for security and NDE applications. This system is based on freely moving a compact radar-on-chip module over the inspected area, while its position and attitude are being tracked. This allows to coherently combine the acquired measurements using Synthetic Aperture Radar (SAR) techniques, yielding real-time, high-resolution images. Specifically, the proposed system was first evaluated using a quasi-monostatic approach and, afterwards, its performance was assessed considering a Multiple-Input Multiple-Output (MIMO) configuration. In addition, a calibration method to reduce positioning errors has been successfully tested.

Finally, the fourth chapter summarizes the design and development of a handheld antenna diagnosis and characterization system. It is based on acquiring samples of the field radiated by the Antenna Under Test (AUT) by moving a handheld probe antenna in front of its aperture. The position and attitude of the probe antenna is tracked so that the acquired field samples can be combined to compute an equivalent currents distribution on the AUT aperture and, ultimately, to retrieve its Far-Field (FF) radiation pattern. First, the proposed system was implemented considering both amplitude and phase measurements and, afterwards, employing amplitude-only acquisitions. The system is of great interest for different applications such as the quick performance evaluation of antennas in laboratory conditions, or the characterization of already deployed antennas and on-board antennas. In particular, the wide operational frequency range of the proposed system, validated from X band to sub-mmWave frequencies, is a significant advantage as there is a growing number of applications (for example for high-capacity communications) exploiting these bands.

Dissertation

This thesis, presented by compendium of publications, consists of the following publications, which are referred to in the text by their Roman numerals. A complete copy of all the publications is included in the final part of the dissertation. The publications are grouped by topic:

[I] **G. Álvarez-Narciandi**, J. Laviada, M. R. Pino and F. Las-Heras, "Phase acquisition techniques for RFID multistatic setups with application to imaging and localization," *Sensors and Actuators A: Physical,* vol. 270, pp. 97–107, Feb 2018.

[II] **G. Álvarez-Narciandi**, J. Laviada, M. R. Pino and F. Las-Heras, "Attitude Estimation Based on Arrays of Passive RFID Tags," *IEEE Transactions on Antennas Propagation,* vol. 66, no. 5, pp. 2534–2544, May 2018.

[III] **G. Álvarez-Narciandi**, A. Motroni, M. R. Pino, A. Buffi and P. Nepa, "A UHF-RFID gate control system based on a Recurrent Neural Network," *IEEE Antennas and Wireless Propagation Letters,* vol. 18, no. 11, pp. 2330–2334, Nov. 2019.

[IV] **G. Álvarez-Narciandi**, M. López-Portugués, F. Las-Heras and J. Laviada, "Freehand, Agile, and High-Resolution Imaging With Compact mm-Wave Radar," *IEEE Access,* vol. 7, pp. 95516–95526, 2019.

[V] **G. Álvarez-Narciandi**, J. Laviada, Y. Álvarez-López, and F. Las-Heras, "Portable Freehand System for Real-time Antenna Diagnosis and Characterization," *IEEE Transactions on Antennas and Propagation,* Early Access, 2020.

Other publications and works related to the topics of the thesis but not included as part of the dissertation

In addition to the above-mentioned references, the following publications also related to the topics of the thesis have been authored or coauthored by Guillermo Álvarez Narciandi during his time as doctoral candidate at Universidad de Oviedo:

International journals

[i] Y. Álvarez, M. García-Fernández, **G. Álvarez-Narciandi**, A. Arboleya, F. Las-Heras, S. García-Cortés and M. FernándezCabanas, "In-situ antenna diagnostics and characterization system based on RFID and remotely piloted aircrafts," *Sensors and Actuators A: Physical,* vol. 269, pp. 29-40, Jan 2018.

[ii] Y. Álvarez, J. Franssen, **G. Álvarez-Narciandi**, J. Pagnozzi, I. González-Pinto Arrillaga and F. Las-Heras, "RFID Technology for Management and Tracking: e-Health Applications," *Sensors,* vol. 18, No. 8, 18 pages, August 2018.

[iii] B. Wu, **G. Álvarez-Narciandi** and J. Laviada, "Multi-Layered Circular Dielectric Structures' Synthetic Aperture Radar Imaging Based on Green's Function Using Non-Uniform Measurements," *Remote Sensing,* vol. 12, No. 7, 1190, April, 2020.

International conferences

[iv] **G. Álvarez-Narciandi**, J. Laviada, Y. Álvarez-López, G. Ducournau, C. Luxey, F. Gianesello and F. Las-Heras, "Portable, Freehand System for Antenna Diagnosis Using Amplitude-Only Data," in *14th European Conference on Antennas and Propagation (EuCAP'20)*, Copenhangen, Denmark, 2020.

[v] **G. Álvarez-Narciandi**, J. Laviada and F. Las-Heras, "Evolution of the Image Quality over Time for a Freehand Monostatic mm-Wave Radar Imager," in *14th European Conference on Antennas and Propagation (EuCAP'20)*, Copenhangen, Denmark, 2020.

[vi] F. Filice, N. Nachabe, F. Gianesello, **G. Álvarez-Narciandi**, J. Laviada, F. Las-Heras and C. Luxey, "3-D Printed High Efficiency Wideband 2x2 and 4x4 Double-Ridged Waveguide Antenna Arrays for Ku-Band Satcom-On-The-Move Applications," in *14th European Conference on Antennas and Propagation (EuCAP'20)*, Copenhangen, Denmark, 2020.

[vii] F. Las-Heras, J. Laviada, Y. Álvarez-López, A. Arboleya, M. García-Fernández and **G. Álvarez-Narciandi**, "Antenna Measurements and Signal Processing

Techniques," in *14th European Conference on Antennas and Propagation (EuCAP'20)*, Copenhangen, Denmark, 2020.

[viii] F. Filice, N. Nachabe, F. Gianesello, J. Laviada, **G. Álvarez-Narciandi**, D. Titz, F. Las-Heras and C. Luxey, "Wideband aperture coupled patch antenna for Ka-band exploiting the generation of surface waves," in *2020 IEEE International Symposium on Antennas and Propagation and North American Radio Science Meeting*, Montreal, Canada, 2020.

[ix] **G. Álvarez-Narciandi**, J. Laviada, Y. Álvarez-López and F. Las-Heras, "Impact of Sparse Measurements in Freehand Setup for Antenna Characterization," in *41st Annual Meeting and Symposium of the AMTA*, San Diego, CA, USA, 2019.

[x] **G. Álvarez-Narciandi**, J. Laviada, Y. Álvarez-López and F. Las-Heras, "Rapidly Deployable Portable System for Real-Time Antenna Diagnostics and Characterization," in *2019 IEEE International Symposium on Antennas and Propagation and USNC-URSI Radio Science Meeting*, Atlanta, GA, USA, 2019.

[xi] **G. Álvarez-Narciandi**, A. Motroni, M. R. Pino, A. Buffi and P. Nepa, "A UHF-RFID gate control system based on a Convolutional Neural Network," in *2019 IEEE International Conference on RFID Technology and Applications (RFID-TA 2019)*, Pisa, Italy, 2019.

[xii] A. Michel, M. R. Pino, **G. Álvarez-Narciandi** and P. Nepa, "Inventory of Piled metal tubes using RFID technology," in *2019 URSI AP-RASC*, New Delhi, India, 2019.

[xiii] A. Michel, M. R. Pino, **G. Álvarez-Narciandi**, M. Arrebola and P. Nepa, "Using the Power Transfer Efficiency for RFID detection in Unusual Scenarios," in *2019 URSI EMTS*, San Diego, CA, USA, 2019.

[xiv] M. R. Pino, A. Michel, **G. Álvarez-Narciandi** and P. Nepa, "Read-Range Estimation of UHF-RFID Tags Placed Inside Metal Pipes," in *13th European Conference on Antennas and Propagation (EuCAP'19)*, Krakow, Poland, 2019.

[xv] **G. Álvarez-Narciandi**, J. Laviada, M. R. Pino and F. Las-Heras, "Passive RFID System for Object Shape Estimation," in *12th European Conference on Antennas and Propagation (EuCAP'18)*, London, UK, 2018.

[xvi] **G. Álvarez-Narciandi**, J. Laviada, M. R. Pino and F. Las-Heras, "3D location system based on attitude estimation with RFID technology," in *2017 IEEE International Conference on RFID Technology and Applications (RFID-TA 2017)*, Warsaw, Poland, 2017.

[xvii] **G. Álvarez-Narciandi**, J. Laviada, M. R. Pino and F. Las-Heras, "Application of MUSIC algorithm to the estimation of objects attitude," in *IEEE-APS*

Topical Conference on Antennas and Propag. in Wireless Comm., Verona, Italy, 2017.

[xviii] **G. Álvarez-Narciandi**, J. Laviada and F. Las-Heras, "Object Attitude Estimation Using Passive RFID Tag Arrays," in *URSI Commision B International Symposium on Electromagnetic Theory (EMTS)*, Espoo, Finland, 2016.

Patents

(a) **G. Álvarez-Narciandi**, J. Laviada and F. Las Heras, "System and Method for the attitude estimation of objects and living beings using electromagnetic scatterers," Patent ES-2562732-B2, August, 2015.

(b) **G. Álvarez-Narciandi**, J. Laviada, Y. Álvarez-López and F. Las Heras, "System and Method for antenna diagnosis," Patent application ES P201900105, 2019.

International research stays

During the development of this doctoral thesis, the author carried out several research stays abroad: at the German Aerospace Centre, at the Department of Information Engineering of the University of Pisa and at the Institute of Electronics, Microelectronics and Nanotechnology (IEMN) of the University of Lille.

1. Institute of Electronics, Microelectronics and Nanotechnology (IEMN), University of Lille, France.
    - Research stay under supervision of Prof. Guillaume Ducournau.
    - Duration: from June 1st 2019 to July 31st 2019.
    - Fundings: Ayudas económicas de movilidad de excelencia para docentes e investigadores de la Universidad de Oviedo.
2. Department of Information Engineering, the University of Pisa, Italy.
    - Research stay under supervision of Prof. Paolo Nepa.
    - Duration: from September 1st 2018 to November 30th 2018.
    - Fundings: ayudas a la movilidad para estancias breves y traslados temporales del Ministerio de Educación 2017 (ref. EST17/00813).
3. Microwaves and Radar Institute, German Aerospace Centre (*Deutsches Zentrum für Luft- und Raumfahrt*), Germany.
    - Research stay under supervision of Dr. Markus Peichl.

- Duration: from 22nd August 2016 to 30th September 2016.
- Fundings: German Aerospace Centre (*Deutsches Zentrum für Luft- und Raumfahrt*).

Research projects and funding

The doctoral candidate has been awarded an FPU grant (*Formación de Profesorado Universitario*, ref. FPU15/06431), funded by Ministerio de Educación of Spain, for the realization of the PhD degree.

The doctoral thesis has also been developed in the framework of several national and regional research projects in which the candidate has been actively involved:

1. MilliHand, RTI2018-095825-B-I00. Ministerio de Ciencia, Innovación y Universidades, proyectos de I+D+I Retos de la Sociedad, 2019-2021.
2. ARTEINE, TEC2017-86619-R. Ministerio de Ciencia, Innovación y Universidades, proyectos de I+D+I Retos de la Sociedad, 2018-2020.
3. FC-GRUPIN-IDI/2018/000191. Fondos FEDER, Plan Regional, Gobierno del Principado de Asturias, 2018-2020.
4. PortEMVision, *New Generation of Portable Electromagnetic Scanners Based on Computer Vision*, TEC2014-55290-JIN. Ministerio de Economía y Competitividad, proyectos de I+D+I para jóvenes investigadores, 2015-2017,
5. FC-15-GRUPIN14-114. Fondos FEDER, Plan Regional, Gobierno del Principado de Asturias, 2015-17.
6. MIRIIEM, *Multiple Information Resources for Improving Inverse EM techniques for reflectometry and imaging applications*, TEC2014-54005-P. Ministerio de Economía y Competitividad, proyectos de I+D Excelencia y proyectos de I+D+I Retos Investigación, 2015-2017.
7. LINE-525-002. Universidad de Oviedo, 2015-2016.

Furthermore, the doctoral candidate has also been involved in several contracts with companies:

1. FUO-282-19, Sistema de posicionamiento y anticolisión multisensorial de alta precisión para entornos industriales hostiles (*Highly accurate multi-sensor positioning and anti-collision system for hostile industrial environments*). TSK (I Programa de Innovación Abierta), 2019.
2. FUO-203-19, Implementación de un sistema de posicionamiento con redes WIFI a través de terminales móviles (*Implementation of a positioning system using WIFI networks and mobile devices*). Arcelor-Mittal, 2019.

Awards and recognition

During his time as doctoral candidate at the University of Oviedo, the candidate has received the following awards:

1. TICRA grant to attend the 14th European Conference on Antennas and Propagation (EuCAP). TICRA, March 2020.
2. Best Student Paper Award (second place). 41st Annual Meeting and Symposium of the Antenna Measurement Techniques Association (AMTA), October 2019.
3. CAJA DE INGENIEROS award to the best academic performance in the 2017 National Awards to Telecommunication Engineers, sponsored by the Official Association of Telecommunication Engineers of Spain.
4. Special Award to the best entrepreneurship initiative for the creation of a technology-based company in the XV Arquímedes Contest with the research project "Imaging system based on the use of RFID localization technology", 2017.

Author's contribution

This section states the contribution of the doctoral candidate and the coauthors for each of the publications that compose this dissertation.

- **Publication [I] "Phase acquisition techniques for RFID multistatic setups with application to imaging and localization"**
  The doctoral candidate developed the processing code for estimating the phase of the signals backscattered by RFID tags. He also carried out the measurements to validate the proposed technique. Dr. Jaime Laviada assisted in developing the processing code and during the measurements. The rest of the coauthors supervised the work.

- **Publication [II] "Attitude Estimation Based on Arrays of Passive RFID Tags"**
  Dr. Jaime Laviada formulated the methodology and assisted with the simulations and the measurements. The doctoral candidate developed the processing code for estimating the attitude of arrays of RFID tags and performed the measurements. The rest of the coauthors supervised the work.

- **Publication [III] "A UHF-RFID gate control system based on a Recurrent Neural Network"**
  This work is the result of a collaboration with the University of Pisa during the research stay of the doctoral candidate. The doctoral candidate designed and developed the system proposed to monitor the transit of goods at checkpoints. Dr. Marcos R. Pino assisted in the development and validation of the system. Mr. Andrea Motroni also assisted in the measurements. The rest of the coauthors supervised the work.

- **Publication [IV] "Freehand, Agile, and High-Resolution Imaging With Compact mm-Wave Radar"**
  Dr. Jaime Laviada formulated the methodology. The doctoral candidate developed the system and performed the measurements. Dr. Miguel López-Portugués assisted in the development of the processing code. Prof. Fernando Las Heras supervised the work.

- **Publication [V] "Portable Freehand System for Real-time Antenna Diagnosis and Characterization"**
  Dr. Yuri Álvarez-López developed the antenna diagnosis code. The doctoral candidate developed the system and performed the measurements. Dr. Jaime Laviada assisted in the measurements. Prof. Fernando Las Heras supervised the work.

List of acronyms

1D	One-Dimensional.
2D	Bi-Dimensional.
3D	Three-Dimensional.
5G	Fifth Generation.
ACA	Adaptive Cross Approximation.
ACS	Array Coordinate System.
AUT	Antenna Under Test.
CATR	Compact Antenna Test Range.
CNN	Convolutional Neural Network.
DoA	Direction of Arrival.
DRWG	Double-Ridged Waveguide.
EMI	Electromagnetic Interference.
ETSI	European Telecommunications Standards Institute.
FF	Far-Field.
FFT	Fast Fourier Transform.
FMCW	Frequency-Modulated Continuous-Wave.
FMM	Fast Multiple Method.
GCS	Global Coordinate System.
GPU	Graphics Processing Unit.
JCR	Journal Citation Reports.
LSTM	Long Short-Term Memory.
MIMO	Multiple-Input Multiple-Output.
MUSIC	Multiple Signal Classification.
NDE	Non-Destructive Evaluation.

NF	Near-Field.
OEWG	Open-Ended Waveguide.
pSRM	Phaseless Sources Reconstruction Method.
RF	Radio Frequency.
RFID	Radio Frequency IDentification.
RMS	Root Mean Square.
RNN	Recurrent Neural Network.
RSSI	Received Signal Strength Indicator.
SAR	Synthetic Aperture Radar.
SCI	Science Citation Index.
SRM	Sources Reconstruction Method.
TCR	Target-to-Clutter Ratio.
UAV	Unmanned Aerial Vehicle.
UCA	Uniform Circular Array.
UHF	Ultra High Frequency.
ULA	Uniform Linear Array.
VNA	Vector Network Analyzer.

Table of contents

CHAPTER

1

Introduction

1.1 Motivation

The tracking and localization of goods across the supply chain, i.e., its traceability, is of great importance. In this regard, RFID is a key technology, which allows the remote identification of objects. The development of this technology has yielded to its adoption for different applications in multiple sectors such as retail [1, 2], healthcare [3, 4] or anti-counterfeiting [5]. In particular, the development of positioning systems has been of great interest [6–14]. Besides position estimations, the attitude of items, which can be obtained using extra sensors apart from the RFID tags, provides complementary information that can be useful for several applications. In this context, an innovative system to estimate the attitude of tagged goods using arrays of RFID tags, presented in Patent (a), was developed

within this dissertation. In addition, a cost-effective and easy-to-deploy system to monitor the transit of goods at checkpoints and docking gates was also proposed.

On the other hand, the advances of positioning systems in terms of affordability and accuracy have enabled the development of many applications that can take advantage of these features [15, 16]. In this regard, in the field of electromagnetic imaging there is a growing interest in portable imaging devices, although current solutions are still rather bulky [17–21] or have low resolution [22]. In contrast, the real-time handheld imaging system developed in the framework of this thesis overcomes the low resolution limitation of previously presented compact imaging systems. In particular, the proposed system achieves that by tracking a mm-Wave radar-on-chip module with a high-accuracy positioning system to apply SAR techniques.

Analogously, the increase of high capacity communications and the deployment of the Fifth Generation (5G) mobile network is driving the use of mmWave and sub-mmWave frequencies. Although several systems have been proposed to assess the performance of already deployed antennas at lower frequencies [23, 24], in these frequency bands the fast and accurate in-situ diagnosis and characterization of antennas remains a challenge. In this regard, a handheld system for antenna diagnosis and characterization, protected in Patent (b), was developed within this thesis. For this purpose, the system exploits the same tracking system that is used for the handheld imaging system, so that the information from the acquired samples of the field radiated by the AUT can be combined. It should be remarked that, although less accurate than conventional antenna measurement ranges, the proposed system provides good results and an enormous flexibility.

Finally, among the challenges derived from handheld measurements, it should be remarked that, in both of the proposed handheld systems, the processing algorithms must be able to deal with non-uniformly spaced data.

1.2 State of the art

The use of electromagnetic signals to build positioning systems is of great interest, and a wide-variety of systems based on different technologies have been developed. In particular, the use of Bluetooth [25, 26], WiFi [27, 28], Ultra Wide Band [29], ZigBee [30] and RFID [31, 32] signals has been evaluated for different applications. On the other hand, the use of positioning systems enables to build advanced electromagnetic applications, especially in the fields of electromagnetic imaging [20, 33] and antenna measurement [23, 34]. In this dissertation both approaches, from electromagnetic signals to positioning systems and vice versa, were adopted. In particular, for the first approach it was decided to use passive

RFID technology due to its cost-effectiveness and its ease of integration in the supply chain processes. Regarding the second approach, flexible measurement systems for NDE and antenna characterization were developed.

This section is devoted to provide a review of the state of the art in the fields of advanced RFID applications (Section 1.2.1), radar imaging (Section 1.2.2) and antenna diagnosis and characterization (Section 1.2.3).

1.2.1 **Advanced RFID applications**

The architecture of RFID systems is based on two different elements. On the one hand, RFID systems comprise RFID tags, which can be either active, semi-passive or passive [35], being the former of special interest due to their lack of batteries and their significantly low cost. On the other hand, the second basic component of an RFID system is the RFID reader, which interrogates or queries the RFID tags. Although there are several RFID standards for different frequency bands and applications, one of the most relevant and widespread is the EPC UHF Gen2 [36]. This standard, which was the one used within this thesis, is defined for RFID systems comprising readers and passive tags, operating in the 860 MHz − 960 MHz Ultra High Frequency (UHF) range (reduced to 865.6 MHz − 867.6 MHz under the European Telecommunications Standards Institute (ETSI) regulations).

Under the EPC UHF Gen2 protocol, the RFID reader sends an interrogation signal to a passive RFID tag, which is powered up and backscatters the signal sent by the reader including its identification code. In addition to the identification code of the tag, some RFID readers are also capable of extracting physical information from the backscattered signals such as the Received Signal Strength Indicator (RSSI) or their phase. Although the read range of passive tags is reduced to less than 10 m, their low-cost and practically lack of maintenance have contributed to the development of a wide range of RFID-based applications in multiple sectors such as retail [1, 2], healthcare [ii] or supply chain and logistics [37].

In particular, the development of positioning systems has been of great interest. Most of them are based on RSSI measurements of the signal backscattered by RFID tags, as this is the parameter provided by most of the commercial readers [6–8]. However, there are other recent developments based on phase information of the backscattered signal such as [9–13], where tag positions are estimated using measurements from several antennas, or [14], where the trajectory of the tagged item is known and only one antenna is used. Apart from position estimations, the knowledge of the attitude of goods provides complementary information, which can be used to automate logistic processes or when handling fragile cargo. This

information can be obtained with inertial sensors (although they are more expensive than RFID tags and require batteries), using RFID tags and antennas with high directivity as proposed in [38], or by means of a computer vision system, which requires line of sight conditions and may raise privacy concerns [39]. In this regard, a system to estimate the attitude of goods based on phase measurements of an array of RFID tags is proposed within this thesis [**II**].

In contrast, in some applications it is not necessary to accurately measure the position of tagged items, but rather to identify specific actions such as entering or exiting from a warehouse area. For this purpose, different approaches were proposed to implement UHF-RFID control gates in the points of interest across the supply chain. Some of them are based on creating controlled reading zones isolated from their surroundings by using tunnel gates [40], while others rely on extra hardware (e.g. motion sensors or cameras) to determine when a cargo was crossing a point of interest [41, 42]. However, although effective, those solutions require extra space, cost and complexity, which in case of using cameras may also result in privacy concerns, as in the previous example in the context of attitude determination. Other alternatives employ the signature captured from different reader antennas to estimate the movement direction of tagged goods [43] or use machine learning techniques and low-level parameters, such as the RSSI or the amount of time passed until a tag first replies to the reader's interrogation signal [44]. Alternatively, the phase of the tag backscattered signal can be employed by taking advantage of the movement of items carried by a forklift [45] or which move along a conveyor belt [46]. In this context, based on the concept of shadowing in RFID systems, which was previously used in device-free localization [47, 48], a simple and easy-to-deploy system to monitor the transit of goods at checkpoints or docking gates from a warehouse was developed during this thesis [**III**].

1.2.2 **Radar imaging**

Electromagnetic imaging [49] enables the formation of camera-like images in low visibility conditions such as fog, clouds, smoke or during the night, and to inspect the inner composition of different objects or beings as it provides some penetration capabilities.

It relies on processing the electromagnetic waves acquired by one or multiple receivers. The interaction of these waves with the media modifies their properties. Therefore, the measured electromagnetic waves can be processed to extract information of the scenario that is being imaged.

Electromagnetic imaging can be employed, under different implementations, for NDE of materials [50, 51], medicine [52], defense and security [53–55], food inspection [56, 57] or obstacle detection [58], among other applications.

The number of technologies to perform electromagnetic imaging is vast; each of them exhibiting several advantages and disadvantages. Passive imaging is carried out by capturing the radiation emitted by a given scene. Usually, the goal of passive imaging is to capture spontaneous radiation and, therefore, high-gain antennas are required, making the size of these systems large [59]. Moreover, the contrast of the achieved electromagnetic images depends on the illumination of the scenario, with outdoor scenarios outperforming indoor ones. On the other hand, sometimes the goal of passive imaging is to capture the radiation emitted by specific sources, such as a circuit boards in order to evaluate Electromagnetic Interference (EMI) [15]. In these cases, antenna gain requirements can be relaxed but the system is limited to detect strong electromagnetic sources.

In contrast to passive imaging, active imaging is based on artificially illuminating the scenario using transmistters. There are several approaches to perform active imaging. One is to resort to inverse scattering techniques, which try to estimate the dielectric permittivity of an object (i.e., its composition) from its scattered field by inversely solving the Maxwell equations. These techniques are usually used at relatively low frequencies as the computational burden quickly becomes prohibitive depending on the electrical size of the object under test [51]. Other systems rely on high directivity antennas (reflectors or lenses) whose beam is mechanically steered to scan a target [33]. Due to their working principles, these systems can only provide focused images on a limited range. Moreover, the stand-off distance is usually large, which can be a useful feature or a handicap depending on the application. Lastly, other systems are based on SAR methods. In these systems, the range resolution depends on the bandwidth, which does not impose a specific size limitation. On the other hand, the lateral resolution is proportional to the size of the (either real or virtual) aperture of the system.

Consequently, although a single transmitter and receiver system can be relatively small, high resolution imaging needs a dense set of transmitters and receivers or relatively large structures to do raster scanning along well-known paths [53]. The required number of transmitters and receivers can be reduced by leveraging MIMO (also known as multistatic) schemes [60, 61]. Alternatively, other systems use the movement of targets to apply inverse SAR techniques [62].

A balance between system size and resolution has been presented in [17] implementing a portable microwave camera operating from 20 to 30 GHz. Moreover, this kind of system can take advantage of multiview approaches to increase both the imaged area and the image quality [18–21]. In addition, a different microwave camera of reduced size based on chaotic excitation SAR, which has low resolution

but can be used in applications where high-fidelity images are not necessary, has been presented in [22].

On the other hand, the quick development of mm-Wave technology has enabled very compact and affordable on-chip radar systems at the expense of reduced penetration capabilities and low resolution due to their small aperture [63–65]. Nonetheless, a much larger synthetic aperture can be achieved by tracking the radar modules. In this context, the system developed within this thesis leverages modern advances in position tracking [15, 16] to build large synthetic apertures by moving the radar module performing freehand trajectories over the area being imaged. Freehand scanning constrained to two dimensions has also been demonstrated in [66] by implementing a system in the X-band and using a railway system to track the position and in [67] by indirectly mapping electromagnetic sources resorting to backpropagation. However, to the best author's knowledge, the system developed within this thesis [**IV**] is the first that performs SAR imaging with a completely Three-Dimensional (3D) freehand scanning and such a compact device. Among the different challenges that had to be overcome, it should be remarked that the potential SAR processing techniques to be used in this system were limited by the irregular sampling of the data obtained with a freehand scan. In particular, a quasi-monostatic approach was first adopted and, afterwards, the system was extended to a MIMO configuration yielding a significantly faster scanning speed and higher-quality images.

1.2.3 **Antenna diagnosis and characterization**

Antennas are a key element in any telecommunication system and, as such, it is necessary to characterize their behavior. A fundamental property of an antenna is its FF radiation pattern, which can be measured using different approaches.

One way is to directly measure the antenna under test in the far-field region ($r \geq 2D_{AUT}^2/\lambda$ and $r \gg \lambda$, where D_{AUT} is the diameter of the minimum sphere that encloses the AUT and λ is the wavelength in free space). The main drawback of these facilities (either in indoor anechoic chambers or outdoor elevated ranges) is that the FF distance may be more than several meters [68]. The Compact Antenna Test Range (CATR) overcomes this limitation creating a plane wave illumination in a quiet zone (where the AUT is placed) by using a reflector to collimate the spherical waves from the feed antenna. On the other hand, CATRs require complex and costly infrastructure as the reflector should be at least three times the size of the AUT. Moreover, its surface must be very accurate in order to achieve good performance and usually additional structures (e.g., serrations) have to be added to mitigate diffraction [68, 69].

Another option is to retrieve the AUT radiation pattern indirectly from amplitude and phase Near-Field (NF) measurements (acquired at a distance from the AUT aperture from several wavelengths -to avoid the reactive coupling- to the FF region). There are three typical near-field measurement topologies depending on the acquisition surface: spherical, cylindrical and planar [70, 71]. In spherical measurements the probe always points towards the AUT and the closed spherical scan surface ensures that all radiation from the antenna under test is measured [72]. In cylindrical acquisitions, the AUT is usually rotated about a single axis while the probe is moved along a line parallel to the rotation axis [73]. This approach is useful for fan-beam antennas whose pattern is directional in one axis and broad in the orthogonal one. Lastly, in NF planar measurement setups the acquisition plane is defined in front of the antenna aperture and the probe heading is constant and orthogonal to the acquisition plane [69]. This technique is best suited for antennas with high directivity since almost all the radiated energy passes through the planar acquisition surface. It should be remarked that using both cylindrical and planar configurations, in contrast to spherical measurements, the scanning surface does not completely encloses the AUT, yielding to truncation errors. As a consequence, the far-field radiation pattern retrieved from those measurements is only valid in an angular margin, which depends on the AUT size, its distance to the scan surface, the size of the scan surface and its shape (planar or cylindrical) [71, 74]. Wider angular margins can be obtained in planar ranges by means of the poly-planar approach (perform several planar scans at different orientations to the AUT) [69]. A detailed description of other error sources such as probe and AUT misalignments, reflections or positioning errors can be found in [71, 75]. The accurate alignment and positioning of antennas becomes more challenging as the frequency increases [76]. In this regard, most of the state-of-the-art mm-Wave antenna characterization systems resort to one [77–81] or more [82] robotic arms for antenna positioning, which are sometimes supported by additional positioning equipment such as laser trackers [77].

In many cases, it is preferable to use amplitude-only data instead of performing a full-acquisition of the field radiated by the AUT. The main reasons for adopting such approach are: i) the use of flexible cables to guarantee the same phase reference is not always possible (e.g, antennas under operational conditions); ii) amplitude-only acquisitions are significantly less demanding than full acquisitions in terms of hardware and, therefore, the overall cost of the measurement equipment is reduced; and iii) despite the continuous development of technology, the acquisition of phase information at high frequencies (e.g., submm-Wave band) is challenging as cable bending before frequency multiplication can have a significant impact in the phase results and, moreover, equipment is not always commercially available beyond the submm-Wave band [83]. For this purpose,

different phase retrieval schemes have been proposed. On the one hand, interferometric techniques are based on mixing the measured signal with a reference signal, whose radiated fields are well-known [84–86]. On the other hand, phase information can also be retrieved using different probes [87–89], which encode the phase information by means of providing the output of several linear combinations of the field at different points, or by using multiple acquisition surfaces [90–94].

It is also relevant that there are situations in which it is necessary to assess the correct operational conditions of an antenna. In this regard, antenna diagnosis aims to detect malfunctions on radiating systems. Several antenna diagnosis methods have been proposed with different scopes.

On the one hand, a large family of antenna diagnosis techniques is devoted to the detection of faulty elements by analyzing the impact of one or more failures in the FF pattern [95, 96]. Since the number of faulty elements is usually expected to be low, this kind of problem can be formulated as a compressed sensing problem taking advantage of the benefits of this technique with respect to sampling [97]. In addition, similar techniques exploiting NF rather than FF observations are also available [98]. Although the number of techniques in this family is large, the general advantages are that they can operate with a small number of samples and that they are computationally efficient. The drawbacks are: i) a limited amount of information is provided by these techniques as they only give information about the status of elements, which is usually reduced to a binary observation (i.e., healthy or not); and ii) a potential relatively wide angular scan may be required when operating in the FF, which is not always possible.

On the other hand, another large family of techniques exploits the Huygens' principle to reconstruct an equivalent currents distribution at a surface enclosing the AUT. These equivalent currents radiate the same fields as the AUT at any point outside the surface enclosing it [99–101]. In addition, in some cases (e.g. planar antennas, aperture antennas) the surface enclosing the AUT can be truncated to a finite size plane, as most of the energy radiated by the AUT is contained in such plane [102].

In contrast to faulty element detection methods, the equivalent currents-based techniques provide information about both the amplitude and phase of the fields around the antenna. Moreover, the FF radiation pattern can be calculated from the reconstructed equivalent currents by means of a near-field to far-field transformation. Consequently, these techniques are able to detect the amplitude and phase of each element of the antenna as well as other undesired effects such as unwanted reflections in the antenna itself or its neighborhood, which can be efficiently removed [103, 104]. This insightful information comes at the expense of computationally intensive algorithms to solve the system of equations. How-

ever, this last point has been alleviated by means of several approaches such as the Fast Multiple Method (FMM) [105, 106], the Adaptive Cross Approximation (ACA) [107] or the use of Graphics Processing Units (GPUs) [108].

Although equivalent currents-based techniques can be employed for antenna diagnosis using arbitrary-geometry measurement and reconstruction domains [100, 109], most of sources reconstruction methods are intended to work with data coming from regular grid acquisitions such as planar [110], cylindrical or spherical [100, 111] acquisitions. However, it is relevant to observe that irregularly sampled data has been recently considered by some diagnosis methods to take into account possible deviations from a regular grid, i.e., positioner errors that can be tracked. In particular, quasi-cylindrical, -spherical and -planar data has been studied for diagnosis and near-field to far-field transformations based on plane or spherical wave expansions [112–114], which can also be formulated in terms of a linear system of equations but relating electromagnetic modes rather than equivalent currents (see [115] for a detailed comparison). In the specific framework of sources reconstruction, irregular sampling has been considered on systems based on a large gondola-positioner in which accurate position control is not possible [34] and on systems based on Unmanned Aerial Vehicles (UAVs) [23]. It should be remarked that the use of amplitude-only data is also of great interest in the context of antenna diagnosis [83]. In particular, a modified version of the Sources Reconstruction Method (SRM) [99], the Phaseless Sources Reconstruction Method (pSRM) [116] has been successfully tested for arbitrary acquisitions obtained with a UAV-mounted probe [23]. In this context, a handheld system which provides fast diagnosis and characterization of antennas, both in laboratory conditions for quick testing and for in-situ measurements (to assess the performance of already deployed antennas), was developed within this thesis [**V**]. In particular, the proposed system considers both a full-acquisition and amplitude-only measurements. It should be remarked that this system faces similar challenges in terms of the irregular distribution of the acquired samples as the aforementioned freehand imaging system developed within this dissertation.

1.3 Research objectives and contributions

The overall goal of this thesis is to explore the development of advanced positioning and tracking systems using electromagnetic signals emitted by sensors or general purpose devices, as well as the design of systems for advanced electromagnetic applications built on positioning systems.

In particular, the specific goals defined in this thesis and the relative contributions are:

- Design of a cost-effective system capable of providing attitude information of tagged items. This is a achieved by using the phase of the signal backscattered by the passive RFID tags of an array attached to the tracked items [xviii], [xvii], [**II**]. The use of the proposed system for localization purposes was evaluated in [xvi] and a technique to retrieve the phase of the signal backscattered by a RFID tag in a bistatic configuration was developed in [**I**].

- Development of a simple and easy-to-deploy system to monitor the transit of tagged goods based on RFID technology. A system based on a reference array of passive RFID tags deployed at the checkpoint going to be monitored was proposed and validated under laboratory conditions [xi], [**III**].

- Implementation of a strategy to ensure a proper sampling when using a handheld scanner. The proposed technique, presented in [**IV**] and [**V**], is based on defining an acquisition volume resembling a planar acquisition domain, which is discretized in cells where the number of samples is limited.

- Development and validation of a real-time handheld imaging system able to provide high-resolution images. The concept of freehand radar imaging using a handheld scanner was presented and validated in [v] and [**IV**]. In particular, the impact of positioning and calibration errors was evaluated, considering both a quasi-monostatic scheme and a MIMO configuration.

- Development and validation of a handheld system for antenna diagnosis and characterization considering both full-acquisitions and amplitude-only measurements. The concept of freehand antenna diagnosis and characterization using a handheld probe was introduced and validated in [x], [ix] and [**V**] considering full-acquisitions. The use of amplitude-only measurements was tested in [iv].

1.4 Innovation and applicability

The systems developed in the framework of this dissertation exhibit several novelties and advances compared to existing state of the art systems.

Regarding the RFID-based systems, on the one hand the retrieval of the attitude of tagged goods can be used to improve the automation of logistic processes or when handling fragile cargo, complementing already available positioning systems. On the other hand, the system proposed to monitor the transit of goods at checkpoints can be employed to enhance the traceability across the supply change in a cost-effective and simple way.

Concerning the handheld imaging system, the proposed solution is able to provide real-time, high-resolution electromagnetic images of the inspected areas. In particular, the presented system, which stands out for its compactness and flexibility, can be used for security and NDE applications, among others.

Finally, the proposed handheld system for antenna measurement allows the fast diagnosis and characterization of antennas. This is of great interest in different applications such as the quick performance evaluation of antennas in laboratory conditions, or the characterization of already deployed and on-board antennas. In particular, the wide operational frequency range of the proposed system, validated from X band to sub-mmWave frequencies, is a significant advantage as there is a growing number of applications (for example for high-capacity communications) exploiting these bands.

1.5 Outline of the thesis

The following chapters of this dissertation are organized according to the previously described contributions. Thus, Chapter 2 covers the development of the RFID-based systems to track the position and attitude of goods. Next, the design and validation of the freehand imaging system is explained in Chapter 3. Following a similar structure to the previous chapter, the freehand systems for antenna diagnosis and characterization are presented in Chapter 4, including the results obtained across different frequency bands. Finally, conclusions and future lines are drawn in Chapter 5.

CHAPTER

2

2. Radiofrequency Identification technology for localization

This chapter is devoted to summarize the results presented in the publications composing this dissertation in the field of RFID technology applied to positioning systems. The development and the increasing use of RFID technology have led to its adoption in multiple sectors. In particular, it is an essential technology for supply chain management and logistics applications, where it can be used for the tracking and localization of goods. In this regard, a system which provides attitude information of tagged goods, complementary to position estimations, based on the use of an array of passive tags is presented in Section 2.1. In addition, a system to monitor the transit of goods at checkpoints and docking gates is introduced in Section 2.2.

2.1 Attitude estimation using arrays of passive RFID tags

This section is devoted to summarize the system developed within this thesis to estimate the attitude of an object using arrays of passive RFID tags. The proposed system is based on acquiring phase measurements from the passive RFID tags that form the array attached to the object that is being tracked using a single antenna connected to an RFID reader. After a set of phase samples from each tag of the array is acquired, a direction finding algorithm is used to estimate the attitude of the object.

In particular, two different array topologies, Uniform Linear Arrays (ULAs) and Uniform Circular Arrays (UCAs), were studied. The basic scheme of a ULA, in which there is a constant inter-element spacing, formed by $N = 3$ tags is depicted in Figure 2.1a. Using a ULA and the proposed method, discussed in Section 2.1.1, unambiguous azimuth estimations in the range $\alpha \in [-90°, 90°]$ can be obtained. The basic scheme of a UCA, in which all the elements are uniformly spaced over a circumference of radius R, formed by $N = 8$ tags is shown in Figure 2.1b. In this case, both azimuth estimations in the range $\alpha \in [-90°, 90°]$ and elevation estimations in the range $\beta \in [-90°, 90°]$ can be retrieved.

2.1.1 Attitude estimation method

As previously stated, the proposed system employs a direction finding algorithm to retrieve the attitude of an array of passive RFID tags based on the phase measurements acquired from a single antenna connected to an RFID reader. In particular, the Multiple Signal Classification (MUSIC) algorithm [117], which is a high-resolution algorithm based on the eigendecomposition of the covariance matrix of the input data, has been selected. This algorithm requires the knowledge of

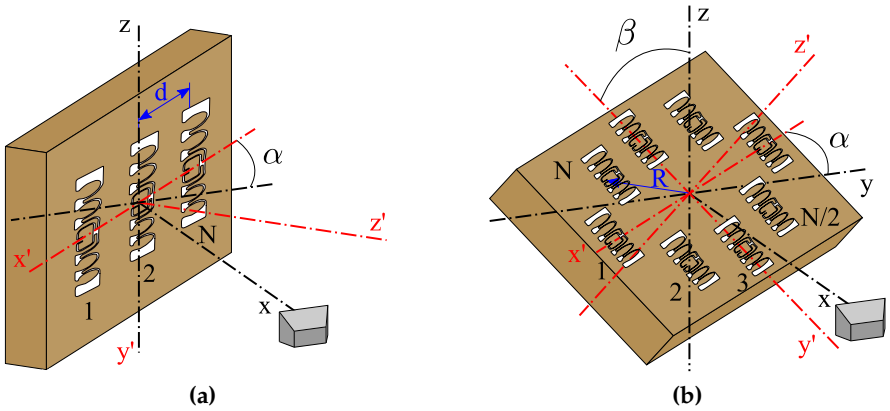

Figure 2.1: Scheme of the proposed setup to retrieve the attitude of an object using a ULA (a) and and a UCA (b).

the array geometry (theoretically or by calibration) to compute the array steering vectors, which are the phase shifts between each of the elements of the array and a reference when an incident plane wave impings the array from a given direction. At this point it should be noted that, if two different incident angles result in the same phase distribution along the elements of the array, i.e. the RFID tags, then an ambiguity in the azimuth and elevation will occur. Therefore, it is necessary to select an appropriate array geometry and to impose constraints if needed to avoid unambiguities.

In this regard, in [118] it was demonstrated that only 3D arrays can have linearly independent steering vectors for every possible incident direction. A sufficient condition for that linear independence is that the array must have at least 4 non-coplanar elements such that if the first element is placed at the origin of coordinates and each of the rest elements are located in a different reference axis, the distance between the first element and the remaining ones is less than $\lambda/2$. However, as previously introduced, we will focus on planar arrays, which are simpler to manufacture than 3D arrays and can be easily used in a practical application, and roll estimations will not be considered.

In [118], it was demonstrated that in planar arrays, such as a UCA, which have at least three non-colinear elements such that if one element is at the origin of coordinates and each of the two remaining ones is in a different axis of the array plane and the distance between them and the first one is less than $\lambda/2$, only pairs of directions have the same steering vectors. Hence, if the previous condition is satisfied, the steering vectors are unique within each of the two subspaces separated by the array plane, making possible to obtain unambiguously the Direction

of Arrival (DoA) of the signals impinging the planar array restraining the search space to one of those two subspaces. In addition, an equivalent condition is given for One-Dimensional (1D) DoA estimations using ULAs: the inter-element spacing should be less than $\lambda/2$. However, in the context of RFID, as it is necessary to account for the round-trip of the signals, the distance requirement has to be reduced to $\lambda/4$.

Once the DoA of the impinging signals has been estimated, it is only necessary to find its relationship with the azimuth and elevation angles of the array, α and β, respectively. In order to derive the expressions that relate the DoA of the impinging signals with the azimuth and elevation angles of the array, a Global Coordinate System (GCS), with coordinates $\boldsymbol{x}$, $\boldsymbol{y}$ and $\boldsymbol{z}$, denoted in black in Figure 2.1a and Figure 2.1b, is defined. Without loss of generality, the center of the array will be considered the origin of the GCS and the transmitter antenna will be placed at the *x-axis*, i.e., $\boldsymbol{r}_{ant} = (x_{ant}, 0, 0)$, and pointing towards the origin of the GCS.

In addition, an Array Coordinate System (ACS), denoted by the primed coordinates $\boldsymbol{x}'$, $\boldsymbol{y}'$, $\boldsymbol{z}'$ and depicted in red in Figure 2.1a and Figure 2.1b, is also defined. The array plane, i.e., where the RFID tags are placed, lies on the *x′-y′ plane* and the *z′-axis* points outwards. Hence, when both the azimuth and the elevation are zero ($\alpha = 0°$ and $\beta = 0°$) the axes of the ACS can be identified with those of the GCS as follows: $\boldsymbol{x}' = -\boldsymbol{y}$, $\boldsymbol{y}' = -\boldsymbol{z}$ and $\boldsymbol{z}' = \boldsymbol{x}$. The relationship between the GCS and the ACS as a function of the azimuth and the elevation angles is given by

$$\left.\begin{aligned} \boldsymbol{x}' &= -\boldsymbol{R}(\alpha,\beta)\cdot\boldsymbol{y} \\ \boldsymbol{y}' &= -\boldsymbol{R}(\alpha,\beta)\cdot\boldsymbol{z} \\ \boldsymbol{z}' &= \boldsymbol{R}(\alpha,\beta)\cdot\boldsymbol{x} \end{aligned}\right\} \tag{2.1}$$

where

$$\boldsymbol{R}(\alpha,\beta) = \boldsymbol{R}_a(\alpha)\boldsymbol{R}_e(\beta) = \begin{pmatrix} \cos(\alpha) & -\sin(\alpha) & 0 \\ \sin(\alpha) & \cos(\alpha) & 0 \\ 0 & 0 & 1 \end{pmatrix} \begin{pmatrix} \cos(\beta) & 0 & \sin(\beta) \\ 0 & 1 & 0 \\ -\sin(\beta) & 0 & \cos(\beta) \end{pmatrix}, \tag{2.2}$$

is the rotation matrix to perform two sequential rotations: first in azimuth, $\boldsymbol{R}_a(\alpha)$, and then in elevation, $\boldsymbol{R}_e(\beta)$.

On the other hand, the direction of arrival of the RFID signals impinging the array is given by the angles ϕ, measured counterclockwise from the *x′-axis* in the *x′-y′ plane*, and θ, which is the polar angle measured from the *z′-axis*. Therefore, taking into account that the direction of arrival of the signals is always the *x-axis*,

in order to compute the azimuth and elevation from the direction of arrival it is only necessary to express the *x-axis* in terms of the axes of the ACS and to identify its coordinates with the direction of arrival in terms of ϕ and θ, yielding the following equations:

$$\left.\begin{aligned} \sin(\alpha) &= \cos(\phi)\sin(\theta) \\ \cos(\alpha)\sin(\beta) &= \sin(\phi)\sin(\theta) \\ \cos(\alpha)\cos(\beta) &= \cos(\theta) \end{aligned}\right\} \tag{2.3}$$

Finally, the azimuth and elevation angles can be computed with the following equations:

$$\left.\begin{aligned} \alpha &= \arcsin(\sin(\theta)\cos(\phi)) \\ \beta &= \arctan(\tan(\theta)\sin(\phi)) \end{aligned}\right\} \tag{2.4}$$

The DoA estimation considering a ULA and a UCA is discussed in Section 2.1.1.1 and in Section 2.1.1.2, respectively.

2.1.1.1 **Uniform Linear Array**

In MUSIC algorithm [117], the general model of the input data, $\boldsymbol{y} = [y_1 \dots y_N]$, for an array of N elements and a single impinging signal is

$$\begin{bmatrix} y_1 \\ \vdots \\ y_N \end{bmatrix} = \boldsymbol{a}(\theta,\phi)s + \mathbf{n} \quad , \tag{2.5}$$

where s is the incident signal to the array transmitted by the reader, $\mathbf{n}$ is a vector modeling the noise at each tag and $\boldsymbol{a}(\theta,\phi)$ is the array steering vector of the incident signal, which has direction of arrival (θ,ϕ). In the case of a ULA, it is assumed that the array can only rotate about the *z-axis* and, thus, $\beta = 0^\circ$, $\phi = 0^\circ$ and $\alpha = \theta$. This is a common situation as when a box or a pallet are stored, they are usually placed upwards but they may be rotated about the axis orthogonal to the plane where they were laid down. Therefore, the array steering vectors, considering the first element of the array as reference, far-field conditions and taking into account the round-trip of the signals, are given by

$$\boldsymbol{a}(\alpha) = \begin{bmatrix} 1 & \dots & e^{-j\frac{4\pi}{\lambda}d\sin(\alpha)(N-1)} \end{bmatrix} \quad , \tag{2.6}$$

where λ is the wavelength of the signal and d is the inter-element spacing (see Figure 2.1a). Taking this into account, the direction of arrival of the impinging

signals can be obtained from the peak of the MUSIC pseudospectrum, whose expression is

$$P_{MUSIC}(\theta,\phi) = \frac{1}{\boldsymbol{a}(\theta,\phi)^H \boldsymbol{V_N} \boldsymbol{V_N^H} \boldsymbol{a}(\theta,\phi)}, \tag{2.7}$$

where $\boldsymbol{V_N}$ is the matrix which contains the eigenvectors of the noise subspace.

2.1.1.2 Uniform Circular Array

In the case of an UCA, the array steering vectors of the incident signal, which has direction of arrival (θ,ϕ) can be particularized to

$$\boldsymbol{a}(\theta,\phi) = \begin{bmatrix} e^{-2jkR\cos(\phi-\gamma_1)\sin(\theta)} \\ \vdots \\ e^{-2jkR\cos(\phi-\gamma_N)\sin(\theta)} \end{bmatrix}, \tag{2.8}$$

where k is the wavenumber, γ_n is the angle of the n-th element of the array measured counterclockwise from the *x'-axis*, and R is the radius of the array (see Figure 2.1b). This expression of the steering vectors corresponds to the traditional equation for a standard angle of arrival problem [119], but a factor of 2 has been introduced in the exponent due to the round-trip of the backscattered signal. It is relevant to remark that, as the positions of the elements of the array have origin symmetry, if the number of elements is even, the array steering vector of the $n + N/2$-th element is the conjugate of the steering vector of the n-th element. Therefore, as shown in [**II**], if a RFID tag of the array is not read but the opposite tag is, it would be possible to estimate the phase of the missing backscattered signal, increasing the robustness of the system.

2.1.2 Impact of positioning errors

The impact of positioning errors in the attitude estimations retrieved with the proposed system was studied through several simulations. In particular, the effect of discrepancies between the expected and the actual inter-element spacing of a ULA and between the expected and the actual radius of a UCA is analyzed. The impact of slightly misplaced RFID tags due to the array manufacturing process, both for the ULA and the UCA case, was assessed in [**II**], where it was concluded that for positioning errors below 5 cm, the errors of the estimated attitude angles were below 5°. All these simulations were performed using MatLab® and considering a frequency in the European RFID band: $f = 866.3$ MHz. In these

simulations, the phase of the received field, which was used to compute the attitude of the simulated array, was set to be proportional to the round-trip distance from the reader to each tag.

2.1.2.1 **Uniform Linear Array**

The impact of discrepancies between the expected and the actual inter-element spacing, d, of a ULA was evaluated simulating an array of $N = 5$ tags with an expected inter-element spacing of $d = \lambda/8$. The proposed system was tested for azimuth values of the simulated array within the interval $[-90°, 90°]$ and for a true inter-element spacing of $d = \lambda/7$, $d = \lambda/8$ and $d = \lambda/9$.

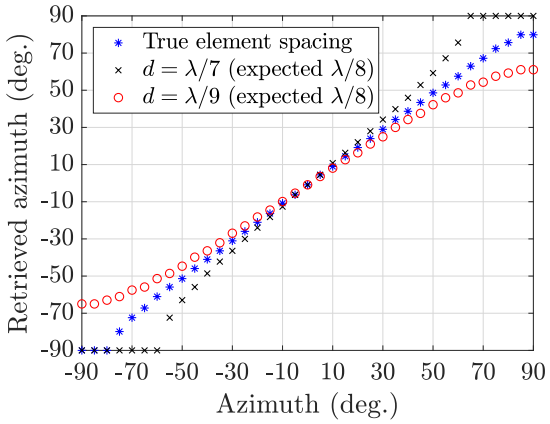

Figure 2.2: Estimated azimuth using a ULA of $N = 5$ tags with a expected inter-element spacing of $d = \lambda/8$ and a true value of $d = \lambda/7$ (black "x"), $d = \lambda/8$ (blue asterisks) and $d = \lambda/9$ (red circumferences).

The obtained results are depicted in Figure 2.2. As it can be seen, there is a good agreement between the estimated and the true azimuth when the expected and the true inter-element spacing are the same (blue asterisks), except for azimuth angles close to $\pm 90°$, for which the incident signals are almost parallel to the array of tags. In contrast, when the inter-element spacing is greater than expected, in this case $d = \lambda/7$, i.e., an error of 6.1 mm, the estimated azimuth is greater (in absolute terms) than its real value (black "x"). It should be pointed out that, in this case, for approximately $|\alpha| < 60°$ the estimated azimuth is $\pm 90°$. This is due to the fact that the maximum of the pseudospectrum is out of the visible region. Analogously, when the inter-element spacing is less than expected, in this case $d = \lambda/9$, i.e., an error of 4.8 mm, the estimated azimuth is smaller (in absolute terms) than its real value (red "circumferences").

2.1.2.2 Uniform Circular Array

In a similar fashion to the tests performed in Section 2.1.2.1, several simulations were carried out in order to study the impact of errors in the radius of a UCA in the the performance of the proposed system. For this purpose, an array of $N = 8$ tags with a expected radius of $R = 12\,\text{cm}$ was considered. The proposed system was tested for azimuth and elevation values of the simulated array within the interval $[-90°, 90°]$, and for a true radius of $R = 10\,\text{cm}$, $R = 12\,\text{cm}$ and $R = 14\,\text{cm}$.

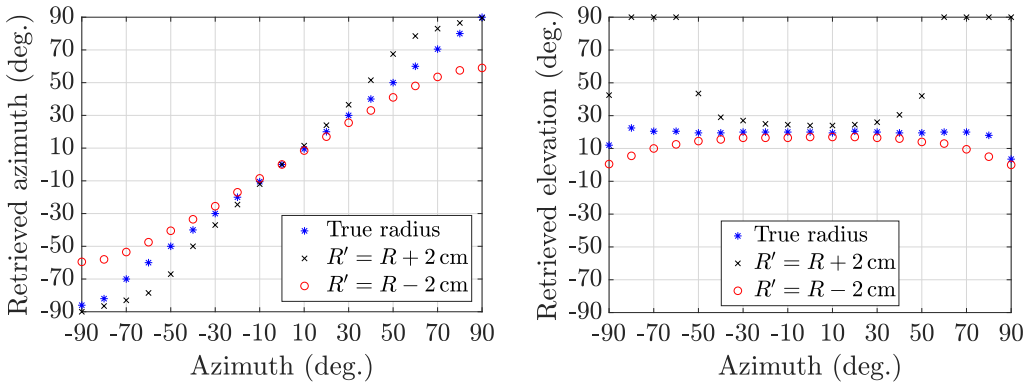

Figure 2.3: Retrieved azimuth, (a), and elevation, (b), for $\beta = 20°$ and $\alpha \in [-90°, 90°]$ when the expected radius of the UCA was equal to its true value (blue asterisks), smaller than expected (red circumferences) or greater (black "x").

The retrieved azimuth and elevation for $\beta = 20°$ and $\alpha \in [-90°, 90°]$ are shown in Figure 2.3a and in Figure 2.3b, respectively. As it can be observed, there is a good agreement between the estimated azimuth and elevation and their true values when the expected radius was equal to its true value (blue asterisks). In contrast, when the expected radius is smaller than its real value, the absolute value of the estimated azimuth is larger than the true azimuth value (red circumferences), and the same happens to the estimated elevation values. It should be remarked that the difference between estimated and true attitude values is greater as the azimuth of the UCA increases. Also, the discrepancies between the retrieved elevation values and the real ones increase as the true elevation angle is larger. When the expected radius is greater than the real one, as opposed to the previous case, the absolute estimated attitude values are smaller than the true ones (black "x"). It should be noted that this behavior is analogous to the one studied in Section 2.1.2.1 for errors in the expected inter-element spacing in ULAs.

2.1.3 **Impact of couplings and the electromagnetic properties of the material under the array**

In order to study the effect of couplings between RFID tags, a ULA of $N = 5$ tags, shown in Figure 2.4, was simulated in Feko® for several values of inter-element spacing d. The simulated tag model was based on the one proposed in [120], the simulated azimuth ranged from $-70°$ to $70°$ and the frequency was set to $f = 866.3\,\text{MHz}$. To compute the phase of the signals backscattered by a given tag, the activated tag was loaded to the complex conjugate impedance of the antenna and the rest of the tags of the array were short-circuited [121].

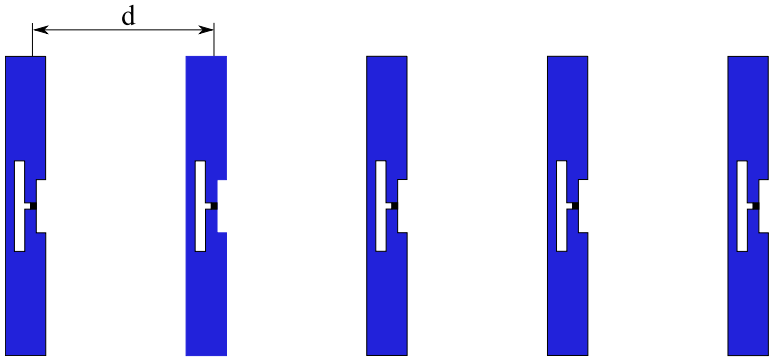

Figure 2.4: Model of the simulated array of tags.

The obtained results are summarized in Table 2.1, where ϵ_{rms} is the Root Mean Square (RMS) error of the estimated azimuth and σ is its standard deviation. As can be seen, as the distance between elements decreases, i.e, there are more couplings between elements, the RMS error increases. It should be remarked that the retrieved azimuth for the different orientation angles of the simulated array had the same trend as the one observed in Section 2.1.2.1 when the true inter-element spacing was greater than the expected one. Therefore, it was decided to compute the azimuth of the simulated ULA considering an expected inter-element spacing greater than its true value. In particular, the expected inter-element spacing was increased by the correction term Δ, which is also included in Table 2.1. The RMS error and the standard deviation of the estimated azimuth obtained considering the correction term, $\epsilon_{rms,\Delta}$ and σ_Δ, respectively, are summarized in Table 2.1. As it can be seen, when the correction term is included, the effect of couplings between elements is compensated. In addition, it must be noted that the simulated tag model is very simple and it was not optimized and, thus, the effect of couplings is expected to be lower in the well-designed commercially available RFID tags.

	$\epsilon_{rms}\,(^\circ)$	$\sigma\,(^\circ)$	$\Delta\,(\mathrm{mm})$	$\epsilon_{rms,\Delta}\,(^\circ)$	$\sigma_\Delta\,(^\circ)$
No coupling	1.3	0.6	—	—	—
$d = \lambda/4$	3.9	1.9	3	2.0	1.5
$d = 3\lambda/16$	7.5	4.4	4	3.5	2.2
$d = 5\,\mathrm{cm}$	11.0	6.0	6	5.1	3.5
$d = \lambda/8$	15.1	8.9	7	6.8	4.5

Table 2.1: RMS error and standard deviation with and without correction of the estimated azimuth retrieved with the simulated ULA of $N = 5$ tags for different values of inter-element spacing.

The effect of the electromagnetic properties of the material below the array of RFID tags was also evaluated by adding a substrate of dielectric material underneath the simulated array. The simulated relative permittivities were not very high as the array of tags would be usually placed above cardboard or plastics with low infill percentage. The results are shown in Table 2.2. As it can be seen, the higher the permittivity is, the higher the effect of couplings is, which, again, can be compensated after a calibration process as previously discussed.

	$\epsilon_{rms}\,(^\circ)$	$\sigma\,(^\circ)$	$\Delta\,(\mathrm{mm})$	$\epsilon_{rms,\Delta}\,(^\circ)$	$\sigma_\Delta\,(^\circ)$
$\epsilon_r = 1$	7.5	4.4	4	3.5	2.2
$\epsilon_r = 1.1$	8.2	4.5	4.5	4.2	2.9
$\epsilon_r = 1.2$	9.1	4.8	5	5.1	4.0
$\epsilon_r = 1.4$	11.6	6.1	6	6.6	5.5

Table 2.2: RMS error and standard deviation with and without correction of the estimated azimuth retrieved with the simulated ULA of $N = 5$ tags for different values of permittivity of the material below the array.

2.1.4 **Measurement results**

The performance of the system was experimentally evaluated through measurements in the facilities of the University of Oviedo in a controlled environment and in an indoor scenario. All measurements were performed with the commercial reader Speedway Revolution Reader of Impinj®. It must be pointed out that this reader randomly introduces an ambiguity of 180° on its phase measurements, i.e, it is not possible to know if the phase value provided by the reader is the true value or that value plus 180°. The phase jumps were corrected with two different approaches (one for the ULA and one for the UCA) as detailed in the following sections. It should be noted that, although not all of the commercially available

RFID readers provide the phase of the signals backscattered by RFID tags, a method to compute its value, considering a multistatic configuration, was proposed in [**I**].

2.1.4.1 **Measurements with a ULA**

In order to assess the performance of the proposed system employing a ULA, an array of $N = 5$ tags was considered. The selected tag model was the *Smartrac ShortDipole* RFID Paper Tag with the Monza 5 chip [122] and the antenna connected to the RFID reader was the *WIRA 30* model of KATHREIN [123]. In addition, the measured azimuth of the array ranged from -90° to 90°. Initially, the inter-element spacing was set to $\lambda/8$ in order to overcome the phase ambiguity introduced by the RFID reader at the expense of higher couplings between tags (if $d = \lambda/8$, the maximum phase difference between consecutive tags is 90° and, thus, the phase ambiguity can be solved). However, after a calibration stage [**II**], in which the phase offset of each tag was measured, it was concluded that the *effective separation* separation between the tags of the array was greater than its *physical separation*, i.e., $\lambda/8$, due to the electromagnetic properties of the surface below the array [122, 124]. As a consequence, in order to compensate this effect, the inter-element spacing was reduced to 3.4 cm ($\lambda/10$).

The results of the first measurements, performed inside the anechoic chamber of the University of Oviedo with the setup shown in Figure 2.5a, after the calibration, are depicted in Figure 2.5b. As it can be seen, the retrieved azimuth (red circumferences) is in good agreement with the true azimuth of the array, shown with blue asterisks. In particular, the accuracy of the system is high among a wide angular range, approximately for $|\alpha| \leq 75^\circ$, with errors below 5° (the dashed blue lines enclose a $\pm 5^\circ$ tolerance region with respect to the true azimuth values).

After the tests performed in a controlled environment, the proposed system was evaluated in an indoor scenario with the setup shown in Figure 2.6a and the same ULA. In this case, the azimuth of the array was modified using a manual positioner. The estimated azimuth values are shown in Figure 2.6b. Analogously to the results obtained inside the anechoic chamber, after the calibration the proposed system shows a good performance within a wide angular range ($|\alpha| \leq 75^\circ$), with a maximum error of $\epsilon_{\alpha,max} = 10.6^\circ$ and a RMS error of $\epsilon_{\alpha,rms} = 4.7^\circ$.

2.1.4.2 **Measurements with a UCA**

The second set of tests was devoted to assess the performance of the proposed system employing a UCA of $N = 8$ tags and $R = 12$ cm, and considering both azimuth and elevation estimations. In particular, the selected RFID tag model

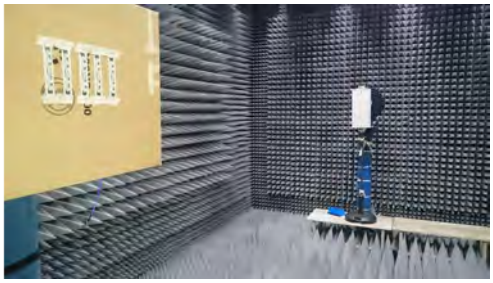

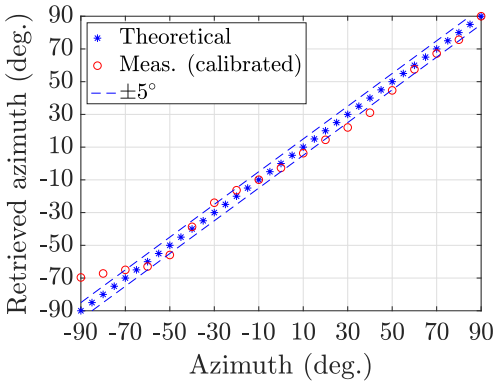

(a) **(b)**

Figure 2.5: Measurement setup in the anechoic chamber of the University of Oviedo (a) and retrieved azimuth for $\alpha \in [-90°, 90°]$ considering a ULA of $N = 5$ tags (b).

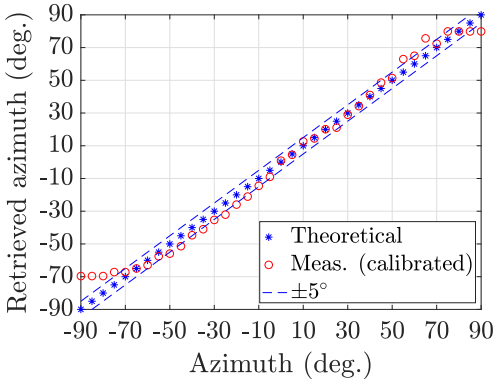

(a) **(b)**

Figure 2.6: Measurement setup in an indoor scenario (a) and retrieved azimuth for $\alpha \in [-90°, 90°]$ considering a ULA of $N = 5$ tags (b).

for this measurements was the *Smartrac Dogbone* [125] with the *Monza R6* chip [126] and the antenna connected to the reader was the *WANTENNAX019* model of CAEN RFID [127]. In this case, the phase ambiguity introduced by the reader is solved making a reference measurement at the initial position and attitude and, then, tracking the phase values to correct the 180° increments. As in the measurements presented in Section 2.1.4.1, the UCA was calibrated following the procedure described in **[II]**.

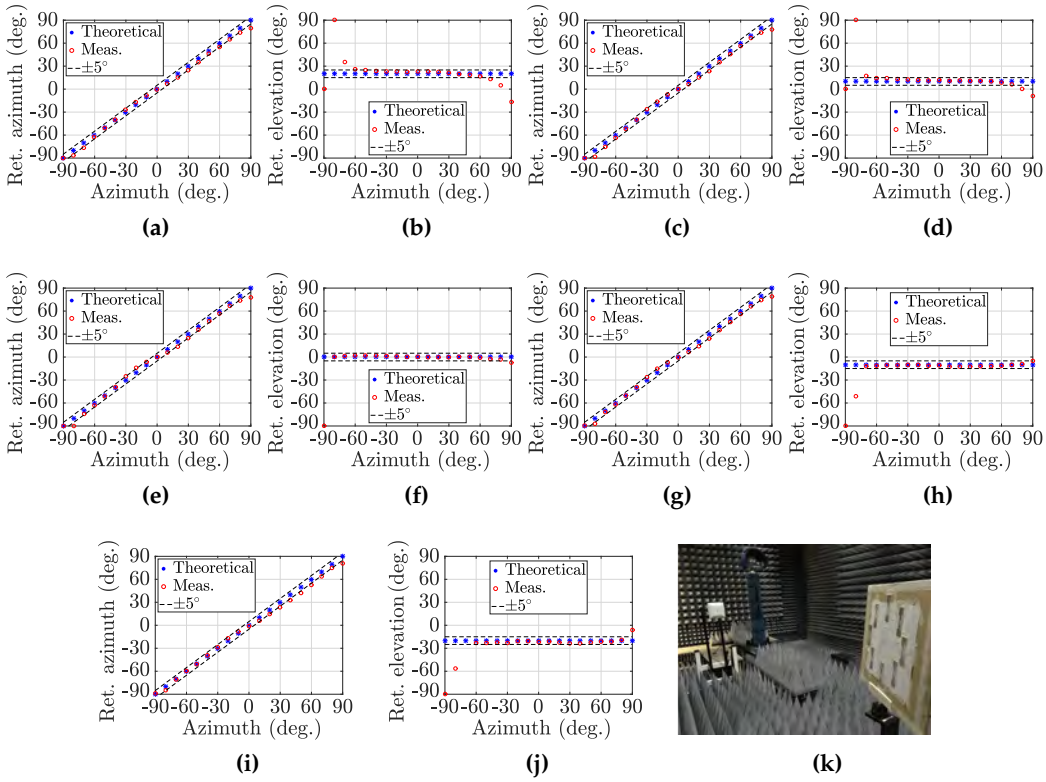

Figure 2.7: Retrieved azimuth and elevation for $\alpha \in [-90, 90]$ with 10° steps and $\beta = 20°$ (a) and (b), respectively; for $\beta = 10°$ (c) and (d), respectively; for $\beta = 0°$ (e) and (f), respectively; for $\beta = -10°$ (g) and (h), respectively; and for $\beta = -20°$ (i) and (j), respectively. The measurement setup is depicted in (k).

The first set of measurements was also performed in the anechoic chamber of the University of Oviedo with the setup depicted in Figure 2.7k. In this case, the RFID tags of the UCA were placed on a piece of cardboard which was attached to a 3D printed plastic support structure. This structure was mounted on a metric goniometer on top of a rotary stage diameter to allow for precise angular adjustment in both azimuth and elevation. The measured attitude ranged from $-90°$ to $90°$ in azimuth and from $-20°$ to $20°$ in elevation (the maximum travel range of the goniometer).

The obtained results after the calibration are depicted from Figure 2.7a to Figure 2.7j. As it can be seen, the estimated azimuth values are very accurate even for grazing angles. The error of the retrieved elevation is also low, but in this case the accuracy is degraded for grazing angles, $|\alpha| > 60°$. In particular, the RMS

error for the azimuth and elevation estimations for $|\alpha| < 70°$ was $\epsilon_{\alpha,rms} = 3.9°$ and $\epsilon_{\beta,rms} = 3.1°$, respectively.

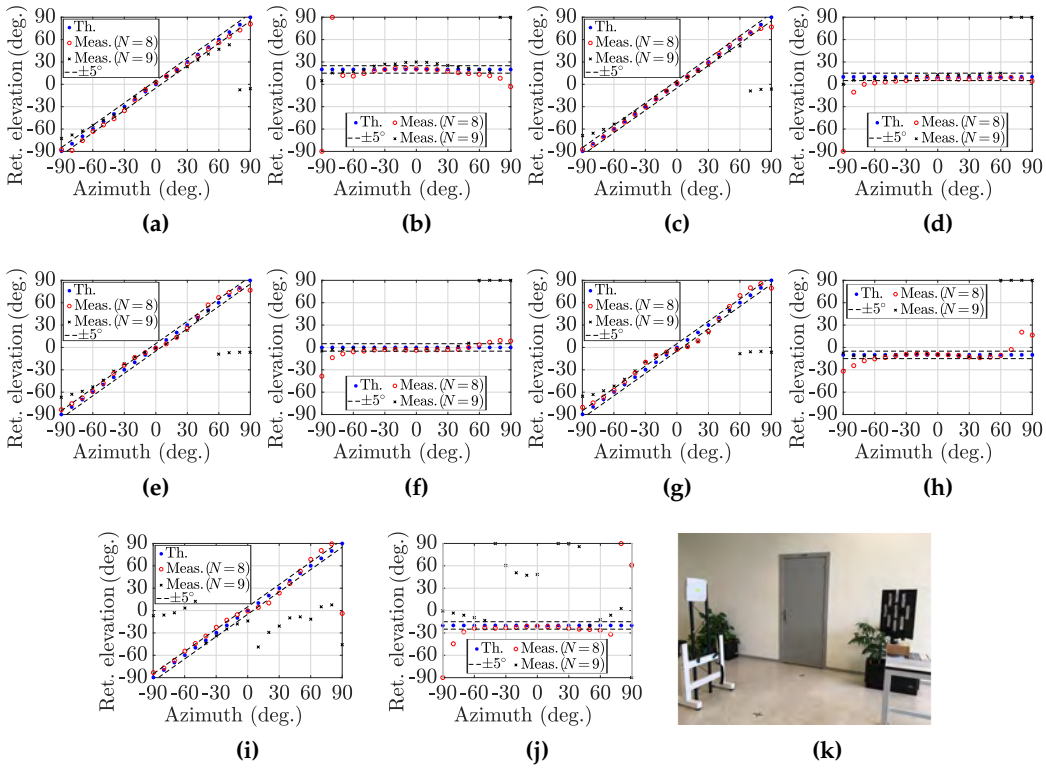

Figure 2.8: Retrieved azimuth and elevation for $\alpha \in [-90, 90]$ with 10° steps and $\beta = 20°$ (a) and (b), respectively; for $\beta = 10°$ (c) and (d), respectively; for $\beta = 0°$ (e) and (f), respectively; for $\beta = -10°$ (g) and (h), respectively; and for $\beta = -20°$ (i) and (j), respectively. The measurement setup is depicted in (k).

After the proposed system was validated employing a UCA in a controlled environment, its performance was tested in an indoor scenario. The measurement setup is displayed in Figure 2.8k. In this case the RFID tags of the UCA were placed on a 3D printed plastic plate instead of on a piece of cardboard. The rest of the structure used to modify the attitude of the UCA remained the same. In addition, for these tests a reference RFID tag placed at the center of the UCA was included to obtain more information without increasing the size of the array, which was recalibrated **[II]**.

The obtained results, considering the phase measurements of the eight tags of the original UCA ($N = 8$) and using all the available data ($N = 9$), are shown from

Figure 2.8a to Figure 2.8j. As it can be observed, although the performance using $N = 8$ tags is good or acceptable for a wide attitude range, there are some values (for example in the $\beta = -20^\circ$ cut) for which the results are very poor. In contrast, the accuracy of the proposed system using a central RFID tag is significantly improved. In particular, the RMS error for the azimuth and elevation estimations for $|\alpha| < 70^\circ$ was $\epsilon_{\alpha,rms} = 5.1^\circ$ and $\epsilon_{\beta,rms} = 4.6^\circ$, respectively.

2.2 Goods transit control at checkpoints using RFID tags

This section is devoted to summarize the system developed within this thesis to estimate if there are goods in transit at a checkpoint and, if so, to estimate their movement direction. This is common problem in warehouses, where the correct discrimination of goods or pallets transiting through a gate or between two warehouse areas is key.

2.2.1 System description

The proposed system relies on the use of a single RFID reader antenna and several passive RFID reference tags. The latter are deployed below the antenna, i.e., in the floor of the checkpoint which is going to be monitored, and arranged in a regular grid as depicted in Figure 2.9. The working principle of the system is based on the fact that when a transpallet, a metallic cart or a forklift moves through the checkpoint being monitored, the tags of the grid below it are shadowed, i.e., they are not read, producing a specific signature for each movement direction, which can be identified. The shadowing of the RFID tags is due to the block of the line-of-sight between them and the antenna of the reader by the metallic parts of the transpallet carrying the goods.

During the operation of the system, the RFID reader performs continuous inventories of the deployed RFID tags. In addition, in order to monitor the complete grid of reference tags over time to extract movement patterns, it is necessary to define time slots in which the reader must be able to read all the tags of the grid. As a consequence, it is possible to build a series of snapshots with information of the whole reference grid which can be used to estimate the movement direction of a transpallet carrying goods. Two important design considerations are the size of the reference grid and the duration of the time slots, t_{win}.

The size of the grid should be comparable to the size of the checkpoint being monitored. For the sake of clarity, the setup depicted in Figure 2.9 will be considered to explain the factors that must be taken into account during the design of the grid of tags. In Figure 2.9, the proposed system is used to monitor a docking

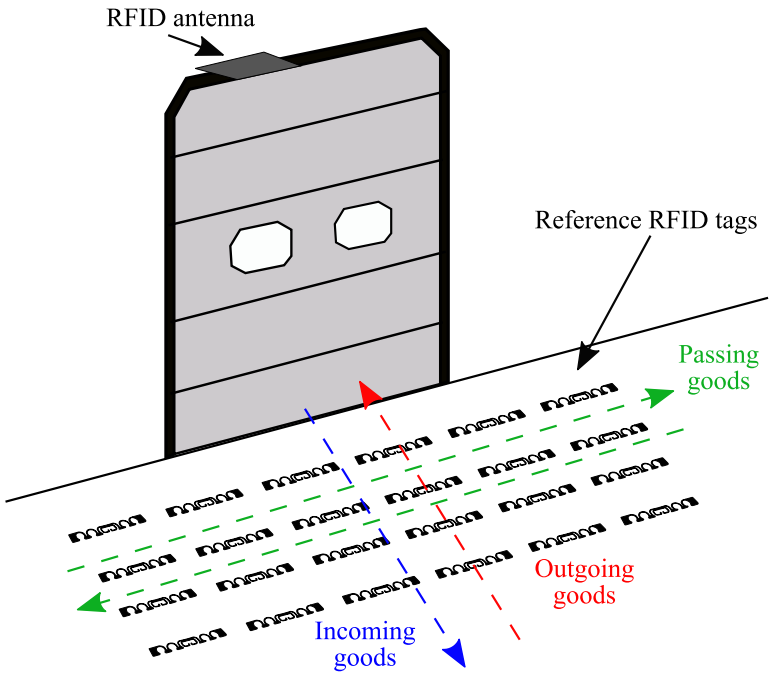

Figure 2.9: Basic scheme of the proposed system. Incoming, outgoing and passing movements are displayed in red, blue and green arrows, respectively.

gate of a warehouse. Therefore, the width of the grid, in this case the number of columns, should be similar to that of the docking gate (six in the example of Figure 2.9). The other dimension, the length of the grid, in this case the number of rows, should contain at least three or four lines of tags, so that when a transpallet moves over the grid it causes a consecutive shadowing of tags in different rows, which can be used to estimate its movement direction. Regarding the distance between the reference tags that form the grid, it should be large enough to reduce the couplings between them, while ensuring the tag shadowing during the transpallet motion. However, it should be remarked that the number of the RFID tags of the grid should not grow indefinitely as the reader must be able to read all of them within the duration of the time slots. In this regard, it should also be considered that other tags will be in the gate surroundings identifying different goods stored in the warehouse.

On the other hand, the duration of the time slots, t_{win}, should be adjusted so that the transpallet or forklift movements can be captured. This means that, if the time slot duration is too long with respect to the transpallet moving speed, some movements could be filtered out. In contrast, if the duration of the time slots is too short, the reader will not be able to read all the tags of the grid in the same

time slot, which would be misinterpreted as a shadowing effect caused by the movement of a transpallet or a forklift.

The shadowing of the tags of the reference grid caused by the movement of a transpallet or a forklift can be monitored through several parameters. In particular, the movement over the grid of tags can manifest in terms of an RSSI reduction, a decrease in the number of readings of each tag within each time slot or, analogously, the appearance of missed tags within a time slot, i.e., tags that were not read at all during a time slot. In this case, the use of RSSI was discarded as this parameter is more dependent from the specific scenario where the system is deployed than the other two (for example it can be influenced by the distance from the reader antenna to the grid, the material of the floor under the tags or the multipath effect typical of indoor scenarios).

During the development of this system, both the evolution of the number of readings of each tag within each time slot, and the binary information of whether a tag was read or missed during a time slot, were used as the input features of two types of neural networks used to estimate the movement direction of a transpallet. In particular, in [**III**], for each tag of the reference grid, the binary attribute read-/missed was used to build sequences that were used to feed a Long Short-Term Memory (LSTM) network [128], which is a particular kind of Recurrent Neural Network (RNN). On the other hand, in [xi], the number of times each tag of the reference grid was read during different time slots was used to create images that were classified using a Convolutional Neural Network (CNN) [129].

2.2.2 **Experimental analysis**

In order to validate the proposed system, laboratory tests were conducted at the research facilities of the Department of Information Engineering of the University of Pisa.

The measurement setup, depicted in Figure 2.10, comprised a reference grid of 24 tags arranged in a 4×6 matrix form with a spacing between tags of 30 cm. The size of the grid was selected so that it could be used to monitor the transpallet motion throughout a gate of width less than 2 m, a typical size for many warehouse and docking area doors. The reader antenna was fixed at the ceiling above the grid at a height of 2.6 m, and a 38 cm wide metallic cart, which was also tagged, was employed to emulate a transpallet. It should be noted that, in a warehouse scenario, usually the width of the transpallet or forklift carrying goods would be larger than 38 cm, yielding a more visible signature as more tags would be shadowed during its movement. In addition, it should be remarked that the architecture of the proposed system exploits the shadowing effect of the transpallet

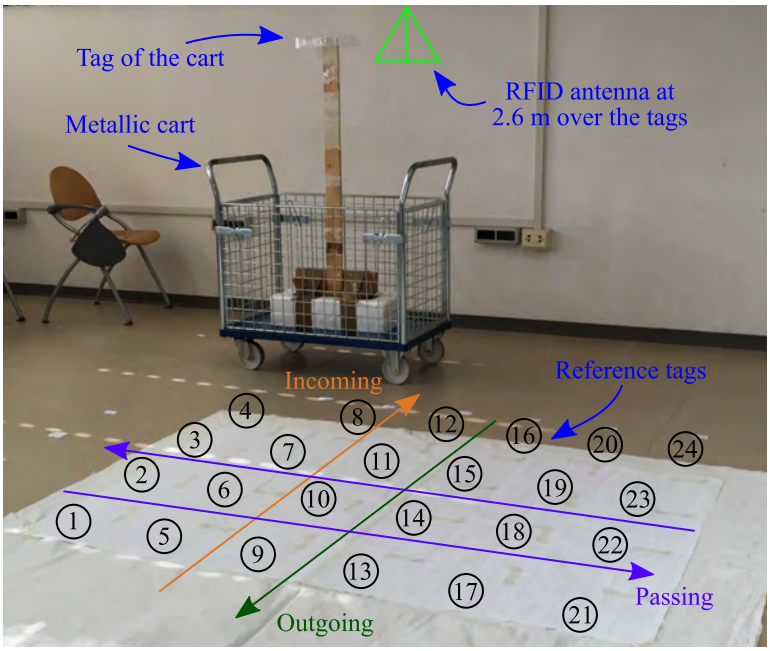

Figure 2.10: Measurement setup at the facilities of the University of Pisa. The numbering of the reference tags is shown to ease the interpretation of the results.

on the reference tags close to it, which is predominant with respect to the multipath phenomena, increasing the robustness of the proposed system with respect to other alternatives.

During the measurements, a total of 159 trajectories were performed while recording data from the tags of the reference grid. Among those trajectories, 50 had an incoming direction, 49 had an outgoing direction, and the last 60 were passing trajectories, i.e., in those trajectories the metallic cart did not cross the reference grid and, instead, it was moved in the orthogonal direction (see Figure 2.10). During each trajectory, the reference tags were queried continuously (before, during and after the metallic cart was moved over the grid), resembling the practical operation of the proposed system. The obtained data was divided in two groups: the first one with 60% of the data to train the neural networks, and the second one with the other 40% to test them. It should be noted that the different measurements were randomly assigned to one of the two groups. The same procedure was followed to train and test both the LSTM network and CNN.

As previously stated, it was decided to use the binary attribute read/missed in a time slot for each tag of the reference grid to feed the LSTM network. Therefore, the data input for the LSTM network are a set of N_{tags} sequences of length M

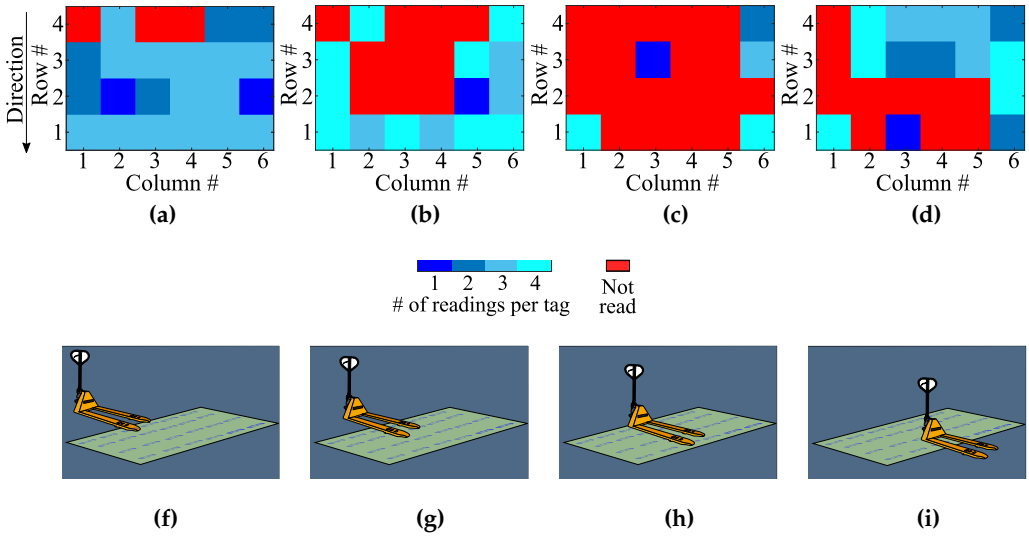

Figure 2.11: Number of readings of each tag of the reference grid during a time slot at four different snapshots of an incoming movement of the metallic cart from its beginning (a) to its end (d). Missed tags are depicted in red. A schematic representation of the metallic cart position within the setup corresponding to the snapshots presented from (a) to (d) is shown from (e) to (h), respectively.

containing read/missed information, where N_{tags} is the number of tags of the reference grid and $M = \lfloor T/t_{win} \rfloor$ is the number of complete time slots within the acquisition time of the trajectory, T. In this regard, it should be remarked that the system can be activated when a tagged transpallet is detected in the surroundings of the gate being monitored. The evolution of the number of readings of each tag of the grid within a time slot at four different snapshots of an incoming trajectory is illustrated from Figure 2.11a to Figure 2.11d. As it can be seen, as the metallic cart crosses the grid of reference tags the number of missed tags grows until the cart starts moving out of the grid. As a consequence, from the pattern extracted from consecutive snapshots of the trajectory of the metallic cart it is possible to infer its movement direction. In particular, as detailed in **[III]**, the network was trained for different LSTM parameters and several values of the time slot duration, reaching a 100% accuracy for $t_{win} = 400\,\text{ms}$. These results are encouraging and pave the way for the deployment of the proposed system in a warehouse to carry out a more extensive validation campaign.

The proposed system was also tested using a CNN. In this case, as previously explained, the number of readings of tag of the reference grid during each time slot was used to build images that were used as the input of the CNN. An ex-

ample of these images for an incoming movement, an outgoing trajectory and a passing one are depicted in Figure 2.12a, Figure 2.12b and Figure 2.12c, respectively. Analogously to the previous example, there is a significant reduction in the number of readings of the reference tags when the metallic cart moves over them (dark-blue pixels of the images), which is followed by an increase of the readings as the metallic cart continues its movement outside the checkpoint defined by the reference grid of RFID tags. It should be remarked that, as it can be observed, each movement direction produces a different pattern. In a similar fashion to the LSTM case, as explained in [xi], the CNN was trained for different parameters and several values of the time slot duration, reaching also a 100% accuracy for $t_{win} = 400\,\text{ms}$, showing a promising performance.

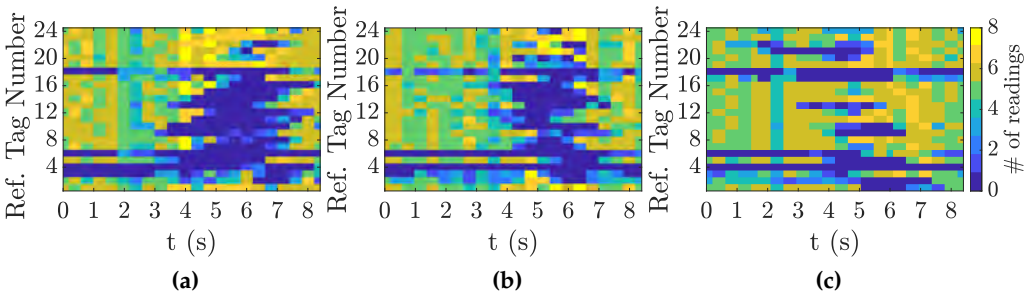

Figure 2.12: Number of readings of each tag of the reference grid within each time slots of an incoming trajectory (a), an outgoing trajectory (b) and a passing trajectory (c) of the metallic cart considering $t_{win} = 400\,\text{ms}$.

Finally, once the movement direction of the transpallet is classified, it is necessary to determine which goods were being transported. In order to do so, it is possible to track the phase history of tagged goods and compare it with the one of the tag of the transpallet. With the purpose of validating this approach, during the measurements a set of static tags was deployed to resemble static goods in the surroundings of the checkpoint. In addition, as depicted in Figure 2.10, two tags were attached to the metallic cart to simulate a tagged transpallet and the transported goods.

The phase history of the tags deployed in the metallic cart and of the static tags during an outgoing trajectory is shown in Figure 2.13. As it can be observed, the phase history of the static tags is approximately flat whilst the phase history of the tags attached to the cart shows two clear stages. First, the phase grows as the cart moves towards the RFID antenna over the reference grid of tags. Second, it decreases as the cart leaves the antenna behind. Therefore, static goods can

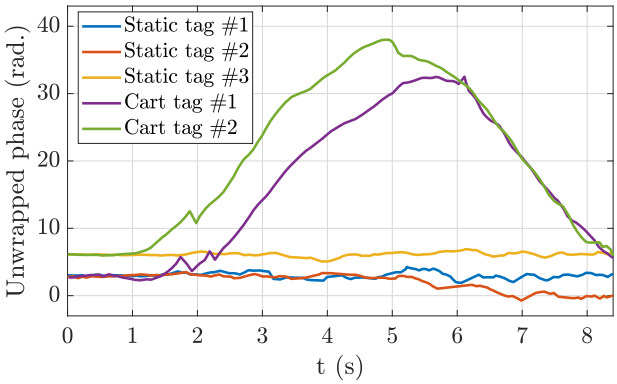

Figure 2.13: Phase history of the three static RFID tags deployed in the surroundings of the reference grid of tags and of the two tags attached to the moving metallic cart during an outgoing trajectory.

be distinguished from the goods on a tagged transpallet crossing a checkpoint comparing the phase history of their tags.

2.3 Concluding remarks

In this chapter two different RFID-based systems, designed for localization and tracking purposes, have been presented.

The first system was designed for the estimation of the attitude of tagged goods using an array of RFID tags [xviii], [xvii], [**II**]. The system employs the phase of the signals backscattered by the RFID tags of the array [**I**]. In particular, the use of a ULA and of a UCA was considered to retrieve azimuth, and both azimuth and elevation estimations, respectively. The impact of array imperfections on the performance of the system was evaluated by means of simulations. In order to assess the accuracy of the system, both approaches have been validated in a controlled environment and in an indoor scenario, showing a good accuracy in a wide angular range. Finally, the use of the proposed system to also obtain position estimations was studied in [xvi].

The second system relies on the use of a reference grid of passive RFID tags and a single antenna connected to a reader to monitor the transit of goods at checkpoints [xi], [**III**]. In order to estimate the movement direction of goods, the system leverages the shadowing effect produced when the RFID tags are blocked by the transpallet or forklift which carries the goods. In particular, the shadowing effect is measured both in terms of missed tags (i.e., tags that were not read in a time slot) and in terms of a reduction in the number of readings of tags.

This information is then used as the input features of a neural network, which determines the movement direction of the tagged goods. The system was evaluated processing the data acquired during a measurement campaign performed at the facilities of the University of Pisa, yielding promising results. In contrast to other alternatives, the required hardware infrastructure of the proposed system is cost-effective and easy-to-deploy.

CHAPTER

3

Freehand radar imaging system

This chapter is devoted to summarize the results presented in the publications composing this dissertation in the field of freehand radar imaging. The concept of freehand radar imaging is illustrated in Figure 3.1, which shows a potential application of the developed system. As it can be seen, the operator of the system is holding with their hand a compact device, which is moved in front of the person under screening describing a freehand trajectory while radar acquisitions are performed. The position of the handheld device is tracked during its movement

so that the acquired radar measurements can be combined in real-time to retrieve high-resolution electromagnetic images of the inspected areas. Among other applications, the proposed system, which increases the flexibility with respect to other existing solutions (costly and bulky), can also be used in the field of NDE.

The rest of the chapter is organized as follows. First, the general architecture of the system is presented in Section 3.1. Second, the processing technique to retrieve high-resolution images is summarized in Section 3.2. Next, the impact of a non-uniform sampling distribution in the image quality is studied in Section 3.3 and the proposed calibration method to enhance the quality of the obtained images is explained in Section 3.4. Finally, some of the results obtained for a quasi-monostatic and a MIMO configuration are presented in Sections 3.5 and 3.6, respectively.

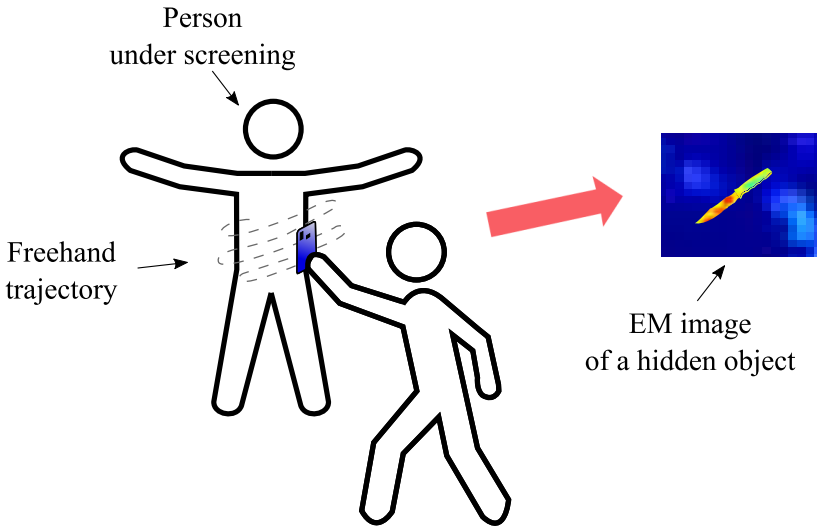

Figure 3.1: Scheme of the proposed freehand radar imaging system.

3.1 System architecture

The original idea behind the system was to develop a handheld scanner able to retrieve high-resolution electromagnetic images in real-time. These features impose several challenges that were necessary to address before building a prototype. First, the reduced size of the system makes necessary to resort to high-frequency devices. In this regard, mm-Wave technology offers a good trade-off between compactness and penetration capabilities. Second, in order to obtain high-resolution images with a compact device (i.e., a small aperture), the acquired

measurements should be coherently combined, resulting in very demanding positioning accuracy requirements. Third, as the scanner will be moved by hand, the acquisitions are not expected to be uniformly spaced, limiting the processing techniques that can be applied to compute the images. Finally, the measurements must be processed on-the-fly to update the image as more measurements are acquired, giving the operator the ability to dynamically choose the areas where to spend more time scanning to refine the image. In order to provide the previous functionalities, the scanning system was structured in three subsystems (See Figure 3.2) which are described in the following subsections.

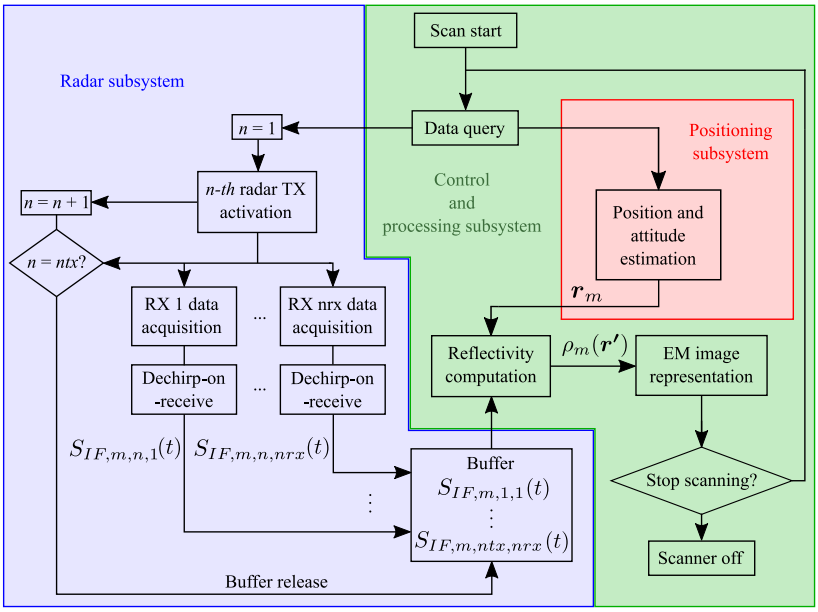

Figure 3.2: Flowchart of the proposed freehand imaging system.

3.1.1 Control and processing subsystem

The control and processing subsystem is the core of the system. Their main functions are summarized over the green background in the general flowchart of the scanning system depicted in Figure 3.2. First, this subsystem sets up the scanning system establishing the communication with the two other subsystems and defining the investigation domain, which will be denoted as volume under test. The volume under test is discretized in a grid where the reflectivity will be computed during the scan to form the electromagnetic images. During the operation of the scanning system the control subsystem is responsible for triggering both

the radar and position acquisitions and for gathering the obtained data. Finally, the newly obtained information is processed so that the reflectivity of the volume under test is updated, generating a set of electromagnetic images at different depths. The retrieved results are displayed in real-time so that the operator can dynamically choose the areas where to spend more time scanning to refine the image, or decide if enough information has been acquired. The operator can also interactively change the plane whose reflectivity is being depicted so as to focus the electromagnetic image on the desired target.

The acquired information is processed in two steps. First, a strategy to ensure a proper sampling to cope with the freehand operation of the scanner is implemented. Second, the resulting data is used to compute the reflectivity of the volume under test according to the method described in Section 3.2.

This subsystem was formed by a conventional laptop for both controlling the scanner and processing the acquired data. This laptop was equipped with an Intel® i7-7700HQ (2.8 GHz), 16 GB of RAM and a NVIDIA® GeForce GTX 1050 graphic card.

As previously explained, since the scanner is moved by hand while continuously new data is acquired, the measurements are not expected to be uniformly spaced. Moreover, the non regular hand movements will result in an uneven sampling distribution. For example, if the operator stops (or moves slowly) at a certain area, the system would keep sampling, yielding a high number of samples for a small region. This kind of locally oversampled areas could result in parts of the image with reflectivity levels higher than other areas just because of this imbalance in the sample density. On the other hand, it is necessary to ensure a proper sampling of the volume under test. Therefore a strategy to avoid electrically large gaps between adjacent samples must be implemented. The impact of a non-uniform sampling distribution is studied in Section 3.3.

The proposed solution to overcome these two challenges consists of defining an observation volume from a canonical surface (i.e. a plane) over the volume under test to mimic a traditional imaging system and filtering acquisitions within it (see Figure 3.3). During the measurements with the proposed imaging system the observation volume was defined from a plane and discretized in cubic cells of size $d \times d \times t$ as shown in Figure 3.3. In addition, in order to avoid strong imbalances between the sample density of different areas, a maximum of Q acquisitions per cell is allowed ($Q = 2$ in the example of Figure 3.3). After Q samples are acquired within a cell, if additional measurements are performed the extra acquisitions are discarded. An example of this situation is shown in Figure 3.3, where the extra acquisitions are depicted in orange circumferences.

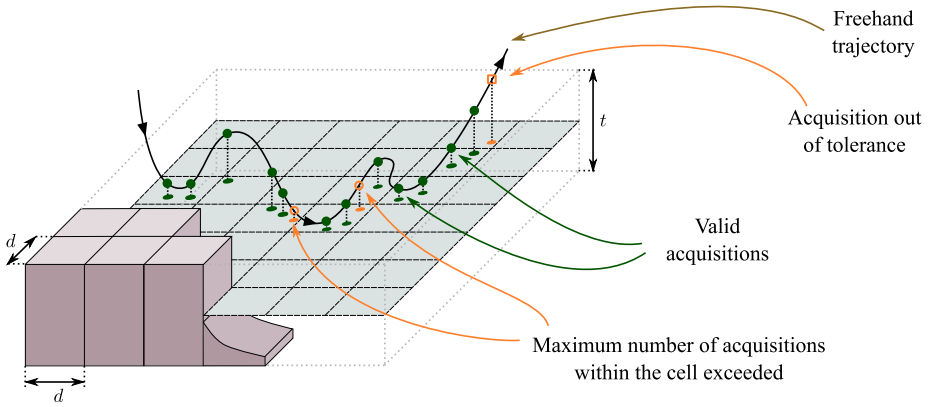

Figure 3.3: Scheme of the observation volume, which is discretized in cubic cells, defined over the volume under test. Within each cell of the observation volume the number of valid acquisitions, depicted in green, is limited (to two in this example). Acquisitions outside the cells are discarded.

On the one hand, the horizontal dimensions d of the cubic cells are intended to play the role of the conventional sampling steps and, therefore, they should be in the order of $\lambda/2$. However, this requirement can be relaxed if more than one sample per cell is considered, i.e. $Q > 1$.

On the other hand, the vertical cell size t provides the necessary flexibility with respect to the canonical surface (e.g., the plane) to the operator of the system, so a handheld scanning can be performed. The parameter t is usually chosen up to $\lambda/2$ to avoid electrically large gaps between adjacent samples. It should be pointed out that when $Q > 1$, the effective sampling step in the vertical dimension would be smaller than the value of the tolerance, t, and, thus, the requirement of $t < \lambda/2$ can be relaxed. Measurements outside the cubic cells, depicted in Figure 3.3 in orange squares, are discarded.

It should be remarked that even though the previously explained techniques mitigate the effect of freehand scanning on the obtained results, some impact of the non-uniformly spaced acquisitions along a non-flat surface is expected on the image quality. In particular, while a lower value of t results in higher quality images, it also entails an increase of the scanning time since many samples would be discarded. Hence, the height of the cubic cells t establishes a trade-off between image quality and acquisition speed.

In order to help the operator of the system during the scan, a visual aid is included in the interface so that the operator knows the distance to the cells bottom and top in order to move the scanner to the corresponding area. In addition, the number of acquired samples per cell is displayed to the operator in a Bi-

Dimensional (2D) image similar to a heat map so the operator can easily check the amount of available data across the observation volume.

Finally, in order to set an upper bound of the radar movement during an acquisition (if the operator is moving the radar too fast), the position of the radar is queried before and after each acquisition is performed and, if the difference is higher than a threshold (1 mm), the sample is discarded.

3.1.2 Radar subsystem

The radar subsystem comprises a commercially available Frequency-Modulated Continuous-Wave (FMCW) mm-wave radar-on-chip module. In particular, the radar module BGT60TR24B manufactured by Infineon® was selected [63].

This subsystem transmits and receives radar signals on demand of the control subsystem enabling the acquisition of the IF signal for further processing. The frequency waveform of the signal transmitted by the radar has an up-chirp saw tooth pattern centered at $f_c = 60\,\text{GHz}$ with a bandwidth of $BW = 6\,\text{GHz}$ and a chirp duration of $T_s = 512\,\mu\text{s}$. The radar module has two transmitting antennas that are sequentially activated and four independent receivers, which perform dechirp-on-receive operations concurrently (See Figure 3.2). The first tests of the system were performed using only one transmitter and one receiver considering a quasi-monostatic configuration as detailed in Section 3.5. After the first proof-of-concept of the system, a MIMO configuration using all the transmitters and receivers of the radar module was evaluated. The obtained results, which are discussed in Section 3.6, show that the MIMO configuration outperforms the quasi-monostatic setup in terms of scanning speed and image quality.

The radar module was embedded in a 3D-printed enclosure designed ad-hoc for the system to ease the manipulation of the radar module as well as to help in the placement of the reflective markers of the positioning system, which will be described below. The top and bottom views of the radar module and the reflective markers embedded in the 3D-printed enclosure can be seen in Figures 3.4a and 3.4b, respectively.

3.1.3 Positioning subsystem

The positioning subsystem estimates the position and the attitude of the radar module. In the prototype developed within this thesis, this subsystem was formed by an optical tracking system. In particular, the motion capture system of Optitrack® was used [130]. This system, which can be easily deployed and calibrated in a matter of minutes, employs infrared cameras (at least four) to track a rigid

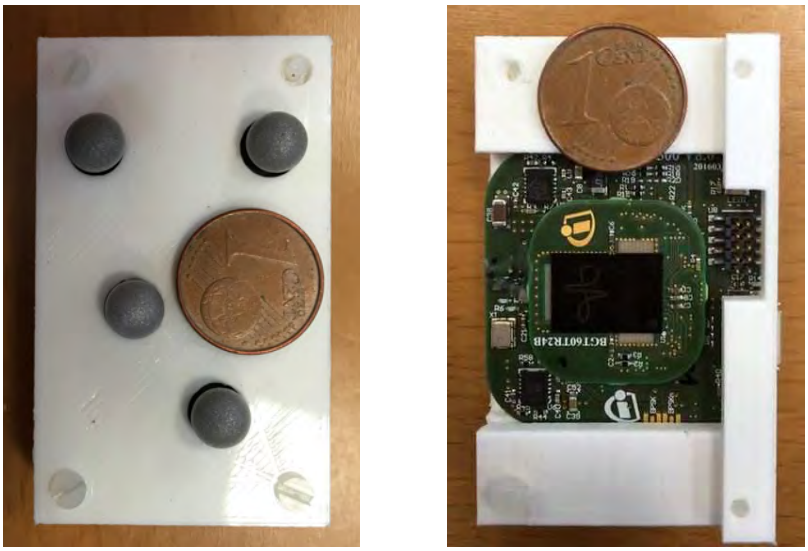

(a) (b)

Figure 3.4: Radar module and reflective markers of the positioning system embedded in the 3D-printed enclosure: top view (a) and bottom view (b). A one euro-cent coin is included for scale purposes.

body formed by a group of reflective markers (See Figure 3.4a). The position retrieved by the system, which is the centroid of the rigid body defined by the deployed markers, must be corrected to match the position of the radar as described in Section 3.4.

3.2 Imaging method

From the point of view of the imaging technique, the presented system faces two major challenges in contrast to conventional SAR imaging as was previously introduced. First, the scanner is freely moved by hand and, consequently, the acquired data will not be equally spaced along a canonical geometry as it is usually assumed in standard SAR techniques for either monostatic [53] or multistatic setups [54, 60]. Second, it is convenient to perform an on-the-fly update of the reflectivity of the volume under test to provide a visual feedback to the operator moving the handheld radar. Taking into account the previous considerations, a delay-and-sum algorithm, adapted to FMCW radar signals, is used to retrieve real-time images with the proposed system. In this section, the general formulation of this algorithm, considering a multistatic configuration with ntx transmitters and nrx receivers, is reviewed. The particularization of the algorithm for the

quasi-monostatic configuration used in Section 3.5 is straightforward considering $ntx = nrx = 1$ and assuming that both the transmitter and the receiver are at the same position.

The signal generated by the *n-th* transmitter of the radar module, expressed in complex form, it given by

$$s_{tx,n}(t) = e^{j2\pi(f_c t + \frac{BW}{2T_s}t^2)} \quad , \tag{3.1}$$

where $|t| < T_s/2$ and the instantaneous frequency is given by

$$f(t) = f_c + \frac{BW}{T_s}t, \tag{3.2}$$

where BW is the bandwidth of the signal and T_s is the chirp duration. The complex form of the signal received by the *p-th* receiver and transmitted by the *n-th* transmitter at the *m-th* radar position, $\boldsymbol{r}_m$, assuming a point target and omitting amplitude variations, is a delayed version of the transmitted signal and is given by

$$s_{rx,m,p,n}(t) = s_{tx,m,n}(t - \tau_{m,p,n}) = e^{j2\pi(f_c(t-\tau_{m,p,n}) + \frac{BW}{2T_s}(t-\tau_{m,p,n})^2)}, \tag{3.3}$$

where $\tau_{m,p,n}$ is the propagation delay, which is proportional to the distance from the *n-th* transmitter at the *m-th* radar position to the point target, $R_{m,n}$, and from the point target to the *p-th* receiver at the *m-th* radar position, $R_{m,p}$. Therefore, the signal transmitted by the *n-th* transmitter and dechirped by the *p-th* receiver when the radar module is at position $\boldsymbol{r}_m$ is given by:

$$s_{IF,m,p,n}(t) = e^{j2\pi(f_b t + f_c\tau_{m,p,n} - \frac{BW}{2T_s}\tau_{m,p,n}^2)}, \tag{3.4}$$

where the beat frequency is $f_b = \frac{BW}{T_s}\tau_{m,p,n}$ [131, 132]. It should be noted that, using a multistatic configuration, for each position $\boldsymbol{r}_m$ of the scanner, a set of $ntx \times nrx$ radar acquisitions will be performed and, thus, the same number of IF signals will be retrieved:

$$\boldsymbol{s}_{IF,m}(t) = [s_{IF,m,1,1}(t) \ldots s_{IF,m,nrx,ntx}(t)]. \tag{3.5}$$

For distributed targets both the received and the IF signals can be expressed as a superposition of 3.3 and 3.4, respectively. However, the radar module radar does not return the complex signal in 3.4 as it lacks an IQ mixer. Nonetheless, thanks to the wideband nature of the signal, the analytic signal can be retrieved by means of an efficient Hilbert transform [133].

To retrieve the images of the volume under test, the reflectivity, ρ, of each point $\boldsymbol{r'}$ in which it is discretized is computed. For this purpose, the contributions of each radar measurement must be coherently combined.

The first step to achieve that is to compensate the extra phase term, which can be approximated by $f_c\tau_{m,p,n} - \frac{BW}{2T_s}\tau_{m,p,n}^2 \approx f_c\tau_{m,p,n}$ for close targets. After that, a range compression is done by making a Fourier transform in the time domain:

$$s_{c,m,p,n}(\mathbf{r}', f) = \mathscr{F}\left\{s_{IF,m,p,n}(t)e^{-j2\pi f_c\tau_{m,p,n}}\right\}, \tag{3.6}$$

where $\mathscr{F}\{\cdot\}$ denotes the Fourier transform operator and

$$\tau_{m,p,n} = \frac{\left\|\mathbf{r}' - \mathbf{r}_{m,p}\right\|_2 + \left\|\mathbf{r}' - \mathbf{r}_{m,n}\right\|_2}{c} = \frac{R_{m,p} + R_{m,n}}{c}, \tag{3.7}$$

where $\mathbf{r}_{m,p}$ and $\mathbf{r}_{m,n}$ are, respectively, the position of the *p-th* receiver and the *n-th* transmitter when the radar is at $\boldsymbol{r}_m$. Finally, in a similar fashion to other standard time-domain techniques [134, 135], the used delay-and-sum algorithm to compute the reflectivity at each point $\boldsymbol{r'}$ after the *m-th* acquisition can be expressed as

$$\rho_m(\mathbf{r}') = \sum_{i=1}^{m}\sum_{p=1}^{nrx}\sum_{n=1}^{ntx} s_{c,i,p,n}\left(\mathbf{r}', \frac{BW}{T_s}\frac{R_{m,p} + R_{m,n}}{c}\right). \tag{3.8}$$

This formulation allows the use of non-uniformly spaced data at the expense of an efficiency reduction when compared to Fast Fourier Transform (FFT) based methods [54, 136]. Moreover, the information of new acquisitions can be directly included in the reflectivity computation by adding additional terms to the external summation in (3.8) to enable real-time updates during the scan.

3.3 Impact of non-uniform sampling

This section is devoted to the assessment of the impact of non-uniform sampling in the image quality. For that purpose, several simulations were conducted using the IF signal model given by 3.4, considering a radar module with one transmitter and one receiver ($ntx = nrx = 1$) and defining an ideal target with the shape of the letter "T". During these simulations no positioning errors were included. First, in order to obtain a reference image, an initial simulation considering a regular acquisition grid of 5.8×7 cm and a total of 4200 samples was performed. The retrieved reference image is depicted in Figure 3.5a. Next, 3D random variations to the regular sampling positions were generated using a normal distribution for several variance values. The images obtained after modifying

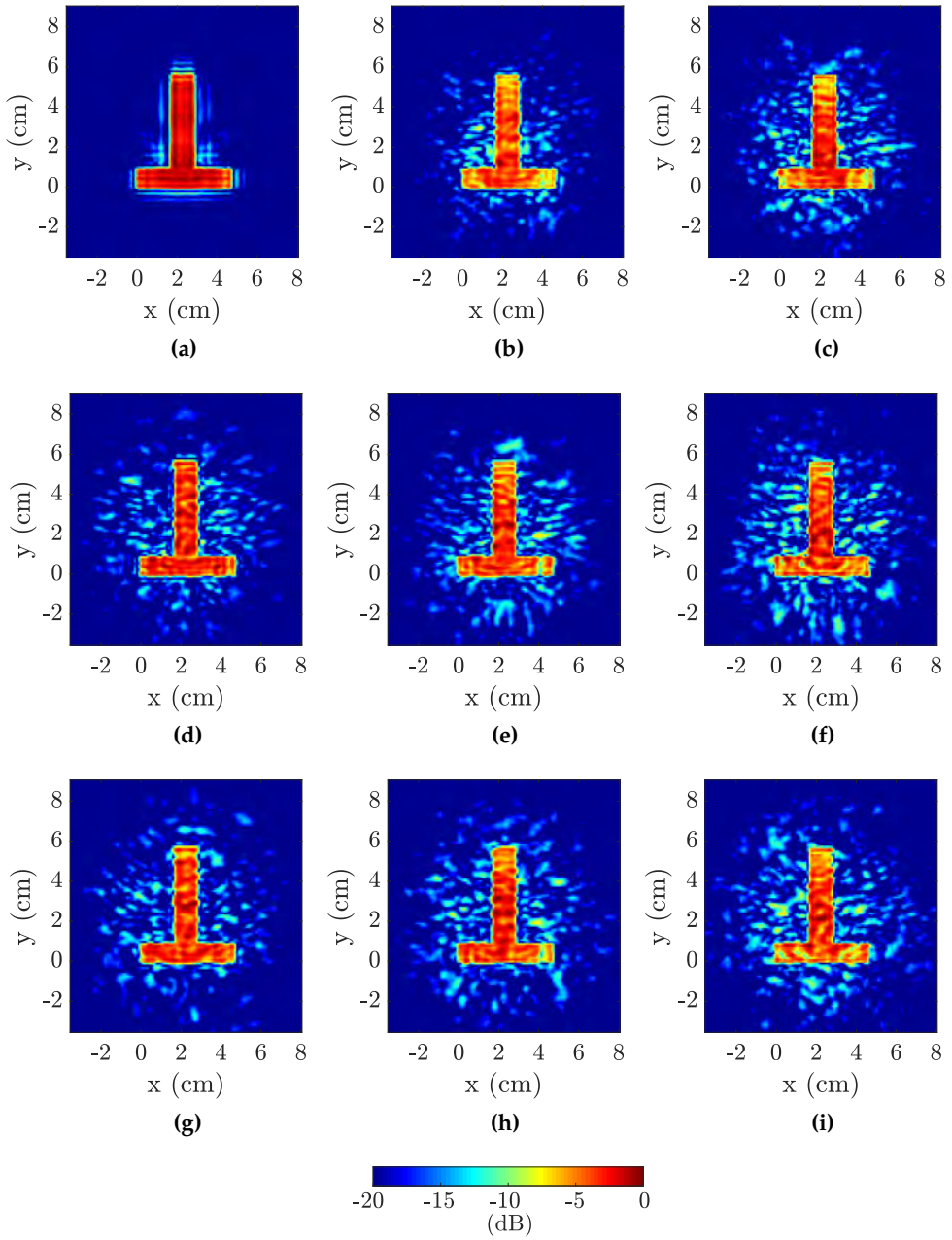

Figure 3.5: Reflectivity image of the simulated target without positioning errors obtained with uniform sampling (a) and modifying the regular acquisition grid in the three dimensions using a normal distribution of $\sigma_x = \sigma_y = 1\,\text{cm}$ and $\sigma_z = 0\,\text{cm}$ (b), $\sigma_x = \sigma_y = 2\,\text{cm}$ and $\sigma_z = 0\,\text{cm}$ (c), $\sigma_x = \sigma_y = 0\,\text{cm}$ and $\sigma_z = 1\,\text{cm}$ (d), $\sigma_x = \sigma_y = \sigma_z = 1\,\text{cm}$ (e), $\sigma_x = \sigma_y = 2\,\text{cm}$ and $\sigma_z = 1\,\text{cm}$ (f), $\sigma_x = \sigma_y = 0\,\text{cm}$ and $\sigma_z = 2\,\text{cm}$ (g), $\sigma_x = \sigma_y = 1\,\text{cm}$ and $\sigma_z = 2\,\text{cm}$ (h) and $\sigma_x = \sigma_y = \sigma_z = 2\,\text{cm}$ (i).

the regular acquisition grid with a 3D normal distribution of $\sigma_x = \sigma_y = 1\,\text{cm}$ and $\sigma_z = 0\,\text{cm}$, $\sigma_x = \sigma_y = 2\,\text{cm}$ and $\sigma_z = 0\,\text{cm}$, $\sigma_x = \sigma_y = 0\,\text{cm}$ and $\sigma_z = 1\,\text{cm}$, $\sigma_x = \sigma_y = \sigma_z = 1\,\text{cm}$, $\sigma_x = \sigma_y = 2\,\text{cm}$ and $\sigma_z = 1\,\text{cm}$, $\sigma_x = \sigma_y = 0\,\text{cm}$ and $\sigma_z = 2\,\text{cm}$, $\sigma_x = \sigma_y = 1\,\text{cm}$ and $\sigma_z = 2\,\text{cm}$ and $\sigma_x = \sigma_y = \sigma_z = 2\,\text{cm}$ are depicted from Figure 3.5b to Figure 3.5i, respectively.

As can be observed, after modifying the flat and regular original acquisition grid, the image is noisier and some artifacts appear. Moreover, as can be observed from the evolution of the image quality from Figure 3.5a to Figure 3.5i, when the non-uniformity of the acquisition grid increases, the impact in the image quality becomes higher. In order to quantify the image quality degradation, the Target-to-Clutter Ratio (TCR) [137, 138] is used. The TCR is given by

$$TCR = 10\log\left(\frac{N_c \sum_{(x,y)\in A_t} |\rho(x,y)|^2}{N_t \sum_{(x,y)\in A_c} |\rho(x,y)|^2}\right), \tag{3.9}$$

where A_t is the region corresponding to the target (i.e. the pixels where the target is located), A_c is the rest of the image, N_t is the number of pixels of A_t and N_c is the number of pixels of A_c. The results, including the quality loss with respect to the reference image, L, are summarized in Table 3.1. In a similar fashion as previously concluded when qualitatively observing the images, when the non-uniformity of the acquisition grid increases, the image quality degradation becomes higher. However, the quality of the retrieved images, though degraded, still enables to clearly recognize the test target. In addition, it should be remarked that the proposed strategy to mitigate the effect of freehand scanning in the image quality presented in Section 3.1 limits the maximum non-uniformity of the acquisitions distribution performed during a scan.

	$\sigma_x = \sigma_y = 0\,\text{cm}$			$\sigma_x = \sigma_y = 1\,\text{cm}$			$\sigma_x = \sigma_y = 2\,\text{cm}$		
σ_z (cm)	0	1	2	0	1	2	0	1	2
TCR (dB)	22.3	17.3	16.9	16.9	16.1	16.1	16.3	15.4	15.2
L (dB)	0	5	5.4	5.4	6.2	6.2	6	6.9	7.1

Table 3.1: TCR of the reference image computed using a regular acquisition grid and TCR of the images obtained after modifying the original acquisition grid using different 3D normal distributions.

3.4 System calibration

In order to retrieve electromagnetic images of the volume under test processing the IF signal of each channel (i.e., a transmitter-receiver pair) according to

(3.8), it is necessary to accurately know the position of each transmitter and receiver. However, as introduced in Section 3.1, the optical tracking system used in the proposed system only provides the position of the centroid of the (virtual) rigid body defined by the (three or more) reflective markers attached to the radar module, and its attitude, (φ, θ, ψ), the yaw, pitch and roll angles. Although the relative positions between the radar antennas can be accurately found from the layout, the position and attitude offsets with respect to the rigid body are unknown and must be estimated. A general scheme to illustrate the problematic of the position and attitude offsets between the data provided by the optical tracking system and the actual position of the radar transmitters and receivers is depicted in Figure 3.6. The position provided by the tracking system, $\boldsymbol{O}_{RB}$, is the centroid of the rigid body defined by the reflective markers attached to the radar module. The position offset, $\boldsymbol{\omega}$, is equal to the difference between $\boldsymbol{O}_{RB}$ and a reference point of the radar module, $\boldsymbol{O}_{radar}$, from which the position of each transmitter and receiver is computed. The attitude offset, given by the angles φ_{err}, θ_{err} and ψ_{err}, is the difference (misalignment) between the attitude of the rigid body in the tracking system coordinate frame, defined by the axes $\boldsymbol{x}_{RB}$, $\boldsymbol{y}_{RB}$ and $\boldsymbol{z}_{RB}$, when $(\varphi, \theta, \psi) = (0, 0, 0)^\circ$ and the actual attitude of the radar module, which can be computed from the three angular rotations required to rotate the radar module coordinate frame, defined by the axes $\boldsymbol{x}_{radar}$, $\boldsymbol{y}_{radar}$ and $\boldsymbol{z}_{radar}$, to the $\boldsymbol{\omega}$ shifted optical tracking system coordinate frame, defined by the axes $\boldsymbol{x}'_{RB}$, $\boldsymbol{y}'_{RB}$ and $\boldsymbol{z}'_{RB}$.

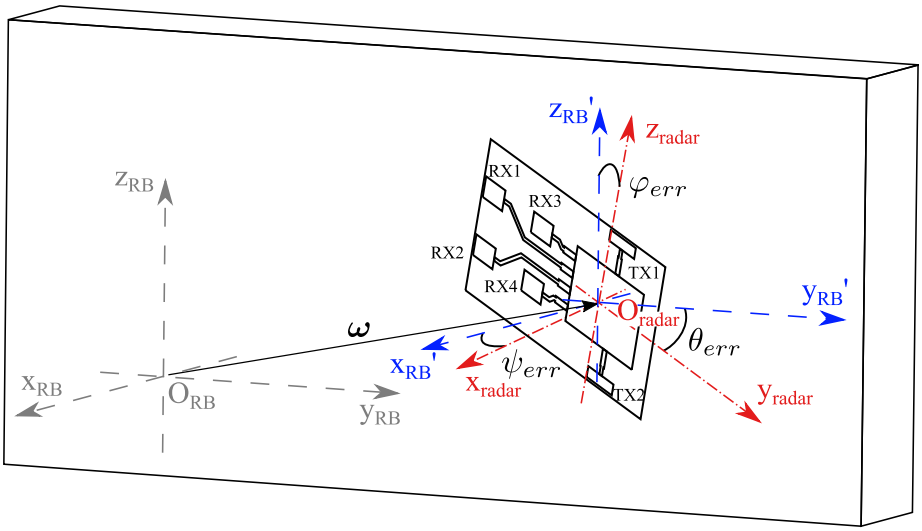

Figure 3.6: General scheme of a situation in which there is a position and attitude offset, $\boldsymbol{\omega}$ and $(\varphi_{err}, \theta_{err}, \psi_{err})$, respectively, between the position and attitude given by the tracking system and actual position and attitude of the radar module.

It is worth noting that any calibration error (i.e., $\boldsymbol{\omega} \neq (0,0,0)$ or the existence of angular misalignment, that is, $\varphi_{err} \neq 0$, $\theta_{err} \neq 0$ or $\psi_{err} \neq 0$) will result in positioning errors for each transceiver of the radar module. This calibration error for the *u-th* radar transceiver, is given by

$$\epsilon_{cal,u} = \boldsymbol{R}(\varphi,\theta,\psi)[\boldsymbol{w} + \boldsymbol{R}_{err}(\varphi_{err},\theta_{err},\psi_{err})\boldsymbol{r}_u - \boldsymbol{r}_u], \tag{3.10}$$

where $\boldsymbol{R}(\varphi,\theta,\psi)$ is the rotation matrix obtained using the pose of the rigid body (yaw, pitch and roll angles) given by the optical tracking system, $\boldsymbol{r}_u$ is a vector containing the relative position of the *u-th* transceiver of the radar module with respect to the reference point $\boldsymbol{O}_{radar}$, and $\boldsymbol{R}_{err}(\varphi_{err},\theta_{err},\psi_{err})$ is the rotation matrix given by the angular misalignment: φ_{err}, θ_{err} and ψ_{err}. The impact of calibration errors in the image quality and the proposed calibration method will be discussed in the next two sections.

3.4.1 **Impact of calibration errors**

The impact of calibration errors in the image quality was studied through several simulations. In particular, an ideal test target consisting of six metallic strips of size 20 mm × 4 mm with a gap between them of 6 mm (three in vertical position and three in horizontal position) was defined. The considered radar model comprised $ntx = 2$ transmitters and $nrx = 4$ receivers with the same layout as the commercial radar used in the developed system. First, a reference image of the test target, considering a regular acquisition grid and no offsets, was computed (see Figure 3.7a). For the rest of the simulations, the same non-uniform acquisition distribution, which was generated by modifying the regular acquisition grid with a 3D normal distribution of $\sigma_x = \sigma_y = \sigma_z = 1$ cm, was considered. In addition, the maximum height variation was set to 1 cm, i.e. $t = 1$ cm, and the horizontal dimension of the considered cells was $d = 2$ mm. The distribution of the samples, projected into a plane parallel to the test target and considering a maximum of $Q = 5$ samples per cell, is depicted in Figure 3.7b. The image of the test target obtained for the previous non-uniform acquisition distribution, $\boldsymbol{\omega} = (0,0,0)$ mm, and $(\varphi_{err},\theta_{err},\psi_{err}) = (0,0,0)^\circ$ is depicted in Figure 3.9a. During the simulations several values of position and attitude offsets, $\boldsymbol{\omega}$ and $(\varphi_{err},\theta_{err},\psi_{err})$, respectively, were considered.

At this point, it is relevant to observe that the attitude of the radar, (φ,θ,ψ), plays a relevant role in this study as the magnitude of the positioning error for each transceiver of the radar module depends on its value (See (3.10)). In particular, if the attitude angles are constant along the scan, then the difference between the position estimated by the tracking system and the actual position of the radar

module would be constant (even for high errors in the estimation of ω) and the image quality would be less affected. On the contrary, the more the attitude of the radar module during a scan varies, the more the value of the positioning error for each transceiver across different acquisition positions changes. This would greatly degrade the coherence of the measured data and, therefore, the quality of the retrieve image would decrease significantly.

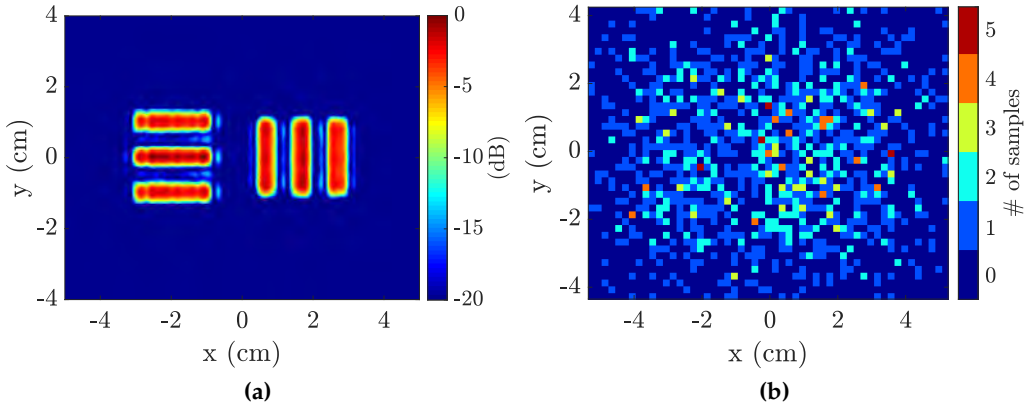

Figure 3.7: Reflectivity image of the test target considering a regular acquisition grid and no offsets (a). Distribution of the acquisition positions considered in the simulations projected into a plane parallel to the test target and using cells of $2 \times 2 \times 10\,\text{mm}$ (b).

An example of how the positioning error of the transceivers of a radar module changes for different acquisition points as a function of how much the attitude of the radar module is modified during a scan can be observed in Figure 3.8a. Each curve of Figure 3.8a depicts a histogram of the positioning errors in the *x-axis* of the six transceivers of a radar module for different attitude variation ranges. The same layout as that of the commercial radar module used in the proposed system was considered. The positioning errors were computed evaluating (3.10) for $\boldsymbol{\omega} = (1,1,1)\,\text{mm}$, $(\varphi_{err}, \theta_{err}, \psi_{err}) = (0,0,0)^\circ$ and a total of 10^5 triplets of attitude angles generated using a uniform distribution $U \in [-\theta^\circ_{max}, \theta^\circ_{max}]$. As it can be seen, as for greater attitude variation ranges, i.e. as θ_{max} increases, the change of the positioning error of each transceiver for different acquisition points becomes larger, which causes a greater coherence degradation. The same happens for the positioning errors in the other two dimensions. The results of an analogous analysis considering $\boldsymbol{\omega} = (1,1,1)\,\text{mm}$ and $U \in [-10^\circ, 10^\circ]$ for different attitude offsets is depicted in Figure 3.8b. In this case, each curve was obtained considering $\varphi_{err} = \theta_{err} = \psi_{err} = att_{err}$. As it can be observed, the greater the value

of the attitude offset is, the greater the positioning errors for different observation points spreads.

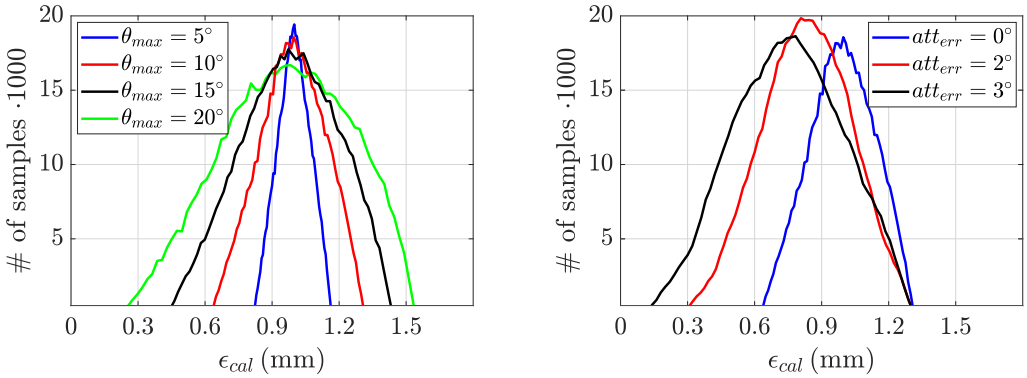

Figure 3.8: Histogram of the positioning errors in the *x-axis* due to calibration errors of the six transceivers of a radar module for $\boldsymbol{\omega} = (1,1,1)$ mm, $(\varphi_{err}, \theta_{err}, \psi_{err}) = (0,0,0)^\circ$ and different attitude variation ranges (a) and for $\boldsymbol{\omega} = (1,1,1)$ mm, $U \in [-10^\circ, 10^\circ]$ and different attitude offsets (b).

The impact of this problematic in the image quality, considering several values of $\boldsymbol{\omega}$, $(\varphi_{err}, \theta_{err}, \psi_{err})$ and different attitude variation ranges, was evaluated comparing the image obtained for each set of parameters with the reference image and the reflectivity image shown in Figure 3.9a, retrieved considering the non-uniform acquisition distribution, $\boldsymbol{\omega} = (0,0,0)$ mm and $(\varphi_{err}, \theta_{err}, \psi_{err}) = (0,0,0)^\circ$. As previously stated, the existence of a position offset, when keeping constant the attitude of the radar module, does not significantly degrade the quality of the image. This can be observed comparing Figure 3.9a with Figure 3.9b, obtained for $\boldsymbol{\omega} = (2,2,2)$ mm, $(\varphi_{err}, \theta_{err}, \psi_{err}) = (0,0,0)^\circ$ and a constant attitude. On the other hand, comparing Figures 3.9c, 3.9d and 3.9e, retrieved for $\boldsymbol{\omega} = (2,2,2)$ mm, $(\varphi_{err}, \theta_{err}, \psi_{err}) = (0,0,0)^\circ$ and $U \in [-5^\circ, 5^\circ]$, $U \in [-10^\circ, 10^\circ]$ and $U \in [-15^\circ, 15^\circ]$, respectively, it can be clearly seen that, as expected, as the attitude range of variation increases, the image quality decreases progressively due to the coherence degradation of the simulated acquisitions. Of course, if the position offset, $\boldsymbol{\omega}$, decreases, the image quality is less affected by these errors, as it can be observed comparing Figure 3.9e and Figure 3.9f. Both images were obtained considering $(\varphi_{err}, \theta_{err}, \psi_{err}) = (0,0,0)^\circ$ and $U \in [-15^\circ, 15^\circ]$, but for the former, of less quality, $\boldsymbol{\omega} = (2,2,2)$ mm, whilst for the latter image, significantly enhanced, $\boldsymbol{\omega} = (1,1,1)$ mm. The effect of an attitude offset can be observed comparing Figures 3.9f, 3.9g, 3.9h and 3.9i, all of them obtained considering $\boldsymbol{\omega} = (1,1,1)$ mm and

$U \in [-15^\circ, 15^\circ]$, and for $(\varphi_{err}, \theta_{err}, \psi_{err}) = (0,0,0)^\circ$, $(\varphi_{err}, \theta_{err}, \psi_{err}) = (1,1,1)^\circ$, $(\varphi_{err}, \theta_{err}, \psi_{err}) = (3,3,3)^\circ$ and $(\varphi_{err}, \theta_{err}, \psi_{err}) = (5,5,5)^\circ$, respectively. As it can be seen, an attitude offset of $(1,1,1)^\circ$ has little effect on the image quality. However, as its value increases, the impact in the image quality becomes more noticeable.

In a similar fashion to the analysis performed in Section 3.3, in order to quantify the image quality degradation due to calibration errors the TCR of the previous images was computed. In particular, the results for $\boldsymbol{\omega} = (0,0,0)$ mm, $\boldsymbol{\omega} = (1,1,1)$ mm and $\boldsymbol{\omega} = (2,2,2)$ mm for different attitude ranges of variation are summarized in Table 3.2. The TCR of the reference image, computed considering a regular acquisition grid was 18.7 dB. Analogously to the qualitative analysis of the retrieved images, it can be concluded that the quality of the image is not significantly affected when the attitude of the radar module is constant or when its variation is reduced. However, as the attitude range of variation increases, the quality of the images is progressively degraded.

	$\boldsymbol{\omega} = (0,0,0)$ cm	$\boldsymbol{\omega} = (2,2,2)$ cm				$\boldsymbol{\omega} = (1,1,1)$ cm
U_{range} $(^\circ)$	± 0	± 0	± 5	± 10	± 15	± 15
TCR (dB)	16.3	16.3	16.0	14.8	12.6	15.4
L (dB)	2.4	2.4	2.7	3.9	6.1	3.1

Table 3.2: TCR of the images of the test target computed for different position offsets and attitude ranges of variation, and quality loss with respect to the reference image.

The results for $\boldsymbol{\omega} = (1,1,1)$ mm and $U = [-15^\circ, 15^\circ]$ for different attitude offsets are summarized in Table 3.3. As it can be seen, although for $(\varphi_{err}, \theta_{err}, \psi_{err}) = (1^\circ, 1^\circ, 1^\circ)$ the impact in the image quality is limited, the image becomes more affected when the value of the attitude offset increases.

	$\boldsymbol{\omega} = (1,1,1)$ cm, $U \in [-15^\circ, 15^\circ]$			
$(\varphi_{err}, \theta_{err}, \psi_{err})$	$(0,0,0)^\circ$	$(1,1,1)^\circ$	$(3,3,3)^\circ$	$(5,5,5)^\circ$
TCR (dB)	15.4	15.5	15.1	14.4
L (dB)	3.1	3.2	3.5	4.2

Table 3.3: TCR of the images of the test target computed for $\boldsymbol{\omega} = (1,1,1)$ mm, $U = [-15^\circ, 15^\circ]$ and different attitude offsets, and quality loss with respect to the reference image.

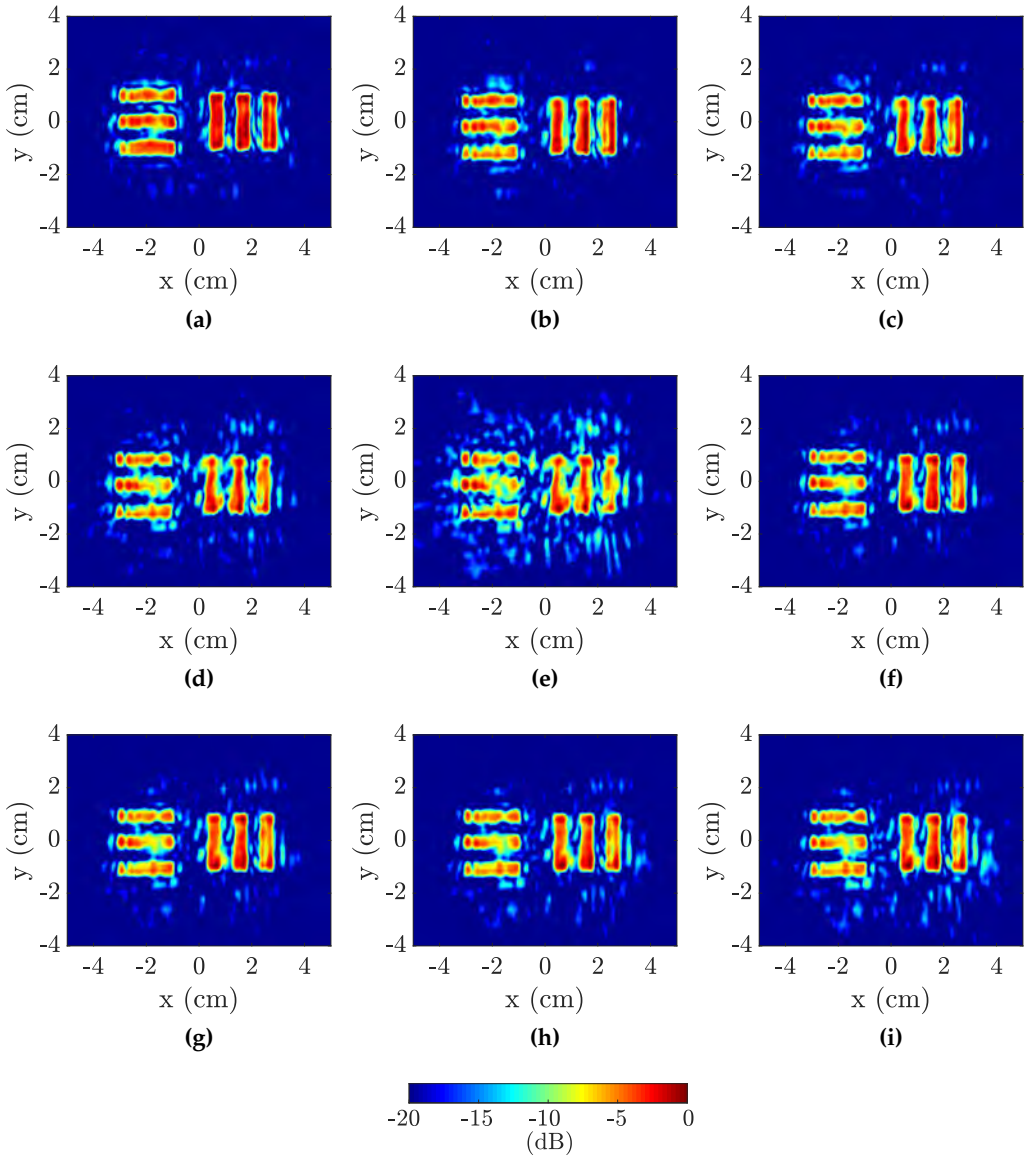

Figure 3.9: Reflectivity image obtained without calibration errors (a), with a position offset of $\boldsymbol{\omega} = (2,2,2)$ mm and a constant attitude (b), with $\boldsymbol{\omega} = (2,2,2)$ mm and attitude values according to a uniform distribution in the interval $U = [-5°, 5°]$ (c), with $\boldsymbol{\omega} = (2,2,2)$ mm and $U = [-10°, 10°]$ (d), $\boldsymbol{\omega} = (2,2,2)$ mm and $U = [-15°, 15°]$ (e), $\boldsymbol{\omega} = (1,1,1)$ mm and $U = [-15°, 15°]$ (f), $\boldsymbol{\omega} = (1,1,1)$ mm, $U = [-15°, 15°]$ and an angular misalignment of $(\varphi_{err}, \theta_{err}, \psi_{err}) = (1°, 1°, 1°)$ (g), $\boldsymbol{\omega} = (1,1,1)$ mm, $U = [-15°, 15°]$ and $(\varphi_{err}, \theta_{err}, \psi_{err}) = (3°, 3°, 3°)$ (h) and $\boldsymbol{\omega} = (1,1,1)$ mm, $U = [-15°, 15°]$ and $(\varphi_{err}, \theta_{err}, \psi_{err}) = (5°, 5°, 5°)$ (i).

3.4.2 Calibration method

As previously explained, in order to achieve high-quality images, it is necessary to estimate the offsets between the position and attitude provided by the optical tracking system and the actual position and attitude of the radar module. For that purpose, during the development of the handheld imaging system a calibration was proposed. A first version of the calibration procedure, considering a quasi-monostatic configuration, was first presented in [**IV**]. However, an enhanced calibration method for a multistatic radar configuration, which will be described here, was later developed to exploit the full capacity of the used radar module.

The proposed calibration procedure entails two steps. The first step aims to find the attitude offset, which is accomplished by taking advantage of the symmetric architecture of the transmitting and receiving antennas of the Radio Frequency (RF) front-end, which are in-phase at 60 GHz according to the manufacturer specifications.

A sketch of the calibration setup to correct the attitude offset is depicted in Figure 3.10a. The sketch shows the radar module, including a basic scheme of its layout, embedded in its enclosure on top of a two stage goniometer and a rotary stage which allows the controlled change of the radar module's attitude. In addition, there is a calibration plane (a flat metal plate), which is aligned with the tracking system coordinate frame (i.e. with the $\boldsymbol{x}_{RB}$, $\boldsymbol{y}_{RB}$ and $\boldsymbol{z}_{RB}$ axes), placed in front of the radar. As it can be seen, if the radar module is perfectly aligned with the calibration plate ($\theta_{err} = \psi_{err} = 0°$), the signal transmitted by TX1 and received by RX2 will be in-phase with the signal transmitted by TX2 and received by RX1. The same holds for other TX-RX pairs such as TX1-RX4 and TX2-RX3 or TX1-RX1 and TX2-RX2. In order to correct rotations about the *z-axis* (i.e. to correct φ_{err}) a polarizer could be used. However, in this case, this offset was corrected by visual inspection since the impact of this offset, once θ_{err} and ψ_{err} are corrected, is minor. Finally, when this process is completed, the pose of the rigid body is reset in the motion capture software so that it matches the one of the radar module.

The complete calibration setup is depicted in Figure 3.10b. In order to calibrate the attitude of the radar module, it was programmed to perform continuous data acquisitions while the signals from each transmitter-receiver pair were monitored. Then, as previously explained, the attitude of the radar was modified until the signals from the corresponding transmitter-receiver pairs were in phase. The dechirped signals, before and after the calibration, are shown in Figure 3.11a and Figure 3.11b, respectively. As it can be seen, none of the previously mentioned transmitter-receiver pairs were in-phase before the calibration (vertical lines show

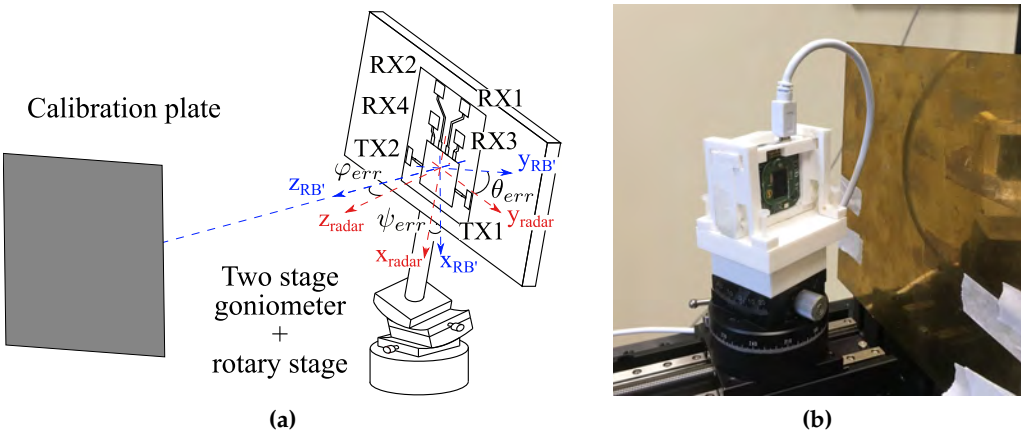

Figure 3.10: Sketch of the proposed calibration setup (a) and realized calibration setup (b).

the maximum of the IF signal retrieved by each receiver). On the other hand, after the calibration, all TX-RX pairs are in-phase.

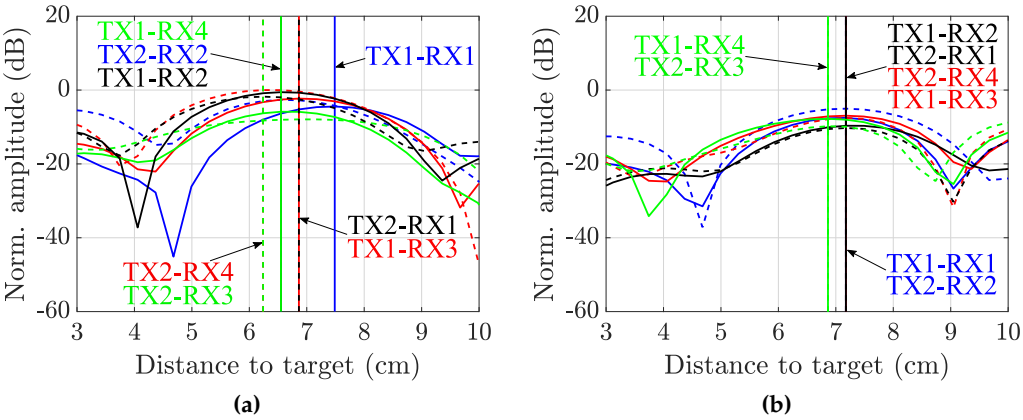

Figure 3.11: Dechirped signals of each transmitter-receiver pair of the radar module before (a) and after the calibration (b).

The second step of the calibration process is to estimate the position offset, $\boldsymbol{\omega}$. For that purpose, several reflective markers are deployed in a plane as a target to be scanned. After the scan is performed, the electromagnetic image of the markers is systematically computed for different values of $\boldsymbol{\omega}$. The optimum value of $\boldsymbol{\omega}$ is obtained when the position of the markers in the electromagnetic image

matches the position of the markers given by the optical tracking system. This means that when the reflectivity image (*xy-plane*) is computed at the *z-coordinate* of the reflective markers given by the tracking system, the high reflectivity areas corresponding to the markers are located at the same positions in the *xy-plane* as those provided by the tracking system and their reflectivity reaches its maximum value. Finally, it should be remarked that the calibration must be done only once after the radar module its embedded in its enclosure with the reflective markers.

3.5 Quasi-monostatic results

The first tests conducted to assess the performance of the proposed system were performed considering a quasi-monostatic configuration, i.e. $ntx = nrx = 1$. During these tests, the size of the cubic cells in which the observation volume was discretized was $1 \times 1 \times 20$ mm and the maximum number of acquisitions per cell was set to $Q = 3$. In addition, the attitude range of variation was limited to $\pm 5^{\circ}$ to mitigate calibration errors. In every experiment, the volume under test was discretized in a 3D grid to compute the reflectivity, as explained in Section 3.2. During the scan, the current reflectivity values of one of the planes of the 3D grid, which can be interactively changed during the measurement process, is shown to the operator. In addition, the distribution of the acquisitions, projected in a plane parallel to the volume under test, is displayed so that undersampled or oversampled areas can be easily observed. The distance to the volume under test and the attitude of the radar module are also shown during the scan to the operator as a visual aid. During all the measurements, the control and processing subsystem was formed by a laptop with the specifications summarized in Section 3.1.

The first measurements were performed using the letter "T" foiled with metal depicted in Figure 3.12a as test target. For the scan the target was hidden in a cardboard box. In this case, the volume under test was divided in eight planes of $22 \times 10\,\text{cm}^2$ separated 2 mm. During the scan a total of $N_{acq} = 3904$ measurements were acquired during 297 s at an average distance to the target of 5.27 cm. The distribution of the acquisitions can be observed in Figure 3.12c. The image update rate was 25.2 frames per second. The computed reflectivity of the target is depicted in Figure 3.12b, where the contour of the target is plotted with a solid-white line. As it can be seen, the test target is well-reconstructed, being clearly distinguishable from the background.

As previously explained in Section 3.1, in order to set an upper bound of the radar movement during an acquisition, the position of the radar is queried before and after each acquisition is performed and, if the difference is higher than 1 mm

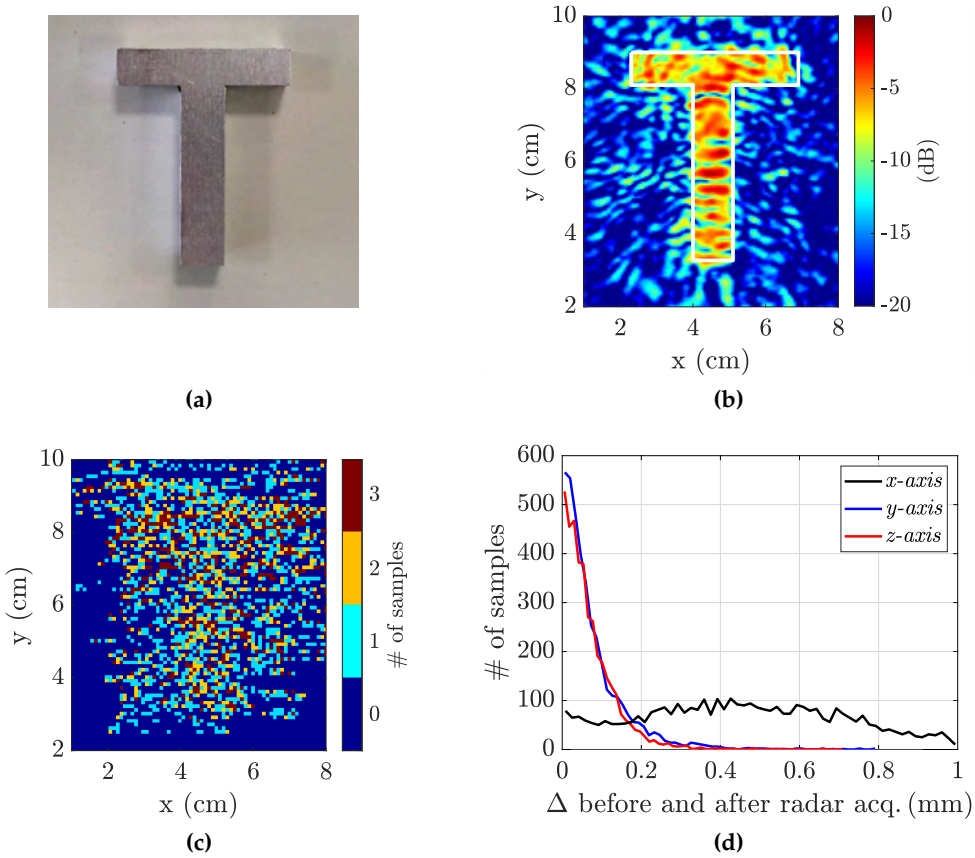

Figure 3.12: Image of the scanned "T" target (a), obtained reflectivity image (b), distribution of the positions of the acquisitions (c) and histogram of the upper bound of the radar movement during each acquisition for each axis (d).

the sample is discarded. This difference was studied for the measurements acquired during this test. In particular, the histogram of the difference between the position of the radar module before and after each acquisition, for each axis, is depicted in Figure 3.12d. As it can be observed, the upper bound is significantly lower for the *y-axis*, with a difference value below 0.2 mm for 96.6% of the data, and the *z-axis*, with a difference value below 0.2 mm for 98.0% of the data, than for the *x-axis*. This is because the scan was performed moving the radar module describing an *s-shape*, being the *x-axis* the main movement direction. Nonetheless, as it can be seen looking at Figure 3.12b, setting a maximum upper bound of the radar movement during an acquisition of 1 mm mitigates the impact of positioning errors in the image quality.

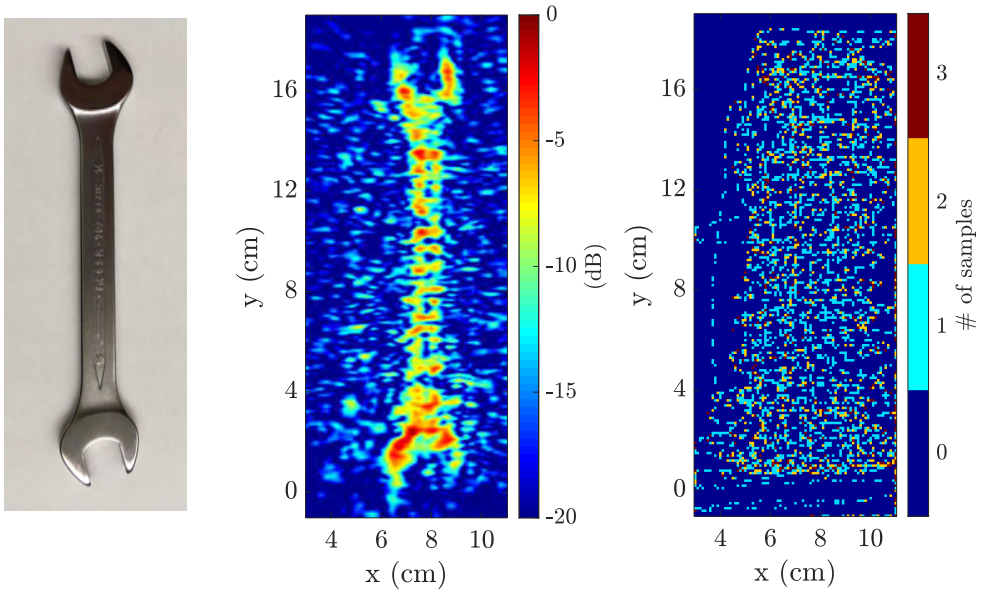

(a) (b) (c)

Figure 3.13: Image of the scanned hand wrench (a), obtained reflectivity image (b) and distribution of the positions of the acquisitions (c).

Another example to illustrate the capabilities of the proposed system with a quasi-monostatic configuration was performed using the hand wrench depicted in Figure 3.13a as test target. In this case, the wrench was also covered with a cardboard box during the scan. The volume under test was divided in seven planes of $11 \times 22\,\text{cm}^2$ separated 2 mm and the image update rate was 26.2 frames per second. During the scan a total of $N_{acq} = 5249$ measurements, whose distribution is shown in Figure 3.13c, were acquired during 269 s at an average distance to the target of 7.8 cm. The obtained reflectivity image is depicted Figure 3.13b. As it can be seen, the handle of the wrench and both of its open ends are well-reconstructed. In addition, it is worth noting that there is a lower reflectivity value in the central part of the handle, where the thickness of the wrench is lower.

The last example considering a quasi-monostatic configuration consisted of scanning a mannequin and a gun, resembling a security application. The measurement setup, comprising the mannequin and the gun, is depicted in Figure 3.14a and a zoomed view of the imaged gun is shown in Figure 3.14b. As it can be seen, the mannequin is covered by aluminum foil as it provides a fair representation of the human skin at mm-wave frequencies. In addition, it should be remarked that this is a worse situation than using a more realistic model of the skin

since the contrast between the body and the metal of the gun would be higher. In this case, the volume under test was divided in eleven planes of $18.6 \times 12.7\,\text{cm}^2$ separated 2 mm and the image update rate was 15.5 frames per second. The lower update rate is caused by the increase of the volume under test (more than 50% bigger than in the wrench case). During the scan a total of $N_{acq} = 24100$ measurements, whose distribution is shown in Figure 3.14c, were acquired during 1162 s at an average distance to the target of 5.8 cm. The obtained results are plotted in Figure 3.14d. In this case, the color of each pixel of Figure 3.14d is proportional to the depth of the point with the highest reflectivity within all the planes in which the volume under test was divided. Moreover, the brightness of each pixel was weighted by the magnitude of the reflectivity corresponding to it [20]. As it can be observed, although the trigger is not detected (it is closer to the mannequin than the rest of the gun, i.e., the height difference between the background and the trigger is smaller, and its size is lower), the shape of the gun is well-reconstructed.

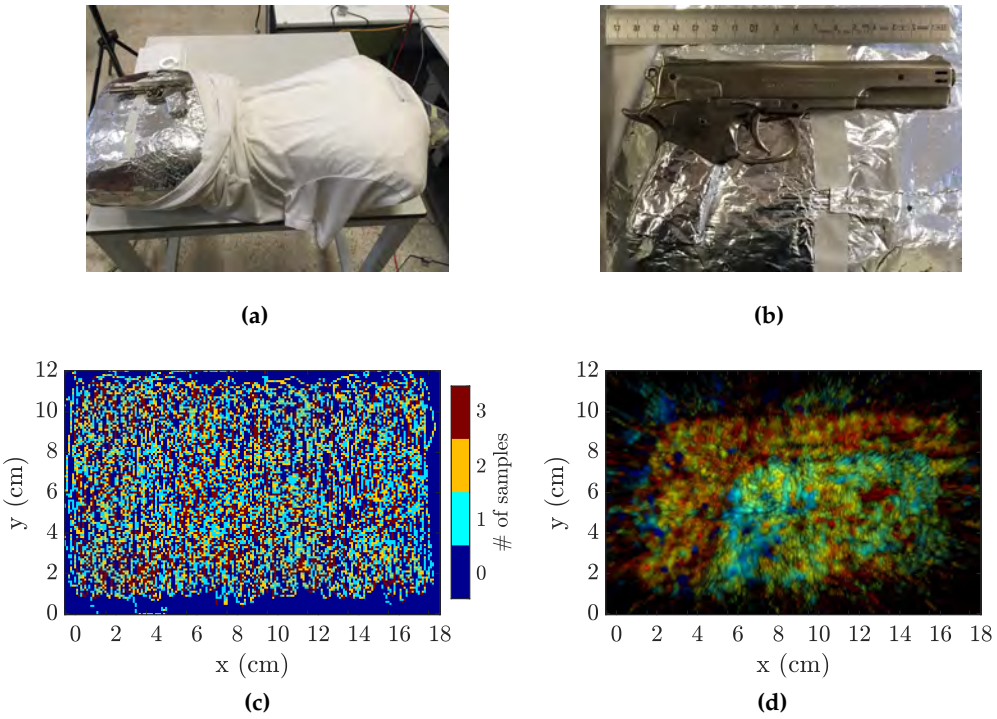

Figure 3.14: Image of the mannequin with the attached gun (a), zoommed image of the gun (b), distribution of the radar acquisitions (c), and reflectivity image obtained after the scan (d).

Finally, it should be remarked that the scanning time could be drastically reduced using more transmitters and receivers, as it will be demonstrated in Section 3.6. In addition, the acquisition speed and the image update rate could be increased by further optimizing the implementation of the system, currently programmed in MatLab®.

3.6 MIMO results

This section is devoted to the assessment of the performance enhancement achieved when switching from a quasi-monostatic scheme to a MIMO, also known as multistatic, configuration exploiting all the transceivers of the radar module. In addition, the impact in the image quality of the use of the calibration procedure described in Section 3.4 is emphasized. During these tests, the size of the cubic cells in which the observation volume was discretized was $1 \times 1 \times 20\,\text{mm}$ and the attitude range of variation was limited to $\pm 15^\circ$ to mitigate calibration errors.

For the first test a two euro coin, a two euro cent coin and a door key, depicted in Figure 3.15a, were used as targets. In a similar fashion to the tests with the letter and the wrench, the coins and the key were covered by a cardboard box during the scan. In this case only one sample per cell was considered. During the scan a total of $N_{acq} = 679$ measurements, whose distribution is shown in Figure 3.15b, were acquired during 88 s at an average distance to the target of 8.4 cm. All the results include the attitude offset calibration.

The computed reflectivity images considering only one transmitter and one receiver of the radar module, before and after the position offset calibration, are depicted in Figure 3.15c and Figure 3.15d, respectively. As it can be seen, the image before calibration is clearly noisy and full of artifacts due to the poor coherency. In particular, the shape of the key is fuzzy and, although the two areas of the image corresponding to the coins exhibit high reflectivity, they are barely distinguishable from clutter. Also, it should be remarked that objects in the image before calibration appear shifted with respect to their actual positions, depicted with solid-white lines. In contrast, the quality of the image after calibration clearly improves, with the shape of the key better defined and being the coins more distinguishable from clutter. Nonetheless, the resolution is still low due to the relatively low number of acquisitions.

The images computed considering the two transmitters and the four receivers of the radar module, before and after the calibration, are shown in Figure 3.15e and Figure 3.15f, respectively.

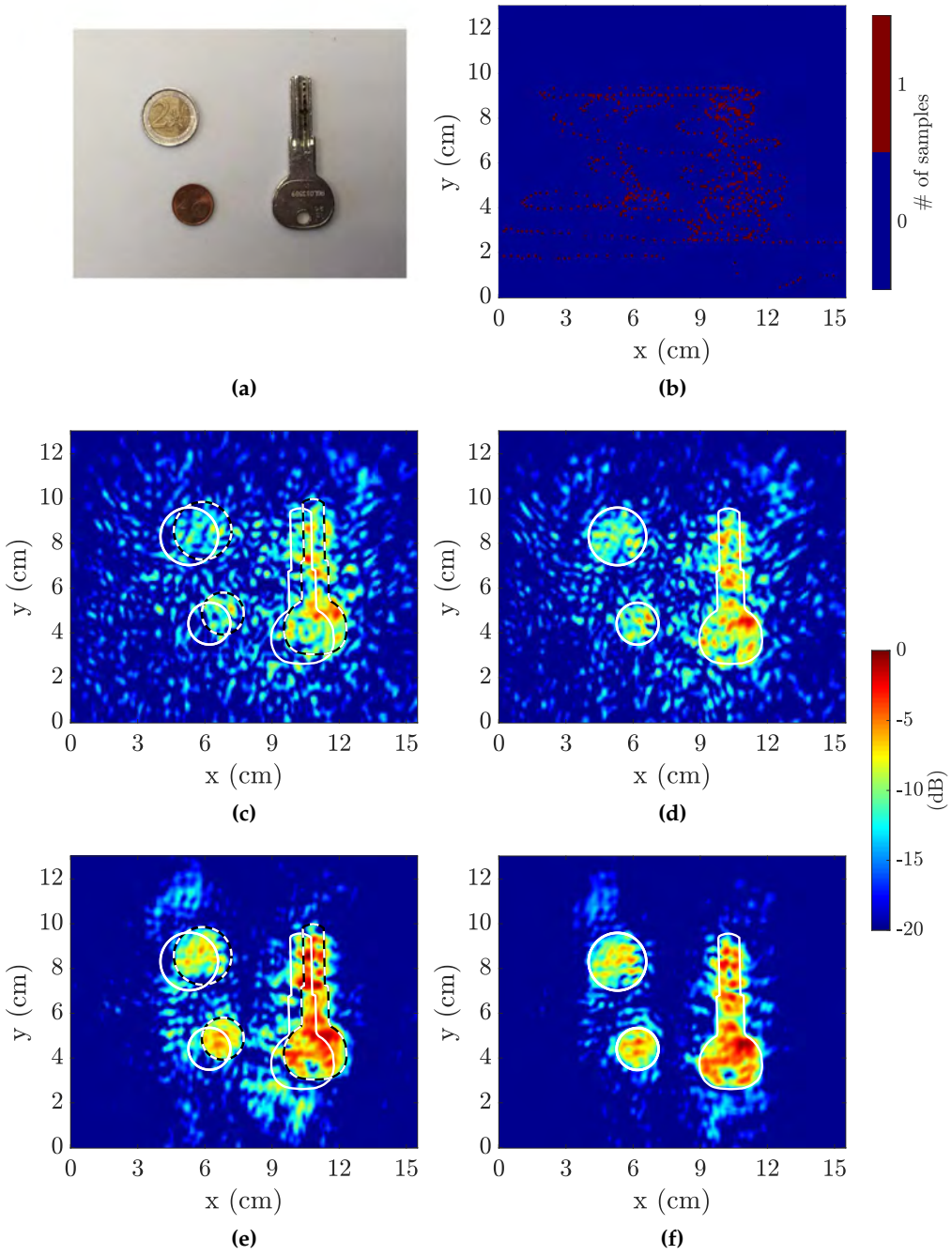

Figure 3.15: Picture of the coins and key used as targets (a), distribution of the positions of the acquired measurements (b), reflectivity image obtained using one TX and one RX before (c), and after the calibration (d), and image using the two TXs and the four RXs of the radar module before (e), and after the calibration (f).

The differences between these two images compared to those obtained considering one TX and one RX can be observed at a glance. In particular, using a MIMO scheme all the targets can be detected and the energy is more confined in the areas corresponding to them. However, without the calibration the targets appear shifted and the energy is more spread, resulting in more artifacts than after the calibration. As it can be seen, in the image obtained after applying the calibration, the shape of all the targets is well-reconstructed, even the small hole of the handle of the door key. In summary, after the calibration the quality of the retrieved images is improved. Also, using a multistatic setup the scanning time is reduced, as more information is gathered for a fixed amount of acquisition points. In a similar fashion, a scan of a given time yields higher-quality images using a multistatic setup.

The TCR of the retrieved images was computed in order to quantify the image quality improvement achieved when switching to a MIMO configuration and when applying the calibration. The obtained results are summarized in Table 3.4. As previously discussed from a qualitative point of view, the maximum TCR is obtained for the image computed with the MIMO configuration and after the calibration, which is used as reference to compute the TCR loss of the other images. Analogously to the previous analysis, the TCR values show an image quality enhancement when switching to a MIMO configuration and when applying the calibration.

	1 TX 1 RX		2 TX 4 RX	
	Pre-Cal	Post-Cal	Pre-Cal	Post-Cal
TCR (dB)	7.8	9.2	12.4	14.3
L (dB)	6.5	5.1	1.9	0

Table 3.4: TCR of the images of the coins and the key computed considering a different number of transmitters and receivers, before and after the calibration, and quality loss with respect to the image obtained after the calibration using the two transmitters and the four receivers of the radar module.

Finally, a test was conducted in order to assess the impact of the number of considered transmitters and receivers of the radar module in the performance of the scanner. For this test the scissors shown in Figure 3.16a, covered by a cardboard box, were used as target. In this case a maximum of two samples per cell was considered. During the scan a total of $N_{acq} = 2640$ measurements, whose distribution is shown in Figure 3.16b, were acquired during 183 s at an average distance to the target of 5.1 cm.

The computed reflectivity images, considering only one transmitter and one receiver, one transmitter and two receivers, one transmitter and four receivers

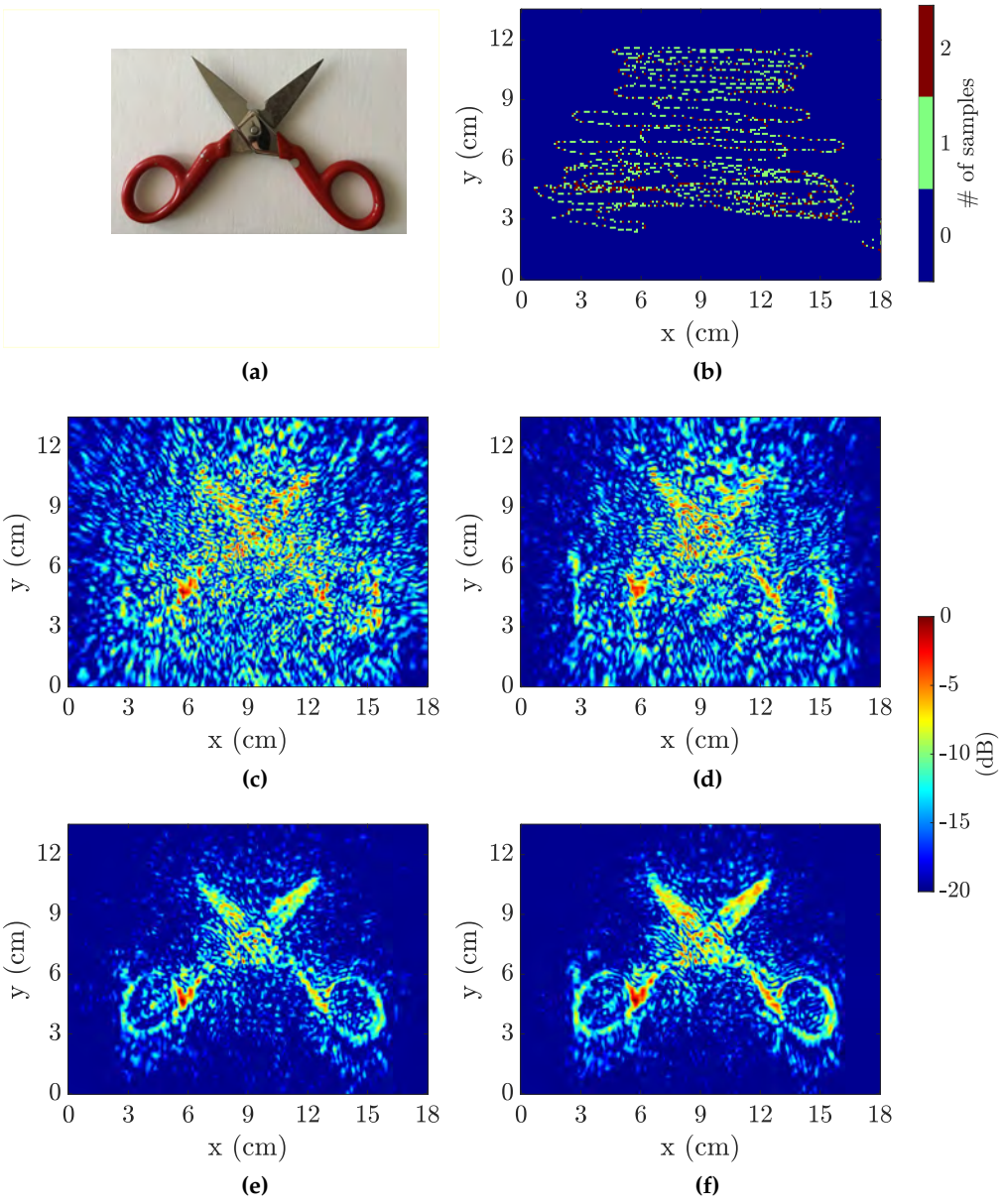

Figure 3.16: Picture of the scanned scissors (a), distribution of the positions of the acquired samples (b) and computed reflectivity image of the volume under test using one TX and one RX (c), one TX and two RXs (d), one TX and four RXs (e), and the two TXs and the four RXs of the radar module (f).

and all of the radar module transceivers (two transmitters and four receivers), are

depicted in Figure 3.16c, Figure 3.16d, Figure 3.16e and Figure 3.16f, respectively. As it can be observed, the quality of the retrieved image is significantly improved as more transmitters and receivers are considered. In particular, when considering one transmitter and four receivers (Figure 3.16e) the blades and the handles of the scanned scissors can be clearly recognized. In addition, when exploiting all the transceivers of the radar module (Figure 3.16f) the clutter is reduced.

3.7 Concluding remarks

In this chapter a handheld imaging system, capable of providing real-time high-resolution images has been presented [v], [**IV**]. It is based on using a compact radar-on-chip module which is freely moved by an operator while its position and attitude are tracked by a high-accuracy positioning system. The data acquired with the radar is coherently combined using SAR techniques yielding high-resolution images, which are updated in real-time. As a consequence, based on that feedback, the operator of the system is able to decide if it is necessary to scan a specific part of the area under scan more thoroughly, or whether enough information has already been acquired and the scanning process can be finished. During this chapter, the impact of positioning errors in the quality of the retrieved images has been studied and a calibration procedure to reduce them has been proposed. The performance of the system, both considering a quasi-monostatic scheme and a MIMO configuration, has been evaluated through several measurements. In particular, it has been shown that using a MIMO configuration the quality of the retrieved images is significantly improved while the scanning time is greatly reduced.

CHAPTER

4

Freehand antenna diagnosis and characterization system

This chapter is devoted to summarize the results presented in the publications composing this dissertation in the field of freehand antenna diagnosis and characterization. The concept of freehand antenna diagnosis and characterization is illustrated in Figure 4.1, which shows a potential application of the developed system. As it can be seen, the operator of the system is holding with their hand a compact device, which is moved in front of the AUT describing a freehand trajectory while the field radiated by the AUT is measured. The position of the handheld device is tracked during its movement so that the acquired field samples can be combined to retrieve an equivalent currents distribution on the AUT aperture, which provides insightful information for antenna diagnosis. Afterwards, the far-field radiation pattern is computed by means of a near-field to far-field transformation from the obtained equivalent currents distribution. First, in order to validate the proposed approach, the acquisition of both amplitude and phase was considered. In a second step, amplitude-only acquisitions were considered, avoiding the need of a phase reference and simplifying the hardware required to perform the field acquisition. This enables the diagnosis of antennas under operational conditions and reduces the overall cost of the equipment.

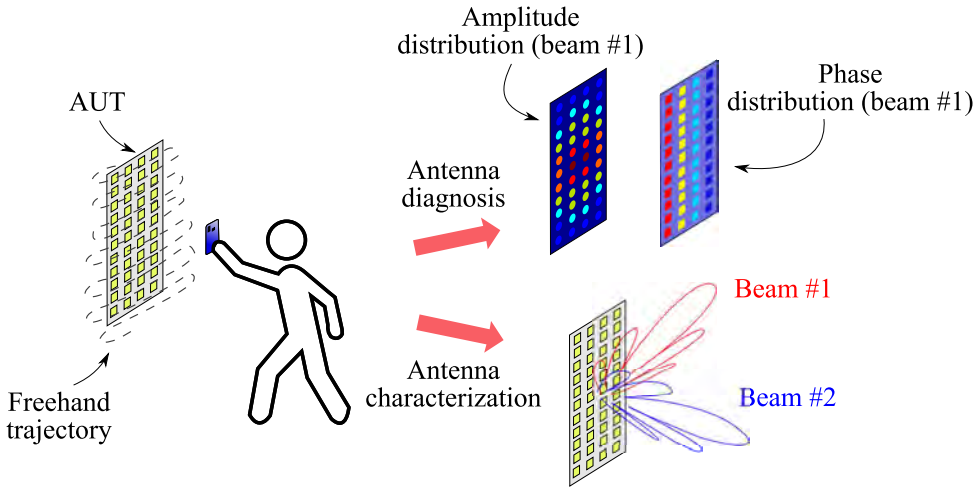

Figure 4.1: Scheme of the proposed freehand antenna diagnosis and characterization system.

Using both of the aforementioned approaches, the proposed system allows the fast diagnosis and characterization of antennas, both in laboratory conditions for quick testing and *in-situ* to assess the performance of already deployed antennas. This system bypasses the need of heavy positioners, providing great flexibility, which becomes particularly useful in those situations in which mechanical

structures cannot be easily deployed as for example when analyzing on-board antennas. Additionally, although several tests at different frequency bands have been performed during the development of the system, as it will be shown in the following sections, it is particularly useful at mm-wave frequencies and beyond because at those frequencies the probe antennas are light and the reflections with the operator are limited.

It should be noted that the proposed system, due to its freehand nature, is not expected to reach the accuracy of conventional antenna measurement ranges. Nonetheless, it enables fast antenna diagnosis and characterization with a good accuracy and with enormous flexibility due to its ease of deployment.

The rest of the chapter is organized as follows. First, the general architecture of the system is presented in Section 4.1. Second, the antenna diagnosis and characterization, both considering full-acquisitions and amplitude-only measurements, is discussed in Section 4.2. Finally, some of the obtained results, employing both approaches of the proposed system, are presented in Section 4.3.

4.1 System architecture

There are many analogies between this system and the freehand radar imaging system presented in Chapter 3. First, acquisitions will not be uniformly acquired as the probe antenna used to measure the field radiated by the AUT is moved by hand. Second, the gathered samples also have to be combined, imposing a frequency-dependent positioning accuracy requirement. In this case, this combination results in an equivalent currents distribution on the AUT aperture.

4.1.1 General architecture

The general architecture of the system is summarized in Figure 4.2. As it can be seen, the system was structured in three subsystems in a similar fashion to the freehand radar imaging system. Each subsystem is described in the following sections, emphasizing the specific features of each subsystem that are modified from the full-acquisition based system to the phaseless approach. In addition, the general architecture summarized in Figure 4.2 is particularized for the full-acquisition and the phaseless approach in Section 4.1.2 and in Section 4.1.3, respectively.

4.1.1.1 Control and processing subsystem

The control and processing subsystem is the core of the system, analogously to the freehand radar imaging system. Their main functions are summarized over

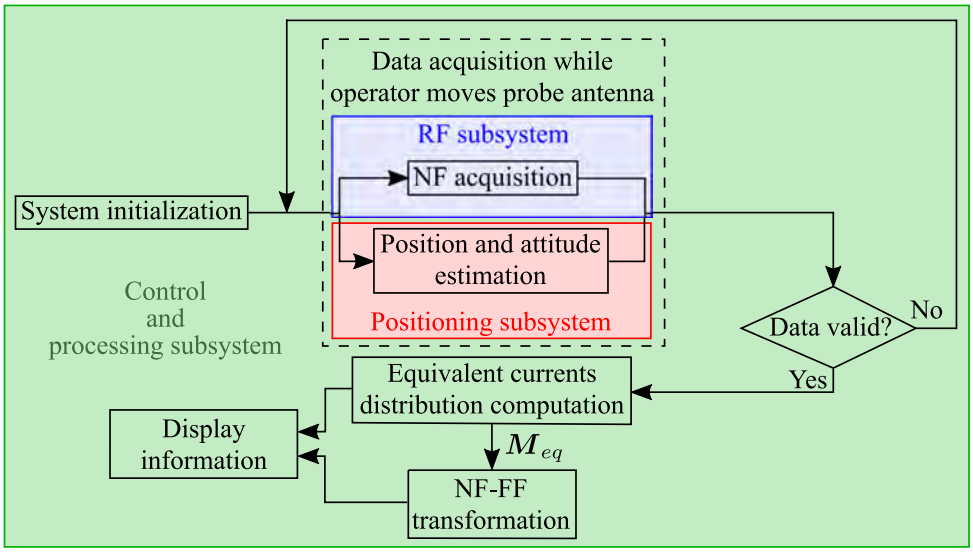

Figure 4.2: General architecture of the proposed freehand antenna diagnosis and characterization system.

the green background in Figure 4.2. This subsystem is in charge of setting up the system, establishing the communication with the RF subsystem and the positioning subsystem and defining the region where the equivalent currents distribution will be computed. During the operation of the system, the control subsystem is responsible for triggering both the field and position acquisitions and for gathering the obtained data. Finally, the obtained information is processed so that an equivalent currents distribution on the AUT aperture is computed, providing diagnosis information and from which the far-field radiation pattern of AUT can be retrieved by means of the corresponding radiation integrals, which correspond to a NF-FF transformation.

This subsystem was formed by the same laptop used for the freehand radar imaging system. The main equipment of this laptop was the following: Intel® i7-7700HQ (2.8 GHz), 16 GB of RAM and a NVIDIA® GeForce GTX 1050 graphic card.

In a similar fashion as for the imaging system, a strategy to ensure a proper sampling, dealing with the freehand operation of the system, must be implemented. In this case, the same idea proposed for the previous system was adopted. Thus, as illustrated in Figure 4.3, at least one acquisition volume, denoted as S_i, is defined in front of the AUT aperture (at least two in the phaseless case). Each acquisition volume is defined from a canonical surface (in this case a plane) and is discretized in cubic cells of size $d \times d \times t$, within which the number of field

acquisitions is limited to a maximum value of Q ($Q = 2$ in the example of Figure 4.3). After the limit is reached, or if the field sample was acquired outside the cubic cells, the sample is discarded. As previously explained in Section 3.1, this approach is designed to ensure a proper sampling while allowing a comfortable movement of the probe and avoiding highly oversampled areas.

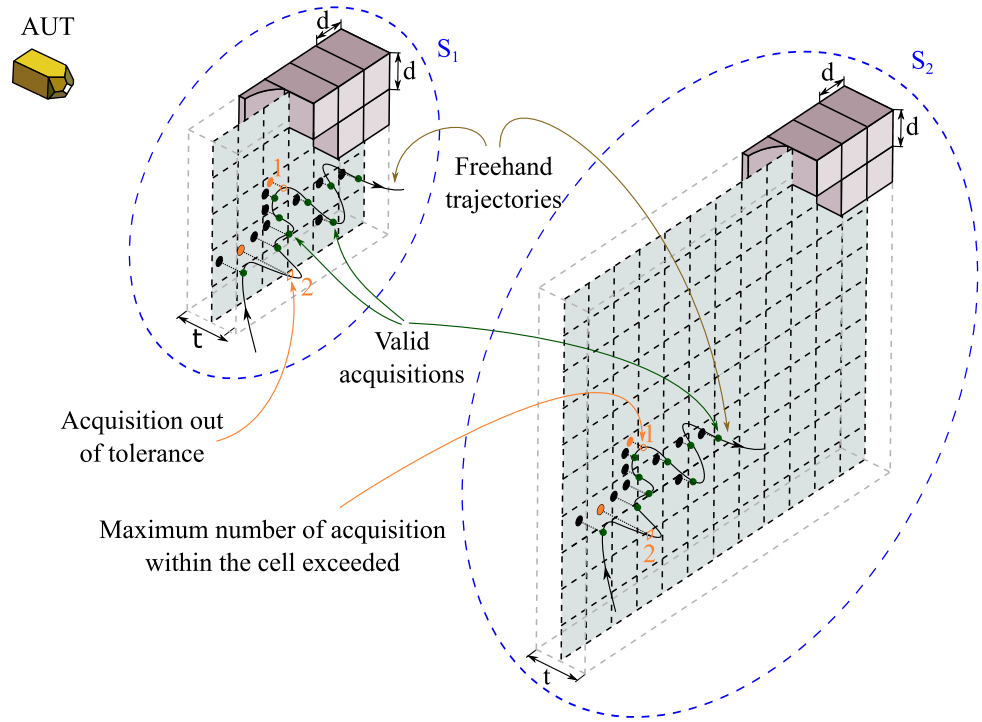

Figure 4.3: Scheme of the proposed acquisition balance strategy to mitigate the effect of an unbalanced sampling distribution.

In addition, as well as in the imaging system, a visual aid is displayed in the interface so that the operator knows the distance to the top and bottom of the cubic cells in order to move the probe antenna to a valid area. The distribution of the field acquisition points, in terms of number of samples per cell, is depicted in a 2D image in the interface shown to the operator. In addition, the amplitude of the acquired field samples (and their phase in the full-acquisition approach) is also depicted in the interface of the system.

Finally, in order to set an upper bound of the probe antenna movement during a field acquisition, the position of the probe is queried before and after each acquisition and, as in the freehand radar imaging system, if the difference is

higher than a frequency-dependent threshold (e.g., 1 mm), the field sample is discarded.

4.1.1.2 **Radiofrequency subsystem**

The RF subsystem comprises both the probe antenna and the equipment to perform the acquisitions of the field radiated by the AUT.

The probe antenna is independent of the followed field acquisition approach (full-acquisition or amplitude-only measurements). However, the used of electrically long Open-Ended Waveguides (OEWGs) is recommended in order to reduce the coupling between the probe antenna and the person who is holding it. This coupling is expected to be similar to the one taking place between the supporting structures and the probe antenna in conventional antenna measurement facilities (e.g., an anechoic chamber). It should be also taken into account the coupling the AUT and the probe antenna. In this regard, the coupling follows the same rules as in conventional planar measurements and, therefore, it is considered that the near-field acquisition can be successfully performed as long as a distance of a few wavelengths is considered [69]. It is relevant to consider that, as in conventional planar range measurements, the distance between the AUT and the acquisition plane (in this case the acquisition volume) also has an impact on the plane truncation error [69].

On the other hand, the equipment required to perform the field acquisitions depends on the measurement approach. In particular, when using the full-acquisition approach it is necessary to acquire both the amplitude and phase of the field radiated by the AUT and, as a consequence, a Vector Network Analyzer (VNA) should be used. The VNA, which can be a portable one, should be connected both to the probe antenna and to the AUT. In contrast, only a power detector or a spectrum analyzer connected the probe are required for amplitude-only measurements.

4.1.1.3 **Positioning subsystem**

The positioning subsystem is devoted to track the movement of the probe antenna during the scan of the field radiated by the AUT. This subsystem must be compatible with the probes, meaning that significant modifications should not be required. In addition, the accuracy of the positioning system should be much higher than the working wavelength of the AUT and it should provide real-time position and attitude information. During the development of this system, the same motion capture system as the one used for the freehand radar imaging was used [130]. In particular, the used motion capture system comprises four infrared

cameras, which can be easily deployed and calibrated in a few minutes, and four reflective markers with a diameter of 6.5 mm. These markers are attached to the probe antenna considered for each measurement by means of a custom 3D-printed structure.

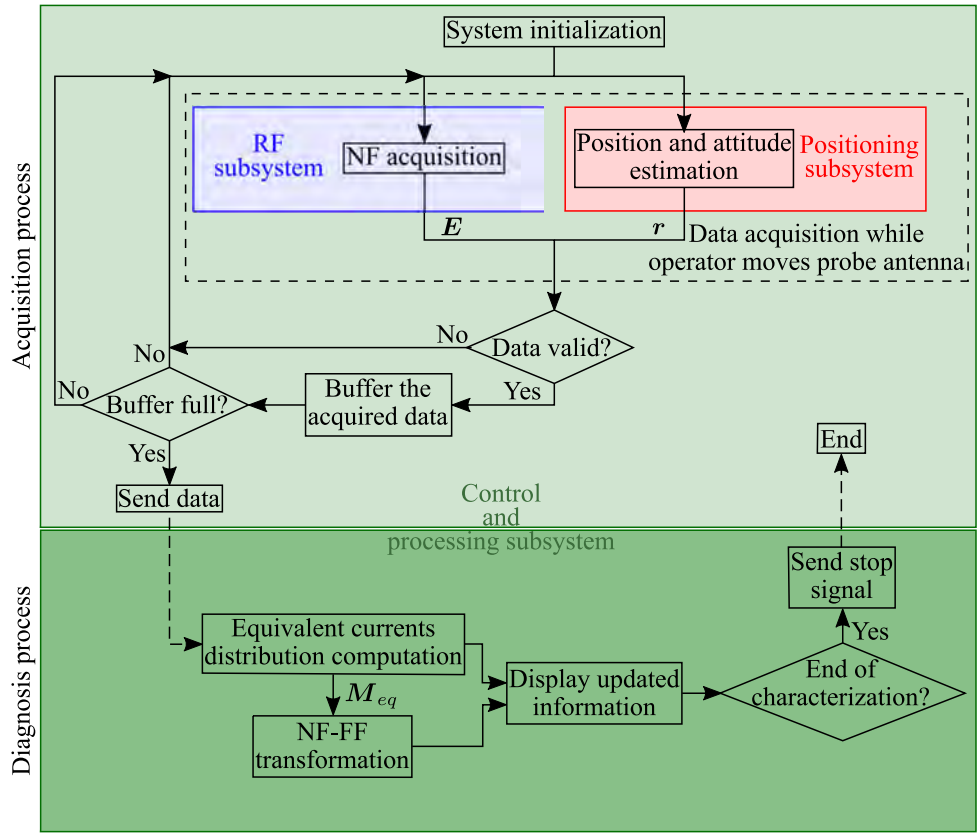

Figure 4.4: Architecture of the full-acquisition based proposed freehand antenna diagnosis and characterization system.

4.1.2 Full-acquisition based system architecture

For the full-acquisition approach the general architecture of the system, depicted in Figure 4.2, was structured in two processes, namely acquisition and diagnosis, with the client-server architecture shown in Figure 4.4. The two processes are run concurrently as the operator of the system performs field acquisitions. The obtained results are updated in real-time and displayed to the operator. As previously stated, during the measurements performed within this thesis both

processes were run on the same laptop. However, this architecture makes possible to run each process on a different machine.

The acquisition process is in charge of the synchronous acquisition of the position and field samples and of balancing their distribution as described in Section 4.1.1.1. Non-discarded acquisitions are buffered until a certain amount of samples is gathered and, after that, the samples are sent to the diagnosis process. The sample buffer avoids an unnecessary computational burden associated to recomputing the equivalent currents for each new acquisition as the operator usually does not require an update rate so high.

The diagnosis process receives and stores the position and field samples. After receiving each set of samples, it computes an equivalent currents distribution and the radiation pattern of the AUT while more data is acquired by the operator. As previously introduced, the retrieved information, currents distribution and radiation pattern of the AUT, is updated and displayed in real-time, alongside with the distribution of the acquired measurements and their amplitude and phase. Once again, it should be remarked that all the previous real-time information is intended to help the operator during the scan. For example, the operator can dynamically change from scanning a certain area to a different one based on the achieved sample density, the lack of impact of new samples in the final result or the field strength of the samples of a given area.

4.1.3 **Phaseless system architecture**

For the amplitude-only approach, the general architecture of the system, depicted in Figure 4.2, was also structured in two stages as shown in Figure 4.5: acquisition and diagnosis.

In contrast to the full-acquisition based approach, the stages take place sequentially. First, all the $n_{acq.vol.}$ acquisition volumes are scanned $(n_{acq.vol.} > 1)$ and, afterwards, the diagnosis of the AUT is performed. In this case, the distribution of the acquired samples is updated and displayed to the operator in real-time, alongside with their amplitude and the previously mentioned visual aids. An equivalent currents distribution and the radiation pattern of the AUT are computed after the acquisition stage is completed to perform the phase retrieval of the field distribution, as it will be discussed in Section 4.2.2. After that, an equivalent currents distribution and the radiation pattern are computed in a similar fashion to the full-acquisition based system. Nonetheless, this approach still provides a flexible and fast antenna diagnosis and characterization as, once the data from the acquisition volumes is gathered, the equivalent currents distribution and the FF radiation pattern of the AUT are retrieved in a matter of seconds.

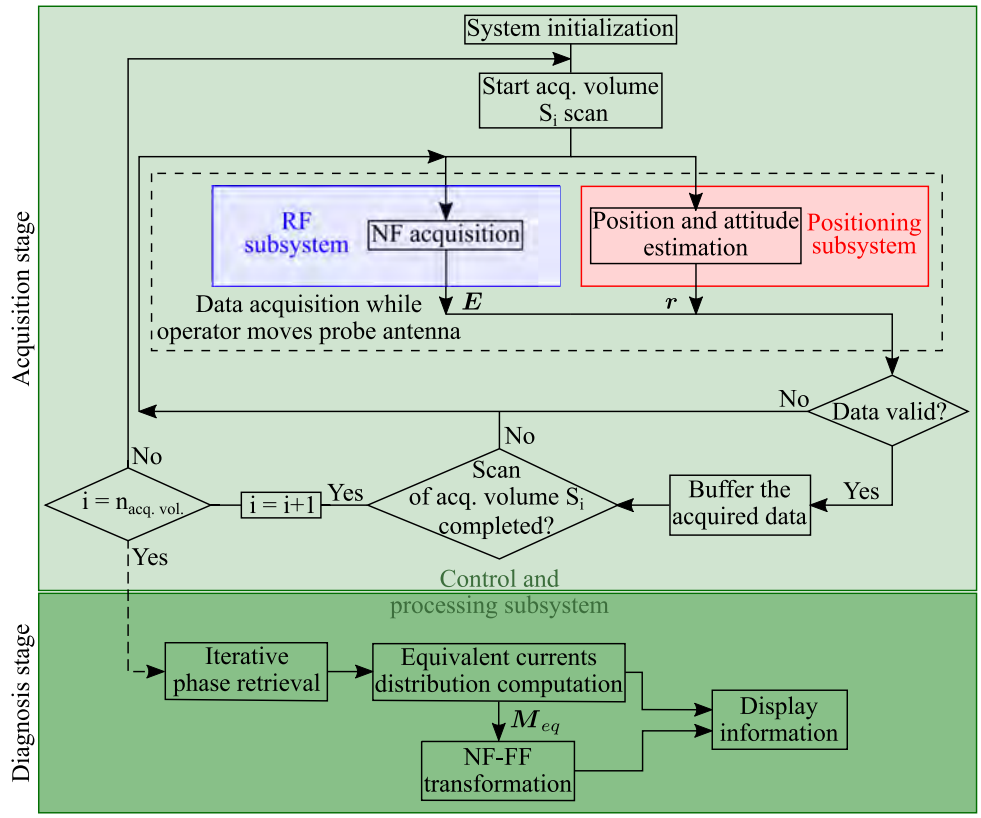

Figure 4.5: Architecture of the amplitude-only based proposed freehand antenna diagnosis and characterization system.

4.2 Antenna diagnosis and characterization method

As previously introduced, the proposed system retrieves an equivalent currents distribution of the AUT from which its far-field radiation pattern is computed, achieving both diagnosis and characterization of the AUT. The SRM [99] and its modified version considering amplitude-only acquisitions, the pSRM [116], are discussed in Section 4.2.1 and in Section 4.2.2, respectively.

4.2.1 Sources reconstruction method (SRM)

Based on the electromagnetic equivalence principle [139], if an antenna is enclosed by a surface S', namely the reconstruction surface, it is possible to find an equivalent electric and/or magnetic currents distribution so that it radiates the same fields outside the reconstruction surface as the antenna bounded by it. The

SRM solves the inverse radiation problem of computing that equivalent currents distribution over S' from the field samples acquired in the observation surface, S. The electric and magnetic equivalent currents distribution at the reconstruction surface, $\boldsymbol{J}_{eq}(\boldsymbol{r'})$ and $\boldsymbol{M}_{eq}(\boldsymbol{r'})$, respectively, are related to the field acquired at the reconstruction surface by means of a set of integral equations derived from the Maxwell equations. As explained in [110], both $\boldsymbol{J}_{eq}(\boldsymbol{r'})$ and $\boldsymbol{M}_{eq}(\boldsymbol{r'})$ can be computed from either magnetic field or electric field observations. Nonetheless, most of antenna diagnosis and characterization systems are based on electric field measurements, which is also the case for the system proposed within this thesis. The expressions which relate the electric fields $\boldsymbol{E}_{J_{eq}}(\boldsymbol{r})$ and $\boldsymbol{E}_{M_{eq}}(\boldsymbol{r})$ at position $\boldsymbol{r} \in S$ to the electric and magnetic currents distributions, $\boldsymbol{J}_{eq}(\boldsymbol{r'})$ and $\boldsymbol{M}_{eq}(\boldsymbol{r'})$, which are defined over the surface S' that radiate those fields are given by the following radiation integrals

$$\boldsymbol{E}_{J_{eq}}(\boldsymbol{r}) = \frac{-j\eta}{4\pi k_0} \int_{S'} k_0^2 \boldsymbol{J}_{eq}(\boldsymbol{r'}) \frac{e^{-jk_0\|\boldsymbol{r}-\boldsymbol{r'}\|}}{\|\boldsymbol{r}-\boldsymbol{r'}\|} + \nabla\left(\nabla\cdot\left(\boldsymbol{J}_{eq}(\boldsymbol{r'})\frac{e^{-jk_0\|\boldsymbol{r}-\boldsymbol{r'}\|}}{\|\boldsymbol{r}-\boldsymbol{r'}\|}\right)\right) dS' \quad (4.1)$$

and

$$\boldsymbol{E}_{M_{eq}}(\boldsymbol{r}) = \frac{-1}{4\pi} \int_{S'} \nabla \times \left(\boldsymbol{M}_{eq}(\boldsymbol{r'})\frac{e^{-jk_0\|\boldsymbol{r}-\boldsymbol{r'}\|}}{\|\boldsymbol{r}-\boldsymbol{r'}\|}\right) dS', \quad (4.2)$$

where k_0 is the wavenumber and η is the intrinsic impedance of the medium. The total electric field can be found by superposition:

$$\boldsymbol{E} = \boldsymbol{E}_{J_{eq}} + \boldsymbol{E}_{M_{eq}}. \quad (4.3)$$

The previous integral equations can be expanded into a matrix form and numerically solved to obtain the equivalent currents distribution. In the presented implementation, a planar reconstruction domain (usually placed at the antenna aperture) is chosen and, therefore, only the equivalent magnetic currents are needed [102]. Therefore, the magnetic currents are discretized by means of known basis functions yielding the following linear system of equations:

$$\overline{\overline{A}} \begin{bmatrix} b_1 \\ b_2 \\ \vdots \\ b_N \end{bmatrix} = \begin{bmatrix} E_{M_{eq},1} \\ E_{M_{eq},2} \\ \vdots \\ E_{M_{eq},M} \end{bmatrix} \quad (4.4)$$

where b_n is the weight of the n-th basis function and $E_{M_{eq},m}$ is the electric field sample at the m-th considered position. The matrix $\overline{\overline{A}}$ has dimensions $M \times N$ where N is the number of basis functions and M is the number of considered field samples. The elements at row m and column n of matrix $\overline{\overline{A}}$ relate the field at the m-th position radiated by the n-th basis function with the corresponding evaluation of the Green's function [99].

The previous system of equations, which is usually overdetermined, is solved by means of an iterative solver, such as the conjugated gradient method, providing the minimum error and energy solution to (4.4). After that, the far-field radiation pattern is computed by using the corresponding radiation integrals [139].

4.2.2 **Phaseless sources reconstruction method (pSRM)**

The modified version of the SRM considering amplitude-only data requires, as previously stated, at least two independent acquisition volumes. In this context, *independent* means that the spatial variation of the field distribution with distance provides enough information for the phase retrieval.

For that purpose, the system of equations of (4.4) has to be reformulated to relate the amplitude of the measured field with the one radiated by the equivalent currents distribution. This yields the following non-linear system of equations, in contrast to the conventional SRM, which can be solved using a non-linear minimization method such as Levenberg-Marquardt solver [140]:

$$\left| \overline{\overline{A}} \begin{bmatrix} b_1 \\ b_2 \\ \vdots \\ b_N \end{bmatrix} \right|^2 = \left| \begin{bmatrix} E_{M_{eq},1} \\ E_{M_{eq},2} \\ \vdots \\ E_{M_{eq},M} \end{bmatrix} \right|^2 , \tag{4.5}$$

where an initial guess of the equivalent currents distribution must be provided. This guess can be obtained from the knowledge of the physical geometry of the AUT assuming a uniform distribution of the currents over the antenna aperture, i.e., $b_i = 1$ over the antenna aperture and $b_i = 0$ elsewhere. It should be remarked that, as previously explained, in the presented implementation a planar reconstruction domain is selected and, as a consequence, only the equivalent magnetic currents are considered [102]. It should be noted that, if linear field components are considered, the integral equations relating the measured field samples and the aperture fields can be decoupled. Once minimization of (4.5) is completed, the obtained equivalent currents distribution is used to estimate the phase of the field samples acquired at each acquisition volume, which are then processed using the

original SRM described in Section 4.2.1 in order to obtain a better estimation. Once the equivalent currents distribution is computed, the far-field radiation pattern of the AUT can be obtained by means of a NF-FF transformation [139].

4.3 Measurement results

The proposed system was tested by means of several measurements at different frequency bands. First, the full-acquisition approach was validated and, afterwards, the performance of the amplitude-only approach was assessed comparing the obtained results with those obtained with a standard measurement range and with those retrieved using the proposed system considering both amplitude and phase acquisitions.

4.3.1 Full-acquisition based system validation

The performance of the proposed system using both the amplitude and phase of the measured field was assessed through several measurements at X band and at Ka band.

4.3.1.1 Measurements in X band

The leaky-wave antenna depicted in Figure 4.6 was measured at 12 GHz with the proposed system and also in a conventional planar range [141] in order to have a reference result. The AUT was measured using an open-ended waveguide WR90 as probe antenna and a VNA (Keysight PNA-X) to measure the radiated signal.

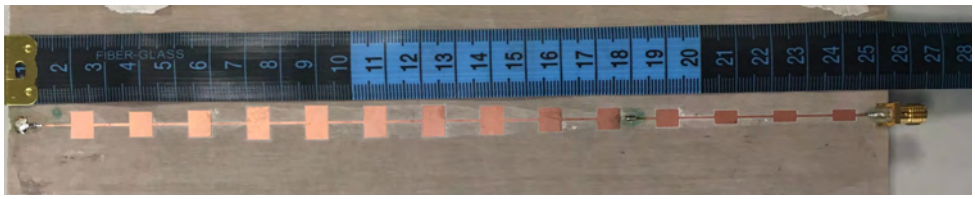

Figure 4.6: Image of the measured leaky-wave antenna.

The setup used to measure the leaky-wave antenna using the proposed system is depicted in Figure 4.7a. The size of the cubic cells used to balance the distribution of the acquisitions was set to $1 \times 1 \times 1$ cm. During the acquisition a total of 937 NF samples were measured at an average distance of 11 cm from the

AUT covering a surface of $27 \times 33\,\mathrm{cm}^2$. Regarding the measurements using the planar range, the setup is shown in Figure 4.7b. In this case, a planar acquisition grid covering an area of $1 \times 1\,\mathrm{m}^2$ with a sampling step of 1 cm both in the x- and in the y- axes was defined at 30 cm from the AUT.

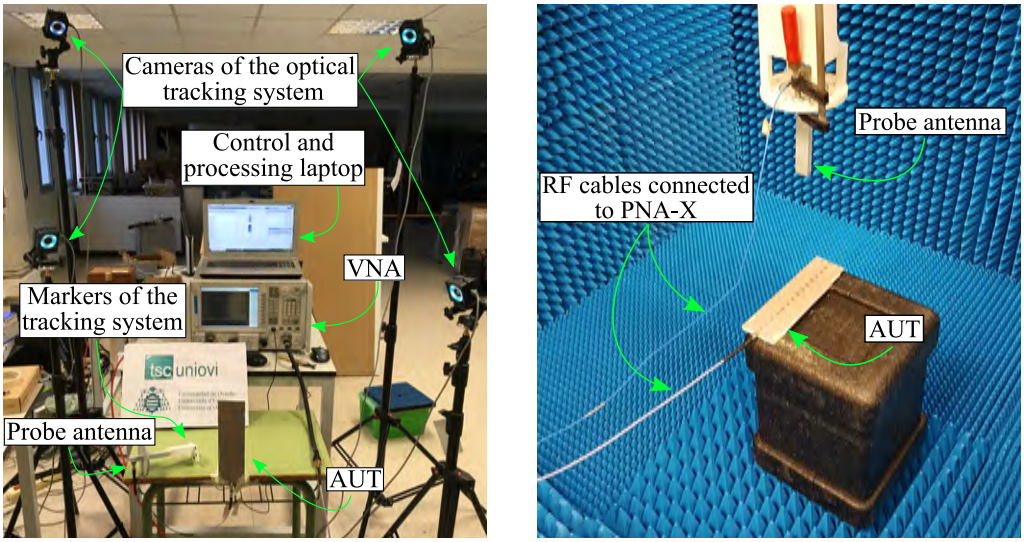

(a) **(b)**

Figure 4.7: Measurement setup using the proposed system (a) and using a conventional planar range.

The normalized amplitude of the equivalent currents distribution obtained with the SRM from the samples acquired using the proposed system and employing the planar range is depicted in Figure 4.8a and Figure 4.8b, respectively. As it can be seen, both distributions are in good agreement. The phase of the equivalent currents distribution retrieved using the proposed system and employing the planar range is shown in Figure 4.8c and Figure 4.8d, respectively. For a better comparison, only the phase where the normalized amplitude of the equivalent currents distribution is above $-15\,\mathrm{dB}$ is plotted. As it can be observed, both phase profiles are in good agreement.

Finally, the far-field pattern was computed from the equivalent currents distribution by means of a NF-FF transformation. In particular, the results of the E-plane cut obtained using the proposed system and the planar range are depicted in Figure 4.9. It should be noted that position of the maximum of the field pattern, which is at $\theta = 22°$, is well estimated using the proposed system. In addition, the $-15\,\mathrm{dB}$ sidelobe at $\theta = 20°$ is also predicted and the rest of the ra-

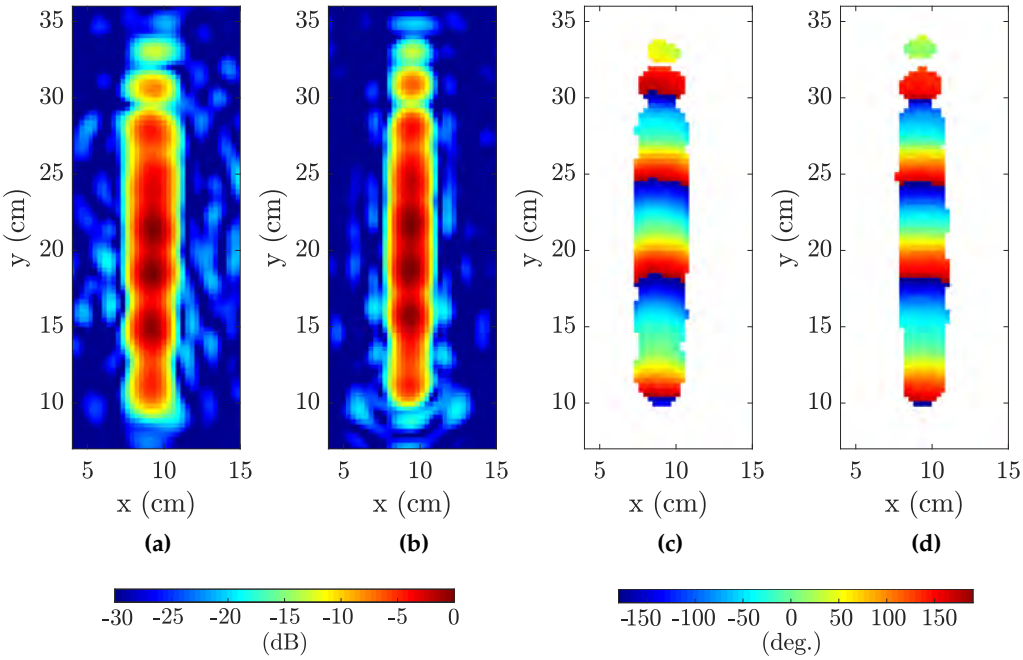

Figure 4.8: Normalized amplitude and phase of the equivalent currents distribution obtained using the proposed system (a) and (c), respectively, and employing the planar range (b) and (d), respectively.

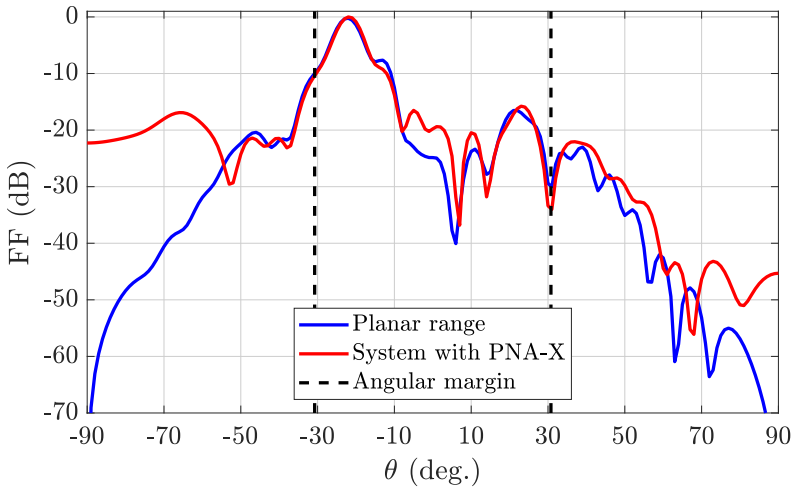

Figure 4.9: E-plane cut of far-field pattern of the leaky-wave antenna.

diation pattern within the angular margin of validity [69] (denoted with vertical dashed lines) is in a fair agreement with the planar range reference results despite the freehand measurements not being performed in an anechoic environment.

4.3.1.2 **Measurements in Ka band**

For the Ka band tests the two-horn antenna array depicted in Figure 4.10a was measured. The distance between the antennas was 2.1 cm and an open-ended waveguide WR28 was used as probe. In addition, as for the X band measurements, a PNA-X was used to measure the amplitude and phase of the radiated signal.

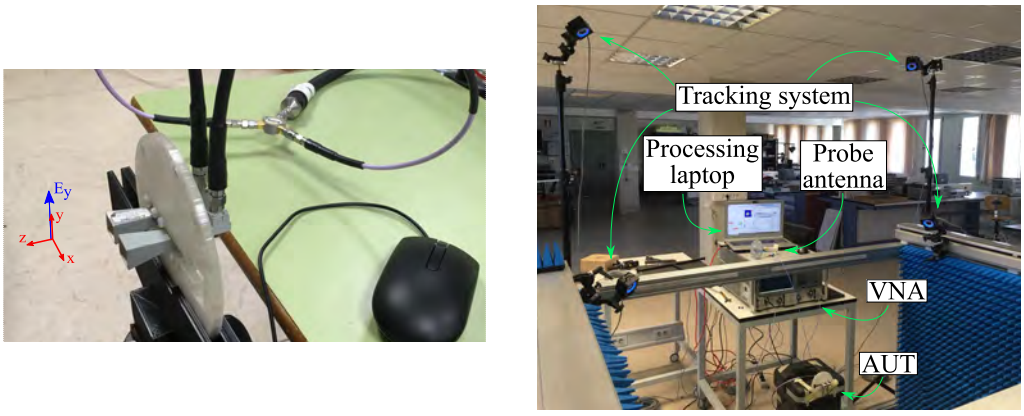

(a) **(b)**

Figure 4.10: Measurement setup using the proposed system (a) and using a conventional planar range.

For the first test the AUT was deployed in the planar range and it was measured both with the planar range and using the proposed system. The measurement setup is depicted in Figure 4.10b, where it is possible to see the infrared cameras attached to the planar range. For the reference measurement the probe was mounted on the planar range positioner. Employing the proposed system the operator moved the probe in front of the AUT inside the planar range. The VNA was configured to measure 201 frequency points between 24 and 32 GHz, being the sweep time 1.45 ms.

During the freehand scan, a total of 4091 samples were acquired in an area of $19.6 \times 23.3\,\text{cm}^2$ at an average distance of 7.1 cm from the AUT in 984 s. In addition, the size of the cubic cells used to balance the distribution of the acquisitions was set to $\lambda/2 \times \lambda/2 \times \lambda/2$ at 32 GHz and the maximum number of samples per cell

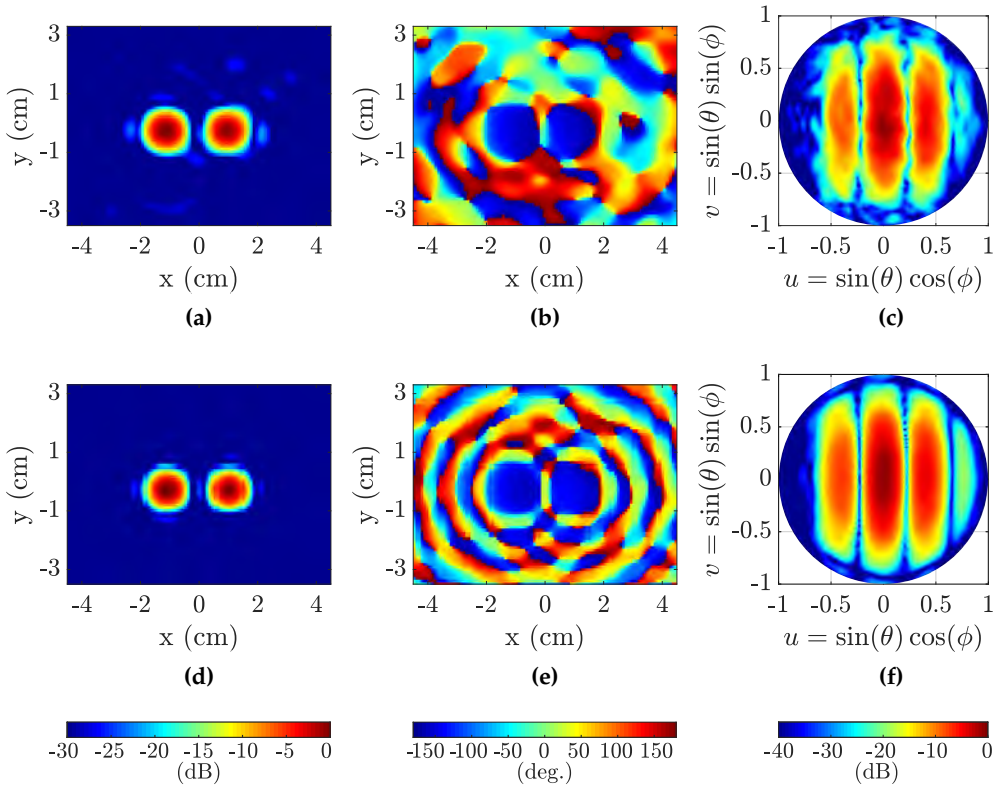

Figure 4.11: Normalized amplitude and phase of the computed equivalent currents distribution obtained using the proposed system (a) and (b), respectively, and employing a standard planar range (d) and (e), respectively. UV representation of the retrieved antenna radiation pattern obtained using the proposed system (c) and employing a standard planar range (f).

was set to 5. Using the planar range, a total of 3135 acquisitions were performed in a regular grid of $24.3 \times 25.2\,\text{cm}^2$ at 10 cm from the AUT using a $\lambda/2$ step at 32 GHz. The step between consecutive samples was $\lambda/2$ at 32 GHz and the total acquisition time was 6173 s.

The normalized amplitude of the reconstructed equivalent currents distribution at 32 GHz obtained with the proposed system and with the planar range is depicted in Figure 4.11a and Figure 4.11d, respectively. As it can be seen, although small artifacts below -20 dB appear when using the proposed system, the results are similar. The same holds for the phase of the reconstructed equivalent currents distribution, which is shown in Figure 4.11b and Figure 4.11e using the proposed system and the planar range, respectively. The UV representation of the far-field

radiation pattern computed from the equivalent currents distribution estimated using the proposed system and the planar range is depicted in Figure 4.11c and Figure 4.11f, respectively. As it can be observed, although the pattern obtained with the proposed system is noisier than the one measured with the planar range, the main and the secondary lobes are well-reconstructed, which demonstrates the accuracy of the proposed system.

For the second test the same two-horn antenna array was deployed outside the planar range and was scanned using the proposed system considering two different sizes of the cubic cells used to balance the distribution of the acquisitions. In particular, during both tests the horizontal size of the cells was set to $d = 2\,\text{mm}$. However, during the first test the value of the vertical size was set to $t = 5\,\text{mm}$, i.e., slightly less than $\lambda/2$ at 32 GHz, whilst during the second test this value was relaxed to $t = 20\,\text{mm}$, i.e., almost 4λ at 32 GHz. The maximum number of samples per cell was set to $Q = 5$ during both measurements. It should be noted that some cables had to be replaced resulting in slightly different phase shifts and, consequently, radiation patterns.

During the measurement considering $t = 5\,\text{mm}$, a total of 6573 samples were acquired during 892 s at an average distance of 3.5 cm from the AUT. The distribution of the acquired samples is depicted in Figure 4.12a. The normalized amplitude and phase of the equivalent currents distribution, computed at 32 GHz, is shown in Figure 4.12b and Figure 4.12c, respectively. During the measurement considering $t = 20\,\text{mm}$ a total of 1766 samples were acquired during 223 s at an average distance of 6.1 cm from the AUT. In this case, the distribution of the acquired samples is depicted in Figure 4.12d and the normalized amplitude and phase of the equivalent currents distribution, computed at 32 GHz, is shown in Figure 4.12e and Figure 4.12f, respectively.

As it can be seen in Figure 4.12b and in Figure 4.12e, there are two areas where the normalized amplitude of the equivalent currents distribution is high, each of them corresponding the aperture of each horn of the array (the area corresponding to the aperture of each horn is enclosed by a black dashed line). As expected, the normalized amplitude of the two regions of the equivalent currents distribution corresponding to the aperture of each horn is similar. In particular, for the measurement considering $t = 5\,\text{mm}$ the amplitude difference between the maximum of each horn was only 0.58 dB. In the case of the measurement considering $t = 20\,\text{mm}$, this difference was 0.12 dB. It should be remarked that both maxima were separated 2.1 cm, matching the physical separation between the two horns. Analogously, as it can be observed comparing Figure 4.12c and Figure 4.12f, the maxima of the normalized amplitude corresponding to each horn are almost in phase: 1.2° difference when $t = 5\,\text{mm}$ was considered and 4.4° when $t = 20\,\text{mm}$ was used.

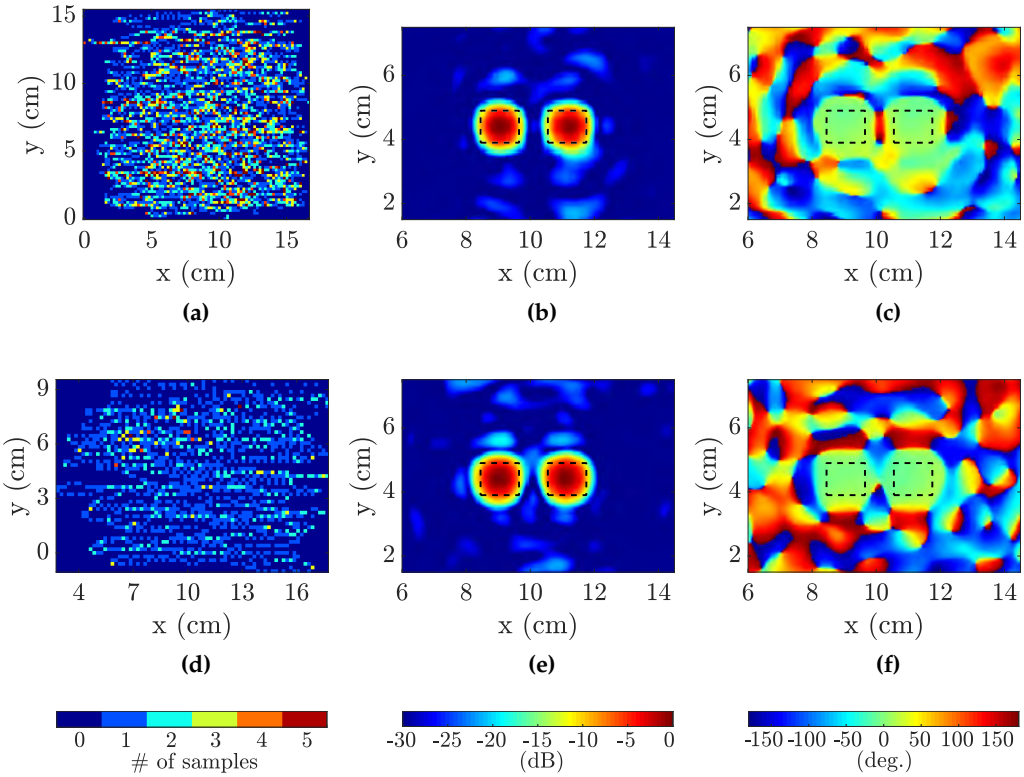

Figure 4.12: Distribution of the positions of the acquired samples (a) and normalized amplitude (b) and phase (c) of the obtained equivalent currents distribution during the measurement considering $t = 5\,\text{mm}$. The same information for the measurement considering $t = 20\,\text{mm}$ is displayed in (d), (f) and (e).

Finally, the H-plane cut of the far-field pattern obtained from both measurements, which was computed performing a NF-FF transformation, is depicted Figure 4.13. In addition, the theoretical pattern, which was obtained considering an array of two elements separated the same distance as the actual two-horn array, fed with equal amplitude and phase and considering an element radiation pattern of $\cos^5(\theta)$, is plotted in red. As it can be seen, in both cases the main lobe ($\theta = 0°$) and the sidelobes ($\theta = \pm 22°$) are well-reconstructed, and the rest of the H-plane cut within the angular margin of validity of the measurements presents a fair agreement with the theoretical pattern.

From the results, it can be concluded that, as expected, although the accuracy is not as high as the one obtained in typical anechoic antenna measurement ranges, the results obtained with the proposed system exhibit good accuracy, en-

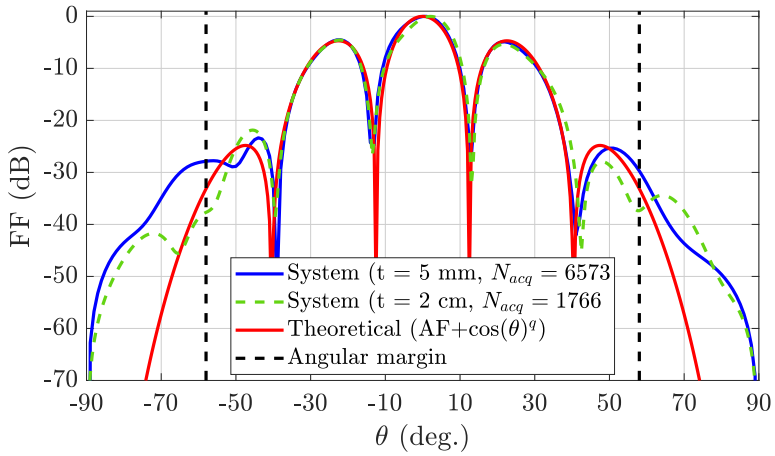

Figure 4.13: H-plane cut of far-field pattern of the two-horn antenna array.

abling a fast diagnosis and characterization of an AUT outside a laboratory facility. In addition, although the results obtained after increasing the size of the cubic cells are noisier than those obtained considering a lower value of t, relaxing the control of the sampling allows for a much faster diagnosis and characterization of antennas.

For the last test a variable attenuator was added to one element of the previous two-horn antenna array as shown in Figure 4.14a. Thus, different amplitudes and phases are applied to each element of the array. In this case the size of the cubic cells to control the distribution of the acquisitions was set to $2 \times 2 \times 5$ mm and the maximum number of samples per cell was set to $Q = 5$. In addition, as in the previous measurements, the VNA was configured to acquire 201 frequency points between 24 and 32 GHz.

During the scan, a total of 7271 acquisitions were performed at an average distance of 3.6 cm from the AUT aperture. The distribution of the acquired samples is depicted in Figure 4.14d. The normalized amplitude and phase of the obtained equivalent currents distribution at 32 GHz is shown in Figure 4.14e and Figure 4.14f, respectively. As it can be seen, one of the two areas where the amplitude of the equivalent currents distribution is high, corresponding to each horn, is attenuated. In order to have a reference for the amplitude and phase difference between each horn caused by the attenuator (along the measured frequency band), each branch of the feeding network was characterized using a VNA. This was accomplished by measuring directly the S_{21} parameter of each branch, and then computing the difference between the two branches. To compare this difference (measured directly with the VNA) with the results obtained with the proposed

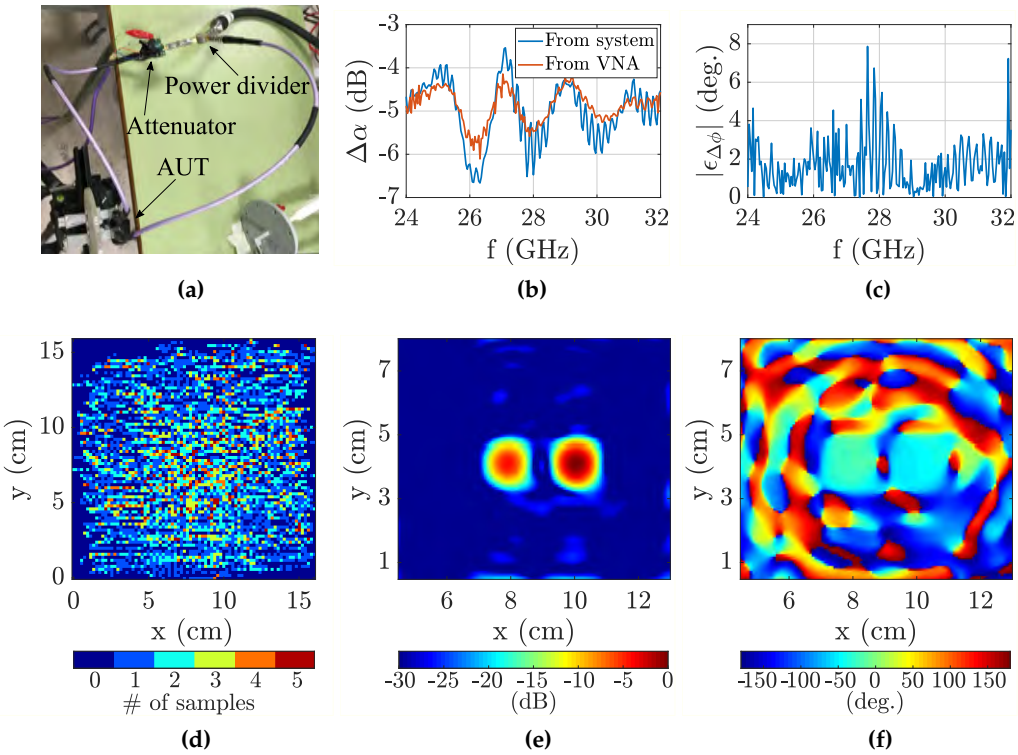

Figure 4.14: Setup using an attenuator connected to one of the horns of the array (a). Amplitude difference between each horn (b) and error of the phase difference computed with the proposed system (c). Distribution of the positions of the acquired samples (d) and normalized amplitude (e) and phase (f) of the obtained equivalent currents distribution at 32 GHz.

system, an equivalent currents distribution was retrieved for each measured frequency. Then, the difference between the normalized amplitude and the phase of the equivalent currents distribution that corresponds to each horn was computed. In particular, this difference was computed at the position of the maximum of the normalized amplitude at the position of each horn. The amplitude difference between each horn, both obtained directly with VNA and employing the proposed system is displayed in Figure 4.14b. As it can be seen, the amplitude difference is very similar in both cases, with errors below 1 dB. Also, the curve obtained with the proposed system presents a higher ripple, probably due to the presence of reflections in the near environment. Regarding the phase difference, in this case the absolute errors between the differences retrieved with the proposed system and the reference values obtained with the VNA, $|\epsilon_{\Delta\phi}|$, are depicted in Figure

4.14c. As it can be observed, in 97% of the cases the error is below 5°, being the maximum error 7.8°.

4.3.2 Amplitude-only system validation

This section is devoted to the assessment of the capabilities of the amplitude-only approach of the proposed system, including measurements at different frequency bands.

4.3.2.1 Measurements in Ka band

The first set of measurements is focused on checking the capabilities of the system by comparing different full acquisition schemes versus the proposed phaseless approach. In particular, during the measurements performed inside the planar range depicted in Figure 4.10b, the field radiated by the AUT (amplitude and phase) was measured at two different acquisition volumes using the proposed system. The results obtained employing the proposed system at 32 GHz, considering phase information, are presented in Section 4.3.1.2, where they are compared with the results retrieved using a standard planar range. In this section the results obtained at 30 GHz using only the amplitude information acquired during two measurements of the AUT using the proposed system are presented and compared with the results achieved considering both amplitude and phase information using the proposed system and the conventional planar range.

First, the main parameters of the two measurements presented in Section 4.3.1.2 (one acquisition volume with the proposed system and the measurement with the planar range) are recalled in Table 4.1, where the parameters of the second acquisition volume measured with the proposed system are also included.

Measurement	# of samples	Avg. dist. to AUT (cm)	Time (s)	Scanned area (cm^2)
Planar range	3135	10	6173	24.3×25.2
Prop. system S1	4091	7.1	984	19.6×23.3
Prop. system S2	2278	4.9	566	16×16

Table 4.1: Summary of the acquisitions performed at Ka band to assess the performance of the amplitude-only approach of the proposed system.

The normalized amplitude of the samples acquired with the proposed system within the acquisition volumes S_1 and S_2, is depicted in Figure 4.15a and Figure 4.15b, respectively. It should be noted that, as expected, the farther the acquisition

volume is from the AUT, the bigger the scanned area must be due to the field spreading.

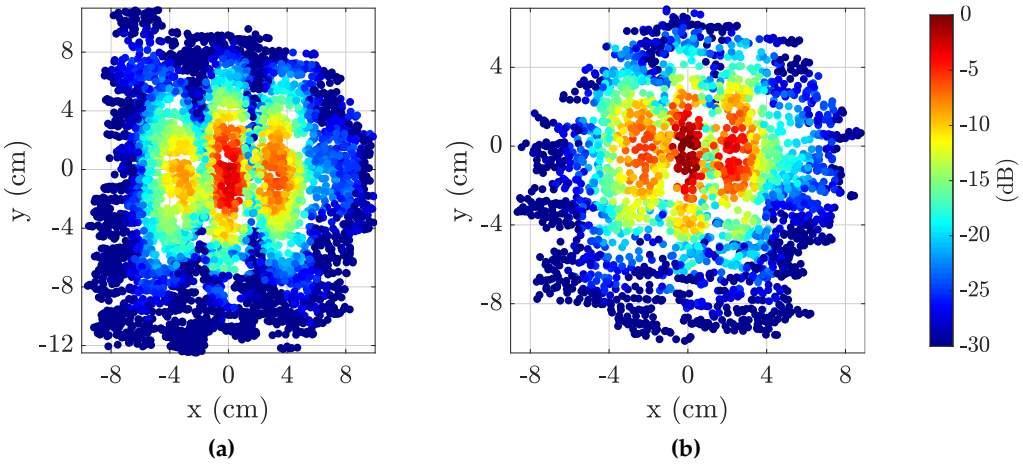

Figure 4.15: Normalized amplitude of the acquired field samples within the acquisition volume the farthest to the AUT, S_1, (a) and within the closest one, S_2, (b).

The normalized amplitude and phase of the equivalent currents distribution obtained applying the SRM to the samples acquired using the planar range, which will be used as reference, are depicted in Figure 4.16a and Figure 4.16b, respectively. The UV representation of the retrieved radiation pattern is shown in Figure 4.16c.

The same results obtained using the full-acquisition approach of the proposed system, i.e. using the amplitude and phase of the measured field samples, and computed with the acquisitions made within S_1 are displayed in Figure 4.16d, Figure 4.16e and Figure 4.16f, respectively. As it can be observed, although the obtained results are noisier than the reference ones due to the freehand non-uniform sampling, they accurately show the status of the antenna elements and its radiation pattern.

Finally, the performance of the amplitude-only approach of the proposed system was evaluated employing only the amplitude of the samples gathered within both acquisition volumes, S_1 and S_2, which is depicted in Figure 4.15a and Figure 4.15b, to perform the diagnosis and characterization of the two-horn antenna array. In particular, the normalized amplitude and phase of the computed equivalent currents distribution, retrieved using the pSRM, are depicted in Figure 4.16g and Figure 4.16h, respectively. In addition, the UV representation of the retrieved

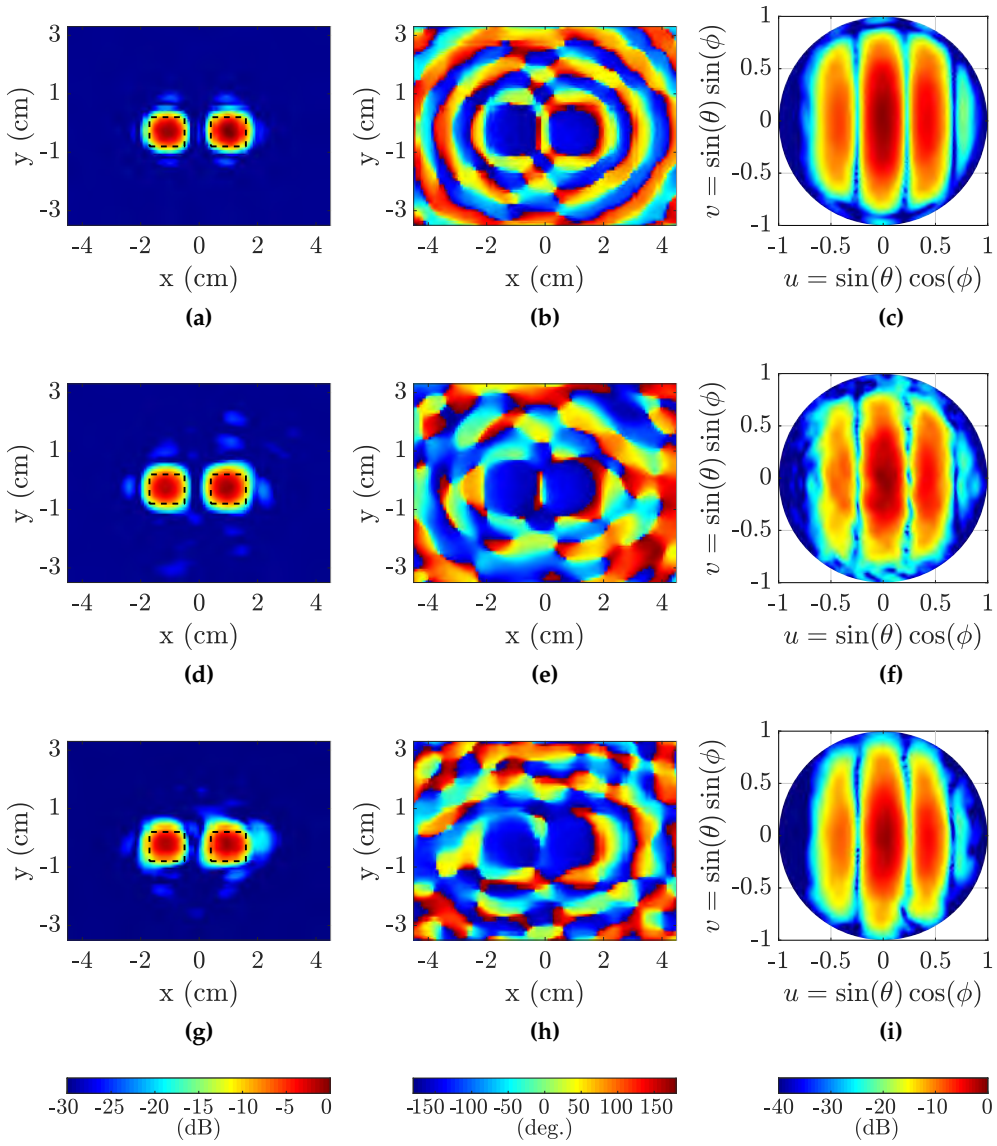

Figure 4.16: Normalized amplitude and phase of the equivalent currents distribution obtained using a standard planar range (a) and (b), respectively, and UV representation of the retrieved radiation pattern (c). The same using the full-acquisition approach of the proposed system is shown in (c), (d) and (f), respectively, and using the phaseless approach in (g), (h) and (i), respectively.

radiation pattern is shown in Figure 4.16i. As it can be seen, the results obtained using amplitude-only data are slightly noisier than the reference ones, in line

with the results retrieved with the full-acquisition approach of the proposed system, that is, using both amplitude and phase data. This is a consequence of the freehand nature of the proposed system, which yields a non-uniform sampling distribution. Nonetheless, the results achieved with both approaches of the proposed system are similar to the reference ones. In particular, these results show the capability of the proposed freehand phaseless system to provide an accurate and fast diagnosis and characterization of an AUT.

4.3.2.2 **Measurements in V band**

The second set of measurements was performed at the facilities of the Institute of Electronics, Microelectronics and Nanotechnology (IEMN) of the University of Lille. In this case, the measurements were accomplished at 60 GHz using first a VNA (Keysight E8361A PNA) to obtain a reference measurement using the full-acquisition approach (employing both amplitude and phase information) of the proposed system. Afterwards, the performance of the phaseless approach of the proposed system was evaluated employing a spectrum analyzer (R&S FSU67) to acquire amplitude-only measurements while the VNA was configured as a source to feed the AUT. In this case, the size of the cubic cells used to balance the distribution of the acquisitions was set to $\lambda/2 \times \lambda/2 \times \lambda/2$ at 60 GHz and the maximum number of acquisitions was set to 5. Again, four infrared cameras were used to track the probe antenna as explained in Section 4.1.1.3.

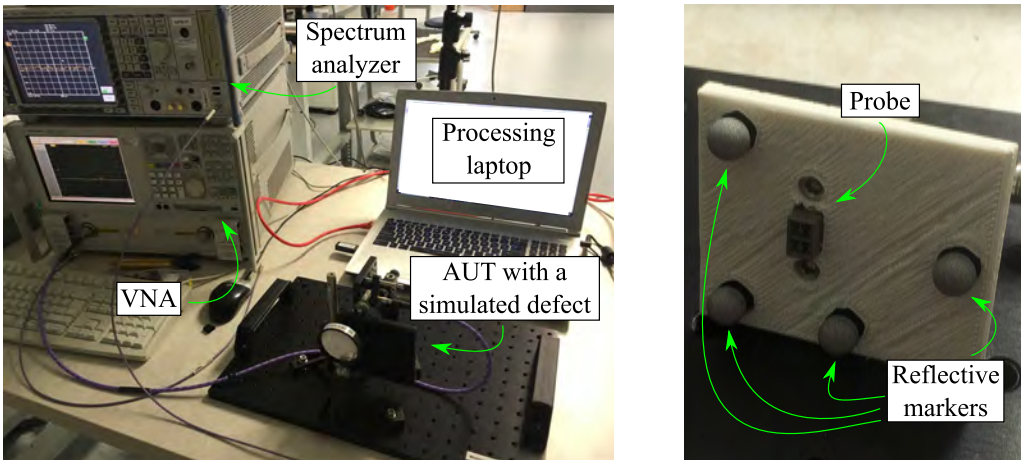

(a) **(b)**

Figure 4.17: Measurement setup (a) and probe antenna (b) for the V band measurements.

The measurement setup is depicted in Figure 4.17a, where it is possible to see the AUT: a PTFE plano-convex lens of 2.54 cm radius (5.1λ at 60 GHz) fed by an open Double-Ridged Waveguide (DRWG) 2×2 array. Four reflective markers were attached to the probe antenna, which was another sample of the same DRWG 2×2 antenna used to feed the lens, to track it with the infrared cameras (See Figure 4.17b).

As previously explained, the AUT, shown in Figure 4.18a was first characterized using the full-acquisition approach of the proposed system, i.e., measuring amplitude and phase of its radiated field. Then, the AUT was characterized using the amplitude-only approach of the proposed system by acquiring amplitude field measurements within two different acquisition volumes with the spectrum analyzer. The main parameters of the full-acquisition measurement and of the amplitude-only scan within each of the two acquisition volumes are summarized in Table 4.2.

Measurement	# of samples	Avg. dist. to AUT (cm)	Time (s)	Scanned area (cm^2)
Amp. & Phase	2351	11.1	505	7.1×7.5
Amp. only S1	3444	8.8	373	8.4×7.1
Amp. only S2	4560	15.3	563	9.1×7.7

Table 4.2: Summary of the acquisitions performed to measure the AUT at V band.

The normalized amplitude of the computed equivalent currents distribution obtained with the SRM and the full-acquisition approach of the proposed system, depicted in Figure 4.18d, is compared with the one retrieved employing the amplitude-only version of the proposed system, which uses the pSRM, and that is shown in Figure 4.18g. The phase of the equivalent currents distribution obtained with the full-acquisition approach and with the amplitude-only version of the proposed system is depicted in Figure 4.19d and Figure 4.19g, respectively. As it can be seen, the region of the computed equivalent currents distribution where the amplitude is high matches the physical dimensions of the lens, whose edge is illustrated with a solid-black line. It should be noted that, in a similar fashion as for the Ka band measurements, although the results obtained with the amplitude-only approach of the proposed system are slightly noisier than those retrieved using phase information, they show a good accuracy.

In addition, several tests were performed in order to assess the diagnosis capabilities of the proposed system. For this purpose, two different defects were introduced to the AUT using aluminum foil.

First, an aluminum strip crossing the lens was used as shown in Figure 4.19b. Once again, first a reference measurement using the full-acquisition approach of the proposed system, acquiring both the amplitude and phase of the field radiated by the AUT, was performed using the VNA. Afterwards, the AUT was measured employing the amplitude-only version of the proposed system with a spectrum analyzer. A summary of the parameters of each scan can be found in the first three rows of Table 4.3.

Defect	Measurement	# of samples	Avg. dist. to AUT (cm)	Time (s)	Scanned area (cm^2)
Al. strip	Amp. & Phase	2833	11.3	821	9.2×6.9
	Amp. only S1	4860	8.8	467	8.8×7.9
	Amp. only S2	5321	13.1	552	10.7×8.2
Al. patch	Amp. & Phase	3090	11.2	758	7.5×7.4
	Amp. only S1	3941	8.9	526	8.3×6.7
	Amp. only S2	4747	13.5	628	9.4×9.1

Table 4.3: Summary of the acquisitions performed to evaluate the diagnosis capabilities of the proposed system.

The normalized amplitude of the equivalent currents distribution retrieved with the full-acquisition approach of the proposed system and only considering amplitude data is depicted in Figure 4.18e and Figure 4.18h, respectively. As it can be seen, in both cases the amplitude of the retrieved equivalent currents distribution vanishes where the aluminum strip was placed. The phase of the equivalent currents distribution computed with both approaches is displayed in Figure 4.19e and in Figure 4.19h, for the full-acquisition scheme and for the amplitude-only case, respectively. Analogously, the phase of the equivalent currents distribution is disrupted where the aluminum strip was placed.

For the second set of experiments, the aluminum strip was replaced by an aluminum patch as shown in Figure 4.18c. As in the previous tests, the AUT with the aluminum patch was measured first using the VNA and the full-acquisition approach of the proposed system. Afterwards, it was measured with the amplitude-only version of the proposed system acquiring amplitude samples within two different acquisition volumes employing the spectrum analyzer. A summary of the parameters of each scan can be found in the last three rows of Table 4.3.

Once again, as it can be observed in Figure 4.18f and in Figure 4.18i, where the normalized amplitude of the equivalent currents distribution retrieved with the full-acquisition approach and computed considering amplitude-only measurements are depicted, respectively, the normalized amplitude vanishes where the aluminum patch was placed. Analogously, the phase of the equivalent currents

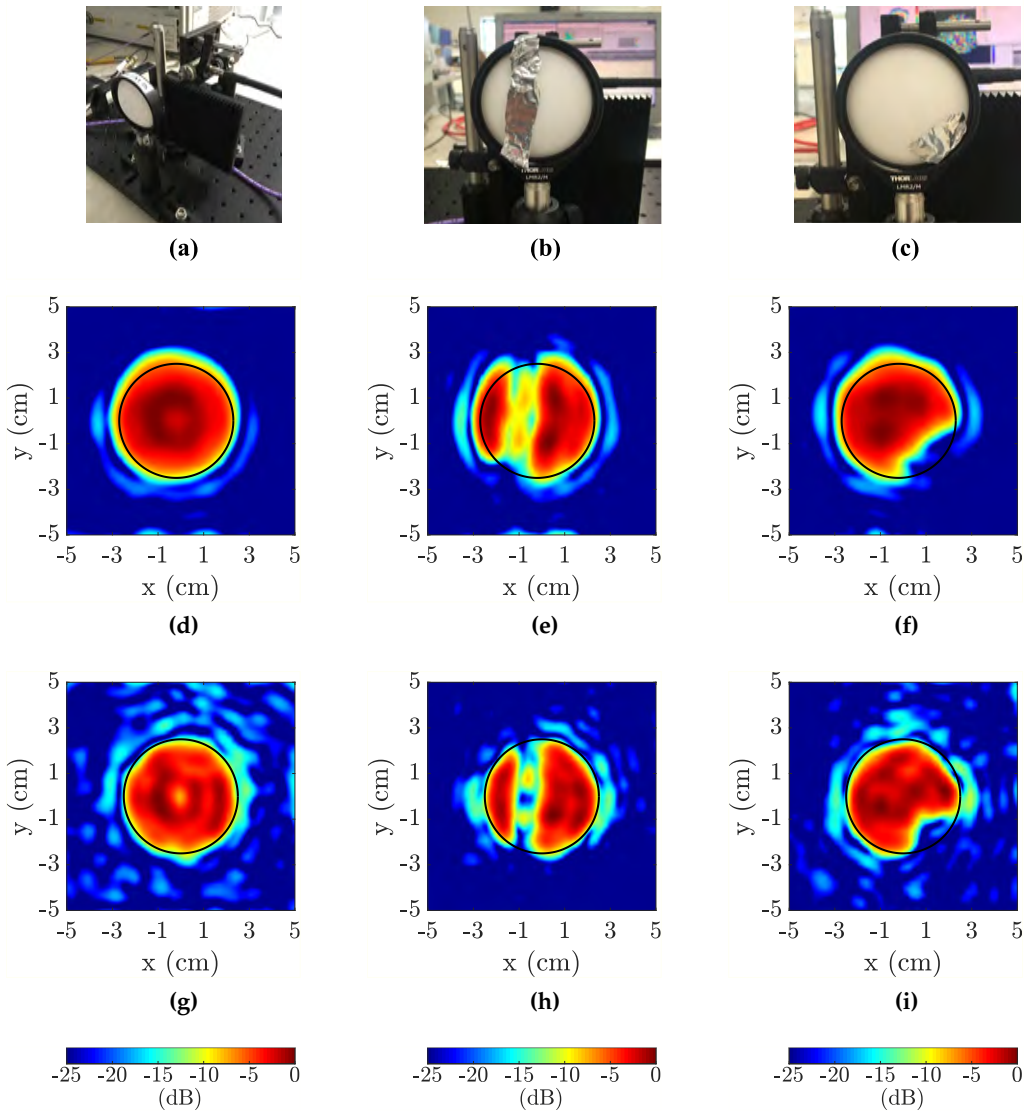

Figure 4.18: Image of the AUT (a) and picture of the AUT with an aluminum strip and with an aluminum patch to simulate an antenna malfunction, (b) and (c), respectively. Normalized amplitude of the equivalent currents distribution of the AUT retrieved with the full-acquisition approach of the proposed system and with its phaseless version, (d) and (g), respectively. The same for the AUT with the aluminum strip, (e) and (h), respectively, and for the AUT with aluminum patch, (f) and (i), respectively.

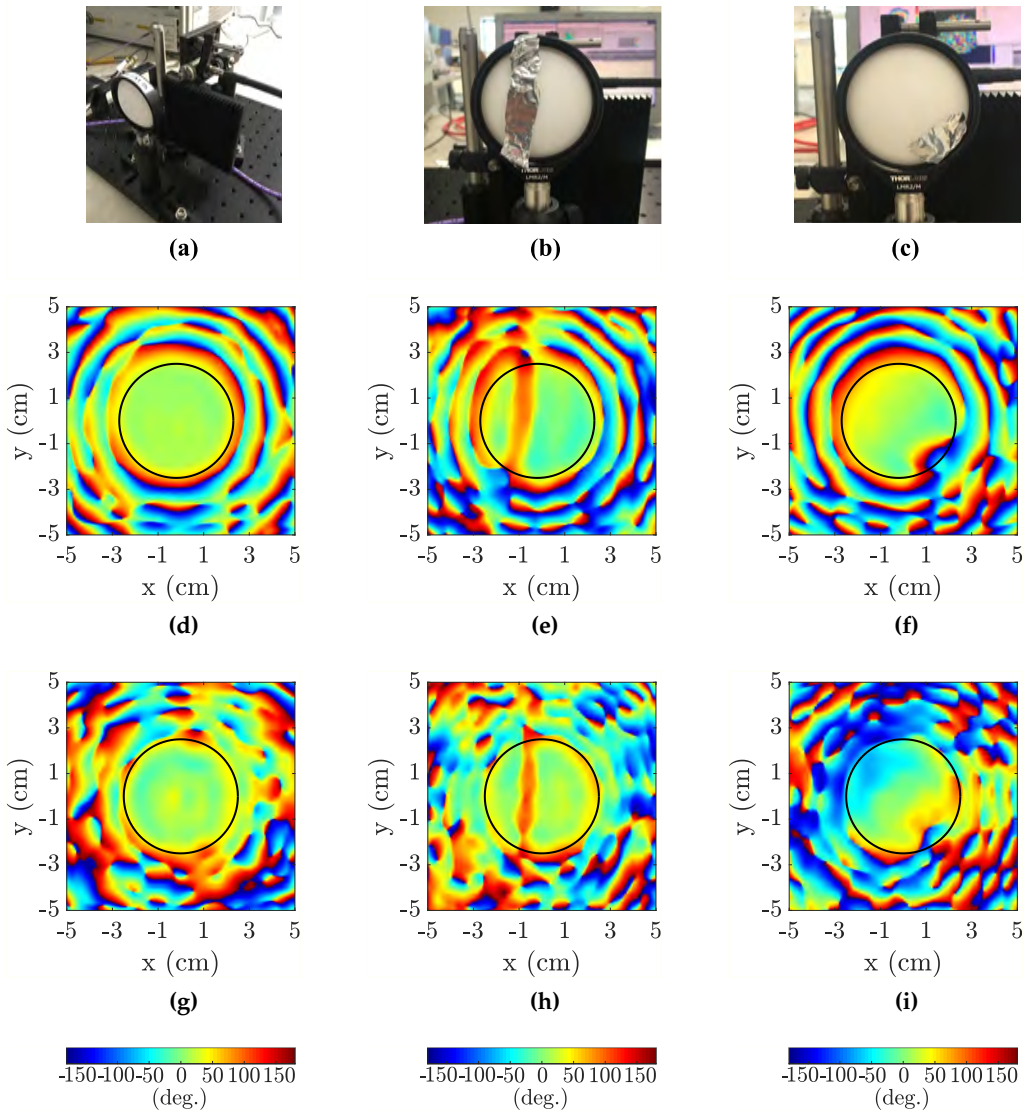

Figure 4.19: Image of the AUT (a) and picture of the AUT with an aluminum strip and with an aluminum patch to simulate an antenna malfunction, (b) and (c), respectively. Phase of the equivalent currents distribution of the AUT retrieved with the full-acquisition approach of the proposed system and with its phaseless version, (d) and (g), respectively. The same for the AUT with the aluminum strip, (e) and (h), respectively, and for the AUT with aluminum patch, (f) and (i), respectively.

distribution is disrupted where the aluminum patch was placed in both cases (see Figure 4.19f and Figure 4.19i, for the results obtained with the full-acquisition approach and for those obtained with the phaseless version of the proposed system, respectively).

These results demonstrate the capability of the proposed system, both considering full-acquisition and also amplitude-only measurements, to provide fast (in a matter of some minutes for a $81\lambda^2$ antenna) and accurate diagnosis of antenna malfunctions at V band.

4.3.2.3 **Measurements at 300 GHz**

Several measurements were performed at 300 GHz, pushing to the limits of the tracking system, to assess the performance of the proposed system. Due the use of a sub-THz frequency, in this case only amplitude measurements were considered. These measurements were also performed at the facilities of the IEMN. The measurement setup is depicted in Figure 4.20a. In this case the AUT was a conical horn antenna. The transmitted signal was generated using a signal generator, whose output signal was upconverted using a signal generator extension module. On the receiving side, the probe antenna, in this case an OEWG depicted in Figure 4.20b, was connected to a spectrum analyzer extension module, which was wired to the spectrum analyzer used for the amplitude-only measurements presented in Section 4.3.2.2. The same tracking system as in the previous measurements, which comprises four infrared cameras, was employed. In this case, the size of the cubic cells used to balance the distribution of the acquisitions was set to $\lambda/2 \times \lambda/2 \times \lambda$ at 300 GHz and the maximum number of samples per cell was set to 5.

As in previous amplitude-only measurements, amplitude samples were acquired within two different acquisition volumes. The main parameters of each scan are summarized in Table 4.4. It should be noted that, as the size of the cubic cells used to balance the distribution of the acquisitions is smaller than in previous measurements due to the higher working frequency, the time required to perform a scan grows as it is more difficult for the operator of the system to keep the probe within each acquisition volume. Even so, the flexibility of the system enables reliable results in a time which is significantly less than that needed when using a conventional antenna measurement facility.

The normalized amplitude of the field samples acquired within each acquisition volume is depicted in Figure 4.21a and in Figure 4.21b, respectively.

The normalized amplitude and phase of the equivalent currents distribution computed using the pSRM employing the amplitude measurements acquired

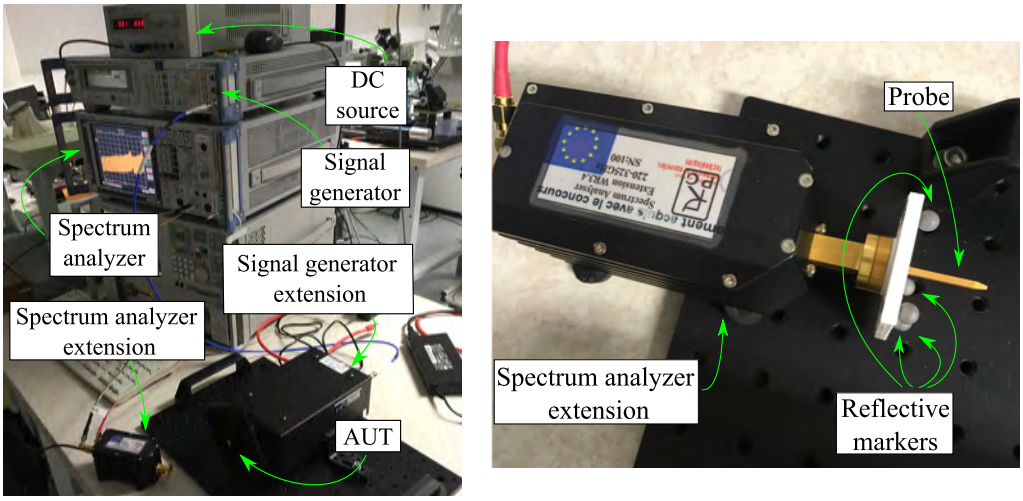

(a) (b)

Figure 4.20: Measurement setup (a) and probe antenna (b) for the 300 GHz measurements.

Measurement	# of samples	Avg. dist. to AUT (cm)	Time (s)	Scanned area (cm^2)
Amp. only S1	6020	4.7	1162	4.1×5.4
Amp. only S2	10314	7.6	2313	5.4×7.7

Table 4.4: Summary of the acquisitions performed to measure the AUT at 300 GHz.

using the proposed system is depicted in Figure 4.22a and Figure 4.22b, respectively. As it can be observed, the area in which the normalized amplitude of the retrieved equivalent currents distribution is high corresponds to the AUT aperture, which is enclosed with a dashed black line in Figure 4.22a. The E-plane cut and the H-plane cut of the retrieved radiation pattern are shown in Figure 4.22c and Figure 4.22d, respectively, along with the reference cuts obtained with the conventional antenna measurement range of the IEMN [142]. As it can be seen, in both cuts of the radiation pattern the main lobe is well-estimated. In addition, the position of the secondary lobes in the H-plane cut within the angular margin of validity is also well-predicted, although the level of the secondary lobes of the pattern retrieved with the proposed system are slightly higher than in the reference pattern. Therefore, it can be concluded that using the proposed

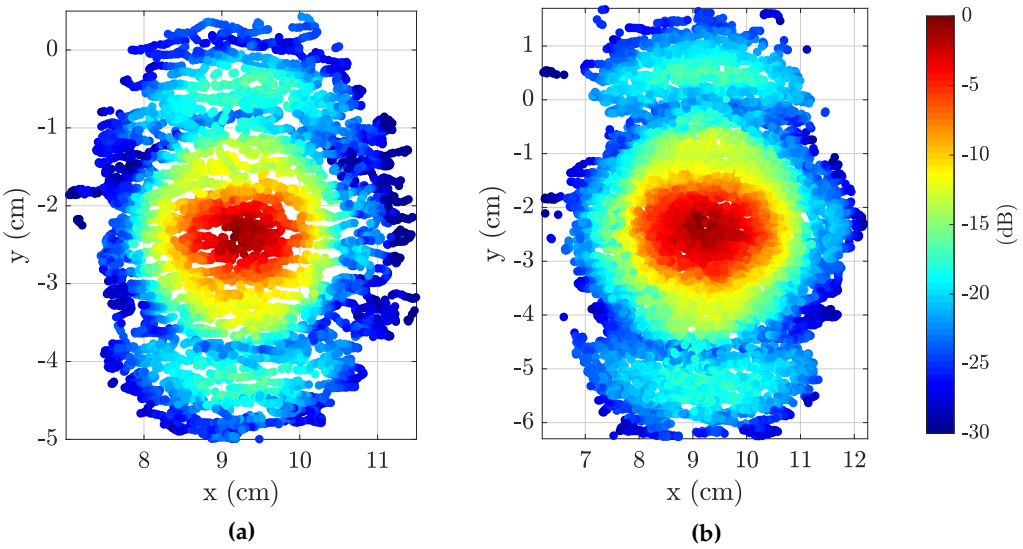

Figure 4.21: Normalized amplitude of the acquired field samples within the acquisition volume closest to the AUT, S_1, (a) and within the farthest one, S_2, (b).

system a good diagnosis and a fair characterization of antennas, even at sub-THz frequencies can be performed in a fast and flexible manner.

4.4 Concluding remarks

This chapter summarizes the results in the field of freehand antenna diagnosis and characterization. The proposed system is based on acquiring samples of the field radiated by the AUT by moving a handheld probe in front of its aperture. The position and attitude of the probe are tracked so that the acquired field samples can be combined to compute an equivalent currents distribution on the AUT aperture. It should be noted that, analogously to the freehand imaging system, in addition to the usage of a processing technique able to consider non-uniform acquisitions, a methodology to balance the distribution of the irregularly acquired samples had to be implement to avoid anomalous solutions during the equivalent currents computation. Afterwards, the FF radiation pattern of the AUT can be retrieved by means of the corresponding radiation integrals. The performance of the proposed system was validated through several measurements. In particular, the system was first evaluated considering full-acquisitions (i.e., amplitude and phase) [x], [ix], [**V**]. In a second step, the performance of the system was assessed considering amplitude-only measurements, avoiding the need of a phase refer-

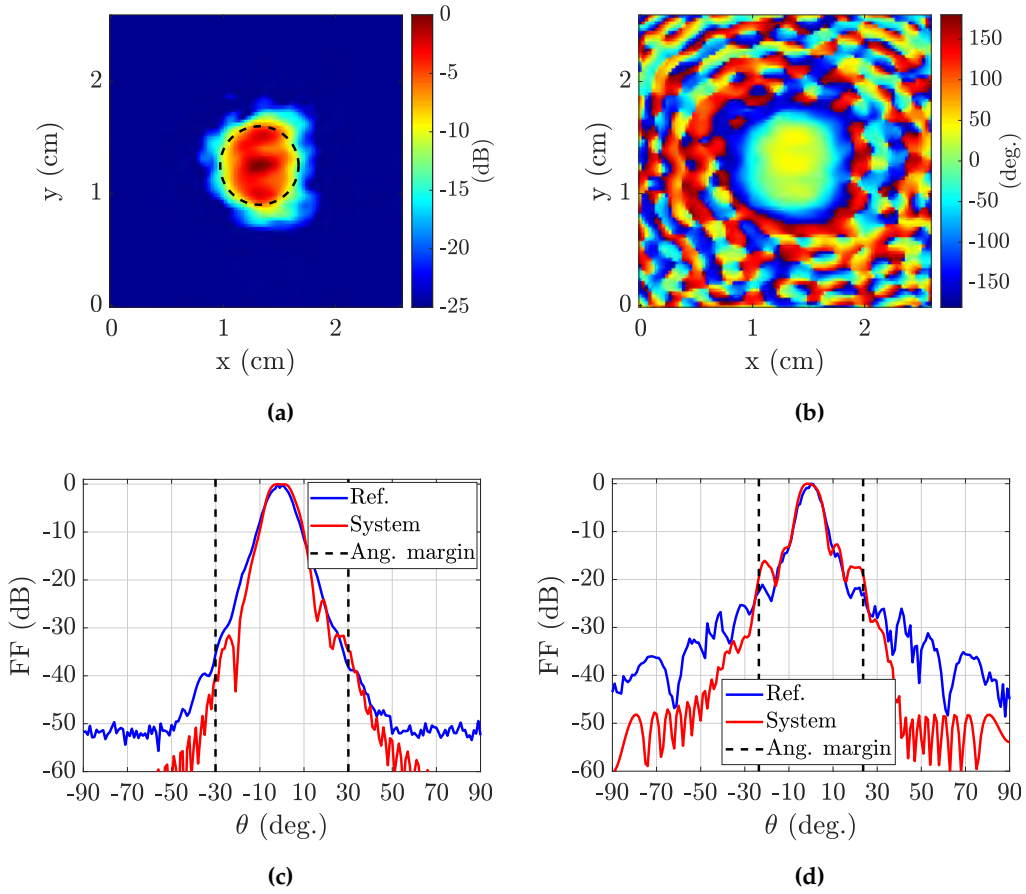

Figure 4.22: Normalized amplitude (a) and phase (b) of the computed equivalent currents distribution of the AUT. E-plane (c) and H-plane (d) cut of the retrieved FF pattern.

ence and simplifying the hardware required to perform the field acquisition [iv]. This enables the diagnosis of antennas under operational conditions, reduces the overall cost of the equipment and extends the maximum working frequency of the proposed system.

CHAPTER

5

Conclusions and future work

5.1 Conclusions

This dissertation, presented by compendium of publications, is mainly based in the publications [**I**]-[**V**], which are summarized in this document. First, chapter 1 presents a review of the state-of-the art related to the proposed systems. Chapter 2 describes the developed RFID-based systems and their validation. A handheld imaging system is presented in Chapter 3 and Chapter 4 introduces a handheld system for the diagnosis and characterization of antennas.

The first of the developed RFID-based systems was designed for the estimation of the attitude of tagged goods using an array of RFID tags [xviii], [xvii], [**II**]. In particular, the system employs the phase of the signals backscattered by the RFID tags of the array [**I**]. The direction of arrival of the RFID signals impinging the array is computed employing the MUSIC algorithm and afterwards, the attitude of the array is estimated. In this regard, the geometry of the array of RFID tags plays an important role. In particular, the use of a ULA makes possible to obtain azimuth estimations, whilst the use of a UCA allows the determination of both the azimuth and the elevation of the array of tags. In this thesis both alternatives have been considered. Specifically, the impact on the system performance of

array imperfections was evaluated by means of simulations and the accuracy of both approaches has been experimentally validated. Results show a good accuracy in a wide angular range, both in a controlled environment and in an indoor scenario. In addition, the use of the proposed system, which can be used to improve the automation of logistic processes, to also obtain position estimations was studied in [xvi].

The second RFID-based system designed within this thesis is devoted to monitor the transit of goods at checkpoints [xi], [**III**]. It relies on the use of a reference grid of passive RFID tags placed on the floor and a single antenna connected to a reader. For the estimation of the movement direction of goods, the system leverages the shadowing effect produced when the RFID tags are blocked by the transpallet or forklift that carries the goods. In this case, the shadowing effect is quantified both in terms of missed tags (i.e., tags that were not read in a time slot) and in terms of a reduction in the number of readings of tags. This information is then used as the input features of a neural network, which determines the movement direction of the tagged goods. A proof-of-concept of the proposed system was validated during a measurement campaign performed at the facilities of the University of Pisa. The main advantages of this system are its reduced hardware complexity, making it cost-effective and easy-to-deploy, and its robustness.

Regarding the handheld imaging system [v], [**IV**], to the best author's knowledge, the proposed solution is the first that performs SAR imaging with a completely 3D freehand scanning and a pocket-size device. In particular, the proposed system employs a compact mm-Wave radar-on-chip module, whose position and attitude is tracked while it is moved over the area under scan, to generate real-time high-resolution electromagnetic images. These images are shown to the operator of the system as more data is acquired, who can adapt the scan of the inspected area accordingly. Initially, the system was tested considering a quasi-monostatic approach showing good results. Afterwards, the system was extended to a MIMO configuration yielding a significantly faster scanning speed and higher-quality images. In addition, a calibration method to reduce positioning errors, which greatly improves the quality of the obtained images, has been proposed.

The handheld system for antenna diagnosis and characterization is based on acquiring samples of the field radiated by the AUT by moving a handheld probe antenna in front of its aperture. The position and attitude of the probe antenna is tracked so that the acquired field samples can be combined to compute an equivalent currents distribution on the AUT aperture. Afterwards, the FF radiation pattern of the AUT can be retrieved by means of the corresponding radiation integrals. Initially, the proposed system was implemented considering both amplitude and phase measurements [x], [ix], [**V**]. In this case, the equivalent currents distribution is retrieved using the SRM. Afterwards, the proposed system was

modified to employ amplitude-only measurements, avoiding the need of a phase reference and simplifying the hardware required to perform the field acquisition [iv]. The use of amplitude measurements allows the diagnosis and characterization of antennas under operational conditions, reduces the overall cost of the equipment and extends the maximum working frequency of the proposed system, which has been tested up to sub-mmWave frequencies. Due to its flexibility, the proposed system is of great interest in different applications such as the quick performance evaluation of antennas in laboratory conditions, or the characterization of already deployed and on-board antennas.

The research developed within this dissertation, performed in the framework of seven national and regional research projects, has been published in high-impact international journals and in contributions to international conferences. In addition, it should be remarked that the research work has achieved significant recognition in the scientific community. In particular, the doctoral candidate received a grant from the company TICRA to attend to the European Conference on Antennas and Propagation (EuCAP) in 2020, and he was awarded with the second place in the Best Student Paper Award in the 41st Annual Meeting and Symposium of the Antenna Measurement Techniques Association (AMTA) in 2019.

5.2 Future work

Both of the RFID-based developed systems have been tested in indoor scenarios, although further improvements such as detecting roll changes can be investigated. In addition, an extensive validation campaign under operational conditions, e.g., in a warehouse, can be of great interest.

Concerning the handheld imaging system, the use of an alternative positioning system, which could be integrated in the handheld device, replacing the motion tracking system, would increase the flexibility of the system. Furthermore, the use of a radar module with a higher number of transmitters and receivers would be of great interest to enhance the scanning speed and the image quality of the retrieved images. In this regard, the development of a more efficient algorithm capable of processing non-uniformly acquired data would also be very valuable.

Finally, regarding the antenna diagnosis and characterization system, the development of a sampling strategy to enable the retrieval of real-time results employing amplitude-only acquisitions would be helpful to assist the system operator. In addition, the use of the proposed system considering modulated signals

could be useful for the characterization of antennas under fully-operational conditions.

Bibliography

[1] G. M. Gaukler, "Item-Level RFID in a Retail Supply Chain With Stock-Out-Based Substitution," *IEEE Transactions on Industrial Informatics*, vol. 7, no. 2, pp. 362–370, May 2011.

[2] M. Hauser, M. Griebel, and F. Thiesse, "A hidden Markov model for distinguishing between RFID-tagged objects in adjacent areas," in *2017 IEEE International Conference on RFID (RFID)*, May 2017, pp. 167–173.

[3] W. Yao, C. Chu, and Z. Li, "The Adoption and Implementation of RFID Technologies in Healthcare: A Literature Review," *Journal of Medical Systems*, vol. 36, no. 6, pp. 3507–3525, Dec 2012.

[4] S. Amendola, R. Lodato, S. Manzari, C. Occhiuzzi, and G. Marrocco, "RFID Technology for IoT-Based Personal Healthcare in Smart Spaces," *IEEE Internet of Things Journal*, vol. 1, no. 2, pp. 144–152, 2014.

[5] D. Zanetti, S. Capkun, and A. Juels, "Tailing RFID Tags for Clone Detection," in *20th Annual Network and Distributed System Security Symposium*, Apr 2013.

[6] X. Chen, L. Xie, C. Wang, and S. Lu, "Adaptive accurate indoor-localization using passive RFID," in *Proc. IEEE Int. Conf. Parallel Distrib. Syst. (ICPADS)*, 2013, pp. 249–256.

[7] S. Shao and R. J. Burkholder, "Item-level RFID tag location sensing utilizing reader antenna spatial diversity," *IEEE Sensors J.*, vol. 13, no. 10, pp. 3767–3774, Oct. 2013.

[8] Y. Alvarez, M. E. D. Cos, and F. Las-Heras, "A received signal strength RFID-based indoor location system," *Sens. Actuators A Phys.*, vol. 255, pp. 118–133, mar 2017.

[9] P. V. Nikitin, R. Martinez, S. Ramamurthy, H. Leland, G. Spiess, and K. V. S. Rao, "Phase based spatial identification of UHF RFID tags," in *2010 IEEE Int. Conf. on RFID*, 2010, pp. 102–109.

[10] S. Azzouzi, M. Cremer, U. Dettmar, T. Knie, and R. Kronberger, "Improved aoa based localization of UHF RFID tags using spatial diversity," in *Proc. IEEE Int. Conf. RFID-Technol. Appl. (RFID-TA)*, 2011, pp. 174–180.

[11] M. Scherhäufl, M. Pichler, and A. Stelzer, "UHF RFID localization based on evaluation of backscattered tag signals," *IEEE Trans. on Instrum. Meas.*, vol. 64, no. 11, pp. 2889–2899, Nov. 2015.

[12] J. Huiting, H. Flisijn, A. B. J. Kokkeler, and G. J. M. Smit, "Exploiting phase measurements of EPC Gen2 RFID tags," in *Proc. IEEE Int. Conf. RFID-Technol. Appl. (RFID-TA)*, 2013, pp. 1–6.

[13] M. Scherhäufl, M. Pichler, and A. Stelzer, "Robust localization of passive UHF RFID tag arrays based on phase-difference-of-arrival evaluation," in *2015 IEEE Topical Conf. Wireless Sensors and Sensor Netw. (WiSNet)*, Jan 2015, pp. 47–49.

[14] A. Buffi and P. Nepa, "The SARFID technique for discriminating tagged items moving through a UHF-RFID gate," *IEEE Sensors Journal*, vol. 17, no. 9, pp. 2863–2870, may 2017.

[15] H. He, P. Maheshwari, and D. J. Pommerenke, "The development of an EM-field probing system for manual near-field scanning," *IEEE Transactions on Electromagnetic Compatibility*, vol. 58, no. 2, pp. 356–363, April 2016.

[16] C. Baer, J. Barowski, and I. Rolfes, "On the usability of low-cost inertial navigation systems for free-hand SAR imaging at GPR-frequencies," in *2017 IEEE Sensors Applications Symposium (SAS)*, March 2017, pp. 1–5.

[17] M. T. Ghasr, M. A. Abou-Khousa, S. Kharkovsky, R. Zoughi, and D. Pommerenke, "Portable real-time microwave camera at 24 GHz," *IEEE Transactions on Antennas and Propagation*, vol. 60, no. 2, pp. 1114–1125, Feb 2012.

[18] J. Laviada, A. Arboleya-Arboleya, Y. Alvarez, B. Gonzalez-Valdes, and F. Las-Heras, "Multiview three-dimensional reconstruction by millimetre-wave portable camera," *Sci. Rep.*, vol. 7, Jul 2017.

[19] J. Laviada, A. Arboleya-Arboleya, and F. Las-Heras, "Multistatic millimeter-wave imaging by multiview portable camera," *IEEE Access*, vol. 5, pp. 19 259–19 268, 2017.

[20] J. Laviada, M. López-Portugués, A. Arboleya-Arboleya, and F. Las-Heras, "Multiview mm-wave imaging with augmented depth camera information," *IEEE Access*, vol. 6, pp. 16 869–16 877, 2018.

[21] J. Laviada, M. T. Ghasr, M. López-Portugués, R. Zoughi, and F. Las-Heras, "Multiview imaging with real-time microwave camera from known positions," in *IEEE Antennas and Propagation Simposium 2018*, Boston, USA, July 2018, pp. 1–3.

[22] M. J. Horst, M. T. Ghasr, and R. Zoughi, "A compact microwave camera based on chaotic excitation synthetic-aperture radar," *IEEE Transactions on Antennas and Propagation*, vol. 67, no. 6, pp. 4148–4161, June 2019.

[23] M. García-Fernández, Y. Álvarez López, A. Arboleya, B. González-Valdés, Y. Rodríguez-Vaqueiro, M. E. De Cos Gómez, and F. Las-Heras Andrés, "Antenna diagnostics and characterization using unmanned aerial vehicles," *IEEE Access*, vol. 5, pp. 23 563–23 575, 2017.

[24] G. Virone, A. M. Lingua, M. Piras, A. Cina, F. Perini, J. Monari, F. Paonessa, O. A. Peverini, G. Addamo, and R. Tascone, "Antenna Pattern Verification System Based on a Micro Unmanned Aerial Vehicle (UAV)," *IEEE Antennas and Wireless Propagation Letters*, vol. 13, pp. 169–172, 2014.

[25] Y. Zhuang, J. Yang, Y. Li, L. Qi, and N. El-Sheimy, "Smartphone-Based Indoor Localization with Bluetooth Low Energy Beacons," *Sensors*, vol. 16, no. 5, 2016. [Online]. Available: https://www.mdpi.com/1424-8220/16/5/596

[26] A. N. Raghavan, H. Ananthapadmanaban, M. S. Sivamurugan, and B. Ravindran, "Accurate mobile robot localization in indoor environments using bluetooth," in *2010 IEEE International Conference on Robotics and Automation*, 2010, pp. 4391–4396.

[27] H. Liu, Y. Gan, J. Yang, S. Sidhom, Y. Wang, Y. Chen, and F. Ye, "Push the Limit of WiFi Based Localization for Smartphones," in *Proceedings of the 18th Annual International Conference on Mobile Computing and Networking*, ser. Mobicom '12. New York, NY, USA: Association for Computing Machinery, 2012, p. 305–316. [Online]. Available: https://doi.org/10.1145/2348543.2348581

[28] M. Kotaru, K. Joshi, D. Bharadia, and S. Katti, "SpotFi: Decimeter Level Localization Using WiFi," *SIGCOMM Comput. Commun. Rev.*, vol. 45, no. 4, p. 269–282, Aug. 2015. [Online]. Available: https://doi.org/10.1145/2829988.2787487

[29] L. Zwirello, T. Schipper, M. Harter, and T. Zwick, "UWB Localization System for Indoor Applications: Concept, Realization and Analysis," *Journal of Electrical and Computer Engineering*, 2012.

[30] Y. Álvarez, E. de Cos, L. Lorenzo, and F. Las-Heras, "Novel Received Signal Strength-Based Indoor Location System: Development and Testing," *EURASIP Journal on Wireless Communications and Networking*, no. 254345, 2010.

[31] M. Bouet and A. L. dos Santos, "RFID tags: Positioning principles and localization techniques," in *2008 1st IFIP Wireless Days*, 2008, pp. 1–5.

[32] S. S. Saab and Z. S. Nakad, "A Standalone RFID Indoor Positioning System Using Passive Tags," *IEEE Transactions on Industrial Electronics*, vol. 58, no. 5, pp. 1961–1970, 2011.

[33] N. Llombart, K. B. Cooper, R. J. Dengler, T. Bryllert, and P. H. Siegel, "Confocal ellipsoidal reflector system for a mechanically scanned active terahertz imager," *IEEE Trans. Antennas Propag.*, vol. 58, no. 6, pp. 1834–1841, June 2010.

[34] A. Geise, O. Neitz, J. Migl, H. Steiner, T. Fritzel, C. Hunscher, and T. F. Eibert, "A crane based portable antenna measurement system — system description and validation," *to appear in IEEE Transactions on Antennas and Propagation*, pp. 1–1, 2019.

[35] W. Alsalih, A. Alma'aitah, and W. Alkhater, "RFID Localization Using Angle of Arrival Cluster Forming," *International Journal of Distributed Sensor Networks*, vol. 10, no. 3, p. 269596, 2014. [Online]. Available: https://doi.org/10.1155/2014/269596

[36] GS1. (2020, 4) EPC UHF Gen2 Air Interface Protocol. [Online]. Available: https://www.gs1.org/standards/epc-rfid/uhf-air-interface-protocol

[37] K. Michael and L. McCathie, "The pros and cons of RFID in supply chain management," in *Int. Conf. Mobile Business (ICMB'05)*, July 2005, pp. 623–629.

[38] F. Inui, "RF tag, RF tag attitude detection apparatus, and RF tag attitude detection system," U.S. Patent 20 050 225 451, Apr. 7, 2004.

[39] C. Rennie, R. Shome, K. E. Bekris, and A. F. D. Souza, "A Dataset for Improved RGBD-Based Object Detection and Pose Estimation for Warehouse Pick-and-Place," *IEEE Robot. and Autom. Lett.*, vol. 1, no. 2, pp. 1179–1185, July 2016.

[40] R. J. Stine, H. L. Markman, and J. E. Markman, "Shielded portal for multi-reading RFID tags affixed to articles," U.S. Patent 9 760 826B1, Mar. 12, 2013.

[41] R. B. Morin, "Method and system for controlling the traffic flow through an RFID directional portal," U.S. Patent 8 487 747B2, May 23, 2008.

[42] M. Goller, C. Feichtenhofer, and A. Pinz, "Fusing RFID and computer vision for probabilistic tag localization," in *2014 IEEE International Conference on RFID (IEEE RFID)*, April 2014, pp. 89–96.

[43] Y. Oikawa, "Simulation evaluation of tag movement direction estimation methods in RFID gate systems," in *2012 IEEE Radio and Wireless Symposium*, Jan 2012, pp. 331–334.

[44] T. Keller, F. Thiesse, J. Kungl, and E. Fleisch, "Using low-level reader data to detect false-positive RFID tag reads," in *2010 Internet of Things (IOT)*, Nov 2010, pp. 1–8.

[45] P. V. Nikitin, G. N. Spiess, H. M. Leland, L. C. Hingst, and J. H. Sherman, "Utilization of motion and spatial identification in mobile RFID interrogator," U.S. Patent 9 047 522B1, Nov. 6, 2010.

[46] A. Buffi and P. Nepa, "The SARFID Technique for Discriminating Tagged Items Moving Through a UHF-RFID Gate," *IEEE Sensors Journal*, vol. 17, no. 9, pp. 2863–2870, May 2017.

[47] B. Wagner, N. Patwari, and D. Timmermann, "Passive RFID tomographic imaging for device-free user localization," in *2012 9th Workshop on Positioning, Navigation and Communication*, March 2012, pp. 120–125.

[48] E. Eckstein, G. Mazoki, and W. Richie, "Article identification and tracking using electronic shadows created by RFID tags," U.S. Patent 20 050 012 613A1, Nov. 6, 2010.

[49] M. Pastorino, *Microwave Imaging*. John Wiley & Sons, Inc., 2010.

[50] S. Kharkovsky, J. T. Case, M. A. Abou-Khousa, R. Zoughi, and F. L. Hepburn, "Millimeter-wave detection of localized anomalies in the space shuttle external fuel tank insulating foam," *IEEE Transactions on Instrumentation and Measurement*, vol. 55, no. 4, pp. 1250–1257, Aug 2006.

[51] F. Boero, A. Fedeli, M. Lanini, M. Maffongelli, R. Monleone, M. Pastorino, A. Randazzo, A. Salvadè, and A. Sansalone, "Microwave tomography for the inspection of wood materials: Imaging system and experimental results," *IEEE Transactions on Microwave Theory and Techniques*, p. early access, 2018.

[52] N. K. Nikolova, "Microwave imaging for breast cancer," *IEEE Microwave Magazine*, vol. 12, no. 7, pp. 78–94, Dec 2011.

[53] D. M. Sheen, D. L. McMakin, and T. E. Hall, "Three-dimensional millimeter-wave imaging for concealed weapon detection," *IEEE Transactions on Microwave Theory and Techniques*, vol. 49, no. 9, pp. 1581–1592, Sep 2001.

[54] X. Zhuge and A. G. Yarovoy, "Three-dimensional near-field MIMO array imaging using range migration techniques," *IEEE Transactions on Image Processing*, vol. 21, no. 6, pp. 3026–3033, June 2012.

[55] J. Gao, Y. Qin, B. Deng, H. Wang, and X. Li, "Novel efficient 3D short-range imaging algorithms for a scanning 1D-MIMO array," *IEEE Transactions on Image Processing*, vol. 27, no. 7, pp. 3631–3643, July 2018.

[56] K. Mizuno, H. Matono, Y. Wagatsuma, H. Warashina, H. Sato, S. Miyanaga, , and Y. Yamanaka, "New applications of millimeter-wave incoherent imaging," in *Proc. of IEEE IMS2005*, Long Beach, California, USA, June 2005.

[57] B. Larumbe, J. Laviada, A. Ibáñez-Loinaz, and J. Teniente, "Real-time imaging with frequency scanning array antenna for industrial inspection applications at W band," *Journal of Infrared, Millimeter, and Terahertz Waves*, vol. 39, no. 1, pp. 45–63, Jan 2018.

[58] Q. Ma, D. S. Goshi, Y. C. Shih, and M. T. Sun, "An algorithm for power line detection and warning based on a millimeter-wave radar video," *IEEE Transactions on Image Processing*, vol. 20, no. 12, pp. 3534–3543, Dec 2011.

[59] L. Yujiri, M. Shoucri, and P. Moffa, "Passive millimeter wave imaging," *IEEE Microwave Magazine*, vol. 4, no. 3, pp. 39–50, Sep. 2003.

[60] S. S. Ahmed, A. Schiessl, and L. P. Schmidt, "A novel fully electronic active real-time imager based on a planar multistatic sparse array," *IEEE Transactions on Microwave Theory and Techniques*, vol. 59, no. 12, pp. 3567–3576, Dec 2011.

[61] F. Gumbmann and L. Schmidt, "Millimeter-wave imaging with optimized sparse periodic array for short-range applications," *IEEE Transactions on Geoscience and Remote Sensing*, vol. 49, no. 10, pp. 3629–3638, Oct 2011.

[62] D. M. Sheen, R. T. Clark, J. Tedeschi, A. M. Jones, and T. E. Hall, "High-resolution 3D microwave imaging of a moving target using optical motion capture," in *Passive and Active Millimeter-Wave Imaging XXII*, D. A. Wikner and D. A. Robertson, Eds., vol. 10994, International Society for Optics and Photonics. SPIE, 2019, pp. 99 – 109. [Online]. Available: https://doi.org/10.1117/12.2519892

[63] I. Nasr, R. Jungmaier, A. Baheti, D. Noppeney, J. S. Bal, M. Wojnowski, E. Karagozler, H. Raja, J. Lien, I. Poupyrev, and S. Trotta, "A highly integrated 60 GHz 6-channel transceiver with antenna in package for smart sensing and short-range communications," *IEEE Journal of Solid-State Circuits*, vol. 51, no. 9, pp. 2066–2076, Sept 2016.

[64] Texas Instruments. (2020, Feb.) 60 GHz Radar-on-Chip. [Online]. Available: https://www.ti.com/tool/IWR6843AOPEVM

[65] Vayyar. (2020, Feb.) System on chip specification. [Online]. Available: http://vayyar.com/technology/

[66] J. T. Case, M. T. Ghasr, and R. Zoughi, "Nonuniform manual scanning for rapid microwave nondestructive evaluation imaging," *IEEE Transactions on Instrumentation and Measurement*, vol. 62, no. 5, pp. 1250–1258, May 2013.

[67] H. He, V. Khilkevich, and D. Pommerenke, "2D imaging system with optical tracking for EMI source localization," in *2015 IEEE Symposium on Electromagnetic Compatibility and Signal Integrity*, March 2015, pp. 107–110.

[68] "IEEE Standard Test Procedures for Antennas," *ANSI/IEEE Std 149-1979*, 1979.

[69] S. Gregson, *Principles of Planar Near-Field Antenna Measurements*, ser. Electromagnetic Waves. Institution of Engineering and Technology, 2007. [Online]. Available: https://digital-library.theiet.org/content/books/ew/pbew053e

[70] A. Yaghjian, "An overview of near-field antenna measurements," *IEEE Transactions on Antennas and Propagation*, vol. 34, no. 1, pp. 30–45, January 1986.

[71] "IEEE Recommended Practice for Near-Field Antenna Measurements," *IEEE Std 1720-2012*, pp. 1–102, Dec 2012.

[72] J. E. Hansen, Ed., *Spherical Near-field Antenna Measurements*, ser. Electromagnetic Waves. Institution of Engineering and Technology, 1988. [Online]. Available: https://digital-library.theiet.org/content/books/ew/pbew026e

[73] W. Leach and D. Paris, "Probe compensated near-field measurements on a cylinder," *IEEE Transactions on Antennas and Propagation*, vol. 21, no. 4, pp. 435–445, July 1973.

[74] F. J. Cano-Fácila, S. Pivnenko, and M. Sierra-Castañer, "Reduction of Truncation Errors in Planar, Cylindrical, and Partial Spherical Near-Field Antenna Measurements," *International Journal of Antennas and Propagation*, vol. 2012.

[75] A. C. Newell, "Error analysis techniques for planar near-field measurements," *IEEE Transactions on Antennas and Propagation*, vol. 36, no. 6, pp. 754–768, June 1988.

[76] L. Boehm, F. Boegelsack, M. Hitzler, and C. Waldschmidt, "The challenges of measuring integrated antennas at millimeter-wave frequencies [measurements corner]," *IEEE Antennas and Propagation Magazine*, vol. 59, no. 4, pp. 84–92, Aug 2017.

[77] D. Novotny, J. Gordon, J. Coder, M. Francis, and J. Guerrieri, "Performance evaluation of a robotically controlled millimeter-wave near-field pattern range at the NIST," in *2013 7th European Conference on Antennas and Propagation (EuCAP)*, April 2013, pp. 4086–4089.

[78] L. Boehm, F. Boegelsack, M. Hitzler, and C. Waldschmidt, "An automated millimeter-wave antenna measurement setup using a robotic arm," in *2015 IEEE International Symposium on Antennas and Propagation USNC/URSI National Radio Science Meeting*, July 2015, pp. 2109–2110.

[79] R. M. Lebrón, J. L. Salazar, C. Fulton, S. Duthoit, D. Schmidt, and R. Palmer, "A novel near-field robotic scanner for surface, RF and thermal characterization of millimeter-wave active phased array antenna," in *2016 IEEE International Symposium on Phased Array Systems and Technology (PAST)*, Oct 2016, pp. 1–6.

[80] D. Titz, F. Ferrero, and C. Luxey, "Development of a Millimeter-Wave Measurement Setup and Dedicated Techniques to Characterize the Matching and Radiation Performance of Probe-Fed Antennas [Measurements Corner]," *IEEE Antennas and Propagation Magazine*, vol. 54, no. 4, pp. 188–203, Aug 2012.

[81] A. Bisognin, D. Titz, F. Ferrero, G. Jacquemod, R. Pilard, F. Gianesello, D. Gloria, C. Laporte, H. Ezzeddine, D. Lugara, and C. Luxey, "Probe-fed measurement system for F-band antennas," in *The 8th European Conference on Antennas and Propagation (EuCAP 2014)*, April 2014, pp. 722–726.

[82] J. R. Guerrieri, D. Novotny, J. Gordon, A. Curtin, M. Allman, K. Hassett, Q. Ton, and S. Caslow, "The new large antenna positioning system for over-the-air testing at the National Institute of Standards and Technology," in *12th European Conference on Antennas and Propagation (EuCAP 2018)*, April 2018, pp. 1–5.

[83] M. S. Castaner, Ed., *Post-processing Techniques in Antenna Measurement*, ser. Electromagnetic Waves. Institution of Engineering and Technology, 2019. [Online]. Available: https://digital-library.theiet.org/content/books/ew/sbew529e

[84] E. N. Leith and J. Upatnieks, "Reconstructed wavefronts and communication theory," *J. Opt. Soc. Amer.*, vol. 52, no. 10, pp. 1123–1130, 1962.

[85] P. J. Napier and R. H. T. Bates, "Antenna-aperture distributions from holographic type of radiation-pattern measurement," *Proc. Inst. Elect. Eng.*, vol. 120, no. 1, pp. 30–34, Jan 1973.

[86] A. Arboleya, J. Laviada, J. Ala-Laurinaho, Y. Álvarez, F. Las-Heras, and A. V. Räisänen, "Phaseless characterization of broadband antennas," *IEEE Transactions on Antennas and Propagation*, vol. 64, no. 2, pp. 484–495, Feb 2016.

[87] R. Pierri, G. D'Elia, and F. Soldovieri, "A two probes scanning phaseless near-field far-field transformation technique," *IEEE Transactions on Antennas and Propagation*, vol. 47, no. 5, pp. 792–802, May 1999.

[88] A. Paulus, J. Knapp, and T. F. Eibert, "Phaseless near-field far-field transformation utilizing combinations of probe signals," *IEEE Transactions on Antennas and Propagation*, vol. 65, no. 10, pp. 5492–5502, Oct 2017.

[89] S. Costanzo and G. Di Massa, "An integrated probe for phaseless plane-polar near-field measurements," *Microwave and Optical Technology Letters*, vol. 30, pp. 293–295, 09 2001.

[90] O. M. Bucci, G. D'Elia, G. Leone, and R. Pierri, "Far-field pattern determination from the near-field amplitude on two surfaces," *IEEE Transactions on Antennas and Propagation*, vol. 38, no. 11, pp. 1772–1779, Nov 1990.

[91] T. Isernia, G. Leone, and R. Pierri, "Radiation pattern evaluation from near-field intensities on planes," *IEEE Transactions on Antennas and Propagation*, vol. 44, no. 5, pp. 701–, May 1996.

[92] H. H. Bauschke, P. L. Combettes, and D. R. Luke, "Phase retrieval, error reduction algorithm, and Fienup variants: a view from convex optimization," *J. Opt. Soc. Am. A*, vol. 19, no. 7, pp. 1334–1345, Jul 2002. [Online]. Available: http://josaa.osa.org/abstract.cfm?URI=josaa-19-7-1334

[93] R. W. Gerchberg and W. O. Saxton, "A Practical Algorithm for the Determination of Phase from Image and Diffraction Plane Pictures," *OPTIK*, vol. 35, no. 2, pp. 237–244, 1972.

[94] J. R. Fienup, "Phase retrieval algorithms: a comparison," *Appl. Opt.*, vol. 21, no. 15, pp. 2758–2769, Aug 1982. [Online]. Available: http://ao.osa.org/abstract.cfm?URI=ao-21-15-2758

[95] O. M. Bucci, A. Capozzoli, and G. D'Elia, "Diagnosis of array faults from far-field amplitude-only data," *IEEE Transactions on Antennas and Propagation*, vol. 48, no. 5, pp. 647–652, May 2000.

[96] J. A. Rodriguez-Gonzalez, F. Ares-Pena, M. Fernandez-Delgado, R. Iglesias, and S. Barro, "Rapid method for finding faulty elements in antenna arrays using far field pattern samples," *IEEE Transactions on Antennas and Propagation*, vol. 57, no. 6, pp. 1679–1683, June 2009.

[97] G. Oliveri, P. Rocca, and A. Massa, "Reliable diagnosis of large linear arrays—a bayesian compressive sensing approach," *IEEE Transactions on Antennas and Propagation*, vol. 60, no. 10, pp. 4627–4636, Oct 2012.

[98] M. D. Migliore, "A compressed sensing approach for array diagnosis from a small set of near-field measurements," *IEEE Transactions on Antennas and Propagation*, vol. 59, no. 6, pp. 2127–2133, June 2011.

[99] Y. Alvarez, F. Las-Heras, and M. R. Pino, "Reconstruction of equivalent currents distribution over arbitrary three-dimensional surfaces based on integral equation algorithms," *IEEE Transactions on Antennas and Propagation*, vol. 55, no. 12, pp. 3460–3468, Dec 2007.

[100] J. Araque and G. Vecchi, "Field And Source Equivalence In Source Reconstruction On 3D Surfaces," *Progress In Electromagnetics Research*, vol. 103, pp. 67–100, 2010.

[101] K. Persson and M. Gustafsson, "Reconstruction of equivalent currents using a near-field data transformation with radome applications," *Progress In Electromagnetics Research*, vol. 54, pp. 179–198, 2005.

[102] F. Las-Heras and T. K. Sarkar, "A direct optimization approach for source reconstruction and NF-FF transformation using amplitude-only data," *IEEE Transactions on Antennas and Propagation*, vol. 50, no. 4, pp. 500–510, April 2002.

[103] J. Araque and G. Vecchi, "Removal of unwanted structural interactions from antenna measurements," in *2009 IEEE Antennas and Propagation Society International Symposium*, June 2009, pp. 1–4.

[104] L. J. Foged, L. Scialacqua, F. Saccardi, J. L. A. Quijano, G. Vecchi, and M. Sabbadini, "Practical Application of the Equivalent Source Method as an Antenna Diagnostics Tool [AMTA Corner]," *IEEE Antennas and Propagation Magazine*, vol. 54, no. 5, pp. 243–249, Oct 2012.

[105] Y. Alvarez, F. Las-Heras, M. R. Pino, and J. A. Lopez, "Acceleration of the sources reconstruction method via the fast multipole method," in *2008 IEEE Antennas and Propagation Society International Symposium*, July 2008, pp. 1–4.

[106] T. F. Eibert and C. H. Schmidt, "Multilevel Fast Multipole Accelerated Inverse Equivalent Current Method Employing Rao–Wilton–Glisson Discretization of Electric and Magnetic Surface Currents," *IEEE Transactions on Antennas and Propagation*, vol. 57, no. 4, pp. 1178–1185, April 2009.

[107] Y. Alvarez, F. Las-Heras, and M. R. Pino, "Application of the adaptive cross approximation algorithm to the sources reconstruction method," in *2009 3rd European Conference on Antennas and Propagation*, March 2009, pp. 761–765.

[108] J. A. Lopez-Fernandez, M. Lopez-Portugues, Y. Alvarez-Lopez, C. Garcia-Gonzalez, D. Martinez, and F. Las-Heras, "Fast Antenna Characterization Using the Sources Reconstruction Method on Graphics Processors," *Progress In Electromagnetics Research*, vol. 126, pp. 185–201, 2012.

[109] F. Cano, M. Sierra-Castañer, S. Burgos, and J. L. Besada, "Applications of sources reconstruction techniques: Theory and practical results," in *Proceedings of the Fourth European Conference on Antennas and Propagation*, April 2010, pp. 1–5.

[110] P. Petre and T. K. Sarkar, "Planar near-field to far-field transformation using an equivalent magnetic current approach," *IEEE Transactions on Antennas and Propagation*, vol. 40, no. 11, pp. 1348–1356, Nov 1992.

[111] Y. Alvarez Lopez, F. Las-Heras Andres, M. R. Pino, and T. K. Sarkar, "An improved super-resolution source reconstruction method," *IEEE Transactions on Instrumentation and Measurement*, vol. 58, no. 11, pp. 3855–3866, Nov 2009.

[112] C. H. Schmidt and T. F. Eibert, "Assessment of irregular sampling near-field far-field transformation employing plane-wave field representation," *IEEE Antennas and Propagation Magazine*, vol. 53, no. 3, pp. 213–219, June 2011.

[113] M. Farouq, M. Serhir, and D. Picard, "Matrix method for far-field calculation using irregular near-field samples for cylindrical and spherical scanning surfaces," *Progress In Electromagnetics Research B*, vol. 63, pp. 35–48, 2015.

[114] ——, "Matrix method for antenna plane wave spectrum calculation using irregularly distributed near-field data: Application to far-field assessment," *Progress In Electromagnetics Research M*, vol. 42, pp. 71–83, 2015.

[115] Y. Alvarez, F. Las-Heras, and M. R. Pino, "On the comparison between the spherical wave expansion and the sources reconstruction method," *IEEE Transactions on Antennas and Propagation*, vol. 56, no. 10, pp. 3337–3341, Oct 2008.

[116] ——, "The Sources Reconstruction Method for Amplitude-Only Field Measurements," *IEEE Transactions on Antennas and Propagation*, vol. 58, no. 8, pp. 2776–2781, Aug 2010.

[117] R. O. Schmidt, "Multiple emitter location and signal parameter estimation," *IEEE Trans. Antennas Propag.*, vol. 34, no. 3, pp. 276–280, Mar. 1986.

[118] L. C. Godara and A. Cantoni, "Uniqueness and linear independence of steering vectors in array space," *J. Acoust. Soc. Am.*, vol. 70, pp. 467–475, 1981.

[119] Y. Wu and H. C. So, "Simple and accurate two-dimensional angle estimation for a single source with uniform circular array," *IEEE Antennas Wireless Propag. Lett.*, vol. 7, pp. 78–80, 2008.

[120] Y. Ziyuan, H. Xiaoxiang, Y. Yang, and T. Liu, "UHF RFID tag antenna performance on various dielectric-background," in *2016 IEEE International Workshop on Electromagnetics: Applications and Student Innovation Competition (iWEM)*, May 2016, pp. 1–3.

[121] P. V. Nikitin and K. V. S. Rao, "Theory and measurement of backscattering from RFID tags," *IEEE Antennas and Propagation Magazine*, vol. 48, no. 6, pp. 212–218, Dec 2006.

[122] Smartrac Technology Gmbh. (2020, 4) Smartrack shortdipole RFID paper tag with Monza 5 chip. [Online]. Available: https://www.smartrac-group.com/shortdipole.html

[123] KATHREIN Solutions Gmbh. (2020, 4) WIRA 30 Antenna Unit. [Online]. Available: https://www.kathrein-solutions.com/products/rfid/antennas/wide-range-30-antennas

[124] M. Kanesan, D. V. Thiel, and S. G. O'Keefe, "The effect of lossy dielectric objects on a UHF RFID meander line antenna," in *Proc. 2012 IEEE Int. Symp. Antennas and Propag.*, July 2012, pp. 1–2.

[125] Smartrac Technology Gmbh. (2029, 4) Smartrac Dogbone Monza R6 RFID tag. [Online]. Available: https://www.smartrac-group.com/files/content/Products_Solutions/PDF/0028_SMARTRAC_DOGBONE.pdf

[126] Impinj. (2020, 4) Chip Monza R6. [Online]. Available: https://support.impinj.com/hc/en-us/articles/202765328-Monza-R6-Product-Datasheet

[127] CAEN RFID. (2020, 4) Wantennax019 antenna. [Online]. Available: https://www.caenrfid.com/en/products/wantennax019/

[128] S. Hochreiter and J. Schmidhuber, "Long Short-Term Memory," *Neural Comput.*, vol. 9, no. 8, pp. 1735–1780, Nov. 1997. [Online]. Available: http://dx.doi.org/10.1162/neco.1997.9.8.1735

[129] A. Krizhevsky, I. Sutskever, and G. E. Hinton, "ImageNet Classification with Deep Convolutional Neural Networks," in *Proceedings of the 25th International Conference on Neural Information Processing Systems - Volume 1*, ser. NIPS'12. USA: Curran Associates Inc., 2012, pp. 1097–1105. [Online]. Available: http://dl.acm.org/citation.cfm?id=2999134.2999257

[130] OptiTrack. (2020, Feb.) Optitrack motion capture system. [Online]. Available: http://www.optitrack.com

[131] A. Meta, P. Hoogeboom, and L. P. Ligthart, "Signal processing for FMCW SAR," *IEEE Transactions on Geoscience and Remote Sensing*, vol. 45, no. 11, pp. 3519–3532, Nov 2007.

[132] J. Barowski, I. Rolfes, and C. Baer, "Real-time imaging system for millimeter wave synthetic aperture radar sensors," in *2017 First IEEE MTT-S International Microwave Bio Conference (IMBIOC)*, May 2017, pp. 1–3.

[133] J. Detlefsen, A. Dallinger, S. Schelkshorn, and S. Bertl, "UWB millimeter-wave FMCW radar using Hubert transform methods," in *2006 IEEE Ninth International Symposium on Spread Spectrum Techniques and Applications*, Aug 2006, pp. 46–48.

[134] Z. Wang, J. Li, and R. Wu, "Time-delay- and time-reversal-based robust Capon beamformers for ultrasound imaging," *IEEE Transactions on Medical Imaging*, vol. 24, no. 10, pp. 1308–1322, Oct 2005.

[135] M. Klemm, I. J. Craddock, J. A. Leendertz, A. Preece, and R. Benjamin, "Improved delay-and-sum beamforming algorithm for breast cancer detection," *International Journal of Antennas and Propagation*, vol. 2008, 2008.

[136] J. Yang, J. Thompson, X. Huang, T. Jin, and Z. Zhou, "FMCW radar near field three-dimensional imaging," in *2012 IEEE International Conference on Communications (ICC)*, June 2012, pp. 6353–6356.

[137] L. Liu, Q. Chen, Y. Han, H. Xu, J. Li, and B. Wang, "Improved clutter removal by robust principal component analysis for chaos through-wall imaging radar," *Electronics*, vol. 9, no. 1, 2019. [Online]. Available: https://www.mdpi.com/2079-9292/9/1/25

[138] M. Garcia-Fernandez, Y. Alvarez-Lopez, A. Arboleya-Arboleya, F. Las-Heras, Y. Rodriguez-Vaqueiro, B. Gonzalez-Valdes, and A. Pino-Garcia, "SVD-Based clutter removal technique for GPR," in *2017 IEEE International Symposium on Antennas and Propagation USNC/URSI National Radio Science Meeting*, July 2017, pp. 2369–2370.

[139] C. A. Balanis, *Advanced Engineering Electromagnetics*. Wiley, 2010.

[140] W. H. Press, B. P. Flannery, S. A. Teukolsky, and W. T. Vetterling, *Numerical Recipes in C: The Art of Scientific Computing*. USA: Cambridge University Press, 1988.

[141] A. Arboleya, Y. Álvarez, and F. Las-Heras, "Millimeter and submillimeter planar measurement setup," in *2013 IEEE Antennas and Propagation Society International Symposium (APSURSI)*, July 2013, pp. 1–2.

[142] C. B. Goncalves, E. Lacombe, C. d. Río, F. Gianesello, C. Luxey, and G. Ducournau, "Compact measurement setup for antennas operating in the 220-325 GHz band," in *2018 International Symposium on Antennas and Propagation (ISAP)*, 2018, pp. 1–2.

Publications

Impact factor report

This section presents the main information regarding the journals where the publications composing this dissertation have been published. Complete references of these journals, which are indexed in the Science Citation Index (SCI) and in the Journal Citation Reports (JCR), can be found in Table P.1.

Table P.1: Complete references of the journals with published works.

Reference	Journal title	Publisher	ISSN	IF	Rank
[**I**]	Sensors and Actuators A-Physical	Elsevier	0924-4247	2.739	Q2
[**II**] [**V**]	IEEE Transactions on Antennas and Propagation	IEEE	0018-926X	4.435	Q1
[**III**]	IEEE Antennas and Wireless Propagation Letters	IEEE	1536-1225	3.510	Q2
[**IV**]	IEEE Access	IEEE	2169-3536	4.098	Q1

2019 metrics are not available yet for publications [**III**] and [**IV**] and neither 2020 metrics for publication [**V**].

Publication I

G. Álvarez-Narciandi, J. Laviada, M. R. Pino and F. Las-Heras, "Phase acquisition techniques for RFID multistatic setups with application to imaging and localization," *Sensors and Actuators A: Physical,* vol. 270, pp. 97–107, Feb 2018.

I

I

Phase acquisition techniques for RFID multistatic setups

Guillermo Alvarez-Narciandi[a,*], Jaime Laviada[a], Marcos R. Pino[a], Fernando Las-Heras[a]

[a] *Área de Teoría de la Señal y Comunicaciones, Departamento de Ingeniería Eléctrica, Universidad de Oviedo, Spain*

Abstract

The aim of this paper is to present two different schemes to retrieve the phase of the field scattered by a UHF RFID tag without requiring a physical connection between the transmitter and the receiver systems. Thus, the phase angle can be comfortably measured in a multistatic, easy to deploy RFID sensor network for different purposes such as location and imaging. The accuracy of both schemes is validated against the one achieved by resorting to a physical connection between the transmitter and the receiver, demonstrating an excellent accuracy. Finally, a localization scheme based on this acquired information is presented to illustrate the use of the proposed phase retrieval approaches.

Keywords: RFID; multistatic; phase retrieval; localization system.

1. Introduction

The identification of objects and people (for instance hospital patients or factory workers) and the capacity to obtain complementary information is essential in many applications such as security or supply chain management. In particular, the availability of the accurate location of an object, its attitude, and the ability to track its position provide a great added value. In order to achieve that, it is necessary to deploy sensor networks in the area of interest. There are different sensing devices based on various principles such as visible light, infrared, ultrasounds or radiofrequency, which is able to work in non-line of sight situations. However, it is desirable to use cost effective hardware to enable the deployment of large sensor networks without very large investments.

A technology that suffices the previous requirements is Radio Frequency IDentification (RFID), which is widely spread for the identification of goods. Among the different RFID standards, the EPCglobal Gen2 [1] (defined for the UHF band) is very mature and a lot of research based on it has been carried out. The basic architecture of these systems consists of an RFID reader, which *interrogates* or queries the RFID tags, and RFID tags, which answer to the reader. There are several types of RFID tags (active, passive or semi-passive [2]), but the passive tags are of special interest since they do not have batteries and their cost is extremely

*Corresponding author
Email address: ganarciandi@tsc.uniovi.es (Guillermo Alvarez-Narciandi)

low (euro cents). Although the read range of passive tags is reduced to less than 10 m, they are powered up and backscatter the information to the receiver with the energy of the signal of the reader. In addition, they hardly require maintenance.

In this context, several passive-RFID location systems have been proposed. Most of them are based on received signal strength (RSS) measurements, as this is the parameter provided by most commercial readers for monostatic as well as multistatic configurations. Among these systems, there are some that consist of deploying RFID tags in the test scenario and mounting one or more readers in the mobile assets. The accuracy of such systems depends mainly on the density of deployed tags [3]. In other RSS-based systems, the objects to be tracked are equipped with RFID tags and several readers are deployed [4, 5, 6]. However, RSS measurements, especially in indoor environments, are subject to fluctuations due to multipath propagation which lead to an accuracy reduction. There are other systems based on phase measurements of the signal backscattered by RFID tags. That information can be used to triangulate the position of the tags [7, 8, 9] or to create synthetic apertures such us in [10], where a reader (whose trajectory must be known) is moved while it queries the RFID tags to be located, or inverse synthetic apertures as presented in [11, 12] (where an RFID reader is static whilst a tag, whose trajectory must be known, is moving). To the best authors' knowledge, these parameters are only provided by some of the most modern readers and only available for monostatic setups. Nevertheless, it has been shown that this information can be exploited to improve already available setups. In addition, the performance of these systems can be enhanced by using several carrier frequencies.

Only little research has been done using bistatic approaches based on either RSS [13] or phase measurements [14, 15]. This approach can be advantageous in some situations in terms of flexibility of the setup, the obtained phase measurements (combining information from the direct path between antennas and the path antenna-tag-antenna) and the potential application of other techniques such as tomography to enable advanced device-free user localization, where the users do not cooperate with the location sensing network, i.e., they do not carry any device of the system such as an RFID tag.

A different approach is proposed in [16], where apart from RFID readers and RFID tags, there is a third kind of devices called RFID listeners. These devices do not play an active role in the communication, they decode the messages between the reader and the tag. However, phase retrieval information has not been exploited by these devices. In fact, they are mostly based on ASK demodulation schemes. Finally, there are some hybrid systems that combine RFID with other technologies such as UltraWide-Band (UWB) [17].

The main contribution of this work is the demonstration of the capability to recover the phase of the signal backscattered by an RFID tag using only the *over the air* received signal for multistatic setups. Also, the unambiguous phase area achieved by these setups, when compared to the monostatic ones, is exploited to tailor a positioning system with centimetric accuracy to show a potential application of the presented phase recovery schemes.

The paper is structured as follows. The different phase retrieval schemes are presented in Section 2. In Section 3 the measurement setups are described and the obtained results are discussed. Finally, in Section 4 the localization system developed to illustrate a potential application of multistatic phase measurements is presented.

2. Phase Acquisition Schemes

2.1. Tag phase model for a given bistatic combination

Modern commercial readers are able to provide the phase angle of the signal backscattered by an RFID tag, usually referred to as tag phase, which is acquired by comparing the phase of the field backscattered by the tag with the phase of the local oscillator, which generates the wave to be modulated by the tag. However, this situation cannot be assumed if there is not a physical connection between the transmitter and the receiver as in the case of multistatic setups. Thus, the tag phase for these setups must be firstly defined.

In this paper, for each transmitter and receiver combination, the phase angle, $\Phi(\vec{r})$, is defined as the *phase difference* between the signal transmitted directly from the transmitter to the receiver and the signal backscattered by the RFID tag. In addition, we will only focus on the case of RFID tags using an ASK scheme, which is the most popular among the multiple ones considered in the standard for UHF RFID [1].

The paths of the signal transmitted by the reader, s_r, and the signal backscattered by the tag, s_{tag}, are depicted in Fig. 1 for a given transmitter and receiver pair. The length of the direct path between the transmitter and the receiver is denoted by R_D. R_T stands for the length of the path from the transmitter to the RFID tag and R_R is the distance from the RFID tag to the receiver.

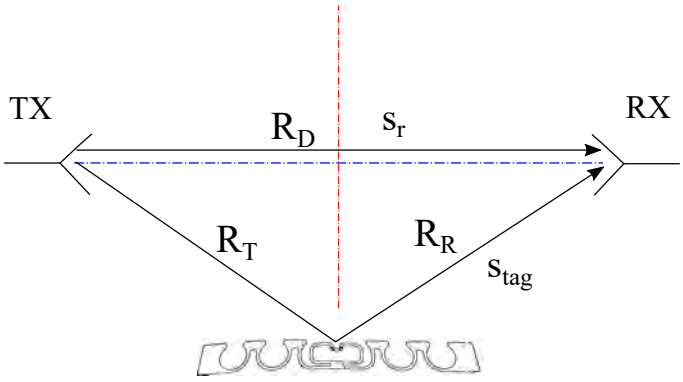

Figure 1: Relevant parameters for the definition of the phase angle for a given transmitter and receiver combination.

In this setup, $\Phi(\vec{r})$ is proportional to the difference between the direct path transmitter-receiver (R_D)

and path of the carrier sent by the reader to the tag (R_T) and the path of its backscattered signal to the receiver (R_R) and is given by:

$$\Phi(\vec{r}) = \left(\frac{2\pi}{\lambda} R_D + \varphi_{Tx-Rx}\right) - \left(\frac{2\pi}{\lambda}[R_T(\vec{r}) + R_R(\vec{r})] + \varphi_{Tx-tag}(\vec{r}) + \varphi_{tag-Rx}(\vec{r})\right) + \varphi_0, \tag{1}$$

where $\vec{r}$ denotes the position of the tag and λ is the wavelength. The terms inside the first parenthesis account for the propagation delay of the carrier sent by the reader to the receiver and for the phase term introduced due to the radiaton pattern of both the transmitting and receiving antennas, φ_{Tx-Rx}. The terms in the second parenthesis account for the propagation delay of the signal sent by the reader to the tag (by means of $R_T(\vec{r})$), for the propagation delay of the signal backscattered by the tag to the receiving antenna (by means of $R_R(\vec{r})$) and for the phase terms introduced by the transmitting antenna, the receiving antenna and the tag antenna: $\varphi_{Tx-tag}(\vec{r}) + \varphi_{tag-Rx}(\vec{r})$ [7]. Finally, φ_0 is the phase offset introduced by the RFID tag.

Since the RFID tag is expected to be in the coverage area provided by the main lobe of the antennas, where the phase is typically constant, and assuming that the phase difference due to the tag orientation is negligible, the previous model can be simplified as:

$$\Phi(\vec{r}) = -\frac{2\pi}{\lambda}(R_T(\vec{r}) + R_R(\vec{r}) - R_D) + \varphi_0. \tag{2}$$

It is relevant to notice that the iso-phase surfaces given by (2) are *ellipsoids* whose foci are the transmitter and the receiver.

Next, the two proposed approaches to retrieved the tag phase based on the *over the air* received RFID signal are presented. In addition, a reference setup, providing equivalent information but based on a wired connection, is also presented.

2.2. Delayed version of the received signal

According to the Gen 2 standard, after the reader sends a query frame, it keeps sending a monochromatic wave at the working frequency. After a given period of time, the RFID tag starts its response by changing the input impedance of its antenna so that the amplitude of the monochromatic wave is modulated. Thus, as shown in the phasor diagram of Fig. 2, the received signal is the vector sum of the signal transmitted by the reader and the signal backscattered by the RFID tag. As a consequence, when the RFID tag uses ASK modulation and encodes a low state, the received signal, s_{rx}, overlaps with the signal transmitted by the reader. Hence, it is possible to obtain the tag phase by comparing the phase of s_{rx} during the two possible states of the reply of the tag.

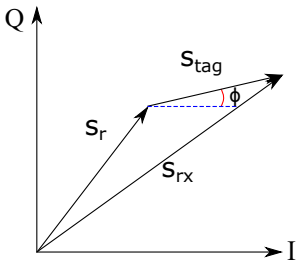

Figure 2: Phasor diagram of the received signal, s_{rx}, which is a vector sum of the signal transmitted by the reader, s_r, and the signal backscattered by the RFID tag, s_{tag}.

In order to further clarify this approach, the signals involved in the demodulation process are plotted in Fig. 3. First, in the upper part, a fragment of the baseband signal of the signal backscattered by the tag is represented, where *Tari* is the reference time interval for a '0' symbol. The duration of the *Tari* is specified by the reader in its query according to the standard [1]. Below the baseband signal, the carrier emitted by the reader, of amplitude A, is represented. In the middle, the received signal, s_r+s_{tag}, where B (whose value has been exaggerated for the ease of interpretation) is the amplitude of the signal backscattered by the tag, is plotted. Finally, at the bottom, a $Tari/2$ delayed version of the received signal, which is used as local oscillator, is depicted. As can be seen, during the high states of the baseband signal (enclosed with dotted red line), the delayed version of the received signal is coincident with s_r and therefore, it can be used to demodulate s_{rx}.

During the first part of the preamble of the signals backscattered by an RFID tag there is a chain, which contains the symbol '0' repeated a different number of times depending on the encoding selected by the reader [1]. The symbol '0' is encoded with a high state during half of the *Tari* and the other half is encoded with a low state. Thus, the standard guarantees that this method can be successfully applied for the different tag messages.

This approach enables the implementation of a wireless multistatic RFID system, as can be seen in the block diagram represented in Fig. 4, but a delay of several microseconds at a frequency around 866 MHz must be introduced. This delay can be achieved by means of digital signal processing, but it would require a high sampling rate as well as relatively large buffers.

Alternatively, large delays can be obtained by using a Surface Acoustic Wave (SAW) delay line. However, the insertion losses of these devices at the UHF RFID frequency band are considerably high (~ 26 dB) [18]. In addition, the delay line should be changed if the modulation parameters of the RFID reader are modified. As a result, the system would be less flexible.

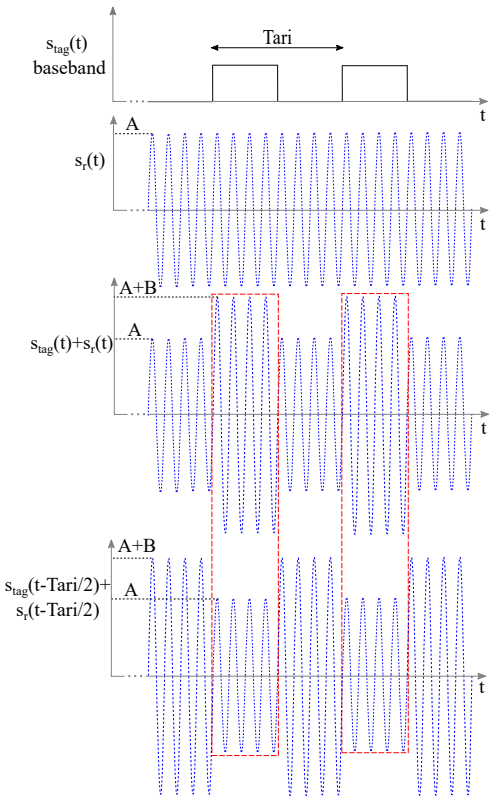

Figure 3: Scheme of the demodulation of the received signal based on delaying it $Tari/2$ to use it as local oscillator.

2.3. Using a Phase Lock Loop

The last approach consists of using a phase lock loop (PLL) at the receiver. The PLL should lock to the frequency of the carrier emitted by the reader but it should not track the small and short frequency variations of the backscattered signal. Hence, it would be possible to use the output signal of the PLL as local oscillator to demodulate the received signal. The block diagram of this approach is illustrated in Fig. 5.

This scheme to demodulate the received signal and retrieve its phase allows the avoidance of wires between transmitter and receiver. Additionally, it simplifies the hardware required with respect to the second approach or, as well as the second approach, it can be implemented via software.

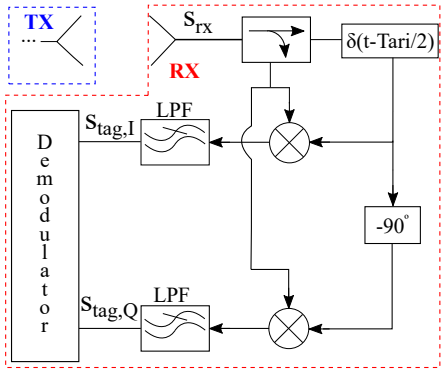

Figure 4: Block diagram of the phase retrieval scheme based on a delayed version of the received signal.

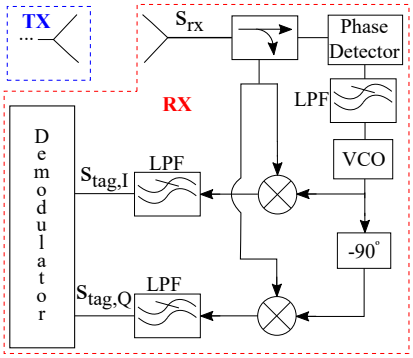

Figure 5: Block diagram of the phase retrieval scheme based on using a PLL.

2.4. Reference phase acquisition setup

This reference scheme is based on the direct connection between the transmitter and receiver as shown in Fig. 6.

Thus, the carrier signal transmitted by the RFID reader is connected to a IQ demodulator, where it is used as the local oscillator signal to obtain the IQ components of the backscattered signal.

It is important to notice that this setup introduces some new delays such as the one introduced from the directional coupler to the IQ mixer (that depends on the electrical length of the used transmission line). Nevertheless, these are fixed delays and, therefore, the dependence of the tag phase with the tag position is still ruled by (2).

Despite the relative simplicity of this scheme, it also imposes several constraints in terms of hardware. First, transmitter and receiver must be connected; and second, an isolator and a coupler have to be used in

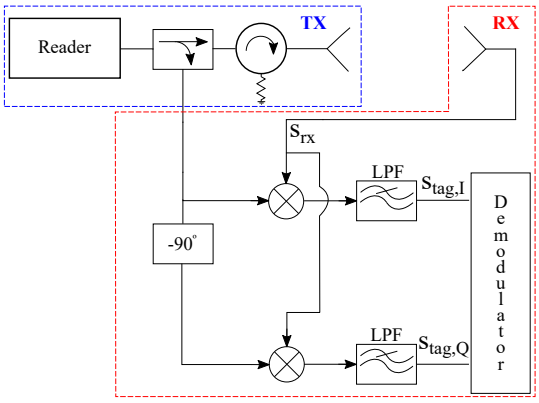

Figure 6: Block diagram of the phase retrieval scheme based on connecting transmitter and receiver through a wire.

this setup.

3. Phase acquisition for a single Tx/Rx link

In this section, the results of the phase measurements obtained with the aforementioned approaches are validated for a single transmitter and receiver combination as depicted in Fig. 1. The *Speedway® Revolution Reader* [19] of *Impinj®* was used to generate the interrogating signals for all the measurements. The PLL was implemented using a damping factor $\xi = 0.6$, a pull-in range of 2 MHz, a phase detector of gain $k_p = 1$, a second order loop filter and a local oscillator with $\omega_0 = 866$ MHz and whose gain was set to $k_0 = 0.003$. In order to test the proposed techniques, they were implemented via software. Specifically, both the signal of the reader, s_r, and the received signal, s_{rx}, were recorded by means of the digital oscilloscope Tektronix CSA7404 using a sampling rate of 10 of gigasamples per second. After that, the signals were interpolated by a factor of 4 and the following steps were performed to estimate the tag phase:

1. First, the IQ components of the received signal are computed using the oscillator signal obtained with one of the schemes presented in Section 2. After low-pass filtering, the IQ components, depicted in Fig. 7, are given by:

$$\begin{aligned} s_I(t) &= \left[\left(s_{tag}\left(t\right) + s_r\left(t\right)\right)\cos\left(\omega_c t + \Phi_{Osc}\right)\right] * h_{LPF}\left(t\right) \approx \\ &\approx \frac{A}{2}\cos\left(\Phi_r - \Phi_{Osc}\right) + \frac{B}{2}x\left(t\right)\cos\left(\Phi_{tag} - \Phi_{Osc}\right) + n_I\left(t\right) \end{aligned} \tag{3}$$

and

$$\begin{aligned} s_Q(t) &= -\left[\left(s_{tag}\left(t\right) + s_r\left(t\right)\right)\sin\left(\omega_c t + \Phi_{Osc}\right)\right] * h_{LPF}\left(t\right) \approx \\ &\approx \frac{A}{2}\sin\left(\Phi_r - \Phi_{Osc}\right) + \frac{B}{2}x\left(t\right)\sin\left(\Phi_{tag} - \Phi_{Osc}\right) - n_Q\left(t\right) \end{aligned} \tag{4}$$

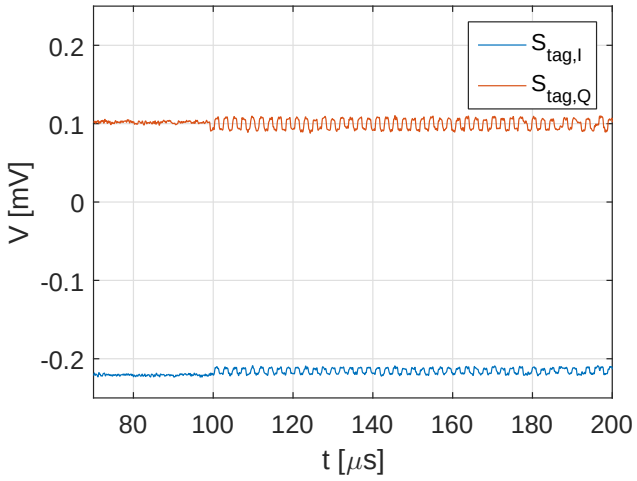

Figure 7: IQ components of the signal backscattered by the tag obtained after performing step 1.

wherein A is the amplitude of the monochromatic wave emitted by the transmitter and B is the amplitude of the signal backscattered by the tag (in general, $A \gg B$); ω_c is the angular carrier frequency; $x(t)$ is the baseband signal of the signal backscattered by the tag; Φ_r is the phase of the signal sent by the reader s_r; Φ_{tag} is the phase of the signal backscattered by the tag, s_{tag}; Φ_{Osc} is the phase of the regenerated local oscillator signal at the receiver; and $n_I(t)$ and $n_Q(t)$ are the noise contributions of the IQ components of the signal. The low pass filter, whose impulse response is $h_{LPF}(t)$, is a Butterworth filter of order 5 and cut-off frequency of 20 MHz.

2. The offset levels of the I and Q components, which are given by

$$Offset_I = \frac{A}{2}\cos\left(\Phi_r - \Phi_{Osc}\right) \tag{5}$$

and

$$Offset_Q = \frac{A}{2}\sin\left(\Phi_r - \Phi_{Osc}\right) \tag{6}$$

respectively, are computed and subtracted from the I and Q components. As can be observed, both depend on a trigonometric function (cosine and sine for I and Q componentes respectively) whose argument is the difference between the phase of the monochromatic signal emitted by the reader, Φ_r, and the phase of the oscillator signal which was used to demodulate the received signal, Φ_{Osc}. Therefore, the phase difference $\Phi_r - \Phi_{Osc}$ can be obtained by means of a two-argument arctangent operation.

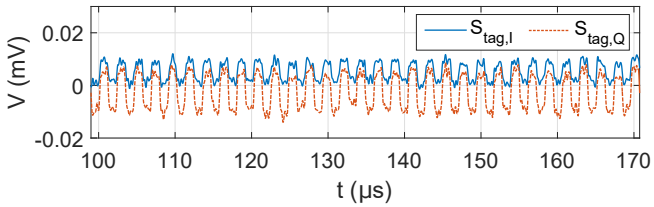

Figure 8: First part of the preamble of the IQ components of the signal backscattered by the tag.

3. The beginning of the preamble of the backscattered signal (Fig. 8) is computed correlating the IQ components obtained in step 2, i.e. without their offset levels, with the preamble defined by the reader in its query.
4. Once the beginning of the preamble is estimated, the position of the high states of the preamble of the signal backscattered by the tag is known. Thus, the phase term $\Phi_{tag} - \Phi_{Osc}$ can be obtained by means of a two-argument arctangent operation applied during the high states of the preamble of the IQ components. This provides an instantaneous tag phase value which is averaged along the acquisition time. Finally, the desired phase angle, $\Phi(\vec{r}) = \Phi_{tag} - \Phi_r$, can be computed subtracting the phase terms estimated during the steps 2 and 4.

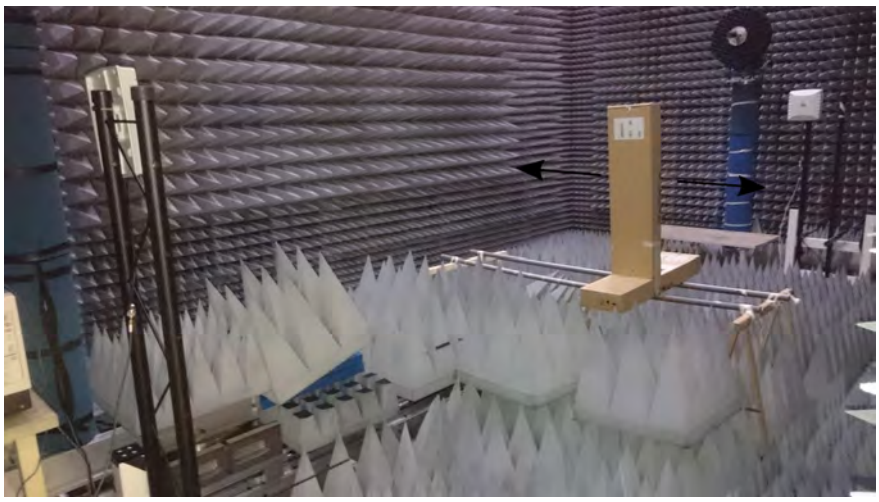

Figure 9: Measurement setup in the anechoic chamber.

Two set of measurements were performed to test the accuracy of the proposed phase retrieval schemes. The first measurements were performed in a controlled environment: the anechoic chamber of the Area of

Signal Theory and Communications of the University of Oviedo. Second, the proposed approaches were tested in an indoor scenario. The setup in the anechoic chamber is shown in Fig. 9, where two antennas were placed opposite to each other at a distance of 4.5 m. In the middle of the imaginary line between both antennas, a structure of two PVC tubes was used as rails to move a cardboard box with an attached RFID tag. During the measurements the RFID tag was moved from −60 cm to 60 cm with 4 cm steps. A line laser was used to align the initial position of the tag right across the line between the two antennas. In addition, the term φ_0 was previously measured and removed so that the theoretical phase values and the ones measured using the reference phase acquisition technique were both $\Phi = 0$ at the center position $(d = 0)$.

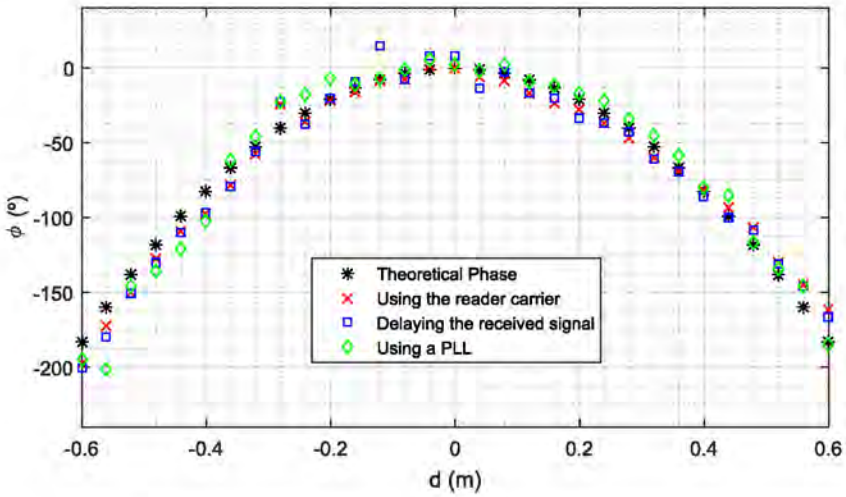

Figure 10: Retrieved phase of the signal backscattered by the tag measured in anechoic chamber using the presented approaches and the theoretical values.

The phase acquired employing the two approaches (using a PLL and delaying the received signal) is plotted in Fig. 10. The theoretical curve given by (2) and the empirical results given by the reference setup (i.e., using the reader carrier) are also depicted in that figure. As can be seen, there is a good agreement between the empirical and theoretical results. The root mean square errors, computed comparing the obtained phase values using each phase retrieval scheme and the theoretical ones, are 7.94, 9.37 and 8.80 degrees for the case of using the reader carrier, delaying the received signal and using a PLL, respectively. If instead of comparing the phase values obtained using the proposed wireless techniques with the theoretical ones, we compare them with the phase values obtained with the reference phase acquisition technique (to account for small positioning errors) the root mean square errors are 5.77 degrees when delaying the received

signal and 11.44 degrees when using a PLL.

Figure 11: Measurement setup in an indoor scenario.

The setup in the indoor scenario is shown in Fig. 11, where the two antennas were placed opposite to each other at a distance of 3 m. In the middle of the imaginary line between both antennas, a cardboard box with an RFID tag attached to it was placed over a table. During the measurements, the RFID tag was moved from −60 cm to 60 cm with 4 cm steps (as in the anechoic chamber measurements). A line laser was used to align the initial position of the tag right across the line between the two antennas. In addition, the term φ_0 was previously measured and removed so that the theoretical phase values and the ones measured using the reference phase acquisition technique were both $\Phi = 0$ at the center position ($d = 0$).

The obtained results for the proposed phase retrieval schemes are depicted in Fig. 12 alongside with the theoretical phase values given by (2). The root mean square errors, computed comparing the obtained phase values using each phase retrieval scheme and the theoretical ones, are 16.98, 18.54 and 20.36 degrees for the case of using the reader carrier, delaying the received signal and using a PLL, respectively. As can be seen, the error values are greater than the ones obtained for the measurements in the anechoic chamber. However, since the measurements were not performed in a controlled environment such as the anechoic chamber, the theoretical model of (2) does not accurately represent the phase variation of the experiment. Therefore, a fairer error value can be computed assuming the phase values obtained using the reference approach as the true ones, and comparing them with the other two wireless phase retrieval schemes. Using this metric, the root mean square errors are 8.26 and 13.11 degrees for the case of delaying the received signal and using a PLL, respectively. Thus, results show that, although the performance of the phase retrieval schemes is

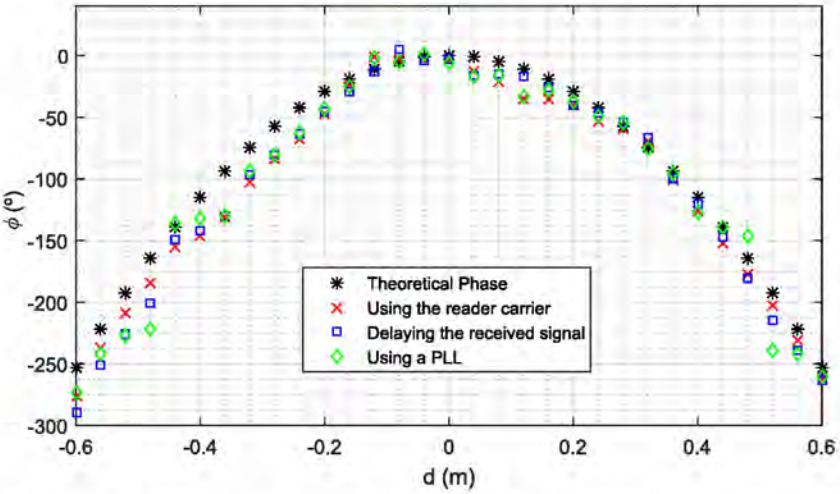

Figure 12: Retrieved phase of the signal backscattered by the RFID tag measured in an indoor scenario using the presented approaches and the theoretical values.

slightly degraded in an indoor scenario, the proposed approaches are still accurate.

4. Application to a positioning system

In order to illustrate the capabilities of multistatic phase measurements of the signal backscattered by an RFID tag, an indoor location system was developed. One of the limitations of traditional location systems that use (multi)monostatic phase measurements is the inherent 2π ambiguity of phase. In contrast, although multistatic systems are also subject to phase ambiguity, the phase variation is slower with the distance, (1), especially in the region between the antennas and, therefore, the unambiguous region is extended.

This is shown in Fig. 13, where the phase which would be measured with a monostatic setup (Fig. 13a) and with a bistatic setup (Fig. 13b) for several positions of a tag is represented. The phase value for each position was computed assuming free space propagation from the transmitting antenna to the tag and back to the transmitting antenna again in the monostatic case and to the receiving antenna in the bistatic case. In the monostatic case, where the antenna is located at $(-2, 0)$ m, there is phase ambiguity for those positions located at a distance $l > \lambda/2$ from the antenna taking into account both the direct and the reverse path of the signal which, at the UHF RFID European band, is approximately 17.3 cm. In contrast, in the bistatic case, the unambiguous zone is enclosed by an ellipse (an ellipsoid in a 3D space) whose foci are the

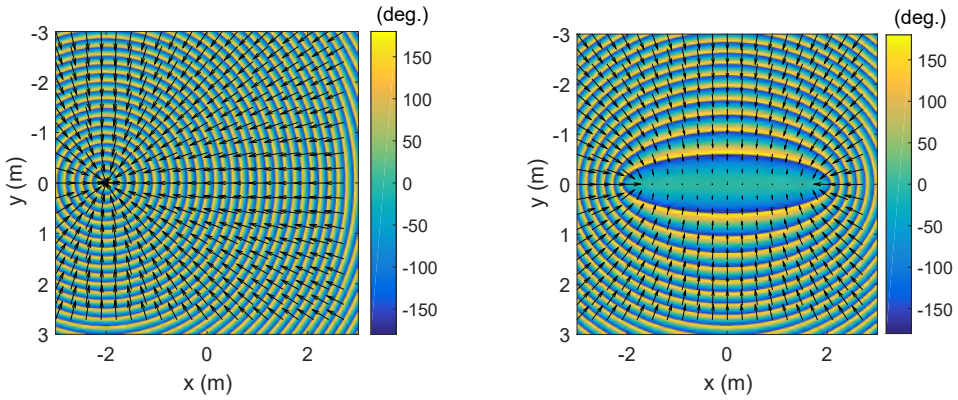

(a) (b)

Figure 13: Tag phase distribution (in degrees) at 866 MHz for : a) monostatic setup with an antenna at $(-2, 0)$ m; b) bistatic setup with antennas at $(-2, 0)$ m and $(2, 0)$ m. The black arrows depict its gradient.

two antennas (separated R_D), whose semi-major axis is given by

$$a = \frac{R_D}{2} + \frac{\lambda}{2}, \tag{7}$$

and whose semi-minor axis is given by

$$b = \sqrt{R_D \frac{\lambda}{2} + \frac{\lambda^2}{4}}. \tag{8}$$

Therefore, the unambiguous phase area in a bistatic setup, assuming that the antennas do not radiate backwards, is

$$A = 2ab \left[\arcsin\left(\frac{R_D}{2a}\right) - \frac{\sin\left(2 \arcsin\left(\frac{R_D}{2a}\right)\right)}{2} \right], \tag{9}$$

which, placing the antennas at $(-2, 0)$ m and $(2, 0)$ m and transmitting at $f = 866$ MHz, is approximately 120 times bigger than in a monostatic setup. The main drawback of the bistatic setup is the sensitivity to small phase errors in the central area between the antennas, i.e., the phase in this area presents little variation, but this can be overcome using more than two antennas to tailor a multistatic setup.

Based on this approach an indoor localization system which uses several antennas was designed. When each of the antennas of the setup queries an RFID tag, the phase of the signal backscattered by that tag is measured at the rest of the antennas (except the ones adjacent to the transmitter, so that the position of each pair of antennas is as different as possible from a quasi-monostatic setup). Then, the position of the

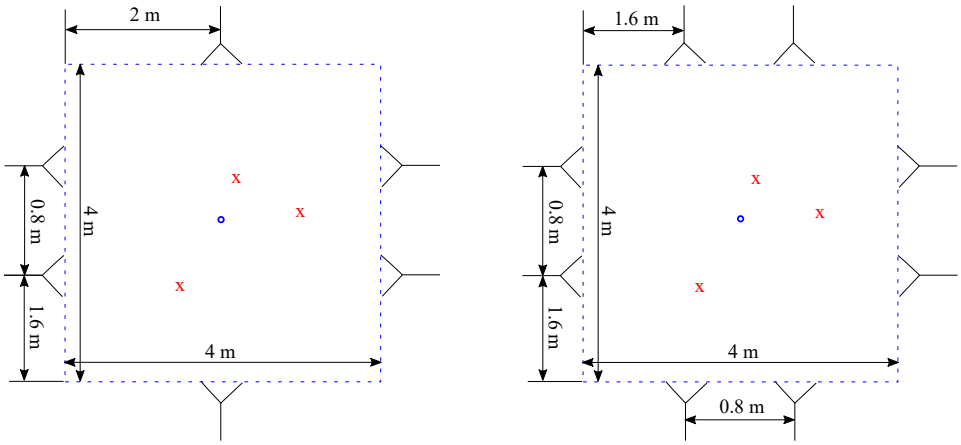

Figure 14: Schematic of the simulation setup using 6 (a) and 8 (b) antennas.

RFID tag is estimated as the one that makes the following cost function minimum

$$J = \sum_{n=1}^{N\cdot(N-3)/2} |\angle e^{j(\Phi_{meas,n}-\Phi_{theor,n})}|^2, \tag{10}$$

where N is the number of antennas and $\Phi_{meas,n}$ and $\Phi_{theor,n}$ are the measured and theoretical phases for the n-th transmitter-receiver antenna pair. To compute the theoretical phases, the area enclosed by the antennas is first discretized. Then, the phase values are computed assuming free space propagation as it was done to obtain Fig. 13b. The upper bound of summation $(N \cdot (N-3)/2)$ is the number of diagonals of a polygon of N sides, i.e., the number of bistatic combinations using N antennas (without considering adjacent antennas). As can be seen, it is necessary to know the position of the antennas with accuracy to precompute the theoretical phase at each point of the grid. In addition, the phase introduced by the tag φ_0 must be firstly measured in a calibration stage so that it can be subtracted from the tag phase estimation.

In order to evaluate the performance of the proposed location system for different configurations, several simulations were carried out. In particular, the two setups shown in Fig. 14 , with 6 and 8 antennas have been considered. As can be observed, the antennas enclose an area of $16\,\mathrm{m}^2$. The red crosses denote the positions of the simulated RFID tags whilst the blue circle indicates the center of the coordinate system.

The results after performing 20 simulations for each position of the RFID tag for the two different setups are summarized in Table 1, 2 and 3. The parameter σ_{noise} denotes the standard deviation in degrees of the simulated phase measurements from the true phase value (althoug the used σ_{noise} may seem high, they are

realistic due to the features of RFID technology and its low cost nature, as shown in Section 3) and ϵ_{rms} the position root mean square error in meters.

Table 1: Position root mean square error obtained for different values of σ_{noise} simulating an RFID tag at $(0.2, 0.5)$ m.

#Antennas	6				8		
σ_{noise} (°)	20	30	40	50	30	40	50
ϵ_{rms} (m)	0.20	0.53	0.82	1.37	0.01	0.04	0.26

Table 2: Position root mean square error obtained for different values of σ_{noise} simulating an RFID tag at $(-0.4, -1)$ m.

#Antennas	6				8		
σ_{noise} (°)	20	30	40	50	30	40	50
ϵ_{rms} (m)	0.01	0.33	1.11	1.74	0.05	0.13	0.37

Table 3: Position root mean square error obtained for different values of σ_{noise} simulating an RFID tag at $(1, -0.1)$ m.

#Antennas	6				8		
σ_{noise} (°)	20	30	40	50	30	40	50
ϵ_{rms} (m)	0.20	0.62	1.11	1.60	0.01	0.07	0.33

As expected, increasing the number of antennas entails a reduction of the positioning error. In fact, in the setup with 8 antennas even when $\sigma_{noise} = 50°$ the error is below 40 cm. With 6 antennas and $\sigma_{noise} = 20°$, which is a more realistic value, the error is below 20 cm. In addition, the use of the proposed multistatic approach results in a strong reduction of local minima as can be seen comparing Fig. 15a and Fig. 15b.

Finally, the designed system was also tested in an anechoic chamber using the measurement setup displayed in Fig. 16. As can be seen, an RFID tag was attached to a cardboard box which was placed in the middle of 6 UHF antennas whose coordinates are shown in Table 4. The box was displaced along the rails and measurements were taken at 4 different positions. All the measurements were performed manually by connecting each pair of antennas sequentially to the RFID reader and the oscilloscope.

In order to mitigate potential phase errors caused mainly by small discrepancies between the antenna measured positions and the real ones (it should be pointed out that measuring the antenna positions accurately is the most time consuming operation during the deployment of the system), the previously described system was complemented by using the RSS of the signals backscattered by the tag in a monostatic setup, which does not imply the use of a more complex infrastructure. Hence, when an antenna queries the tag, the phase of the signal backscattered by it is measured at the other deployed antennas and its RSS is measured at the interrogator antenna. The information hybridization algorithm steps are the following:

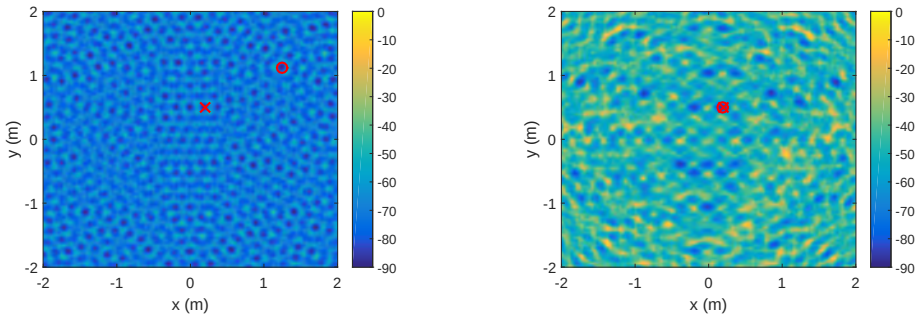

(a) (b)

Figure 15: Cost function evaluated for the setup shown in Fig. 14a using a monostatic approach (a) and the proposed bistatic approach (b). The red circunmference depicts the simulated tag position and the red cross depicts the estimated tag position.

Table 4: Antenna coordinates of the localization system setup

Antenna	1	2	3	4	5	6
x_{coord} (m)	0.02	0.74	2.13	0.63	0.04	−1.22
y_{coord} (m)	0	0	1.90	3.75	3.70	2.02

1. A first estimate of the area where the RFID tag is located is performed using the RSS measurements. To do so, the algorithm proposed in Section 2.1 of [20], which is based on the attenuation differences between the antennas, is applied. Finally, the area of the RFID tag is limited within a circumference radius of 0.5 m and centered on the estimated position by the RSS algorithm.
2. Once the possible locations of the RFID tag are limited, the phase-based algorithm is applied. The reduction of the research domain eliminates local minima.

The results using multistatic phase measurements are shown in Fig. 17. In addition, the same positioning algorithm was used with monostatic phase measurements in order to compare the results of both schemes. As can be seen, despite a small offset in the order of 7 cm, the accuracy of the position estimations using multistatic phase measurements is excellent, with a rms error of 8 cm. On the other hand, the position estimations obtained with monostatic phase measurements are less accurate with a rms error of 35 cm. Also, the estimations are less precise, i.e., the computed positions do not follow the pattern of the real positions of the tag (a straight line), the estimated positions are scattered (the variability of the position estimations is larger). It is worth mentioning that the stronger the multipath in an indoor scenario is, the more impact it would have in the accuracy of the localization system. However, based on the previous simulations and the measurement results of Section 3, it can be inferred that the accuracy of the system would still be high

Figure 16: Setup of the proposed localization system.

in an indoor scenario.

5. Conclusions

It has been demonstrated in this paper that the phase angle of an RFID tag can be extracted from the *over the air* transmitted signal without the need of resorting to a physical connection between the transmitter and receiver. Thus, the phase information can be easily exploited to build advanced systems based on multistatic topologies.

For this purpose, two different phase acquisition schemes have been proposed with different advantages and drawbacks. The first one takes advantage of the properties of the RFID signal and it is based on demodulating using a $Tari/2$ delayed version of the received signal. Although this approach simplifies the setup, it implies the use of a delay line of a relatively high nominal delay for UHF frequencies (a SAW delay line) and whose insertion losses are very high. This also limits the encoding of the backscattered RFID signal (which modifies the value of *Tari*) to the one with the *Tari* value of the delay line. However, both disadvantages can be avoided if digital processing is used at the expense of using high sample rates and large data buffers. The second approach is based on the use of a PLL that can track the continuous wave emitted by the reader but it is slow enough so that it is not affected by the short periods when the tag reflects the impinging signal. This scheme is more flexible since it only uses the *over the air* transmitted signal and does not impose any constraints on the encoding used by the tag signal. Although both methods have been

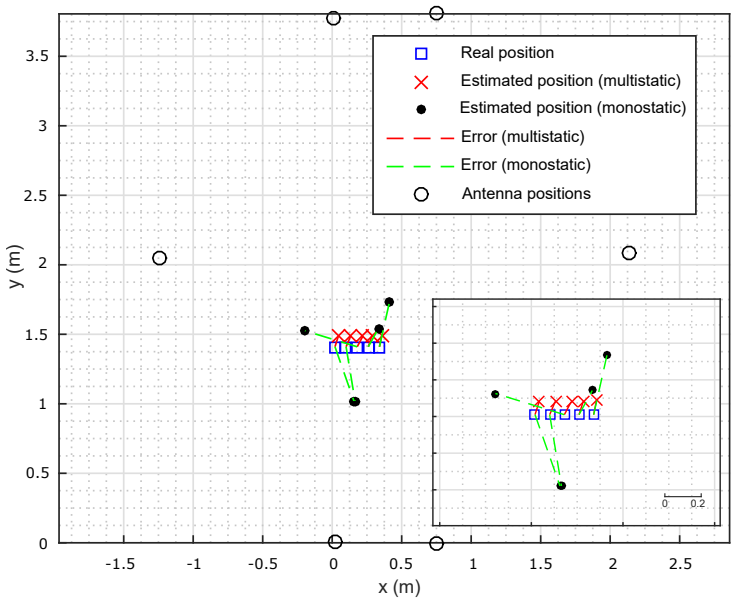

Figure 17: Real positions of the RFID tag (blue squares) and estimated positions by the multistatic (red crosses) and the monostatic (black dots) localization system . The area surrounding the real positions of the RFID tag is zommed for the sake of clearness. The antenna positions are represented with black circumferences.

successfully validated for RFID tags in the UHF band, it is expected that they can be directly extended to other working bands.

In addition, the advantages of using multistatic phase measurements in some scenarios have been remarked emphasizing on the increase of the unambiguous region and the reduction of local minima due to the slower phase variation of this approach. A localization system was developed as a proof of concept to illustrate a potential use for the proposed measurement setup. The system was evaluated by means of simulation and measurements in test scenario in anechoic chamber. The results show a centimetric accuracy on the tag estimated position.

6. Acknowledgements

This work has been supported by the Gobierno del Principado de Asturias (PCTI)/FEDER-FSE under project GRUPIN14-114; by the Ministerio de Ciencia e Innovación of Spain/FEDER under projects TEC2014-55290-JIN and MIRIIEM-TEC2014-54005-P and under the FPU grant FPU15/06431.

References

[1] GS1, EPC radio-frequency identity protocols generation-2 UHF RFID (11 2016).
URL http://www.gs1.org/sites/default/files/docs/epc/Gen2_Protocol_Standard.pdf

[2] W. Alsalih, A. Alma'aitah, W. Alkhater, RFID localization using angle of arrival cluster forming, Int. J. Distrib. Sensor Networks 10 (3) (Mar. 2014).

[3] A. A. N. Shirehjini, A. Yassine, S. Shirmohammadi, An RFID-based position and orientation measurement system for mobile objects in intelligent environments, IEEE Trans. Instrum. Meas. 61 (6) (Jun. 2012).

[4] Y. Alvarez, M. E. D. Cos, F. Las-Heras, A received signal strength RFID-based indoor location system, Sens. Actuators A Phys. 255 (2017) 118–133.

[5] S. Shao, R. J. Burkholder, Item-level RFID tag location sensing utilizing reader antenna spatial diversity, IEEE Sensors J. 13 (10) (2013) 3767–3774.

[6] X. Chen, L. Xie, C. Wang, S. Lu, Adaptive accurate indoor-localization using passive RFID, in: Proc. IEEE Int. Conf. Parallel Distrib. Syst. (ICPADS), 2013, pp. 249–256.

[7] P. V. Nikitin, R. Martinez, S. Ramamurthy, H. Leland, G. Spiess, K. V. S. Rao, Phase based spatial identification of UHF RFID tags, in: 2010 IEEE Int. Conf. on RFID, 2010, pp. 102–109.

[8] S. Azzouzi, M. Cremer, U. Dettmar, T. Knie, R. Kronberger, Improved aoa based localization of UHF RFID tags using spatial diversity, in: Proc. IEEE Int. Conf. RFID-Technol. Appl. (RFID-TA), 2011, pp. 174–180.

[9] J. Huiting, H. Flisijn, A. B. J. Kokkeler, G. J. M. Smit, Exploiting phase measurements of EPC Gen2 RFID tags, in: Proc. IEEE Int. Conf. RFID-Technol. Appl. (RFID-TA), 2013, pp. 1–6.

[10] R. Miesen, F. Kirsch, M. Vossiek, UHF RFID localization based on synthetic apertures, IEEE Trans. Autom. Sci. Eng. 10 (3) (Jul. 2013).

[11] A. Buffi, P. Nepa, Advanced SARFID: a localization technique for UHF RFID tags, in: URSI Int. Symp. Electromagn. Theory (EMTS), 2016.

[12] A. Buffi, P. Nepa, The SARFID technique for discriminating tagged items moving through a UHF-RFID gate, IEEE Sensors Journal 17 (9) (2017) 2863–2870.

[13] B. Wagner, N. Patwari, D. Timmermann, Passive RFID tomographic imaging for device-free user localization, in: 2012 9th Work. Positioning, Navig. Commun., 2012, pp. 120–125.

[14] M. Scherhäufl, M. Pichler, E. Schimbäck, D. J. Müller, A. Ziroff, A. Stelzer, Indoor localization of passive UHF RFID tags based on phase-of-arrival evaluation, IEEE Trans. Microw. Theory Techn. 61 (12) (2013) 4724–4729.

[15] M. Scherhäufl, M. Pichler, A. Stelzer, UHF RFID localization based on evaluation of backscattered tag signals, IEEE Trans. on Instrum. Meas. 64 (11) (2015) 2889–2899.

[16] D. D. Donno, F. Ricciato, L. Catarinucci, A. Coluccia, L. Tarricone, Challenge: Towards distributed RFID sensing with software-defined radio, in: Proc. of the Annu. 16th Int. Conf. on Mobile Comput and Netw., 2010, pp. 97–104.

[17] A. Guerra, N. Decarli, F. Guidi, D. Dardari, Energy sprinklers for passive UWB RFID, in: 2014 IEEE International Conference on Ultra-WideBand (ICUWB), 2014, pp. 356–361.

[18] Triquint Semiconductor, Saw delay line (10 2016).
URL http://www.richardsonrfpd.com/resources/RellDocuments/SYS_31/856716.pdf

[19] Imping, Imping low level user data (10 2016).
URL https://support.impinj.com/hc/en-us/articles/202755318-ApplicationNote-Low-Level-User-Data-Support

[20] Y. Alvarez-Lopez, G. A. Narciandi, F. Las-Heras, Sensor network and inertial positioning hybridisation for indoor location and tracking applications, Int. J. Sensor Networks (Accepted for publication).

Publication II

G. Álvarez-Narciandi, J. Laviada, M. R. Pino and F. Las-Heras, "Attitude Estimation Based on Arrays of Passive RFID Tags," *IEEE Transactions on Antennas Propagation,* vol. 66, no. 5, pp. 2534–2544, May 2018.

II

Attitude Estimation Based on Arrays of Passive RFID Tags

Guillermo Alvarez-Narciandi, Jaime Laviada, Marcos R. Pino, and Fernando Las-Heras, *Senior Member, IEEE*

***Abstract*—In this contribution a method to estimate the attitude of an object using uniform arrays of RFID tags is presented. This technique is based on using the MUSIC algorithm with the phase measurements of the signals backscattered by the RFID tags of the array. Two array topologies have been studied (uniform linear arrays (ULA) and uniform circular arrays (UCA)). The performance of the system has been assessed by means of simulations and measurements in a controlled environment and in an indoor scenario. Results show that, after calibration, the attitude can be estimated with an error of a few degrees for a large range of orientations as long as the signals sent by the RFID reader do not imping the tags at grazing angles.**

***Index Terms*—RFID; attitude estimation; MUSIC; Uniform Circular Array; Uniform Linear Array.**

I. Introduction

THE use of Radio Frequency IDdentification (RFID) technology enables optimized tracking and warehouse management resulting in an improvement of logistics efficiency and the subsequent cost savings [1]. The low cost and lack of maintenance of passive RFID tags, which do not require a battery, make them suitable to track pallets or boxes providing identification with non line of sight (NLOS) conditions. RFID readers can be equipped on forklifts or deployed along the supply chain to query the tags identifying the different goods. During this process, the RFID reader sends a signal to a tag attached to a product, which backscatters the signal including its code. Once the reader receives the backscattered signal, the code of the tag, which identifies the product, can be obtained.

In addition to the code of the tag, physical information of the signal such as the received signal strength (RSS) and its phase can be retrieved. During the last years, research effort has been made to develop systems and techniques that exploit this information. In particular, the development of positioning systems has been of great interest. Most of them are based on RSS measurements of the signal backscattered by RFID tags, as this is the parameter provided by most of the commercial readers [2], [3], [4]. However, there are other recent developments based on phase information of the backscattered signal such as [5], [6], [7], [8], [9], where tag positions are estimated using measurements from several antennas, or [10], where the trajectory of the tagged item is known and only one antenna is used. In general, these phase-based approaches are developed by resorting to RFID tags working in the UHF bands according to the EPC Gen2 standard [11] and the different regional frequency regulations.

Apart from location estimations, the knowledge of the attitude of goods provides complementary information, which can be very useful to automate logistic processes or when handling with fragile cargo. This information can be obtained with inertial sensors (although they are more expensive than RFID tags and require batteries), using RFID tags and antennas with high directivity as proposed in [12], or by means of a computer vision system (which requires line of sight conditions) [13].

In this paper a novel technique to estimate the attitude of objects based on using an array of RFID tags and a single antenna is presented. The proposed method employs phase measurements of the RFID tags of the array and a direction finding algorithm to estimate the attitude of the array. Some previous work regarding azimuth estimations was presented in [14].

Multiple signal classification (MUSIC) [15] has been selected as the direction finding algorithm, as it has demostrated a good performance for a large variety of situations [16], [17]. This is a high resolution algorithm which is based on the eigen-decomposition of the covariance matrix of the input data and requires the knowledge of the array geometry (theoretically or by calibration) to compute the array steering vectors. The steering vectors are the phase shifts between each of the elements of the array and a reference when an incident plane wave impings the array from a given direction.

If two different incident angles result in the same phase distribution along the elements (tags), then an ambiguity in the azimuth and elevation happens. In [18] it was demonstrated that only 3D arrays can have linearly independent steering vectors for every possible incident direction. A sufficient condition for that linear independence is that the array must have at least 4 non-coplanar elements such that if the first element is placed at the origin of coordinates and each of the rest elements are located in a different reference axis, the distance between the first element and the other 3 must be less than $\lambda/2$.

In addition, it was demonstrated that in planar arrays, such as a uniform circular array (UCA), only pairs of directions have the same steering vectors if the array has at least 3 non-colinear elements such that if one element is at the origin of coordinates and each of the other two is in a different axis of the array plane and the distance between theese two elements and the first one is less than $\lambda/2$. Hence, if the previous condition is satisfied, the steering vectors are unique within each of the two subspaces separated by the array plane. Thus,

This work has been supported by the Gobierno del Principado de Asturias (PCTI)/FEDER-FSE under project GRUPIN14-114; by the Ministerio de Economía y Competitividad of Spain /FEDER under projects TEC2014-55290-JIN and MIRIIEM-TEC2014-54005-P and under the FPU grant FPU15/06431.

Guillermo Alvarez-Narciandi, Jaime Laviada, Marcos R. Pino, and Fernando Las-Heras are with the Departamento de Ingeniería Eléctrica, Universidad de Oviedo, Spain (e-mail: ganarciandi@tsc.uniovi.es; jlaviada@tsc.uniovi.es; mpino@tsc.uniovi.es; flasheras@tsc.uniovi.es).

it is possible to obtain unambiguously the direction of arrival (DoA) of the signals impinging the planar array restraining the search space to one of those two subspaces.

Finally, in [18] an equivalent condition is also given for 1D DoA estimations using uniform linear arrays (ULA), in which the space between elements is uniform: the element spacing must be less than $\lambda/2$.

Taking that into account, we will focus in two different flat arrays: 1) uniform linear arrays; 2) uniform circular arrays, in which all the elements of the array are uniformly spaced over a circumference of a given radius. Using the proposed method, unambiguous azimuth, α, estimations can be retrieved with an ULA in an angular range of $[-90°, 90°]$ and both azimuth and elevation, β, can be obtained using an UCA for $\alpha \in [-90°, 90°]$ and $\beta \in [-90°, 90°]$.

The rest of the paper is organized as follows: first, the attitude estimation method is described in Section II. In Section III the numerical results of the simulations carried out to test the system are presented. After that, in Section IV the results of the measurements performed to evaluate the real performance of the system are discussed and finally, the conclusions are drawn.

II

II. Attitude Estimation Method

The proposed scheme to retrieve the attitude of an object is based on a uniform array of N RFID tags and, at least, one antenna. As previously stated, this work focuses on flat tags arrays. In particular, ULA and UCA topologies are considered enabling to estimate either only azimuth (α) or azimuth and elevation (β), respectively. Roll estimation is not considered as it would require the use of a 3D array. An example of this scheme for an ULA of $N = 3$ and an UCA of $N = 8$ tags is depicted in Fig. 1a and Fig. 1b, respectively.

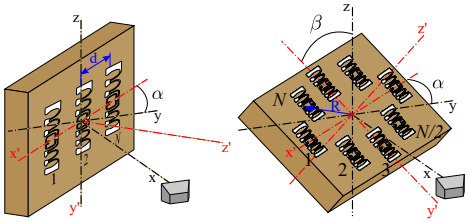

(a) (b)

Figure 1. Scheme of the proposed setup to retrieve the attitude of an object using an ULA of $N = 3$ tags (a), and using an UCA of $N = 8$ tags (b).

In order to define the attitude estimation, it is necessary to define a global coordinate system (GCS) whose coordinates are denoted as x, y and z. Without loss of generality, the center of the array will be considered the origin of the GCS and the transmitter antenna will be placed at the x-axis ($\vec{r}_{ant} = (x_{ant}, 0, 0)$) and pointed towards the origin of the GCS. In addition, an array coordinate system (ACS), denoted by the primed coordinates x', y', z', is also defined. The array plane, i.e., where the RFID tags are placed, lies on the *x'-y' plane* and the *z'-axis* points outwards. Hence, when both the azimuth and elevation are zero ($\alpha = 0°$and $\beta = 0°$) the axes of the ACS can be identified with those of the GCS as follows: $x' = -y$, $y' = -z$ and $z' = x$. The ACS can be aligned with the GCS performing one rotation in azimuth in the ULA case and two sequential rotations (first in azimuth and then in elevation) in the UCA case. Therefore, the azimuth angle is the angle between the y-axis of the GCS and the *-x'-axis* of the ACS; in the case of using an UCA, the elevation angle is the angle between the *z-axis* of the GCS and the *-y'-axis* of the ACS.

The goal of the attitude estimation is to find the rotation angle or pair of angles, which enables to translate the coordinates from the GCS to the ACS. The attitude estimation method relies on phase measurements of the signals backscattered by the tags, which are used to estimate the direction of arrival of the RFID signals impinging into the array and, afterwards, to compute the aforementioned rotation angles defined in Fig. 1. The direction of arrival of the signals of the RFID reader is given by the angles ϕ, measured counterclockwise from the *x'-axis* in the *x'-y' plane*, and θ, which is the polar angle measured from the *z'-axis*. As it will be shown later, these angles are univoquely related to the rotation angles α and β.

In order to estimate the direction of arrival the MUSIC algorithm is used. The general model of the input data, $\mathbf{y} = [y_1 \dots y_N]$, for an array of N elements and a single impinging signal is

$$\begin{bmatrix} y_1 \\ \vdots \\ y_N \end{bmatrix} = \boldsymbol{a}(\theta, \phi)s + \mathbf{n} \quad , \tag{1}$$

where s is the incident signal to the array transmitted by the reader, $\mathbf{n}$ is a vector modeling the noise at each tag and $\boldsymbol{a}(\theta, \phi)$ is the array steering vector of the incident signal, which has direction of arrival (θ, ϕ). The expression of $\boldsymbol{a}(\theta, \phi)$ will be particularized in the next two subsections for the ULA and the UCA case. The direction of arrival of the impinging signals can be obtained from the peak of the MUSIC pseudospectrum, whose expression is

$$P_{MUSIC}(\theta, \phi) = \frac{1}{\boldsymbol{a}(\theta, \phi)^H \boldsymbol{V_N} \boldsymbol{V_N^H} \boldsymbol{a}(\theta, \phi)}, \tag{2}$$

where $\boldsymbol{V_N}$ is the matrix which contains the eigenvectors of the noise subspace. In Fig. 2a the pseudospectrum computed for an ULA of $N = 5$ tags, $d = \lambda/8$ and $\alpha = -40°$ is depicted whilst in Fig. 2b the pseudospectrum (in 2D) obtained with an UCA of $N = 8$ tags, $R = 12\,\text{cm}$, $\beta = -50°$ and $\alpha = 30°$ is shown. As can be seen in Fig. 2, the attitude of an array of passive RFID tags can be inferred from the peak of the pseudospectrum.

Finally, the azimuth and elevation angles can be computed, respectively, from the estimated direction of arrival with the following equations:

$$\alpha = \arcsin(\sin(\theta)\cos(\phi)), \tag{3}$$

$$\beta = \arctan(\tan(\theta)\sin(\phi)). \tag{4}$$

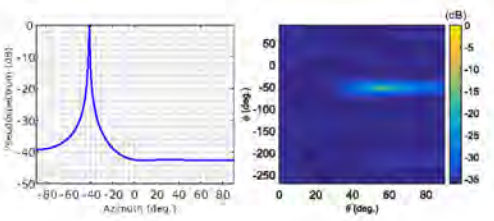

(a) (b)

Figure 2. MUSIC 1D pseudospectrum obtained with an ULA of $N = 5$ tags, $d = \lambda/8$ and $\alpha = -40°$, (a), and MUSIC 2D pseudospectrum obtained with an UCA of $N = 8$ tags, $R = 12$ cm, $\beta = -50°$ and $\alpha = 30°$, (b).

It must be pointed out that the angles are restricted to the ranges $\alpha \in [-90°, 90°]$ and $\beta \in [-90°, 90°]$ (in the UCA case) and, consequently, the signals never imping the array from the back. Otherwise, an ambiguity would happen and it could only be resolved by resorting to additional arrays or readers. To obtain equations 3 and 4, first, the expression of the axes of the ACS in terms of the GCS axes, α and β was derived:

$$x' = -\boldsymbol{R}(\alpha, \beta) \cdot y, \tag{5}$$

$$y' = -\boldsymbol{R}(\alpha, \beta) \cdot z, \tag{6}$$

$$z' = \boldsymbol{R}(\alpha, \beta) \cdot x, \tag{7}$$

where

$$\boldsymbol{R}(\alpha,\beta) = \boldsymbol{R}_a(\alpha)\boldsymbol{R}_e(\beta) = \begin{pmatrix} \cos(\alpha) & -\sin(\alpha) & 0 \\ \sin(\alpha) & \cos(\alpha) & 0 \\ 0 & 0 & 1 \end{pmatrix} \begin{pmatrix} \cos(\beta) & 0 & \sin(\beta) \\ 0 & 1 & 0 \\ -\sin(\beta) & 0 & \cos(\beta) \end{pmatrix}, \tag{8}$$

is the rotation matrix to perform two sequential rotations (first in azimuth, $\boldsymbol{R}_a(\alpha)$, and then in elevation, $\boldsymbol{R}_e(\beta)$). Second, taking into account that the direction of arrival of the signals is always the *x-axis*, the *x-axis* was expressed in terms of the axes of the ACS in the GCS coordinates, α and β (Eq. 5, 6 and 7). Then, the coordinates of *x-axis* in the ACS were identified with the direction of arrival in terms of θ and ϕ (Eq. 9, 10 and 11).

$$\sin(\alpha) = \cos(\phi)\sin(\theta), \tag{9}$$

$$\cos(\alpha)\sin(\beta) = \sin(\phi)\sin(\theta), \tag{10}$$

$$\cos(\alpha)\cos(\beta) = \cos(\theta). \tag{11}$$

A. Uniform Linear Array

As previously stated, the ULA can only estimate azimuth rotations and, therefore, it is assumed that the array can only rotate along z-axis. This is a common situation as when a box or a pallet are stored, they are usually placed upwards but they may be rotated. Therefore, $\beta = 0°$, $\phi = 0°$ and $\alpha = \theta$. Hence, considering far field conditions and taking into account the round-trip of the signals, the phase difference between two consecutive tags is given by

$$\Delta\varphi = 2\frac{2\pi}{\lambda} d \sin(\alpha) \quad , \tag{12}$$

where λ is the wavelength of the signal and d is the spacing between elements (see Fig. 1a). Consequently, the maximum unambiguous inter element separation is $\lambda/4$ and the expression of the array steering vectors, considering the first element as reference, can be particularized to

$$\boldsymbol{a}(\alpha) = \begin{bmatrix} 1 & \dots & e^{-j\frac{4\pi}{\lambda}d\sin(\alpha)(N-1)} \end{bmatrix} \quad . \tag{13}$$

It is important to note that, in contrast to standard MUSIC, a 2 factor has been included in the exponent to account for the round-trip of the backscattered signals [19].

B. Uniform Circular Array

In the case of an UCA, the array steering vector of the incident signal, which has direction of arrival (θ, ϕ) can be particularized to

$$\boldsymbol{a}(\theta,\phi) = \begin{bmatrix} e^{-2jkR\cos(\phi-\gamma_1)\sin(\theta)} \\ \vdots \\ e^{-2jkR\cos(\phi-\gamma_N)\sin(\theta)} \end{bmatrix}, \tag{14}$$

where k is the wavenumber and γ_n is the angle of the n-th element of the array measured counterclockwise from the *x'-axis*, and R is the radius of the array. This expression of the steering vectors corresponds to the traditional equation for a standard angle of arrival problem [20], but again a factor of 2 has been introduced in the exponent due to the round-trip of the backscattered signal. As a consequence, the maximum element spacing given in [18] for planar arrays must be reduced to $\lambda/4$.

It is relevant to notice that the positions of the elements of the array have origin symmetry. Therefore, if the number of elements is even, the value of $\gamma_{n+N/2}$ can be expressed in terms of γ_n as follows [20]:

$$\gamma_{n+N/2} = \frac{2\pi}{N}\left(\frac{N}{2} + n - 1\right) = \gamma_n + \pi, \tag{15}$$

and thus, if the phase of the impinging signal at the origin of coordinates is zero, the steering vector of the n-th element is the conjugate of the steering vector of the $n+N/2$-th element:

$$a_n(\theta,\phi) = a^*_{n+N/2}(\theta,\phi). \tag{16}$$

II

As a consequence, if an RFID tag of the array is not read but its opposite element is, it would be possible to estimate the phase of the missing backscattered signal:

$$\angle a_n(\theta,\phi) = -\angle a_{n+N/2}(\theta,\phi). \quad (17)$$

This increases the robustness of the proposed system. However, in practice, the read phase does not correspond to a wave with zero phase at the origin of coordinates and, consequently, there is a phase offset, γ, due to the distance between the antenna and the center of the array, so that the phasor diagram of the backscattered signals is rotated as depicted in Fig. 3.

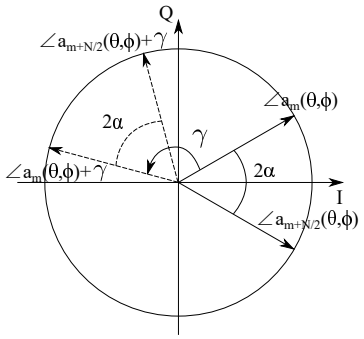

Figure 3. Phasor diagram of the signals backscattered by two opposite RFID tags of the array and its rotated version.

Hence, to enable the estimation of the phase of missing backscattered signals, the value of the phase offset must be computed. This can be done solving the following system of equations as long as, at least, a pair of opposite RFID tags is read. As it can be inferred, the more pairs are read, the more accurate is the estimation of γ.

$$\angle a_n(\theta,\phi) + \angle a_{n+N/2}(\theta,\phi) - \gamma = 0 \quad n = 1 \ldots \frac{N}{2}. \quad (18)$$

III. Numerical Results

In order to evaluate the performance of the proposed method several simulations were conducted. Specifically, the effect of errors in the position of the elements of the array, both the ULA and the UCA, was assesed to test the robustness of the method. Also, the impact of discrepancies between the expected and the actual radius of the UCA is analysed. An analogous analysis was performed for the ULA case taking into account the differences between the expected and the actual element spacing. However, the results of this last study are not reported here as they were presented in [14]. All these simulations, whose results are reported in Sections III-A and III-B, were performed using MatLab software and using a frequency in the European RFID band: $f = 866.3\,\text{MHz}$. In these simulations, the phase of the received field was set to be proportional to the round-trip distance from the reader to the tag. The obtained phase was introduced in (2) to compute the tilts. In addition, the effect of the couplings and the electromagnetic properties of the surface below the tags was evaluated by means of simulations using the software Feko. The obtained results are discussed in Section III-C.

A. Uniform Linear Array

The effect of misplacement of tags in an ULA was evaluated through several simulations. The simulated azimuth ranged from $-70°$ to $70°$ with steps of $10°$. For every azimuth angle each simulation was repeated 50 times. Also, the number of elements of the simulated ULA was $N = 5$, the element spacing was set to $\lambda/8$ and the signal to noise ratio (SNR) for the simulations was set to $20\,\text{dB}$. The choice of an element spacing of $\lambda/8$ instead of the maximum value to avoid unambiguities, $\lambda/4$, was made to try to thoroughly replicate the measurement setup of Section IV-A, in which the element spacing was reduced to overcome the phase ambiguity introduced by the RFID reader as will be explained. The positioning errors in each direction of the array plane were generated randomly using a uniform distribution defined in the interval $[-a, a]$, where the value of a (the maximum possible value of the error) was modified from 0 (without positioning errors) to $5\,\text{cm}$. The error of the estimated azimuth for each value of a is depicted with blue asterisks in Fig. 4. As it can be seen, for approximately $a < 1.5\,\text{cm}$ the error is below $5°$ (below the green line).

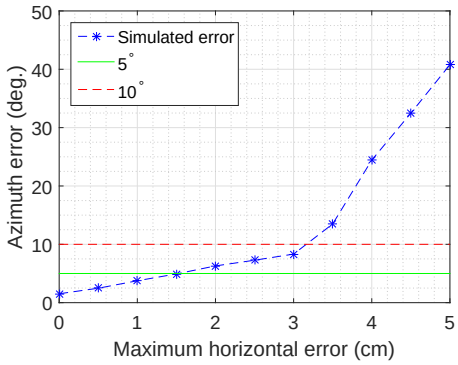

Figure 4. Retrieved azimuth error for $\alpha \in [-70, 70]$ with an ULA of $N = 5$ for different positioning errors (blue asterisks).

B. Uniform Circular Array

1) Effect of discrepancies between the theoretical radius and the real one: Several simulations were carried out in order to see how errors on the array radius affect the performance of the system. The obtained results are shown in Fig. 5, where the estimated azimuth and elevation are depicted when: i) the theoretical value of the radius is equal to its real value (blue asterisks); ii) the expected value is bigger than its real value (red circles); and iii) the expected value is smaller than the real one (black "x"). As it can be seen, when the expected

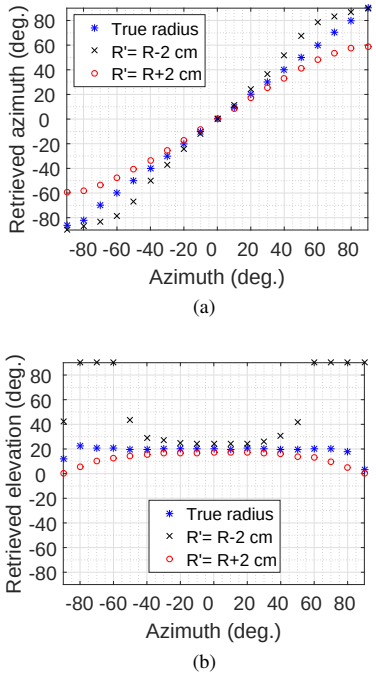

Figure 5. Retrieved azimuth, (a), and elevation, (b), for $\alpha \in [-90, 90]$ with 10° steps and $\beta = 20^\circ$ when the expected radius of the UCA was equal to its real value (blue asterisks), smaller than expected (red circles) or greater (black "x").

radius is smaller than the real value the absolute estimated azimuth values are larger than the real ones and the same happens to the estimated elevation values. It should be noted that the difference between estimated and real attitude values are greater as the azimuth of the UCA is increased. Also, the discrepancies between the retrieved elevation values and the real values increase as the true elevation angle is larger. When the expected radius is greater than the real one, as opposed to the previous case, the absolute estimated attitude values are smaller than the real ones. This behaviour is similar to the one reported in [14] for errors in the expected element spacing in ULAs.

2) Effect of positioning errors of the RFID tags: This subsection evaluates the effect on the performance of the system of slightly misplaced RFID tags due to the array manufacturing process. The simulated attitude covered the interval $[-70^\circ, 70^\circ]$ in azimuth and $[-70^\circ, 70^\circ]$ in elevation with steps of 10°. For every pair of attitude angles, each simulation was repeated 20 times. Also, the number of elements of the simulated UCA was $N = 8$ and the signal to noise ratio (SNR) for the simulations was set to 20 dB. As in subsection III-A, the positioning errors in each direction of the array plane were generated randomly using a uniform distribution defined in the interval $[-a, a]$, where the value of a (the maximum possible value of the error) was modified from 0 (without positioning errors) to 5 cm. The error of the estimated azimuth and elevation for each value of a is depicted in Fig. 6a and Fig. 6b respectively. The green line encloses the area where the error of the estimated attitude is below 5° and the red dashed line encloses the area where the error is below 10°. By analysing the results of the simulations, the error in both azimuth (Fig. 6a) and elevation (Fig. 6b) is below 5° when $a < 6$ mm.

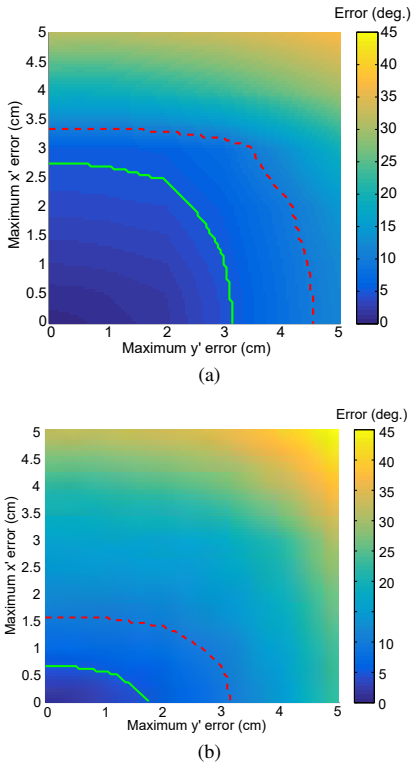

Figure 6. RMS error of the retrieved azimuth, (a), and the retrieved elevation, (b), for different values of positioning error of the RFID tags of the UCA in both directions of the array plane. The green line encloses the area where the error is below 5° and the red dashed line encloses the area where the error is below 10°.

C. Effect of couplings and electromagnetic properties of the material under the tags

In order to test the effect of couplings between tags an ULA of *N=5* tags was simulated in Feko for several values of element spacing *d*. The simulated tag model is based on the one proposed in [21]. The simulated azimuth ranged from -70° to 70° and the frequency was set to $f = 866.3$ MHz. To compute the phase of the signals backscattered by a given tag, the activated tag was loaded to the complex conjugate

impedance of the antenna and the rest of the tags of the array were short-circuited [22].

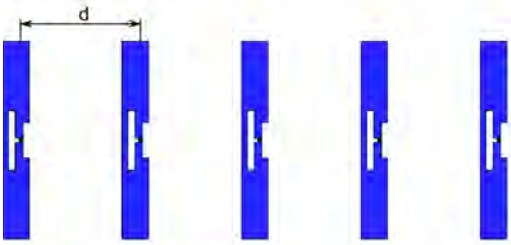

Figure 7. Simulated array of tags.

The obtained results are summarized in Table I, where ϵ_{rms} is the root-mean-square (RMS) error of the estimated azimuth, σ is the standard deviation, Δ is the correction term added to the expected value of the element spacing (d), and $\epsilon_{rms,\Delta}$ and σ_Δ are the RMS error and the standard deviation of the estimated azimuth after the correction respectively. As can be seen, as the distance between elements decreases, i.e, there are more couplings between elements, the RMS error increases. However, after the expected inter element spacing is increased by Δ, the effect of couplings between elements is mitigated. In addition, it must be noted that the simulated tag model is very simple and it was not optimized and, thus, the effect of couplings is expected to be lower in the well-designed commercially available RFID tags.

Table I
RMS ERROR AND STANDARD DEVIATION WITH AND WITHOUT CORRECTION OF THE ESTIMATED AZIMUTH WITH AN ULA OF $N = 5$ TAGS FOR DIFFERENT ELEMENT SPACING.

	ϵ_{rms} (°)	σ (°)	$\epsilon_{rms,\Delta}$ (°)	σ_Δ (°)	Δ(mm)
No coupling	1.3	0.6	—	—	—
$d = \lambda/4$	3.9	1.9	2.0	1.5	3
$d = 3\lambda/16$	7.5	4.4	3.5	2.2	4
$d = 5$ cm	11.0	6.0	5.1	3.5	6
$d = \lambda/8$	15.1	8.9	6.8	4.5	7

The effect of the electromagnetic properties of the material below the array of RFID tags was also tested by adding a substrate of dielectric material underneath the simulated array. The simulated relative permitivities are not very high as the array of tags would be usually placed above cardboard or plastics with low infill percentage. The results are shown in Table II. As can be seen, the higher the permitivity is, the higher the effect of couplings is, which, again, can be compensated after a calibration process.

Table II
RMS ERROR AND STANDARD DEVIATION WITH AND WITHOUT CORRECTION OF THE ESTIMATED AZIMUTH WITH AN ULA OF $N = 5$ TAGS FOR DIFFERENT PERMITIVITY OF THE MATERIAL BELOW THE ARRAY.

	ϵ_{rms} (°)	σ (°)	$\epsilon_{rms,\Delta}$ (°)	σ_Δ (°)	Δ (mm)
$\epsilon_r = 1$	7.5	4.4	3.5	2.2	4
$\epsilon_r = 1.1$	8.2	4.5	4.2	2.9	4.5
$\epsilon_r = 1.2$	9.1	4.8	5.1	4.0	5
$\epsilon_r = 1.4$	11.6	6.1	6.6	5.5	6

IV. Experimental results

Once the performance of the system was characterized by means of simulations, several measurements were performed: first, in a controlled environment and after that, in an indoor scenario. All the measurements were performed with the commercial reader *Speedway Revolution Reader* of *Impinj* [23]. It must be pointed out that this reader randomly introduces an ambiguity of 180° on its phase measurements, i.e, it is not possible to know if the phase value provided by the reader is the true value or that value plus 180°. The phase jumps were corrected with two different approaches (one for the ULA and one for the UCA) as detailed in the following subsections.

A. ULA

The proposed system was tested using an ULA of $N = 5$ RFID tags inside the facilities of the Area of Signal Theory and Communications of the University of Oviedo. The selected tag model was the *Smartrac ShortDipole* RFID Paper Tag with the Monza 5 chip [24] and the antenna was the *WIRA 30* model of *KATHREIN* [25]. The setup is depicted in Fig. 8, where the ULA was attached to a cardboard box. The ULA was placed onto a platform to manually perform azimuth rotations. Finally, the ULA and the transmitter antenna were aligned using a cross-line laser.

Figure 8. Measurement setup in an indoor environment using an ULA.

The measured azimuth covered from $-90°$ to $90°$ with $5°$ steps. Here, in order to overcome the phase ambiguity introduced by the reader, the element spacing was reduced to $\lambda/8$ at the expense of higher couplings between the tags. As a consequence, the maximum phase difference between two consecutive tags was reduced to $90°$ (see Ec. 12), which made possible to find, without ambiguity, the correct combination of phase values as those which produce the highest and narrowest maximum in the visible region of the MUSIC pseudospectrum. Prior to the tests, a calibration stage with the array at $\alpha = 0°$ was performed. In this calibration, the offset of each tag of the ULA was measured. Also, a misalignment of the ULA with respect to the rotation axis of 3 cm in both x-axis and y-axis was corrected. The obtained results are depicted in Fig. 9, where the real azimuth values of the ULA are depicted with blue asterisks, the retrieved azimuth values with $d = \lambda/8$ are shown with black "x" and the retrieved azimuth values,

where the physical element spacing was reduced to 3.4 cm, are presented with red circles.

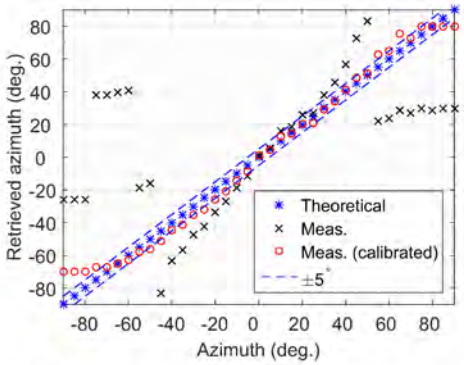

Figure 9. Retrieved azimuth for $\alpha \in [-90, 90]$ without calibration (black "x"), with calibration (red circles) and real values (blue asterisks).

As can be seen, the initial results, where the physical element spacing was $\lambda/8$, show a similar behaviour as the simulations presented in Fig. 2 of [14], where the element separation was greater than expected. Thus, the estimated azimuth is greater than the real values. The greater *effective separation* between tags than the *physical value* was due to the electromagnetic properties of the surface below the tags [24], [26]. However, the results after the calibration of the array, where the physical distance between tags was reduced so that the the *effective* element spacing was $\lambda/8$, show a good performance of the system in a wide angular range (from $-75°$ to $75°$) with maximum error $\epsilon_{\alpha,max} = 10.6°$ and RMS error $\epsilon_{\alpha,rms} = 4.7°$.

B. UCA

The selected RFID tag model for the measurements discussed below was the *Smartrac Dogbone* [27] with the *Monza R6* chip [28] of *Impinj* and the antenna was the *WANTENNAX019* model of *CAEN RFID* [29]. In this case, the phase ambiguity introduced by the reader was solved by calibrating the system at an initial position and attitude and, then, traking the phase values to correct $180°$ increments.

1) Anechoic chamber: The first set of measurements were conducted in the anechoic chamber of the Area of Signal Theory and Communications of the University of Oviedo. The setup is depicted in Fig. 10, were the transmitter antenna was aligned with the center of the UCA by means of a cross-line laser. The RFID tags of the UCA were placed on a piece of cardboard which was attached to a 3D printed plastic support structure. This structure was mounted on a metric goniometer on top of a rotary stage diameter to allow for precise angular adjustment in both azimuth and elevation. The measured attitude ranged from $-90°$ to $90°$ in azimuth and from $-20°$ to $20°$ in elevation. The elevation range was limited by the maximum travel of the goniometer. The UCA had $N = 8$ RFID tags and radius of $R = 12$ cm. The geometry of the UCA was modified in order to minimize couplings between the RFID tags. In particular, the angular separation between RFID tags was not constant in order to increase the distance between tags in the x'-axis.

Figure 10. Measurement setup in the anechoic chamber of the University of Oviedo.

Prior to the measurements, a calibration of the UCA was performed for two reasons: first, to compensate the different offset values of the RFID tags; second, to mitigate the effect of small positioning errors of each of the tags of the array, couplings between tags, and misalignments of the UCA and the transmitter antenna. The calibration, formalized in Eq. 19, consisted of matching the theoretical phase values for each RFID tag to the measured ones for the different attitude values by making small changes in their positions, in their offset and in the value of the radius of the UCA (Fig. 11).

$$\underset{\substack{\vec{r}_{tag,1},\ldots,\vec{r}_{tag,N},\\ \xi_1,\ldots,\xi_N,R}}{\arg\min} \left|\varphi_{th}(\vec{r}_{tag,1},\ldots,\vec{r}_{tag,N},\xi_1,\ldots,\xi_N,R) - \varphi_{meas}\right| \quad (19)$$

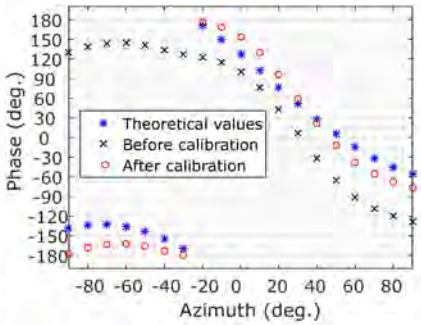

Figure 11. Measured phase of one of the RFID tags of the UCA for $\alpha \in [-90, 90]$ and $\beta = -10°$ before and afer calibrating and theoretical values.

II

The correction terms obtained after the calibration are shown in Table III. Also, the radius was increased 25 mm to compensate the effect described in Section III-B1.

Table III
CORRECTIONS ON THE POSITION OF THE RFID TAGS OF THE UCA OF THE SETUP OF THE ANECHOIC CHAMBER.

Tag #	1	2	3	4	5	6	7	8
z_{corr} (cm)	18	18	18	18	18	18	18	18
y_{corr} (mm)	8	-2	-2	2	6	2	0	-2
Offset (deg.)	-10	-30	-5	-49	-24	-11	-3	1

In Fig. 12 the retrieved azimuth and elevation and the expected values for $\alpha \in [-90, 90]$ with 10° steps and $\beta = 10^\circ$ for two different expected radius values are depicted.

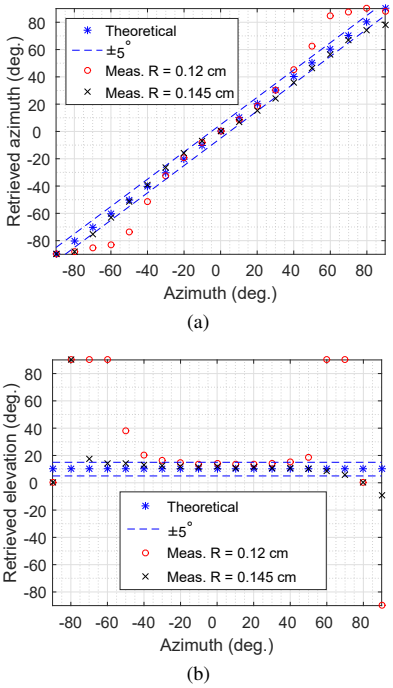

Figure 12. Retrieved azimuth, (a), and elevation, (b), for $\alpha \in [-90, 90]$ with 10° steps and $\beta = 10^\circ$ for $R = 12$ cm (red circles) ans for $R = 14.5$ cm (black "x").

As can be seen, when the expected radius value is increased, the retrieved attitude matches its real value. The difference between the theoretical positions of the UCA elements and the corrected ones are not only due to positioning errors, but also to the electromagnetic properties of the surface below the tags and couplings between them. This effect makes the *effective separation* between tags larger than their *physical value* [27], [26]. It must be pointed out that the correction on the z-axis, z_{corr}, accounts for the vertical displacement of the center of the UCA with respect to the rotation center of the goniometer (the rotation center of the goniometer is only 4.7 cm above its scale and, hence, there are not enough space to place the center of the UCA on the rotation center). The corrections on the *y-axis*, y_{corr}, represent errors on the horizontal positions of the tags.

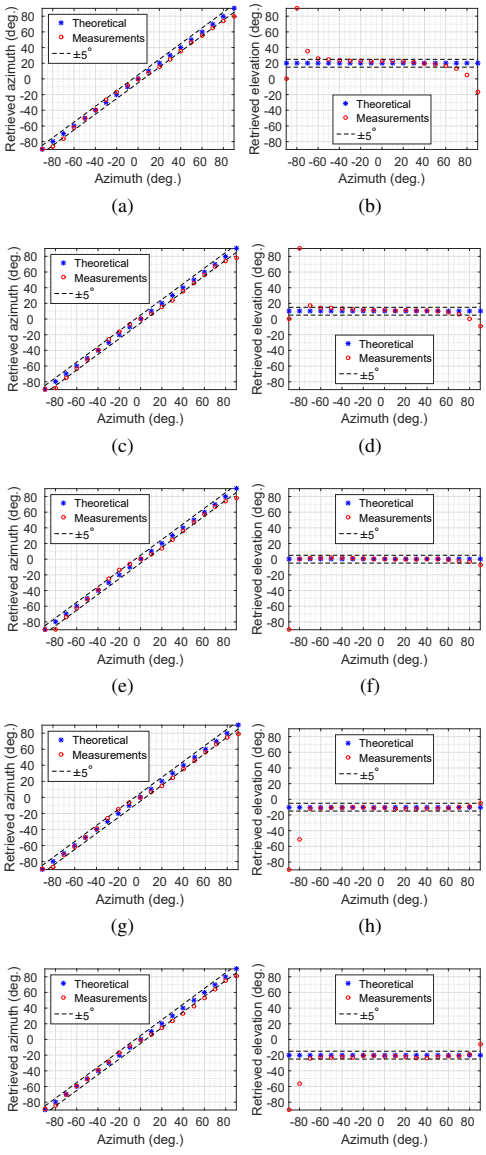

Figure 13. Retrieved azimuth and elevation for $\alpha \in [-90, 90]$ with 10° steps and $\beta = 20^\circ$ (a, b); $\beta = 10^\circ$ (c, d); $\beta = 0^\circ$ (e, f); $\beta = -10^\circ$ (g, h); and $\beta = -20^\circ$, (i, j).

The obtained results after the calibration are depicted in Fig. 13 for 5 cuts in elevation (from $-20°$ to $20°$ in $10°$ steps) and azimuth ranging from $-90°$ to 90 in $10°$ steps. As can be seen, the estimated azimuth values are very accurate even for grazing angles. The error of the retrieved elevation is also low, but in this case the accuracy is degraded for grazing angles. This fact is coherent with the higher error sensitivity for the elevation estimation already observed when analyzing the impact of innacuracies in tag positions in azimuth and elevation estimations as shown in Fig. 6a and Fig. 6b, respectively. The maximum and RMS error, ϵ_{max} and ϵ_{rms} respectively, for both azimuth and elevation for $|\alpha| < 60°$ and $|\alpha| < 70°$ are shown in Table IV. Results show that the system provides an accurate estimation of the attitude of the UCA for a wide angular range in azimuth, $[-60°, 60°]$, and for all the elevation values that was possible to measure, $[-20°, 20°]$.

Table IV
MAXIMUM AND RMS ERROR FOR AZIMUTH AND ELEVATION OF THE ATTITUDE ESTIMATED IN THE ANECHOIC CHAMBER.

	$\epsilon_{\alpha,max}$ (°)	$\epsilon_{\alpha,rms}$ (°)	$\epsilon_{\beta,max}$ (°)	$\epsilon_{\beta,rms}$ (°)
$\|\alpha\| < 60$	7.5	3.8	5.8	2.3
$\|\alpha\| < 70$	7.5	3.9	15.6	3.1

2) Indoor environment: Once the presented system was validated in a controlled environment, its performance was tested in an indoor scenario. The setup, in a corridor in the research facility of the Area of Signal Theory and Communications of the University of Oviedo, is displayed in Fig. 14. As in the setup presented in section IV-B1, the UCA and the transmitter antenna were aligned by means of a cross-line laser. However, in this case the RFID tags of the UCA were placed on a 3D printed plastic plate instead of on a piece of cardboard. The rest of the structure, built to carefully modify the attitude of the UCA, remained the same. During these tests, it was decided to include a reference RFID tag in the center of the UCA to obtain more information without increasing the size of the array. The array was recalibrated as in Section IV-B1 and the obtained values are shown in Table V.

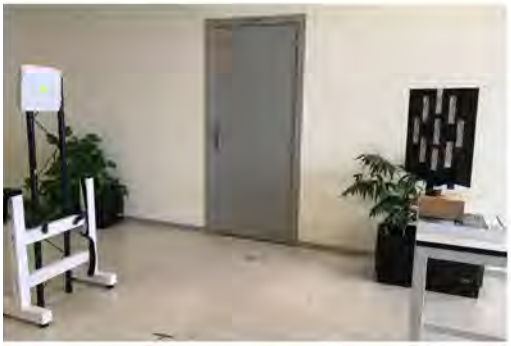

Figure 14. Indoor measurement setup.

The obtained results, discarding the phase measurements of the central tag ($N = 8$) and using all the available data ($N = 9$), are shown in Fig. 15 for 5 cuts in elevation (from $-20°$ to $20°$ in $10°$ steps) and azimuth ranging from $-90°$ to $90°$ in $10°$ steps.

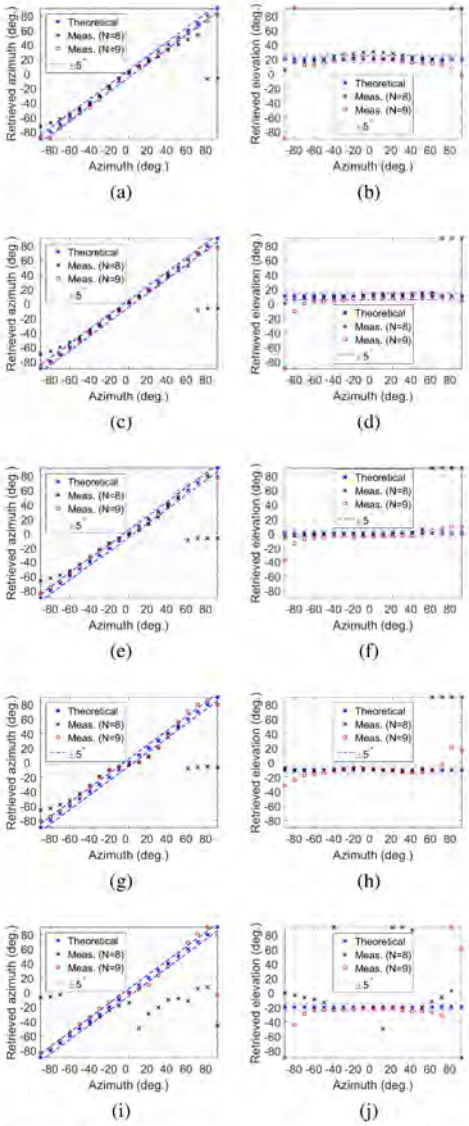

Figure 15. Retrieved azimuth and elevation for $\alpha \in [-90, 90]$ with $10°$ steps and $\beta = 20°$ (a, b); $\beta = 10°$ (c, d); $\beta = 0°$ (e, f); $\beta = -10°$ (g, h); and $\beta = -20°$, (i, j).

As can be seen, although the performance using $N = 8$ tags is good or acceptable for wide attitude range, there are some

II

Table V
CORRECTIONS ON THE POSITION OF THE RFID TAGS OF THE UCA OF THE SETUP OF THE INDOOR SCENARIO.

Tag #	1	2	3	4	5	6	7	8
z_{corr} (cm)	21	21	15	15	20.4	21	21	21
y_{corr} (mm)	23	37	6	33	-8	-4	8	16
Offset (deg.)	55	43	27	62	43	66	77	58

values, specially for $\beta = -20^\circ$, for which the results are very poor. The error values are summarized in Table VI. However, due to the number of outliers in the azimuth estimations, the median error (6.0° for $|\alpha| < 60^\circ$ and 7.0° $|\alpha| < 70^\circ$) and the third quartil (9.5° for $|\alpha| < 60^\circ$ and 11.7° $|\alpha| < 70^\circ$) are more representative than the RMS error this time. As depicted in Fig. 15, the accuracy of the proposed system using a central RFID tag is significantly improved, specially in elevation estimations, as shown in Table VII, where the error values are summarized. The error values are below 10° in a wide range of attitude values and without increasing the size of the array.

Table VI
MAXIMUM AND RMS ERROR FOR AZIMUTH AND ELEVATION OF THE ATTITUDE ESTIMATED IN THE INDOOR SCENARIO WITH $N = 8$.

	$\epsilon_{\alpha,max}$ ($^\circ$)	$\epsilon_{\alpha,rms}$ ($^\circ$)	$\epsilon_{\beta,max}$ ($^\circ$)	$\epsilon_{\beta,rms}$ ($^\circ$)
$\|\alpha\| < 60$	71.7	24.5	110.0	36.8
$\|\alpha\| < 70$	79.0	29.8	110.0	38.8

Table VII
MAXIMUM AND RMS ERROR FOR AZIMUTH AND ELEVATION OF THE ATTITUDE ESTIMATED IN THE INDOOR SCENARIO WITH $N = 9$.

	$\epsilon_{\alpha,max}$ ($^\circ$)	$\epsilon_{\alpha,rms}$ ($^\circ$)	$\epsilon_{\beta,max}$ ($^\circ$)	$\epsilon_{\beta,rms}$ ($^\circ$)
$\|\alpha\| < 60$	9.9	5.0	8.9	3.7
$\|\alpha\| < 70$	11.2	5.1	11.8	4.6

V. CONCLUSIONS

In this contribution a novel method to compute the attitude of objects based on phase measurements of RFID passive tags of uniform arrays is presented. Two array topologies were studied: ULAs and UCAs. With the former, azimuth estimations can be obtained whereas with the latter, both azimuth and elevation can be retrieved. In order to evaluate the performance of the proposed method several simulations and measurements were carried out.

The simulations focused on how positioning errors of each of the elements of the array and discrepancies between the expected dimensions of the array and the real ones affect the performance of the system. In the ULA case it was shown that the accuracy of the system was below 5° for uniformly distributed errors up to $1.5\,$cm. In the UCA case it was shown that both azimuth and elevation errors were below 5° for uniformly distributed errors up to $0.6\,$cm, being the estimated elevation more sensitive to positioning errors than the retrieved azimuth. In addition, it was shown that having an UCA radius greater than expected results in greater retrieved azimuth and elevation than the real attitude of the array.

The system with an ULA of $N = 5$ RFID tags was tested in an indoor environment. The obtained results show a good performance with an RMS error below 5° for $\alpha \in [-75^\circ, 75^\circ]$ after the array calibration. For greater azimuth values the accuracy of the system decreases, although in those cases the signals imping the array at grazing angles.

In addition, the proposed method was tested for 2D attitude retrieval with an UCA of $N = 8$ tags and also with a reference tag in the center of the array. Results show a good performance of the system in both an anechoic chamber and an indoor scenario. As in the case of the ULA, it should be remarked that the calibration is critical to ensure a good accuracy on the attitude estimations. Concerning this, the corrections regarding couplings between tags can be done in advance taking into account the selected tag models. Thus, it would only be necessary to measure the offset of the given tags of the array before deploying it. The use of a reference tag improves the performance of the system achieving an RMS error close to 5° for azimuth estimations and below 5° for the retrieved elevation in a range of $\beta \in [-20^\circ, 20^\circ]$ and $\alpha \in [-70^\circ, 70^\circ]$.

REFERENCES

[1] K. Michael and L. McCathie, "The pros and cons of RFID in supply chain management," in *Int. Conf. Mobile Business (ICMB'05)*, July 2005, pp. 623–629.
[2] X. Chen, L. Xie, C. Wang, and S. Lu, "Adaptive accurate indoor-localization using passive RFID," in *Proc. IEEE Int. Conf. Parallel Distrib. Syst. (ICPADS)*, 2013, pp. 249–256.
[3] S. Shao and R. J. Burkholder, "Item-level RFID tag location sensing utilizing reader antenna spatial diversity," *IEEE Sensors J.*, vol. 13, no. 10, pp. 3767–3774, Oct. 2013.
[4] Y. Alvarez, M. E. D. Cos, and F. Las-Heras, "A received signal strength RFID-based indoor location system," *Sens. Actuators A Phys.*, vol. 255, pp. 118–133, mar 2017.
[5] P. V. Nikitin, R. Martinez, S. Ramamurthy, H. Leland, G. Spiess, and K. V. S. Rao, "Phase based spatial identification of UHF RFID tags," in *2010 IEEE Int. Conf. on RFID*, 2010, pp. 102–109.
[6] S. Azzouzi, M. Cremer, U. Dettmar, T. Knie, and R. Kronberger, "Improved aoa based localization of UHF RFID tags using spatial diversity," in *Proc. IEEE Int. Conf. RFID-Technol. Appl. (RFID-TA)*, 2011, pp. 174–180.
[7] M. Scherhäufl, M. Pichler, and A. Stelzer, "UHF RFID localization based on evaluation of backscattered tag signals," *IEEE Trans. on Instrum. Meas.*, vol. 64, no. 11, pp. 2889–2899, Nov. 2015.
[8] J. Huiting, H. Flisijn, A. B. J. Kokkeler, and G. J. M. Smit, "Exploiting phase measurements of EPC Gen2 RFID tags," in *Proc. IEEE Int. Conf. RFID-Technol. Appl. (RFID-TA)*, 2013, pp. 1–6.
[9] M. Scherhäufl, M. Pichler, and A. Stelzer, "Robust localization of passive UHF RFID tag arrays based on phase-difference-of-arrival evaluation," in *2015 IEEE Topical Conf. Wireless Sensors and Sensor Netw. (WiSNet)*, Jan 2015, pp. 47–49.
[10] A. Buffi and P. Nepa, "The SARFID technique for discriminating tagged items moving through a UHF-RFID gate," *IEEE Sensors Journal*, vol. 17, no. 9, pp. 2863–2870, may 2017.
[11] GS1. (2016, 11) EPC radio-frequency identity protocols generation-2 UHF RFID. [Online]. Available: http://www.gs1.org/sites/default/files/docs/epc/Gen2_Protocol_Standard.pdf
[12] F. Inui, "RF tag, RF tag attitude detection apparatus, and RF tag attitude detection system," U.S. Patent 20 050 225 451, Apr. 7, 2004.
[13] C. Rennie, R. Shome, K. E. Bekris, and A. F. D. Souza, "A dataset for improved rgbd-based object detection and pose estimation for warehouse pick-and-place," *IEEE Robot. and Autom. Lett.*, vol. 1, no. 2, pp. 1179–1185, July 2016.
[14] G. A. Narciandi, J. Laviada, and F. Las-Heras, "Object attitude estimation using passive RFID tag arrays," in *2016 URSI Int. Symp. Electromagn. Theory (EMTS)*, Aug 2016, pp. 572–574.
[15] R. O. Schmidt, "Multiple emitter location and signal parameter estimation," *IEEE Trans. Antennas Propag.*, vol. 34, no. 3, pp. 276–280, Mar. 1986.

[16] Z. Ye and C. Liu, "2-D DOA estimation in the presence of mutual coupling," *IEEE Trans. Antennas Propag.*, vol. 56, no. 10, pp. 3150–3158, Oct 2008.
[17] A. Ferreol, P. Larzabal, and M. Viberg, "On the asymptotic performance analysis of subspace DOA estimation in the presence of modeling errors: case of MUSIC," *IEEE Trans. Signal Process.*, vol. 54, no. 3, pp. 907–920, March 2006.
[18] L. C. Godara and A. Cantoni, "Uniqueness and linear independence of steering vectors in array space," *J. Acoust. Soc. Am.*, vol. 70, pp. 467–475, 1981.
[19] G. A. Narciandi, J. Laviada, M. R. Pino, and F. Las-Heras, "Application of MUSIC algorithm to the estimation of objects attitude," in *Int. Conf. Electromagn. Adv. Appl. (ICEAA)*, 2017.
[20] Y. Wu and H. C. So, "Simple and accurate two-dimensional angle estimation for a single source with uniform circular array," *IEEE Antennas Wireless Propag. Lett.*, vol. 7, pp. 78–80, 2008.
[21] Y. Ziyuan, H. Xiaoxiang, Y. Yang, and T. Liu, "UHF RFID tag antenna performance on various dielectric-background," in *2016 IEEE International Workshop on Electromagnetics: Applications and Student Innovation Competition (iWEM)*, May 2016, pp. 1–3.
[22] P. V. Nikitin and K. V. S. Rao, "Theory and measurement of backscattering from rfid tags," *IEEE Antennas and Propagation Magazine*, vol. 48, no. 6, pp. 212–218, Dec 2006.
[23] Imping. (2016, 10) Imping low level user data. [Online]. Available: https://support.impinj.com/hc/en-us/articles/202755318-ApplicationNote-Low-Level-User-Data-Support
[24] Smartrac Technology Gmbh. (2016, 10) Smartrack shortdipole RFID paper tag with Monza 5 chip. [Online]. Available: https://www.smartrac-group.com/files/content/Products_Services/PDF/0018_SMARTRAC_SHORTDIPOLE.pdf
[25] KATHREIN Solutions Gmbh. (2017, 8) Wira 30 antenna unit. [Online]. Available: https://www.kathrein-solutions.com/files/52010086_52010087_wira_30_93636225c.pdf
[26] M. Kanesan, D. V. Thiel, and S. G. O'Keefe, "The effect of lossy dielectric objects on a UHF RFID meander line antenna," in *Proc. 2012 IEEE Int. Symp. Antennas and Propag.*, July 2012, pp. 1–2.
[27] Smartrac Technology Gmbh. (2017, 6) Smartrac dogbone monza r6 rfid tag. [Online]. Available: https://www.smartrac-group.com/files/content/Products_Services/PDF/0028_SMARTRAC_DOGBONE.pdf
[28] Impinj. (2017, 6) Chip monza r6. [Online]. Available: https://support.impinj.com/hc/en-us/articles/202765328-Monza-R6-Product-Datasheet
[29] CAEN RFID. (2017, 8) Wantennax019 antenna. [Online]. Available: https://www.caenrfid.com/en/products/wantennax019/

Guillermo Alvarez-Narciandi Guillermo Alvarez-Narciandi received the M.Sc. degree in Telecommunication Engineering from the University of Oviedo, Gijón, Spain, in 2016, where he is currently working toward the Ph.D. degree (with the support of a FPU grant from the Spanish Government). He was a Visiting Student at Stanford University, CA, USA, in 2014. He received the Special Award to the Best Entrepreneurship Initiative in the XV Arquímedes national contest in 2017 for the development of a RFID-based location system. He received the 2015 EPIGIJON Industrial Partners Society Award to the Best Applied Project for the development and testing of a hybrid RSS-inertial Indoor Positioning System. He has co-authored a patent on attitude estimation using RFID technology. His main research interests are location systems, attitude estimation systems, RFID technology and imaging techniques.

Jaime Laviada Jaime Laviada was born in Gijón, Spain. He received the M.S. degree in telecommunication engineering and the Ph.D. degree from the Universidad de Oviedo, Spain (http://www.uniovi.es), in 2005 and 2010, respectively. In 2006, he joined the research group Signal Theory and Communications of the Universidad de Oviedo, where he has been involved in multiple national and European projects as well as contracts with several companies. In 2015, he moved to the Antennas Group of the Universidad Pública de Navarra with a national postdoctoral fellowship collaborating in several applied research projects. Finally, he moved back to the Universidad de Oviedo where he currently holds a position as assistant professor. In addition, he has been a Visiting Scholar in the Electromagnetics and Communications Lab, Pennsylvania State University, during 2007 and 2008 as well as in the Applied Microwave NonDestructive Testing Laboratory, Missouri S&T, during 2017.

His research interests include numerical techniques applied to electromagnetic imaging, antenna measurements, method of moments, and antenna pattern synthesis.

Marcos R. Pino Marcos R. Pino was born in Vigo, Spain, in 1972. He received the M.Sc. and Ph.D. degrees in telecommunication engineering from the University of Vigo, Spain, in 1997 and 2000, respectively.

In 1998, he was a Visiting Scholar at the ElectroScience Laboratory, The Ohio-State University, Columbus, OH, USA. From 2000 to 2001, he was with the University of Vigo as Assistant Professor. Since 2001, he has been with the Electrical Engineering Department, University of Oviedo, Spain, where he is currently Associate Professor teaching courses on communication systems and antenna design.

His research interests include antenna design for different applications (RFID, satellite broadcasting, . . .), both near-field and far-field measurement techniques and facilities, efficient computational techniques applied to solve EM problems, such as evaluation of radar cross section or EM scattering from targets in the presence of rough surfaces.

Fernando Las-Heras Fernando Las-Heras (M'86, SM'08) received the M.S. in 1987 and the Ph.D. in 1990, both in Telecommunication Engineering, from the Technical University of Madrid (UPM). He was a National Graduate Research Fellow (1988-1990) and he held a position of Associate Professor at the Department of Signal, Systems and Radiocommunications of the UPM (1991-2000). From December 2003 he holds a Full-Professor position at the University of Oviedo where he was the Vice-dean for Telecommunication Engineering at the Technical School of Engineering at Gijón (2004-2008). As of 2001 he heads the research group Signal Theory and Communications TSC-UNIOVI at the Dept. of Electrical Engineering of the University of Oviedo. He was a Visiting Lecturer at the National University of Engineering in Peru in 1996, a Visiting Researcher at Syracuse University, New York, in 2000, and a short term Visiting Lecturer at ESIGELEC in France from 2005 to 2011. He held the Telefónica Chair on "RF Technologies", "ICTs applied to Environment" and "ICTs and Smartcities" at the University of Oviedo (2005-2015). Member of the board of directors of the IEEE Spain Section (2012-2015), member of the board IEEE Microwaves & Antennas Propagation Chapter (AP03/MTT17) (2016-2017), member of the Science, Technology and Innovation Council of Asturias (2010), and president of the professional association of Telecommunication Engineers at Asturias. He has led and participated in a great number of research projects and has authored over 190 technical journal papers, mainly in the areas of antennas, propagation, metamaterials and inverse problems with application to antenna measurement (NF-FF, diagnostics and holography), electromagnetic imaging (security and NDT) and localization, developing computational electromagnetics algorithms and technology on microwaves, millimeter wave and THz frequency bands.

II

Publication III

G. Álvarez-Narciandi, A. Motroni, M. R. Pino, A. Buffi and P. Nepa, "A UHF-RFID gate control system based on a Recurrent Neural Network," *IEEE Antennas and Wireless Propagation Letters,* vol. 18, no. 11, pp. 2330–2334, Nov. 2019.

III

A UHF-RFID gate control system based on a Recurrent Neural Network

Guillermo Alvarez-Narciandi, Andrea Motroni, Marcos R. Pino, Alice Buffi and Paolo Nepa

III

***Abstract*—This paper presents a novel, cost-effective and easy-to-deploy solution to discriminate the direction of goods crossing a UHF-RFID gate in warehouse scenario. The system is based on a grid of UHF-RFID tags deployed on the floor underneath the gate equipped with a single reader antenna. When a transpallet crosses the gate, it shadows the tags of the deployed grid differently, according to the specific direction, namely incoming or outgoing. Such distinguishable signature is employed as input of a recurrent neural network. In particular, the number of readings for each tag is aggregated within short time-windows and a sequence of binary read/missed tag data over the time is extracted. Such temporal sequences are used to train a Long Short-Term Memory neural network. Classification performance of the proposed method is shown through a set of measurements in indoor scenario.**

***Index Terms*—UHF-RFID Gate; RFID machine learning; RFID neural network; Recurrent neural network.**

I. Introduction

THE use and development of Radio Frequency IDentification (RFID) technology led to a growing number of applications based on it. In 2018 more than 15 billion of RFID tags were sold (a 23% increase with respect to 2017) [1], showing the technology growth. In particular, the RFID technology was successfully used in the context of access control, warehouse management and logistics. One specific problem in warehouse scenario is the correct discrimination of goods or pallets transiting through a gate or between two warehouse areas. For such purpose, a UHF-RFID gate can be installed at the points of interest. To correctly discriminate if the pallet is incoming, outgoing or not-crossing the gate, several systems were proposed in the state of the art. Since a warehouse is a harsh environment due to multipath propagation and the presence of a large number of RFID tags, several setups were proposed apart from conventional localization systems [2]. Some solutions rely on creating shielded reading zones using tunnel gates [3] or using additional hardware such as light or motion sensors [4] or cameras [5] to determine the movement direction of goods, at the expense of higher complexity and cost of the system. Moreover, the use of cameras may raise privacy issues. Other solutions employ more than one antenna to estimate the motion direction of the goods by comparing the signature of tagged items measured from each antenna [6] or creating different interrogation zones [7]. Keller et al. [8] suggest to use various aggregated features based on the low-level reader data (Electronic Product Code, *Received Signal Strength Indicator* - RSSI, timestamp, reading antenna) to discriminate moving tags in forklift truck applications, with multiple antennas. Other solutions exploited the phase of the tag backscattered signal to discriminate tags carried out by a forklift [9] or moving along a conveyor belt [10].

Recently, machine learning techniques were employed in RFID systems for localization purposes [11], [12] and for classification of tag actions in UHF-RFID gates [13]. This paper presents a novel solution to discriminate the crossing goods from the not-crossing throughout a UHF-RFID gate in a warehouse scenario. Furthermore, the crossing goods are distinguished between incoming or outgoing. The system employs a Recurrent Neural Network (RNN) exploiting data acquired by a single reader antenna and a grid of UHF-RFID reference tags.

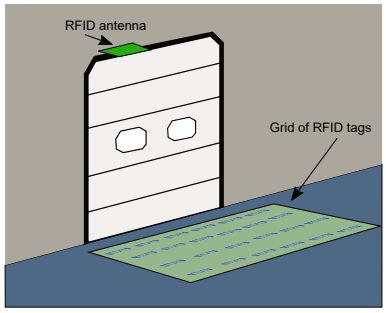

Figure 1. Basic scheme of the UHF-RFID gate control system with a single reader antenna and a grid of reference tags.

II. Classification Method Description

The proposed system for the UHF-RFID gate is based on a grid of reference tags deployed on the floor underneath the gate and a single reader antenna (Figure 1). Therefore, when a transpallet moves over the grid, tags are shadowed due to the

This work has been supported by the Gobierno del Principado de Asturias (PCTI)/FEDER under project IDI/2018/000191; the Ministerio de Educación y Formación Profesional of Spain under the FPU grant FPU15/06431 and EST17/00813, and by the Ministerio de Ciencia, Innovación y Universidades under project ARTEINE (TEC2017-86619-R). This work has also been supported by Region of Tuscany - Regional Government (POR FESR 2014-2020-Line 1-Research and Development Strategic Projects) through the Project IREAD4.0 under Grant CUP 7165.24052017.112000028.

Guillermo Alvarez-Narciandi and Marcos R. Pino are with the Departamento de Ingeniería Eléctrica, Universidad de Oviedo, Spain (e-mail: alvareznguillermo@uniovi.es; mpino@uniovi.es); Andrea Motroni and Paolo Nepa are with the Department of Information Engineering, University of Pisa, Italy (e-mail: andrea.motroni@ing.unipi.it; paolo.nepa@unipi.it); Alice Buffi is with the Department of Energy, Systems, Territory and Constructions Engineering, University of Pisa, Italy (e-mail: alice.buffi@unipi.it).

III

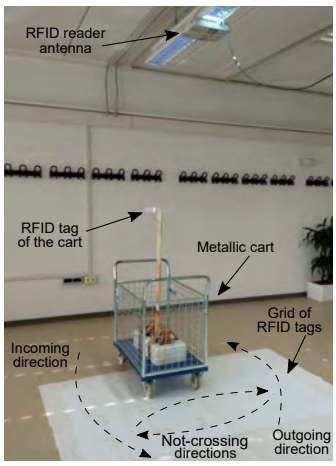

Figure 2. Measurement setup of the proposed system for the UHF-RFID gate.

presence of metallic parts and some of them are not detected by the reader antenna. Thus, the pattern of shadowed tags can be used as a signature of the transpallet incoming, outgoing or not-crossing actions. Such principle resembles the solutions proposed in [14], [15] which are based on the shadowing of the signal backscattered by a set of RFID tags deployed within the area of interest for localization purpose.

An important design consideration is the size of the grid of reference tags. The grid width should be at least similar to the width of the gate to be monitored. In the other dimension, the number of grid rows (i.e. the length of the grid) should be at least three or four, so that the transpallet movement causes a consecutive shadowing of tag rows, which is a useful information for direction discrimination. On the other hand, the number of tags should not grow indefinitely as the reader must be able to detect all of them within a certain time window. In this regard, it should also be considered that other tags will be in the gate surroundings identifying different goods stored in the warehouse. The distance between the reference tags should be large enough to reduce the coupling effect, while ensuring the tag shadowing during the transpallet motion.

A. The Recurrent Neural Network

To perform the transpallet action classification a Recurrent Neural Network (RNN) was trained. This type of neural network was proven to be very successful in sequence processing or sequential processing of non-sequence data [16]. The basic working principle of a RNN is that when there is an input to the network, x_t, it computes the new state, h_t, based on the previous state h_{t-1} and the input according to an activation function f:

$$h_t = f(W_{hh}h_{t-1} + W_{xh}x_t). \tag{1}$$

Then, in sequence-to-one (or sequence labeling) problems (as the problem discussed in this paper) the output is usually computed based on the last state. In the proposed system, we employed a particular kind of RNN, that is the Long Short-Term Memory (LSTM) network [17]. LSTM networks solve the problems of vanishing or exploding gradient, and have shown great performance in speech recognition [18] or image caption generation [19] applications. They have a block structure where each cell has an internal cell state, $\boldsymbol{c}_t$ and a hidden state $\boldsymbol{h}_t$. The above parameters are updated based on the network input $\boldsymbol{x}_t$ at time t, and the previous hidden state, $\boldsymbol{h}_{t-1}$, as follows:

$$\boldsymbol{c}_t = \boldsymbol{f} \circ \boldsymbol{c}_{t-1} + \boldsymbol{i} \circ \boldsymbol{g}, \tag{2}$$

$$\boldsymbol{h}_t = \boldsymbol{o} \circ \tanh(\boldsymbol{c}_t), \tag{3}$$

where $\circ$ denotes the element-wise product. The other parameters are the network input gate $\boldsymbol{i}$ and the cell candidate $\boldsymbol{g}$, which control the input amount which is written into the cell; the forget gate $\boldsymbol{f}$, which controls how much the cell state of the previous time step is forgotten; the output gate $\boldsymbol{o}$, which computes the hidden state of the current time state. These parameters can be calculated throughout the following equation:

$$\begin{pmatrix} \boldsymbol{i} \\ \boldsymbol{f} \\ \boldsymbol{o} \\ \boldsymbol{g} \end{pmatrix} = \begin{pmatrix} \sigma \\ \sigma \\ \sigma \\ \tanh \end{pmatrix} \boldsymbol{W} \begin{pmatrix} \boldsymbol{h}_{t-1} \\ \boldsymbol{x}_t \end{pmatrix}, \tag{4}$$

Where $\boldsymbol{W}$ is the weighting matrix; σ is the sigmoid function, and $tanh$ is the hyperbolic tangent function. The size of the network input, $\boldsymbol{x}_t$, corresponds to the number of input features of the network, N_{feat}. The size is of the hidden state vectors, $\boldsymbol{h}_t$, as well as the size of the internal cell state, $\boldsymbol{c}_t$, $\boldsymbol{i}$, $\boldsymbol{f}$, $\boldsymbol{o}$ and $\boldsymbol{g}$, is given by the number of hidden units (NHU) of the cell, which controls the amount of information remembered between time steps. Finally, the size of the weighting matrix $\boldsymbol{W}$ is $(4 \cdot NHU) \times (N_{feat} + NHU)$.

B. Data Pre-processing

The input features of the neural network should provide representative and distinguishable signatures of each type of movement of the transpallet. In addition, they should be chosen to make the system independent on the application scenario, and to avoid any calibration step to minimize deployment time.

First, it should be noted that, as the existence of moving goods and their direction discrimination are based on the information collected from a set of reference RFID tags, an appropriate acquisition time must be defined. The latter, denoted as t_{win}, must be long enough to query all reference tags. The duration of the time windows should be adjusted so that the transpallet movements can be captured. This means that, if the time window is too long with respect to the transpallet moving speed, some movements could be filtered out. On the other hand, if the time window is too short the reader may not be able to read all the reference tags within the same time window, and the system can misinterpret that phenomenon as a shadowing effect.

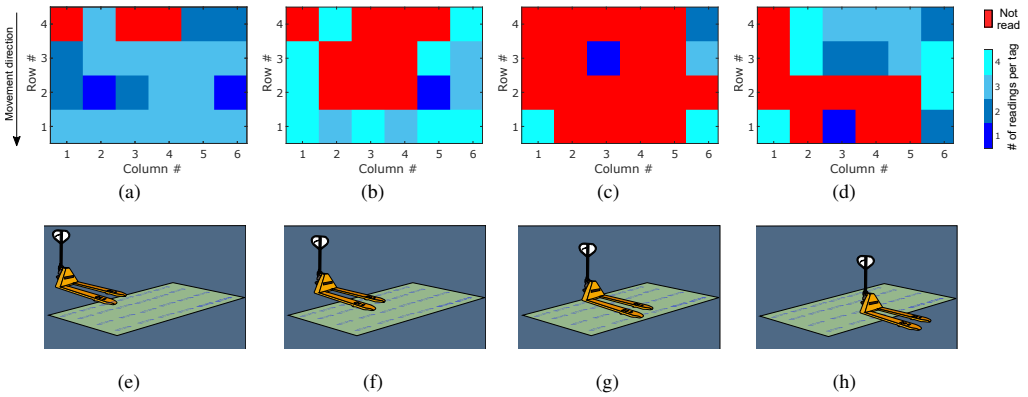

Figure 3. Number of readings of each grid tag during a sample incoming movement of the metallic cart. Consecutive time windows of duration of 200 ms were shown from (a) to (d). Missed tags are depicted in red. A schematic representation of the metallic cart position within the setup corresponding to the snapshots presented from (a) to (d) is shown from (e) to (h), respectively.

The RFID reader is configured to perform continuous inventories and, as explained before, in order to introduce meaningful information to the neural network, the measured data is aggregated within time windows of a predefined duration. As a consequence, when the system is activated (for example when a tagged transpallet is detected in the surroundings of the gate) a set of features are extracted from the measured data in a $N_{feat} \times M$ matrix form. Then, such set feeds the network, where N_{feat} is the number of features and M is the number of time windows within the total acquisition time. Among the potential features, the two parameters described below were considered:

- The number of times each reference tag was read during each time window: in the absence of a moving transpallet the number of readings within each time window should be approximately constant depending on the number of RFID tags present on the surroundings of the gate. However, when a transpallet moves over the grid of reference tags, it shadows the tags underneath and, hence, the number of successful readings decreases. Therefore, a pattern can be extracted from the fluctuations on the number of readings during time windows of each reference tag.
- Whether each reference tag was read or was missed during each time window: this provides a binary information for each tag in each time window. If during a certain time window the tag was detected at least once, then the binary data is set to "read". In a similar fashion to the previously explained feature, if a tag is shadowed by a transpallet, it would not be read in that time window, so being classified as "missed".

Both parameters provide analogous information, as it was observed during the experimental analysis of the system. However, since the number of readings depends on the amount of detected tags in the surroundings of the gate (i.e. tagged stocked goods waiting to be delivered), it was decided to use the binary read/missed tag data, for each tag in a specific time window. The binary data is equal to 1 if the tag is read or equal to 0 if it is undetected.

The use of RSSI values of the signals backscattered by the tags of the grid was discarded as this parameter depends on the distance from the reader antenna to the grid, the material of the floor under the gate grid, and on the multipath effect typical of an indoor scenario.

Thus, the input of the neural network consists of one sequence, i.e. one feature, per reference tag with the read/missed, whose length depends on the duration of the time window and on the transpallet speed during the specific action.

III. Experimental Analysis

In order to validate the proposed system, laboratory tests were conducted at the research facilities of the Department of Information Engineering of the University of Pisa. The measurement setup is depicted in Figure 2. A total of 24 EasyRFID Dogbone tags were arranged in a 4×6 grid with a 30 cm separation between them. The size of the grid was selected so that it could be used to monitor the transpallet motion throughout a gate of width less than 2 m, a typical size for many warehouse and docking area doors. The reader antenna was fixed at the ceiling above the grid at a height of 2.6 m, and a 38 cm wide metallic cart was employed to emulate a transpallet. Then, a total of 159 trajectories were performed while recording data from the tags: 50 incoming, 49 outgoing and 60 passing nearby the grid without crossing the gate. For each test, the reference tags were queried continuously, thus before, during and after the metallic cart moved over the grid. This resembles the practical operation of the proposed system, ensuring that fluctuations in the tag readings are recorded. Each acquisition was around $T = 10\ s$ long, so the value $M = \lfloor T/t_{win} \rfloor$ ranged from $M = 50$ when $t_{win} = 200\ ms$ to $M = 12$ when $t_{win} = 800\ ms$. The obtained results were used to build a data set to train and test the neural network. The train and test data sets were built using 60% and 40% of the data respectively. The different measurements were randomly assigned to each group, but keeping the class

III

balance, i.e. similar proportion of incoming, outgoing or not-crossing trajectories.

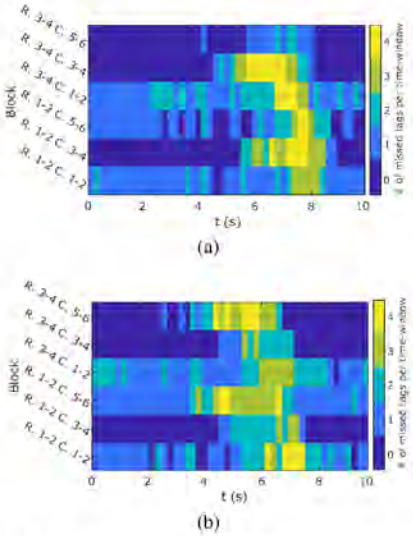

Figure 4. Number of missed tags clustered in groups of 2×2 tags, for (a) an incoming trajectory of the metallic cart and (b) a not-crossing trajectory. The R: r_1 - r_2 indicates the rows of the clustered tags. The C: c_1 - c_2 indicates the columns of the clustered tags.

First, the two previously explained potential features during some trajectories of the cart were observed. In particular, the number of readings of the reference tags acquired during four meaningful time windows of 200 ms for an incoming trajectory is depicted from Figures 3a to 3d (from the beginning to the end). In addition, in order to clarify the position of the metallic cart during the four presented snapshots of the incoming trajectory, a schematic representation of the metallic cart and the setup is depicted for each time window from Figures 3e to 3h. The red blocks represent the missed tag data. As can be observed, when the transpallet moves forwards, it shadows mainly the reference tags aligned along columns #3 and #4. In addition, as the transpallet crosses the gate, moving out from the grid, the shadowed tags are read again.

Besides, just in order to facilitate the interpretation of the data, the tags in the grid were clustered in six blocks by grouping them in 2×2 sub-grids and their data were aggregated. In particular, the number of missed tags within each block is illustrated in Figure 4a for the same incoming trajectory summarized in Figure 3. The number of tags that are missed within each block for each time window ranges from zero (all tags are read) to four (none of the tags of the block were read during a given time window). As can be seen, during the cart movement over the grid (during the interval between 6 s and 8 s) there is a significant increase in the number of RFID tags that were missed. Another example for a not-crossing trajectory is depicted in Fig. 4b.

As previously explained, the data acquired during the laboratory tests were divided into a training data set with 60% of the trajectories and a test data set with the remaining ones. In addition, the network input consisted of $N_{feat} = 24$ features: one sequence of read/missed per each reference tag of the grid. Then, the LSTM network was trained using a different number of hidden units for different values of the duration of the time window. The obtained results are depicted in Figure 5 in terms of Test Accuracy, namely the ratio between the number of correctly classified actions and the total number of classified actions. As can be observed, the test accuracy approaches the value of 1 for 50 hidden units and a time window of 400 ms. The usage of 50 hidden units also provides an accuracy greater than 0.9 for the other studied values of time window duration. The test accuracy obtained using more than 50 hidden units decreases showing that the network might be overfitting.

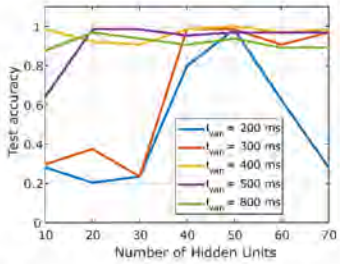

Figure 5. Test accuracy as a function of the number of hidden units of the LSTM network for different duration values of the time windows.

IV. Conclusion

A novel system to discriminate the direction of pallets crossing a UHF-RFID gate in a warehouse scenario was presented. The system is based on an easy-to-deploy grid of reference tags placed underneath the gate and a single reader antenna placed at the gate top over of the grid, making the system cost-effective. The transpallet movement causes the shadowing of the reference tags producing a distinguishable signature of its trajectory. The architecture of the proposed system exploits the shadowing effects of the transpallet on the reference tags close to it, which is predominant with respect to the multipath phenomena. The number of readings of each reference tag is aggregated within time windows using a binary attribute per tag (read or missed) as input features (one for every reference tag deployed on the grid) of a Long Short-Time Memory recurrent neural network. The test accuracy can approach the value of 100% for a proper time-window duration and number of hidden units. Although other state-of-the-art systems show similar performance, the required hardware infrastructure of the proposed system is cost-effective and easy-to-deploy. In addition, the system is more robust against multipath and should be adaptable to other scenarios without the need of retraining the network. The proposed system can find application also for discriminating the transit of a forklift through a point of interest. Furthermore, the proposed system is able to deliver real-time results as, once the neural network was trained, the transpallet action classification can be performed in a few milliseconds.

REFERENCES

[1] Everything RF. (2019, 3) More than 15 billion rain rfid tag chips sold in 2018. [Online]. Available: https://www.everythingrf.com/News/details/7797-More-than-15-Billion-RAIN-RFID-Tag-Chips-Sold-In-2018

[2] L. M. Ni, Y. Liu, Y. C. Lau, and A. P. Patil, "LANDMARC: indoor location sensing using active RFID," in *Proceedings of the First IEEE International Conference on Pervasive Computing and Communications, 2003. (PerCom 2003).*, March 2003, pp. 407–415.

[3] R. J. Stine, H. L. Markman, and J. E. Markman, "Shielded portal for multi-reading RFID tags affixed to articles," U.S. Patent 9 760 826B1, Mar. 12, 2013.

[4] R. B. Morin, "Method and system for controlling the traffic flow through an RFID directional portal," U.S. Patent 8 487 747B2, May 23, 2008.

[5] M. Goller, C. Feichtenhofer, and A. Pinz, "Fusing RFID and computer vision for probabilistic tag localization," in *2014 IEEE International Conference on RFID (IEEE RFID)*, April 2014, pp. 89–96.

[6] Y. Oikawa, "Simulation evaluation of tag movement direction estimation methods in rfid gate systems," in *2012 IEEE Radio and Wireless Symposium*, Jan 2012, pp. 331–334.

[7] Yujian, Yangwei, and Y. Zhang, "Estimating the direction of motion based on active rfid," in *The 5th International Conference on New Trends in Information Science and Service Science*, vol. 2, Oct 2011, pp. 286–290.

[8] T. Keller, F. Thiesse, J. Kungl, and E. Fleisch, "Using low-level reader data to detect false-positive rfid tag reads," in *2010 Internet of Things (IOT)*, Nov 2010, pp. 1–8.

[9] P. V. Nikitin, G. N. Spiess, H. M. Leland, L. C. Hingst, and J. H. Sherman, "Utilization of motion and spatial identification in mobile RFID interrogator," U.S. Patent 9 047 522B1, Nov. 6, 2010.

[10] A. Buffi and P. Nepa, "The sarfid technique for discriminating tagged items moving through a uhf-rfid gate," *IEEE Sensors Journal*, vol. 17, no. 9, pp. 2863–2870, May 2017.

[11] F. Geigl, C. Moik, S. Hintereggerz, and M. Goller, "Using machine learning and RFID localization for advanced logistic applications," in *2017 IEEE International Conference on RFID (RFID)*, May 2017, pp. 73–74.

[12] M. Hauser, M. Griebel, and F. Thiesse, "A hidden Markov model for distinguishing between RFID-tagged objects in adjacent areas," in *2017 IEEE International Conference on RFID (RFID)*, May 2017, pp. 167–173.

[13] A. Buffi, E. D'Andrea, B. Lazzerini, and P. Nepa, "UHF-RFID smart gate: Tag action classifier by artificial neural networks," in *2017 IEEE International Conference on RFID Technology Application (RFID-TA)*, Sep. 2017, pp. 45–50.

[14] E. Eckstein, G. Mazoki, and W. Richie, "Article identification and tracking using electronic shadows created by RFID tags," U.S. Patent 20 050 012 613A1, Nov. 6, 2010.

[15] B. Wagner, N. Patwari, and D. Timmermann, "Passive RFID tomographic imaging for device-free user localization," in *2012 9th Workshop on Positioning, Navigation and Communication*, March 2012, pp. 120–125.

[16] K. Gregor, I. Danihelka, A. Graves, and D. Wierstra, "DRAW: A recurrent neural network for image generation," *CoRR*, vol. abs/1502.04623, 2015. [Online]. Available: http://arxiv.org/abs/1502.04623

[17] S. Hochreiter and J. Schmidhuber, "Long short-term memory," *Neural Comput.*, vol. 9, no. 8, pp. 1735–1780, Nov. 1997. [Online]. Available: http://dx.doi.org/10.1162/neco.1997.9.8.1735

[18] H. Sak, O. Vinyals, G. Heigold, A. Senior, E. McDermott, R. Monga, and M. Mao, "Sequence discriminative distributed training of long short-term memory recurrent neural networks," in *Interspeech*, 2014.

[19] O. Vinyals, A. Toshev, S. Bengio, and D. Erhan, "Show and tell: A neural image caption generator," *CoRR*, vol. abs/1411.4555, 2014. [Online]. Available: http://arxiv.org/abs/1411.4555

III

III

Publication IV

G. Álvarez-Narciandi, M. López-Portugués, F. Las-Heras and J. Laviada, "Free-hand, Agile, and High-Resolution Imaging With Compact mm-Wave Radar," *IEEE Access*, vol. 7, pp. 95516–95526, 2019.

IV

IEEE Access
Multidisciplinary | Rapid Reviews | Open Access Journal

Received May 31, 2019, accepted July 9, 2019, date of publication July 17, 2019, date of current version August 2, 2019.

Digital Object Identifier 10.1109/ACCESS.2019.2929522

Freehand, Agile, and High-Resolution Imaging With Compact mm-Wave Radar

GUILLERMO ÁLVAREZ-NARCIANDI, MIGUEL LÓPEZ-PORTUGÉS, FERNANDO LAS-HERAS, (Senior Member, IEEE), AND JAIME LAVIADA

Department of Electrical Engineering, University of Oviedo, 33203 Gijón, Spain

Corresponding author: Guillermo Álvarez-Narciandi (alvareznguillermo@uniovi.es)

This work was supported in part by the Ministerio de Educación y Formación Profesional of Spain under the FPU Grant FPU15/06431, in part by the Ministerio de Ciencia, Innovación y Universidades under Project RTI2018-095825-B-I00, and in part by the Principado de Asturias/FEDER under Project IDI/2018/000191.

IV

ABSTRACT The aim of this paper is to present a freehand scanning system with a compact mm-wave radar. In order to achieve high-resolution images, the system exploits the free movements of the radar to create a synthetic aperture. However, in contrast to conventional synthetic aperture radar (SAR), in which canonical acquisition surfaces (e.g., planes or cylinders) are used, the system allows for a given tolerance compatible with real hand-made trajectories. Moreover, different techniques are studied to compensate for the impact of irregular sampling to reduce the artifacts in the image. As a result, real-time scanning can be readily performed even by inexperienced users. The scanning system, comprising a commercial motion capture system and an mm-wave module, can be easily deployed and calibrated. Several results involving different objects are shown to illustrate the performance of the system.

INDEX TERMS SAR imaging, mm-wave imaging, FMCW radar, real-time imaging, freehand scanner.

I. INTRODUCTION

Electromagnetic imaging [1] enables to inspect the inner composition of different objects or beings. This technology can be employed, under different implementations, for nondestructive evaluation of materials [2], [3], medicine [4], defense and security [5]–[7], food inspection [8], [9], obstacle detection [10], among other applications.

A very desirable feature for any of the previous system is compactness. This feature is obviously linked to the working frequency and, therefore, it is hard to achieve in microwave systems. However, *mm-wave* systems can be very compact enabling on-chip systems [11], [12] at the expense of some penetration capabilities. Moreover, the quick development of this technology in the last years has enabled a wide variety of robust and affordable devices.

Although the range resolution depends on the bandwidth, which does not impose a specific size limitation, the lateral resolution of a mm-wave imaging system is proportional to the size of the aperture of the system. Consequently, although a single transmitter and receiver system can be relatively small, high resolution imaging requires of relatively bulky structures formed by large antennas based on reflectors or lenses [13], raster scanning along well-known paths [5] or large arrays [14].

A balance between system size and resolution has been recently presented in [15] implementing a portable microwave camera operating from 20 to 30 GHz. Furthermore, this kind of system can take advantage of multi-view approaches to increase the imaged area and the image quality [16]–[19].

In this paper, compactness is moved a step forward by performing high-resolution imaging with a single *radar-on-chip*. For this purpose, the radar is moved over the volume to be imaged to build a synthetic aperture.

In order to apply the imaging algorithm in real-time, the position of the radar is tracked by means of a motion capture system. It is interesting to observe that this kind of tracking was already successfully employed to directly map electromagnetic sources for electromagnetic compatibility purposes using a 3D manual scanning [20]. In a similar fashion, the tracking system was also used to indirectly map sources by means of backpropagation using a manual scanning system constrained to two dimensions [21]. A study of the feasibility of using inertial navigation systems for imaging applications has been presented in [22].

The associate editor coordinating the review of this manuscript and approving it for publication was Laxmisha Rai.

In the context of electromagnetic imaging, freehand scanning constrained to two dimensions has also been demonstrated in [23] by implementing a system in the X-band and using a railway system to track the position. However, to the best authors' knowledge, it is the first time that a completely 3D freehand scanning with such a compact device is presented.

This paper is organized as follows. First, the structure of the scanner and its workflow is presented. Second, the radar processing implemented in the demonstrator is explained. Next, the results of several simulations performed to assess the impact of positioning errors and nonuniform sampling in the scanner results are summarized. After that, the calibration procedure for the radar system is introduced and the obtained measurement results are presented. Finally, the conclusions are drawn.

IV

II. FREEHAND MM-WAVE IMAGING

A. SYSTEM ARCHITECTURE

The scanning system main goals, which imply several challenges in terms of positioning accuracy and data processing algorithms, are the following:

- High resolution images: in order to provide high resolution images with a *compact* system, a radar module in the mm-wave band is chosen. In addition, the measurements are acquired along a *synthetic aperture* and coherently combined to improve the resolution. For this purpose, the position of the radar must be acquired with an accuracy much smaller than the wavelength, i.e., submillimeter position accuracy is required.
- Freehand system: the scanner must build the images while it is freely moved so that the operator can dynamically choose the areas where to spend more time scanning to refine the image. As a consequence, due to the nature of the freehand movement of the scanner, the measurements of the radar are not expected to be uniformly spaced.
- Real-time operation: the measurements must be processed on-the-fly and the image must be updated as more data is acquired by the scanner.

In order to provide the previous functionalities, the scanning system, whose scheme is depicted in Fig. 1, was structured in three subsystems:

- Control and processing subsystem: it is in charge of setting up the scanning system, i.e., establishing the communication with the other two subsistems and defining the volume under test, in which the reflectivity will be computed to create the radar images in real-time. In addition, the control subsystem is responsible for querying both the radar frames and the position of the radar, and processing the obtained information, as illustrated in the workflow depicted in Fig. 2. This subsystem is formed by a conventional PC or a laptop, which is interfaced with the radar subsystem with a USB cable and with the positioning subsystem by an Ethernet connection.
- Radar subsystem: it comprises a commercial FMCW mm-wave radar module, in this case the radar-on-chip BGT60TR24B by Infineon® [11]. This subsystem transmits and receives the radar signals on demand of the control subsystem enabling the acquisition of the IF signal for further processing. The frequency waveform of the signal transmitted by the radar has an up-chirp saw tooth pattern centered at $f_c = 60\,\text{GHz}$ with a bandwidth of $BW = 6\,\text{GHz}$ and a chirp duration of $T_s = 512\,\mu\text{s}$. The RF frontend includes 2 transmitting and 4 receiving antennas. However, for this system a *quasimonostatic* configuration, with one transmitting and one receiving antenna, was considered. The radar module was embedded in a 3D-printed enclosure designed ad-hoc for it to ease the manipulation of the radar as well as to help in the placement of the reflective markers of the positioning system (Figs. 3a and 3b).

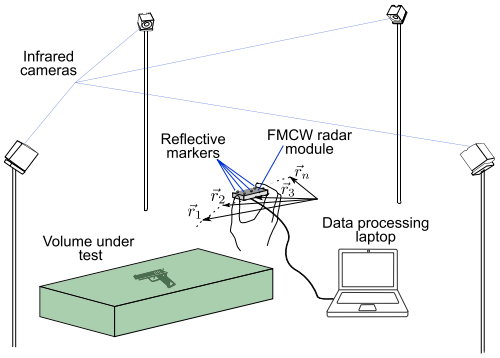

FIGURE 1. Scheme of the proposed scanning system.

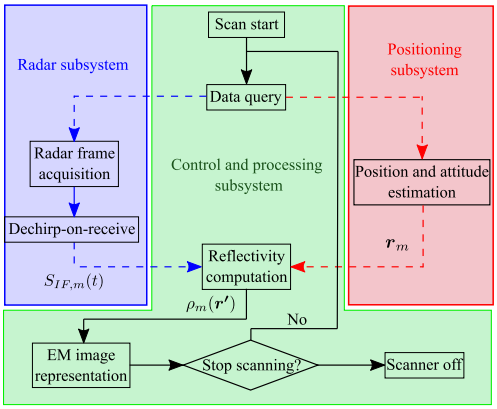

FIGURE 2. Workflow of the scanning system.

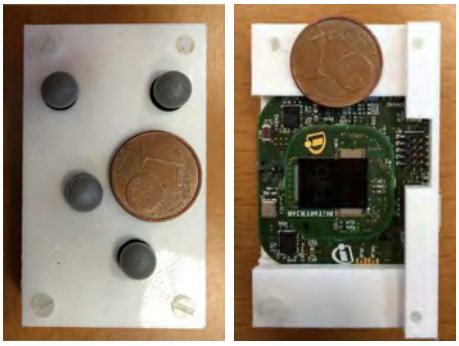

(a) (b)

FIGURE 3. Radar module enclosure: (a) top view and reflective markers for the positioning system (b) and bottom view. A one euro-cent coin is included for scale purposes.

- Positioning subsystem: it estimates the position and the attitude of the radar module by means of an optical tracking system. This subsystem is formed by the motion capture system of Optitrack® [24]. The infrared cameras of the system track the reflective markers attached to the radar module (see the scheme of the system in Fig. 1). The position retrieved by the positioning system, which is the centroid of the rigid body defined by the deployed markers, must be corrected to match the position of the radar as the described in Section III-D. This commercial setup, which requires a minimum of four cameras, can be easily deployed and calibrated in a matter of minutes.

B. IMAGING TECHNIQUE

Due to the freehand nature of the proposed imaging system, the acquired data are not expected to be equally spaced along a canonical geometry as it is usually assumed in conventional synthetic aperture radar (SAR) techniques [25]. For this reason, a *delay and sum* algorithm, adapted to the particularities of the FMCW radar signal, is used.

In order to update the image, which shows the reflectivity of the scene, the algorithm requires the current radar position $\mathbf{r}$ and the previous dechirped signal provided by the radar module (see workflow in Fig. 2). Since the signal transmitted by the radar, expressed in complex form, is given by

$$s_{tx}(t) = e^{j2\pi(f_c t + \frac{1}{2}\alpha t^2)}, \tag{1}$$

where $|t| < T_s/2$ and

$$\alpha = \frac{BW}{T_s}, \tag{2}$$

is the slope rate, then if a point target is assumed, the signal received by the radar, without considering amplitude variations, will be given by a delayed version of the transmitted signal

$$s_{rx}(t) = s_{tx}(t-\tau) = e^{j2\pi(f_c(t-\tau)+\frac{1}{2}\alpha(t-\tau)^2)}, \tag{3}$$

where τ is proportional to the distance from the radar position to the point target (R):

$$\tau = \frac{2R}{c}. \tag{4}$$

Thus, the input dechirped signal, obtained by mixing the received and transmitted signals [26], [27] will be given by:

$$s_{IF}(t) = e^{j2\pi(\alpha\tau t + f_c\tau - \frac{1}{2}\alpha\tau^2)}, \tag{5}$$

which has beat frequency $f_b = \tau\alpha$. If the object under test is not a point target but a *distributed target*, then the received signal can be expressed as a superposition of signals given by (3) and so will be the IF signal. In practice, the radar does not return the complex signal in (5) as it lacks of an IQ mixer. However, thanks to the wideband nature of the signal, the analytic signal can be easily retrieved by means of an efficient Hilbert transform [28].

The reflectivity ρ at each point $\mathbf{r}'$ of the grid in which the volume under test is discretized is estimated by coherently summing the contribution of the signal received by the radar at each acquisition position. In order to achieve this coherent combination, the extra phase term, which can be approximated by $f_c\tau - \frac{1}{2}\alpha\tau^2 \approx f_c\tau$ for close targets, is firstly compensated and, after that, a range compression is performed by doing a Fourier transform in the time domain. Thus, the following auxiliary signal is firstly constructed at each radar position for each observation position $\mathbf{r}'$:

$$s_{c,m}(\mathbf{r}', f) = \mathscr{F}\left\{s_{IF,m}(t)e^{-j2\pi f_c \tau_m(\mathbf{r}',\mathbf{r}_m)}\right\}, \tag{6}$$

where $\mathscr{F}\{\cdot\}$ denotes the Fourier transform operator and $s_{IF,m}(t)$ is the IF signal acquired at the m-th radar position denoted by $\mathbf{r}_m$ and $\tau_m(\mathbf{r}', \mathbf{r}_m) = 2\frac{\|\mathbf{r}'-\mathbf{r}_m\|_2}{c}$, which is the propagation delay between the radar position and the observation point.

This auxiliary signal will peak at the beat frequency, which is expected to be proportional to the distance to the target

$$f_{b,m} = \alpha\tau_m = \frac{2\alpha\left\|\mathbf{r}' - \mathbf{r}_m\right\|_2}{c}, \tag{7}$$

and, therefore, standard time-domain techniques, similar to the ones used in UWB imaging (e.g., [29], [30]), can be used. In particular, the following delay and sum algorithm can be formulated with a simple change of variable:

$$\rho_m(\mathbf{r}') = \sum_{i=1}^{m} s_{c,i}(\mathbf{r}', \frac{2\alpha\left\|\mathbf{r}' - \mathbf{r}_i\right\|_2}{c}), \tag{8}$$

Although this algorithm is not as efficient as other implementations relying on Fast Fourier Transforms (e.g., [31]) but requiring equally spaced data, it is still able to provide real-time reflectivity estimations for areas of several squared centimeters as it will be illustrated later.

IV

III. PRACTICAL CONSIDERATIONS

Conventional imaging algorithms are applied to data acquired at equally-spaced positions over canonical geometries (e.g., [5], [25]). Although the scanning system can take samples at very regular intervals, due to the lack of a perfectly steady hand, the samples will not be equally spaced. Moreover, the relatively arbitrary trajectories do not guarantee to cover a given surface with a single pass. This results in a number of issues to be solved or mitigated.

A. SAMPLES DISTRIBUTION

The acquired samples will not be equally spaced along a canonical surface. In this paper, the ideal target surface is a *plane*. Depending on the movement speed, more or less samples will lay on some specific areas. This could result in areas of the image with reflectivity levels higher than other areas because of this imbalance in the sample density.

In order to mitigate this issue, the flat surface is split into squared *macrocells* and only a pre-established number of samples are used by the imaging algorithm in each macrocell. This situation is shown in Fig. 4, in which only two samples per macrocell are used by the imaging algorithm independently on the number of samples acquired inside the macrocell.

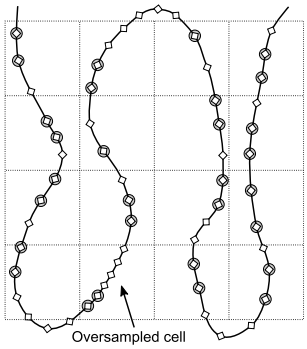

FIGURE 4. Distribution of the acquisition points for the imaging algorithm: Diamonds denote acquisition points and gray circles denote points used by the imaging algorithm.

As a complement to assist during the scanning, the amount of samples per macrocell is shown in a 2D image similar to a *heat map* so the operator can easily check the amount of available data along the scanning surface.

In the presented implementation, the size of the macrocells is chosen as $1 \times 1\,\text{mm}^2$ and the number of samples per cell is set to 3. During the data acquisition, it is not possible to foresee if the scanner will move back to a cell, providing the opportunity to acquire samples well-spaced in the cells. For this reason, a simple algorithm based on retaining the first samples is used.

B. ACQUISITION ALONG A NON-FLAT SURFACE

Despite the previous strategy, the samples will not be perfectly distributed and, therefore, some impact is expected in the image. Moreover, although scanning along a flat surface is targeted, some flexibility must be granted to the operator, who cannot describe perfectly bidimensional trajectories.

In order to assess the effect of these issues, several systematic simulations were conducted using the IF signal model given by (5). For this purpose, an ideal target with the shape of the letter "T" was defined and several simulations were performed randomizing the horizontal positions and height where the samples were taken. First, a 2D regular grid of sampling locations was defined in order to obtain a reference reflectivity image (Fig. 5a). Then, 3D radom variations to the regular sampling positions were generated using a normal distribution for several variance values. The obtained results keeping the horizontal distribution of the regular grid points but adding height variations according to a normal distribution of $\sigma = 1\,\text{cm}$, $\sigma = 1.5\,\text{cm}$ and $\sigma = 2\,\text{cm}$ are depicted in Figs. 5b, 5c and 5d, respectively. As can be observed, after adding height variations to the sampling points originally distributed in a regular grid contained in a flat surface, the image is noisier and some artifacts appear the more nonuniformity is introduced in the sampling positions. However, the quality of the retrieved reflectivity image, though degraded, still enables to clearly recognize the test object.

An analogous analysis was performed modifying both height and horizontal position. As can be seen in Fig. 5e, retrieved with the sampling positions depicted in the *heat map* of Fig. 5g, which were obtained modifying the original sampling grid with a normal distribution of $\sigma = 1\,\text{cm}$ in each horizontal direction, and in Fig. 5f, in which the height of the sampling positions depicted in Fig. 5g was also modified using a normal distribution of $\sigma = 1\,\text{cm}$, the results are similar to those previously presented in this section. Hence, it is possible to conclude that, although due to the nonuniform sampling the resulting reflectivity images are noisier and some artifacts appear, the retrieved image is still accurate.

In order to allow for height variations in a certain tolerance range, the macrocells are extended from 2D rectangles to cuboids. According to the previous study, a small height tolerance would result in better quality images but many samples would be discarded due to the small size and, therefore, the overall scanning time would be increased as many areas should be resampled. Moreover, as it will be analyzed next, other factors such as the positioning error have also an impact, which can be a more limiting factor. In this work, squared macrocells of 1 mm of side and a height tolerance of $\pm 1\,\text{cm}$ were considered.

C. IMPACT OF POSITIONING ERROR

Positioning errors arise from two reasons (assuming that the errors due to the accuracy of the optical tracking system can be neglected compared to them):

1) Calibration error: the optical tracking system provides the position of the centroid of the markers attached to the radar enclosure. As a consequence, there is an offset between the position estimated by the localization system and the radar position, which has to be

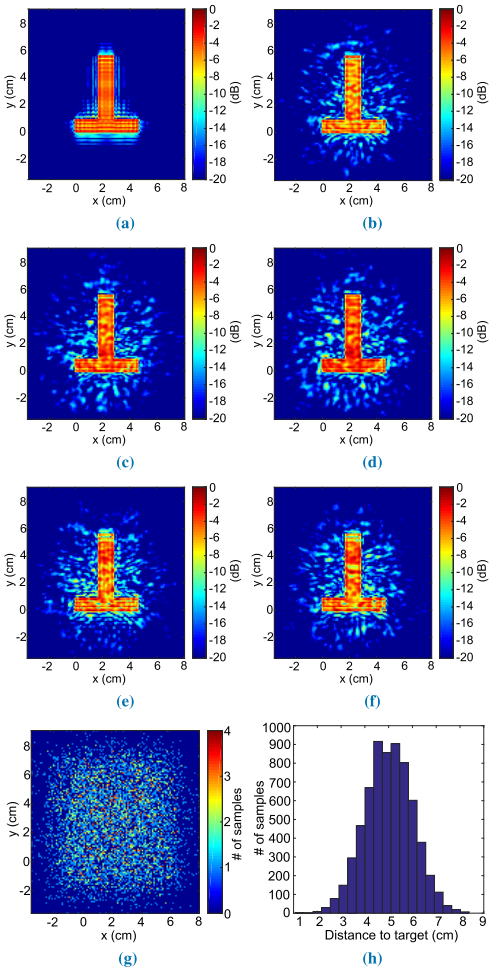

FIGURE 5. Reflectivity image of the simulated target computed with (a) uniform sampling and without positioning errors. Reflectivity image computed modifying the height of the regular positions by adding values obtained using a normal distribution of (b) $\sigma = 1$ cm, (c) $\sigma = 1.5$ cm and (d) $\sigma = 2$ cm. Reflectivity image obtained for (e) nonuniform sampling positions in a 2D plane and also (f) modifying the height of the sampling positions. The heat map of the simulated radar positions used to obtain images (e) and (f) is depicted in (g) and the histogram of the height of the simulated radar positions used to compute (f) is shown in (h).

estimated in a calibration stage. During the scanning process, the position estimated by the optical tracking system has to be corrected taking into account the previously estimated offset and the attitude of the rigid body defined by the reflective markers.

2) Delay between the radar acquisition and the position query: during the scanning process, the position of the radar and the radar data are requested simultaneously. However, since they are independent systems, a perfect synchronization is not guaranteed. Therefore, the position of the radar module when the radar data is acquired can be slightly different to its position when the tracking system was queried.

The impact of the calibration error will be firstly studied by evaluating its effect for the same ideal target shown in Fig. 5a. For this purpose, several simulations for different values of the offset between the radar position and the centroid of the reflective markers, denoted by $\boldsymbol{w}$, were performed.

At this point, it is relevant to observe that the attitude of the radar, in terms of yaw, pitch and roll (φ, θ and ψ, respectively), plays a relevant role in this study as the magnitude of the error, in each dimension is given by

$$\epsilon_{cal} = \boldsymbol{R}(\varphi, \theta, \psi)\boldsymbol{w}, \tag{9}$$

where $\boldsymbol{R}(\varphi, \theta, \psi)$ is the rotation matrix computed for the attitude angles of the rigid body defined by the reflective markers provided by the tracking system [32]. If the attitude angles were constant along the scanning, then the *relative* position between the acquired sampling points, even for high errors in the estimation of $\boldsymbol{w}$, would be error free. Moreover, it is straightforward to prove that the higher the range of the attitude angles along the scan, the higher the error between real and the estimated radar positions (Fig. 6). For this reason, a threshold for the maximum values of the attitude angles is used in these simulations. This threshold will be the same for all the angles and will be denoted by θ_{max}. This threshold can be easily implemented in measurements by discarding those positions where at least one attitude value is outside the range $\pm\theta_{max}$.

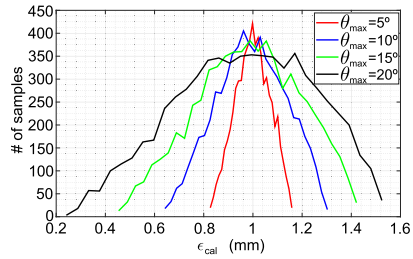

FIGURE 6. Histogram of the error between the real and the estimated radar position in the x-axis for 6536 observations, $w = (1, 1, 1)$ mm and different values of yaw, pitch and roll generated using a uniform distribution $[-\theta_{max}, \theta_{max}]$.

The obtained results are summarized in Fig. 7, where, as expected, the greater the offset is, the worse is the quality of the reconstructed image. This can be easily checked comparing Figs. 7a and 7c for $\boldsymbol{w} = (1, 1, 1)$ mm and $\boldsymbol{w} = (2, 2, 2)$ mm respectively. The same holds for the maximum value of the attitude angles of the scanner, which can be seen comparing Figs. 7c and 7g. Both images were obtained for an offset value of 2 mm in each of the three coordinate axes

IV

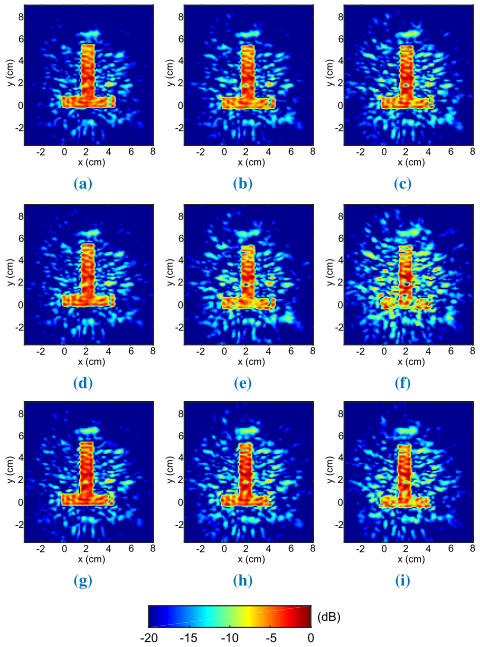

FIGURE 7. Reflectivity image of the simulated target computed for $w = (1, 1, 1)$ mm and $\theta_{max} = 10°$ (a), $w = (1, 2, 1)$ mm and $\theta_{max} = 10°$ (b), $w = (2, 2, 2)$ mm and $\theta_{max} = 10°$ (c), $w = (1, 1, 3)$ mm and $\theta_{max} = 10°$ (d), $w = (1, 3, 1)$ mm and $\theta_{max} = 10°$ (e), $w = (3, 3, 1)$ mm and $\theta_{max} = 10°$ (f), $w = (2, 2, 2)$ mm and $\theta_{max} = 5°$ (g), $w = (3, 3, 3)$ mm and $\theta_{max} = 5°$ (h) and $w = (4, 4, 2)$ mm and $\theta_{max} = 5°$ (i).

but the quality of Fig. 7c, obtained for $\theta_{max} = 10°$ is lower than the quality of Fig. 7g, which was obtained for $\theta_{max} = 5°$. It should be pointed out that, as can be observed comparing Figs. 7d and 7e, an offset in one of the axes parallel to the area under scan has a higher impact on the quality of the obtained images than an offset in the axis in the orthogonal direction.

In conclusion, the maximum value of each attitude angle, which can be controlled by software discarding the measurements taken when the attitude of the scanner is over a given threshold, should be imposed taking into account the maximum accuracy of the offset between the radar position and the centroid of the reflective markers that can be achieved during the calibration procedure. According to our experience, a value of 5° provides a good trade-off between scanning speed and image quality.

The second positioning error, related to the synchronization imperfections, can be mitigated following an approach similar to the ones previously used. Thus, the position can be acquired before polling the radar and after retrieving the radar data. If the distance between the two positions is larger than a given threshold, this data can be discarded. This situation usually happens if the radar module is moved too fast.

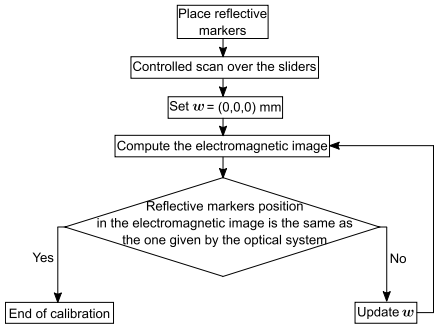

FIGURE 8. Workflow of the calibration procedure.

This analysis will be performed with real data in the Results section.

D. POSITIONING SYSTEM CALIBRATION

As previously stated, the optical tracking system provides the position of the centroid of the reflective markers attached to the radar enclosure. As a consequence, there is an offset between the position provided by localization system and that of the radar. This offset must be estimated in order to correct the position estimations of the tracking system and coherently combine the radar measurements. The calibration procedure, summarized in Fig. 8, consists of the following steps:

1) The radar enclosure is mounted onto a support structure, which is adjusted to be moved over a platform with two sliders (Fig. 9a). Thus, the scanner can be moved only over a plane parallel to the area under scan and the attitude angles are fixed.
2) Several reflective markers (Fig. 9b) are placed in the area under scan and their positions are measured with the optical tracking system.
3) A scan was performed moving the radar along the sliders.
4) The offset values for each axis are initially zero and, after that, they are optimized until the position of the reflective markers in the electromagnetic image matches the one given by the optical tracking system and the maximum of the reflectivity is inside the plane which corresponds to the actual vertical coordinate of the markers.

The offset values obtained after the calibration are $\boldsymbol{w} = (-2, -5.4, 12)$ mm. The reflectivity image for the three markers before and after the calibration are depicted in Figs. 9c and 9d respectively. As can be seen, after the calibration, the three areas with high reflectivity, i.e., the markers of the tracking system, were shifted to the location of the markers given by the tracking system. In addition, the amount of noise was reduced, the image was better focused and the shape of the markers is circular, as their actual shape. It should

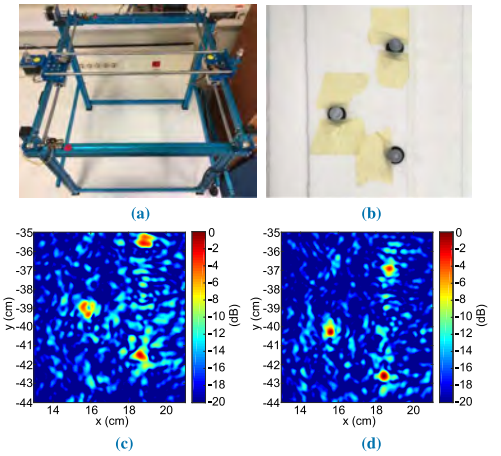

FIGURE 9. Calibration platform with the sliders (a), reflective markers used to calibrate the scanner (b), reflectivity image obtained before the calibration (c) and after the offset w was estimated (d).

be noticed that the calibration must be done only once when the radar is attached to the reflective markers.

IV. RESULTS

Several measurements were conducted to assess the performance of the system. In order to help the system operator during the scanning process, several visual aids were displayed in the interface of the control laptop. In particular, the attitude angles and the height of the scanner provided by the tracking system are depicted along the heat map to control the number of samples acquired over each part of the volume under test.

First, a test with a letter "T" foiled with metal was used as test target in order to compare the measurement results with the numerical results presented in Section III-C. Second, a test with a mannequin and a gun, resembling a security application, was performed. In each case, the volume under test was defined by means of a 3D point grid, which was divided in a set of planes, where the reflectivity was computed. During the scanning process, the electromagnetic image, i.e., the reflectivity computed in one of the planes in which the volume under test was divided, is shown to the operator along the heat map with the sampling information. The operator can interactively change the plane whose reflectivity is being depicted so as to focus the electromagnetic image on the desired target. All the measurements were performed using a laptop for both controlling the scanner and processing the acquired data. This laptop was equipped with a Intel® i7-7700HQ (2.8 GHz), 16 GB of RAM and a NVIDIA® GeForce GTX 1050 graphic card.

A. TEST TARGET

A 3D test target with the shape of the letter 'T' (Fig. 10a) was scanned with the radar. The positions at which radar

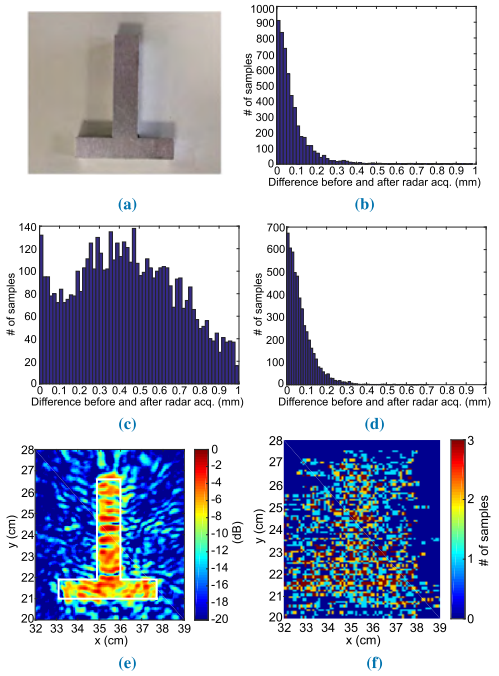

FIGURE 10. Letter used as a test target (a), histogram of the difference between the positions estimated before and after the radar acquisition in the *y-axis* (b), in the *x-axis* (c) and in the *z-axis* (d), reflectivity image obtained after the scan (e) and heat map depicting where the radar data was acquired (f).

acquisitions were performed are depicted in Fig. 10f and the reflectivity image is shown in Fig. 10e, where the contour of the scanned letter is plotted with a white line. The reflectivity was estimated in a set of 8 planes of $22 \times 10\,\text{cm}^2$, the total acquisition time was 297 s and the update frame rate of the image was 25.2 frames per second. The average distance from the radar to the target was 5.27 cm. As can be seen, the test letter is well-reconstructed being the quality of the image comparable to Figs. 7b, 7d and 7h.

In addition, an analysis of the upper bound of the error, due to the delay between the position estimation and the radar acquisition, was performed. In order to do so, the workflow of the scanner was modified to query its position to the tracking system before and after the radar acquisition. Hence, an upper bound of the error can be obtained by computing the difference between the two position estimations (measurements for which the difference between the two position acquisitions was greater than 1 mm were discarded by software). The histograms of the absolute value of the difference between the two position acquisitions are depicted in Figs. 10b and 10c for each of the axes of the plane parallel to the volume under test and in Fig. 10d for

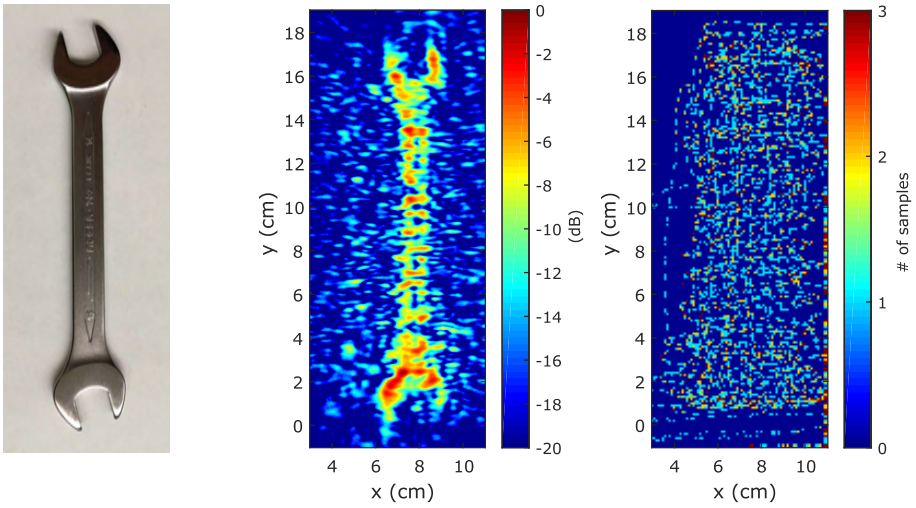

FIGURE 11. Image of the (a) hand wrench used as a target, (b) reflectivity obtained after the scan and (c) heat map depicting where the radar data was acquired.

the orthogonal direction. As can be seen, the displacement upper bound for nearly all the acquisitions is below 0.3 mm in Figs. 10b and 10d. However, as expected, this upper bound is higher in the axis of the main movement direction of the *s-shape* path described with the scanner during the data acquisition (Fig. 10c). In order to limit this upper bound, the speed of the scanning process is limited by software. As previously described, this can be achieved by discarding the radar data when the difference between the two position acquisitions explained before is greater than a given distance. Particularly, this distance was set to 2 mm for the tests presented in this manuscript.

B. TEST WITH A HAND WRENCH

Another example to illustrate the performance of the system was carried out with the hand wrench depicted in Fig. 11a. The positions at which radar acquisitions were performed are depicted in Fig. 11c and the obtained reflectivity image is shown in Fig. 11b.

In this case the reflectivity was computed in a set of 7 planes of $11 \times 22\,\text{cm}^2$ during a total acquisition time of 269 s. The update rate of the reflectivity image was 26.2 frames per second and the average distance from the radar to the target was 7.8 cm. As can be seen, the handle of the wrench and both of its open ends are well-reconstructed. Also, it is worth noting that there is a lower reflectivity value in the central part of the handle, where the thickness of the wrench is lower.

C. TEST WITH A MANNEQUIN

The setup comprising the mannequin and the gun is depicted in Fig. 12a and a zoomed view of the imaged gun is shown in Fig. 12b. As can be seen, the mannequin is covered by aluminum foil as it provides a fair representation of the human skin at mm-wave frequencies. In addition, it should be pointed out that this is a worse situation than using a more realistic model of the skin since the contrast between the body and the metal of the gun would be higher. The reflectivity was estimated in a set of 11 planes of 18.6 × 12.7 cm, the total acquisition time was 1162 s and the update frame rate of the image was 15.5 frames per second (it should be noted that the lower update rate is due to the increase of the reconstruction volume). The average distance from the radar to the target was 5.8 cm. It should be pointed out that the proposed system was implemented in MatLab® and could be further optimized to increase the framerate (which would also speed up the samples acquisition). Furthermore, the acquisition time could be drastically reduced using more than one receiving antenna, i.e., by taking samples at more than one location for each position of the scanner. To give an idea of the increasing number of receivers that manufacturers are integrating in a single chip, Vayyar has recently announced a chip with 72 transmitters and 72 receivers [33]. The results are plotted in Fig. 12c, where the color of each pixel of the 2D image is proportional to the depth of the point with highest reflectivity within all the planes in which the volume under test was divided. Moreover, the brightness of each pixel was weighted by the reflectivity magnitude corresponding to it [18]. The heat map depicting the horizontal positions where the radar acquisitions were performed is shown in Fig. 12d. Although the trigger is not detected (it is closer to the mannequin than the rest of the gun, i.e., the height difference between the background and the trigger is smaller, and its size is smaller), the shape of the pistol is well-reconstructed.

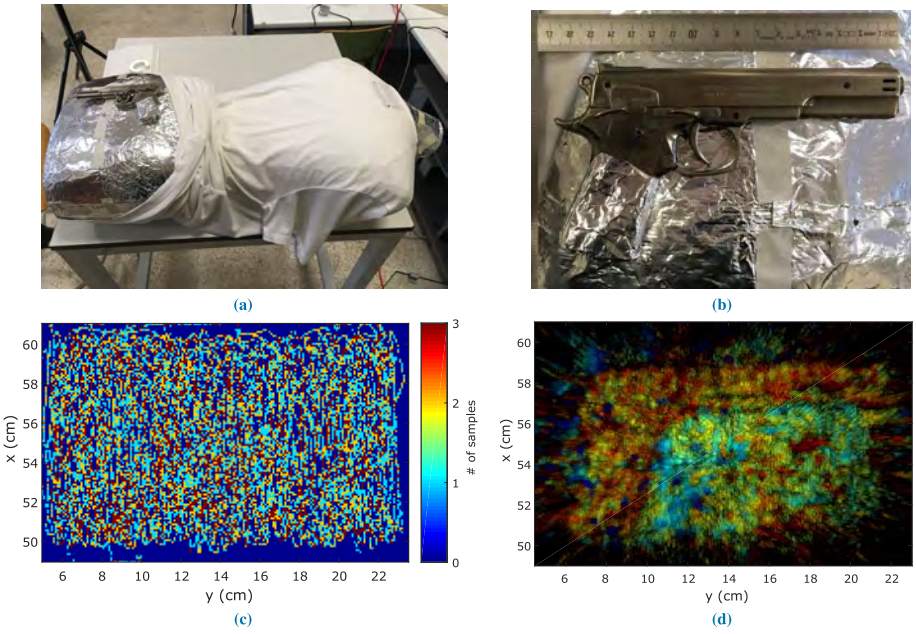

FIGURE 12. Image of the (a) mannequin with an attached gun, (b) the imaged gun zoomed, (c) heat map depicting where the radar data was acquired, and (d) reflectivity image obtained after the scan.

V. CONCLUSION

In this manuscript a mm-wave freehand scanner based on a FMCW radar was presented. The proposed system also comprises an optical tracking system to estimate the position of the radar and a conventional laptop to process the measurements using a delay and sum algorithm to obtain high-resolution real-time reflectivity images.

The main focus of the manuscript was devoted to present the architecture of the system, to assess the problems that arise due to the real-time operation and freehanded movement of the scanner and how to overcome and mitigate them and to evaluate the performance of the system with several test targets. In particular, the effect of nonuniform sampling and positioning errors was addressed by means of simulations. Results show that nonuniform sampling and positioning errors cause an increase of noise in the reflectivity image and the appearance of some artifacts and, hence, some strategies to mitigate these effects were developed (restricting the maximum value of the attitude of the radar, dividing the volume under test in 3D macrocells and controlling the synchronization of the tracking system and the radar). However, the main source of error are positioning errors which, in the presented prototype, are mainly due to calibration errors. At this point, it should be remarked that this problem could be drastically reduced with an industrial fabrication of the scanning system (comprising the radar and the markers).

Regarding the real-time performance of the system, several radar acquisitions are buffered prior to the reflectivity update to speed up the system and results show that high update rates for the reflectivity image can be achieved. In spite of that, higher volumes under test slow down the update rate of the scanner and the required time to scan middle size areas (hundreds of seconds) limits the direct usage of the presented prototype for some of its potential applications. However, the presented prototype paves the way for ultrafast scans as the processing algorithm can be optimized and the number of transmitters and receivers in the radar chip can be increased to speed up the data acquisition. Finally, the laboratory tests show that both simple and complex targets can be imaged and high-resolution reflectivity estimations can be obtained.

REFERENCES

[1] M. Pastorino, *Microwave Imaging*. Hoboken, NJ, USA: Wiley, 2010.
[2] S. Kharkovsky, J. T. Case, M. A. Abou-Khousa, R. Zoughi, and F. L. Hepburn, "Millimeter-wave detection of localized anomalies in the space shuttle external fuel tank insulating foam," *IEEE Trans. Instrum. Meas.*, vol. 55, no. 4, pp. 1250–1257, Aug. 2006.
[3] F. Boero, A. Fedeli, M. Lanini, M. Maffongelli, R. Monleone, M. Pastorino, A. Randazzo, A. Salvadè, and A. Sansalone, "Microwave tomography for the inspection of wood materials: Imaging system and experimental results," *IEEE Trans. Microw. Theory Techn.*, vol. 66, no. 7, pp. 3497–3510, Jul. 2018.
[4] N. K. Nikolova, "Microwave imaging for breast cancer," *IEEE Microw. Mag.*, vol. 12, no. 7, pp. 78–94, Dec. 2011.

IV

[5] D. M. Sheen, D. L. McMakin, and T. E. Hall, "Three-dimensional millimeter-wave imaging for concealed weapon detection," *IEEE Trans. Microw. Theory Techn.*, vol. 49, no. 9, pp. 1581–1592, Sep. 2001.

[6] X. Zhuge and A. G. Yarovoy, "Three-dimensional near-field MIMO array imaging using range migration techniques," *IEEE Trans. Image Process.*, vol. 21, no. 6, pp. 3026–3033, Jun. 2012.

[7] J. Gao, Y. Qin, B. Deng, H. Wang, and X. Li, "Novel efficient 3D short-range imaging algorithms for a scanning 1D-MIMO Array," *IEEE Trans. Image Process.*, vol. 27, no. 7, pp. 3631–3643, Jul. 2018.

[8] K. Mizuno, H. Matono, Y. Wagatsuma, H. Warashina, H. Sato, S. Miyanaga, and Y. Yamanaka, "New applications of millimeter-wave incoherent imaging," in *IEEE MTT-S Int. Microw. Symp. Dig.*, Long Beach, CA, USA, Jun. 2005, p. 4 and 632.

[9] B. Larumbe, J. Laviada, A. Ibáñez-Loinaz, and J. Teniente, "Real-time imaging with frequency scanning array antenna for industrial inspection applications at W band," *J. Infr., Millim., THz Waves*, vol. 39, no. 1, pp. 45–63, Jan. 2018.

[10] Q. Ma, D. S. Goshi, Y. C. Shih, and M. T. Sun, "An algorithm for power line detection and warning based on a millimeter-wave radar video," *IEEE Trans. Image Process.*, vol. 20, no. 12, pp. 3534–3543, Dec. 2011.

[11] I. Nasr, R. Jungmaier, A. B. D. Noppeney, J. S. Bal, M. Wojnowski, E. Karagozler, H. Raja, J. Lien, I. Poupyrev, and S. Trotta, "A highly integrated 60 GHz 6-channel transceiver with antenna in package for smart sensing and short-range communications," *IEEE J. Solid-State Circuits*, vol. 51, no. 9, pp. 2066–2076, Sep. 2016.

[12] Texas Instruments. (Mar. 2019). *77 GHz Radar-on-Chip for Short-Range Radar Applications*. [Online]. Available: http://www.ti.com/product/AWR1642

[13] N. Llombart, K. B. Cooper, R. J. Dengler, T. Bryllert, and P. H. Siegel, "Confocal ellipsoidal reflector system for a mechanically scanned active terahertz imager," *IEEE Trans. Antennas Propag.*, vol. 58, no. 6, pp. 1834–1841, Jun. 2010.

[14] S. S. Ahmed, A. Schiessl, and L.-P. Schmidt, "A novel fully electronic active real-time imager based on a planar multistatic sparse array," *IEEE Trans. Microw. Theory Techn.*, vol. 59, no. 12, pp. 3567–3576, Dec. 2011.

[15] M. T. Ghasr, M. A. Abou-Khousa, S. Kharkovsky, R. Zoughi, and D. Pommerenke, "Portable real-time microwave camera at 24 GHz," *IEEE Trans. Antennas Propag.*, vol. 60, no. 2, pp. 1114–1125, Feb. 2012.

[16] J. Laviada, A. Arboleya-Arboleya, Y. Alvarez, B. Gonzalez-Valdés, and F. Las-Heras, "Multiview three-dimensional reconstruction by millimetre-wave portable camera," *Sci. Rep.*, vol. 7, Jul. 2017, Art. no. 6479.

[17] J. Laviada, A. Arboleya-Arboleya, and F. Las-Heras, "Multistatic millimeter-wave imaging by multiview portable camera," *IEEE Access*, vol. 5, pp. 19259–19268, 2017.

[18] J. Laviada, M. López-Portugués, A. Arboleya-Arboleya, and F. Las-Heras, "Multiview mm-Wave imaging with augmented depth camera information," *IEEE Access*, vol. 6, pp. 16869–16877, 2018.

[19] J. Laviada, F. Las-Heras, M. T. Ghasr, and R. Zoughi, "Multiview imaging with real-time microwave camera from known positions," in *Proc. IEEE Int. Symp. Antennas Propag.*, Boston, MA, USA, Jul. 2018, pp. 613–614.

[20] H. He, P. Maheshwari, and D. J. Pommerenke, "The development of an EM-field probing system for manual near-field scanning," *IEEE Trans. Electromagn. Compat.*, vol. 58, no. 2, pp. 356–363, Apr. 2016.

[21] H. He, V. Khilkevich, and D. Pommerenke, "2D imaging system with optical tracking for EMI source localization," in *Proc. IEEE Symp. Electromagn. Compat. Signal Integrity*, Mar. 2015, pp. 107–110.

[22] C. Baer, J. Barowski, and I. Rolfes, "On the usability of low-cost inertial navigation systems for free-hand SAR imaging at GPR-frequencies," in *Proc. IEEE Sensors Appl. Symp. (SAS)*, Mar. 2017, pp. 1–5.

[23] J. T. Case, M. T. Ghasr, and R. Zoughi, "Nonuniform manual scanning for rapid microwave nondestructive evaluation imaging," *IEEE Trans. Instrum. Meas.*, vol. 62, no. 5, pp. 1250–1258, May 2013.

[24] OptiTrack. (Feb. 2019). *Optitrack Motion Capture System*. [Online]. Available: http://www.optitrack.com

[25] M. Soumekh, *Synthetic Aperture Radar Signal Processing with MATLAB Algorithms*. Hoboken, NJ, USA: Wiley, 1999.

[26] A. Meta, P. Hoogeboom, and L. P. Ligthart, "Signal processing for FMCW SAR," *IEEE Trans. Geosci. Remote Sens.*, vol. 45, no. 11, pp. 3519–3532, Nov. 2007.

[27] J. Barowski, I. Rolfes, and C. Baer, "Real-time imaging system for millimeter wave synthetic aperture radar sensors," in *1st IEEE MTT-S Int. Microw. Symp. Dig.*, May 2017, pp. 1–3.

[28] J. Detlefsen, A. Dallinger, S. Schelkshorn, and S. Bertl, "UWB millimeter-wave FMCW radar using Hubert transform methods," in *Proc. IEEE 9th Int. Symp. Spread Spectr. Techn. Appl.*, Aug. 2006, pp. 46–48.

[29] Z. Wang, J. Li, and R. Wu, "Time-delay- and time-reversal-based robust capon beamformers for ultrasound imaging," *IEEE Trans. Med. Imag.*, vol. 24, no. 10, pp. 1308–1322, Oct. 2005.

[30] M. Klemm, I. J. Craddock, J. A. Leendertz, A. Preece, and R. Benjamin, "Improved delay-and-sum beamforming algorithm for breast cancer detection," *Int. J. Antennas Propag.*, vol. 2008, Apr. 2008, Art. no. 761402.

[31] J. Yang, J. Thompson, X. Huang, T. Jin, and Z. Zhou, "FMCW radar near field three-dimensional imaging," in *Proc. IEEE Int. Conf. Commun. (ICC)*, Jun. 2012, pp. 6353–6356.

[32] G. Álvarez-Narciandi, J. Laviada, M. R. Pino, and F. Las-Heras, "Attitude estimation based on arrays of passive RFID tags," *IEEE Trans. Antennas Propag.*, vol. 66, no. 5, pp. 2534–2544, May 2018.

[33] Vayyar. (May 2019). *System on Chip Specification*. [Online]. Available: http://vayyar.com/technology/

GUILLERMO ÁLVAREZ-NARCIANDI received the M.Sc. degree in telecommunication engineering from the University of Oviedo, Gijón, Spain, in 2016, where he is currently pursuing the Ph.D. degree (with the support of a FPU grant from the Spanish Government). He was a Visiting Student with Stanford University, CA, USA, in 2014. He received the Special Award to the Best Entrepreneurship Initiative from the XV Arquímedes National Contest, in 2017, for the development of a RFID-based location system. He received the 2015 EPIGIJON Industrial Partners Society Award to the Best Applied Project for the development and testing of a hybrid RSS-inertial Indoor positioning system. He has coauthored a patent on attitude estimation using RFID technology. His main research interests include location systems, attitude estimation systems, RFID technology, radar systems, and imaging techniques.

MIGUEL LÓPEZ-PORTUGUÉS received the degree in computer science and the Ph.D. degree from the University of Oviedo, Spain, in 2008 and 2017, respectively, where he is currently a Research Assistant with the TSC-UNIOVI Group. His main research interests include parallel and high-performance computing, computer vision, and fast iterative methods applied to electromagnetic and acoustic scattering problems.

FERNANDO LAS-HERAS (M'86–SM'08) received the M.S. degree and Ph.D. degrees in telecommunication engineering from the Technical University of Madrid (UPM), in 1987 and 1990, respectively. He was a National Graduate Research Fellow, from 1988 to 1990. He was an Associate Professor with the Department of Signal, Systems, and Radiocommunications, UPM, from 1991 to 2000. Since 2003, he has been a Full Professor with the University of Oviedo, where he was the Vice-Dean of telecommunication engineering with the Technical School of Engineering, Gijón, from 2004 to 2008. As of 2001, he heads the Signal Theory and Communications Research Group (TSC-UNIOVI), Department of Electrical Engineering, University of Oviedo. He was a Visiting Lecturer with the National University of Engineering, Peru, in 1996, a Visiting Researcher with Syracuse University, NY, USA, in 2000, and a short term Visiting Lecturer with ESIGELEC, France, from 2005 to 2011. He was the Telefónica Chair of RF Technologies, ICTs Applied to Environment, and ICTs and Smartcities with the University of Oviedo, from 2005 to 2015. He is a member of the Board of Directors of the IEEE Spain Section, from 2012 to 2015, a member of the Board of the IEEE Microwaves & Antennas Propagation Chapter (AP03/MTT17), from 2016 to 2017, a member of the Science, Technology, and Innovation Council of Asturias, in 2010, and the President of the Professional Association of Telecommunication Engineers, Asturias. He has led and participated in a great number of research projects. He has authored over 190 technical journal papers, mainly in the areas of antennas, propagation, metamaterials, and inverse problems with applications to antenna measurement (NF-FF, diagnostics, and holography), electromagnetic imaging (security and NDT) and localization, developing computational electromagnetics algorithms and technology on microwaves, millimeter wave, and THz frequency bands.

JAIME LAVIADA was born in Gijón, Spain. He received the M.S. degree in telecommunication engineering and the Ph.D. degree from the Universidad de Oviedo, Spain, in 2005 and 2010, respectively.

In 2006, he joined the Signal Theory and Communications Research Group, University of Oviedo, where he has been involved in multiple national and European projects as well as contracts with several companies. In 2015, he moved to the Antennas Group, Universidad Pública de Navarra, with a national Postdoctoral fellowship in collaboration with several applied research projects. Finally, he moved back to the Universidad de Oviedo, where he is currently an Assistant Professor. In addition, he was a Visiting Scholar with the Electromagnetics and Communications Laboratory, Pennsylvania State University, from 2007 to 2008, and the Applied Microwave Nondestructive Testing Laboratory, Missouri S&T, in 2017. His research interests include numerical techniques applied to electromagnetic imaging, antenna measurements, the method of moments, and antenna pattern synthesis.

• • •

IV

IV

Publication V

G. Álvarez-Narciandi, J. Laviada, Y. Álvarez-López, and F. Las-Heras, "Portable Freehand System for Real-time Antenna Diagnosis and Characterization," *IEEE Transactions on Antennas and Propagation*, Early Access, 2020.

Portable Freehand System for Real-time Antenna Diagnosis and Characterization

Guillermo Álvarez-Narciandi, Jaime Laviada, Yuri Álvarez-López, *Senior Member, IEEE*, and Fernando Las-Heras, *Senior Member, IEEE*

***Abstract*—This paper presents an agile system for antenna diagnosis. The system is operated by means of freehand movements of the probe antenna avoiding the need of bulky positioners and thus providing portability to the system. For that purpose, the probe antenna position, which is required by the antenna diagnosis algorithm, is retrieved by means of an affordable and quickly-deployable motion capture system. The probe position and the acquired field are used to characterize the antenna under test by computing an equivalent currents distribution on the antenna aperture and its far-field pattern in real-time. To achieve that, an *ad hoc* workflow is designed including a method for spatially balancing the acquired field samples. Although the system is not intended to provide an accuracy comparable to the one achieved by anechoic chamber facilities, it opens a new horizon of possibilities for *in situ* agile characterization of antennas enabling the detection of faulty elements or radiation pattern deviations. Results at Ku and Ka bands, supported by attached multimedia material, are presented to illustrate the capabilities of the system.**

***Index Terms*—Antenna measurements; antenna diagnosis; freehand; equivalent currents; sources reconstruction method; mm-wave antenna.**

I. Introduction

ANTENNA diagnosis aims to detect malfunctions of radiating systems so the corresponding repair actions can be launched. This approach has been widely studied in last decades resulting in a large number of robust methods with different scopes.

On one hand, a large family of antenna diagnosis techniques is devoted to the detection of *faulty elements* by analyzing the impact of one or more failures in the far-field pattern [1], [2]. Since the number of faulty elements is usually expected to be low, this kind of problem can be formulated as a compressed sensing problem taking advantage of the benefits of this technique with respect to sampling [3]. In addition, similar techniques exploiting near-field rather than far-field observations are also available [4]. Although the number of techniques in this family is large, the general advantage is that they can operate with a small number of samples as well as their computational efficiency. The drawbacks are: i) the limited amount of information provided by these techniques as they only provide information about status of elements, which is usually reduced to a binary observation (i.e., healthy or not); ii) a potential relatively wide angular scan can be required when operating in the far-field, which is not always possible.

On the other hand, another large family of techniques exploits the Huygens' principle to reconstruct an equivalent currents distribution at a surface enclosing the antenna under test (AUT). These equivalent currents radiate the same fields as the AUT at any point outside the surface enclosing it [5], [6], [7]. In some cases (e.g. planar antennas, aperture antennas) the surface enclosing the AUT can be truncated to a finite size plane, as most of the energy radiated by the AUT is contained in such plane [8].

In the last years, several equivalent currents-based techniques have been implemented, due to their potential for antenna diagnosis and characterization using arbitrary-geometry measurement and reconstruction domains [6], [9]. Apart from antenna diagnosis, these techniques have been proved to be efficient for removing unwanted structural interactions [10], [11].

In this contribution, the Sources Reconstruction Method (SRM) described in [8] and [5] will be considered. This inverse problem is solved by expanding the unknown currents into known basis functions, whose coefficients are related to the field observations by means of a linear system of equations.

In contrast to the faulty element detection methods, the equivalent currents-based techniques provide information about the amplitude and phase of the fields around the antenna. Moreover, the far-field radiation pattern can be calculated from the reconstructed equivalent currents by means of a near-field to far-field transformation. Consequently, these techniques are able to detect the amplitude and phase of each element of the antenna as well as other undesired effects such as unwanted reflections in the antenna itself or its neighborhood. This insightful information comes at the expense of computationally intensive algorithms to solve the system of equations. However, this last point has been alleviated by means of several approaches such as the fast multiple method (FMM) [12], [13], the adaptive cross algorithm (ACA) [14] or the use of GPUs [15].

Despite the robustness of the previous diagnosis approaches, these techniques usually resort to relatively bulky and heavy equipment in order to provide reliable sampling of the radiated fields. This paper aims to present an *agile diagnosis system*, exploiting the basis of some of the previous approaches, to provide *real-time diagnosis* from *freehand* movements so that the system can bypass the need of heavy positioners. The

This work has been partially supported by the Ministerio de Ciencia, Innovación y Universidades of Spain /FEDER under project RTI2018-095825-B-I00, by the Gobierno del Principado de Asturias under project GRUPIN-IDI-2018-000191 and under the FPU grant FPU15/06431.

The authors are with the Department of Electrical Engineering, University of Oviedo, Gijón, 33203, Spain. (e-mail: alvareznguillermo@uniovi.es; laviadajaime@uniovi.es; alvarezyuri@uniovi.es; flasheras@uniovi.es).

system is mostly intended to work at mm-wave frequencies at which the impact of a non-anechoic environment is in general significantly smaller than at lower frequencies. Although it clearly has an impact in the accuracy, it will be shown that the system is still able to accurately detect the status of the elements and provide a fair estimate of the far-field radiation pattern.

Regarding the kind of diagnosis method, the source reconstruction, conveniently modified to consider the particularities of the system, is used as it provides the more complete information about the amplitude and phase distribution of the antenna as well as its radiation pattern.

The proposed system entails a number of challenges. The first one is the physical implementation as it requires an accurate position tracking as well as portable components. However, current technologies in terms of affordable infrared cameras, providing position reports with an accuracy in the order of ~100-200 μm, as well as portable VNAs make possible to easily implement the system by means of commercial components. In particular, the idea of increasing the flexibility of the acquisition schemes by means of using camera-based positioning systems has been presented in [16] and [17] to directly map either the electric or the magnetic field strength radiated by a device under test onto its predefined 3D model manually. In addition, the same authors also proposed the use of a camera-based positioning system to track a probe under 2D constrained movements in order to map electromagnetic sources by means of backpropagation in [16] and [18]. Although this system improves the flexibility with respect to conventional mechanical acquisition systems, it imposes several constraints that limit its applicability in some scenarios. In particular, it requires a planar structure made of electrically transparent material (such as foam) to ensure a planar scan and a gimbal stabilizer to maintain the orientation of the scanning probe. In addition, it uses an FFT-based method, which requires a regular acquisition grid (missing points are set to zero). The use of a motion capture system in the context of radar imaging was presented in [19].

The second major challenge comes from the fact of acquiring data irregularly sampled due to the freehand scanning. Most of source reconstruction methods are intended to work with data coming from regular grid acquisitions such as planar [20], cylindrical or spherical [6], [21] acquisitions. However, it is relevant to observe that irregularly sampled data has been recently considered by some diagnosis methods to take into account possible deviations from a regular grid, i.e., positioner errors that can be tracked. In particular, quasi-cylindrical, -spherical and -planar data has been studied for diagnosis and near-field to far-field transformations based on plane or spherical wave expansions [22], [23], [24], which can also be formulated in terms of a linear system of equations but relating electromagnetic modes rather than equivalent currents (see [25] for a detailed comparison). In the specific framework of source reconstruction, irregular sampling has been considered on systems based on a large gondola-positioner in which accurate position control is not possible [26] and on systems based on unmanned air vehicles [27], [28]. However, none of the previous works are focused on dealing with the kind of irregularities which can appear when performing freehand scanning.

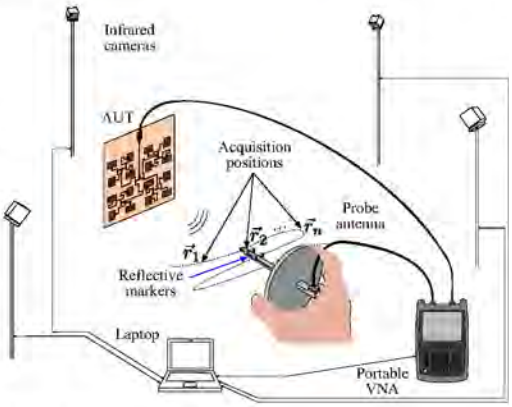

Fig. 1. Scheme of the proposed system.

The main contribution of this manuscript, which extends the conference paper presented in [29], is a setup to perform freehand antenna diagnosis complemented by a modified source reconstruction method to provide real-time results which takes into account the irregular sampling due to the freehand scanning.

This paper is organized as follows. First, the system architecture is presented and the workflow of the system is described in Section II. Validation of the system with measurements from different AUTs is presented in Section III, discussing and comparing them with those obtained using a planar range. Finally, the conclusions are drawn in Section IV.

II. Description of the System

The presented system aims to characterize an antenna under test by means of the equivalent sources computed on a surface enclosing the AUT. The sources are computed from near-field samples measured at arbitrary positions by means of freehand movements of the probe antenna. The relevant hardware components, the system flowchart and the modified source reconstruction method are described next.

A. Hardware

The main components of the system are depicted in Fig. 1. The system comprises three major subsystems: i) electromagnetic field acquisition subsystem; ii) positioning subsystem; iii) processing subsystem. In general, commercial off-the-shelf components will be used for the implementation.

The *electromagnetic field acquisition subsystem* comprises a probe antenna and a vector network analyzer (VNA). As in conventional antenna measurements, the VNA is connected to the AUT as well as to the probe antenna (e.g., an open-ended waveguide) to acquire the S_{21} parameter. In the presented implementation, two different VNAs have been used. The first

one is a Fieldfox N9950A, which is a portable VNA with capabilities to perform measurements up to 14 GHz. The second VNA is a Keysight PNA-X, which provides better capabilities in terms of dynamic range, time sweep and frequency range at the expenses of larger dimensions and weight in line with standard laboratory analyzers.

In order to perform the antenna diagnosis, it is necessary to know the radiated field but also the position at which the field samples are acquired. Thus, the second major component of the system is the *positioning subsystem*. This subsystem is devoted to acquire both the position and attitude of the probe antenna. The positioning subsystem must meet several requirements. First, it must be compatible with the probes so it does not require significant, if any, modifications of the probe. Second, it must be accurate enough so that positioning error has a low or negligible impact in the final result. The latter criteria is met as long as the positioning error is much smaller than the working wavelength. Third, the positioning system must provide real-time position information.

In the implementation presented in this contribution, a motion capture system [30] has been adapted to work as positioning subsystem. The system comprises four infrared cameras at fixed positions and four markers with a diameter of 6.5 mm, which can be easily attached to most of probes. The system can be easily calibrated in a few minutes by means of its own calibration software and moving a wand with markers at known positions. The system provides up to 240 positions per second, which is enough for a real-time system. In our setup, the calibration shows an error in the range of $100-200\,\mu$m. Thus, this error is expected to have a negligible impact in the final results up to 15 GHz if the criteria of $\lambda/100$ is assumed as in IEEE standards for antenna measurements [31], [32]. However, since other sources of error are expected to have a larger impact (e.g., reflections due to the lack of an anechoic environment), the positioning error can be relaxed. In particular, under a criterion of $\lambda/10$, the setup is expected to provide fair results up to 150 GHz.

The third pillar of the presented system is the *processing subsystem*. This subsystem processes the acquired radiated field and positions by means of a source reconstruction method (SRM) to obtain the antenna diagnosis information. In addition, it also triggers the synchronous acquisition of the position and radiated field. The flowchart of this processing is detailed later in section II-B. This processing subsystem is implemented by means of one or two conventional PCs [1] since the sample acquisition and the SRM can be run in independent computers to alleviate the computational cost.

B. Flowchart

The system is based on continuously moving the probe antenna over the antenna under test so that the radiated field is sampled at different positions. During this process, the system continuously updates the antenna characterization in terms of equivalent currents in the aperture and of far-field pattern. Those functionalities are implemented by means of the flowchart shown in Fig. 2.

[1] In general, laptops are preferred due to portability concerns.

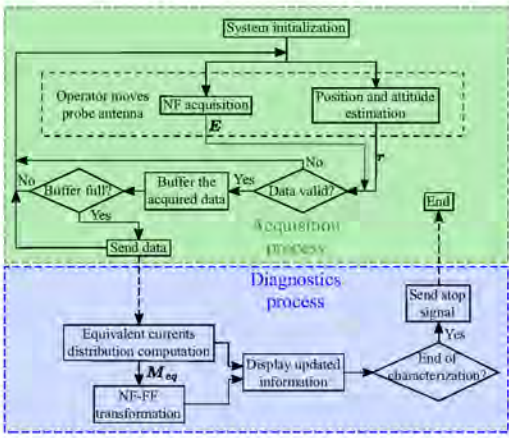

Fig. 2. Workflow of the proposed system.

The workflow involves two independent processes, which can be run in different machines, both in parallel to the operator movements. The *acquisition process* is in charge of the synchronous acquisition of the position and field samples. In order to balance the sample distribution, the approach detailed in section II-D is used, resulting in some discarded samples based on the acquisition position. In addition, in order to ensure that the main lobe of the probe antenna points to the front as in a conventional planar range and that the desired polarization is measured, the orientation of the probe antenna is monitored and measurements when the yaw, pitch or roll angles of the probe are above a given threshold are also discarded. According to the performed measurements, a threshold value of 5° provides a good trade-off between scanning speed and accuracy. Furthermore, in order to set an upper bound of the probe movement during a frequency sweep, the position of the probe is queried before and after the sweep and, if the difference is higher than a given frequency-dependent threshold, the sample is discarded. In particular, for the measurements discussed in this paper this threshold was set to 1 mm in the case of the mm-wave frequency measurements and to 2 mm in the case of the X-band measurements. Non-discarded samples are buffered until a certain amount of samples is gathered and, after that, the samples are sent to the *diagnosis process*. The sample buffer avoids an unnecessary computational burden associated to recomputing the equivalent currents for each new acquisition as the operator usually does not require an update rate so high.

The *diagnosis process* receives and stores the position and field samples. After receiving each set of samples, it computes the equivalent currents distribution and the radiation pattern of the AUT (see next section for further details) while more data is acquired by the operator. The diagnosis information (currents distribution and radiation pattern) is updated and displayed in real-time, alongside with a heatmap depicting where measurements have been acquired. In addition, the

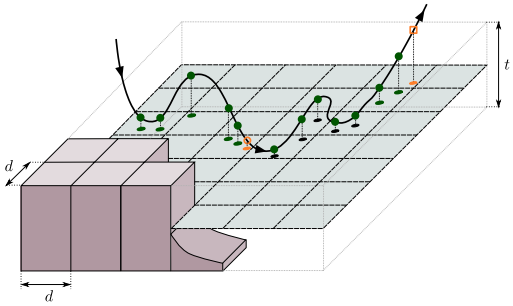

Fig. 3. Sampling distribution balance by setting maximum number of samples per cell. In order to help in the visualization of the trajectory and sampling position, only a few cells are shown together with the center of the cells. Orange samples are discarded either because the maximum number of samples is exceeded (e.g., the empty orange circle sample) or because the maximum vertical tolerance is exceeded (e.g, the empty orange square sample). A maximum of two samples per cell is considered.

V

amplitude and phase of the acquired fields are shown on a bidimensional grid. All the previous real-time information is intended to aid the operator to decide how to proceed to scan. For example, the operator can dynamically change from scanning a certain area to a different one based on the achieved sample density, the lack of impact of new samples in the final result, energy of the sampling area, etc.

C. Source Reconstruction Method

The acquired field and position samples are processed by means of a source reconstruction method (SRM) [5]. In the presented implementation, a planar reconstruction domain (usually placed at the antenna aperture) is chosen and, therefore, only the equivalent magnetic currents are needed [8]. The magnetic currents are discretized by means of known basis functions yielding the following linear system of equations:

$$\overline{\overline{A}} \begin{bmatrix} b_1 \\ b_2 \\ \vdots \\ b_N \end{bmatrix} = \begin{bmatrix} E_1 \\ E_2 \\ \vdots \\ E_M \end{bmatrix} \tag{1}$$

where b_n is the weight of the n-th basis function and E_m is the field sample at the m-th considered position. The matrix $\overline{\overline{A}}$ has dimensions $M \times N$ where N is the number of basis functions and M is the number of considered NF samples. The elements at row m and column n of matrix $\overline{\overline{A}}$ relate the field at the m-th position radiated by the n-th basis function with the corresponding evaluation of the Green's function [5].

The previous system of equations, which is usually overdetermined, is solved by means of an iterative solver, such as the conjugated gradient method**,** providing the minimum error and energy solution to (1). After that, the far-field radiation pattern is computed by using the corresponding radiation integrals [33].

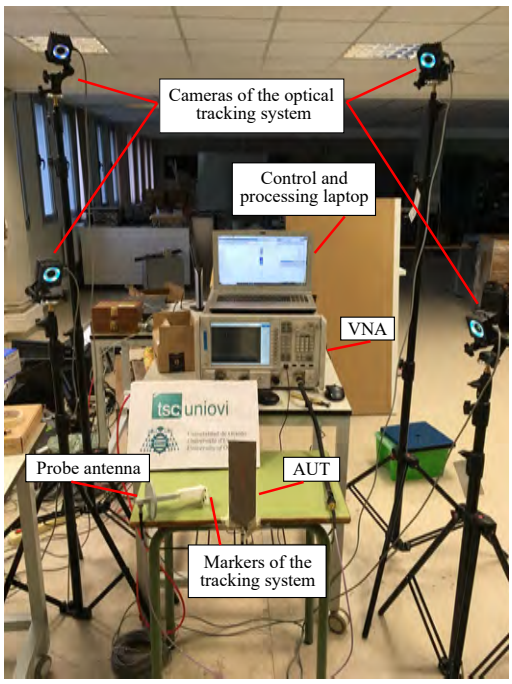

Fig. 4. Measurement setup.

D. Sampling distribution balance

The acquisition process is continuously registering positions and field samples. This fact, together with the non regular hand movements, will result in an uneven sampling distribution. For example, if the operator stops (or moves slowly) at a certain area, the system would keep sampling yielding a high number of samples for a small region. This kind of *locally* oversampled areas can result in an anomalous solution of (1) due to the higher weight that would be given to them. For this reason, an approach to locally balance the sample distribution is required.

In this work, the uneven sampling problem is solved by limiting the number of local samples per given surface area. This is implemented by splitting the observation volume, i.e., the volume in which the samples are acquired, into non-overlapped cells and setting a maximum number of samples per cell P. In particular, only the first P samples acquired inside a given cell are considered so any additional acquisition in that cell is discarded. The system of equations given in (1) can be easily implemented by updating the matrix $\overline{\overline{A}}$ with new rows corresponding to these new acquisitions.

In our implementation, the cells are chosen so that the acquisition *macroscopically* mimic a conventional planar range acquisition. In particular, cells are shaped as rectangular cuboids with dimensions $d \times d \times t$ (see Fig. 3). On one hand, the horizontal dimensions d of the cuboids are intended to play the role of the conventional sampling steps and, therefore,

Fig. 5. Measured two horn antenna array.

they should be in the order of $\lambda/2$. However, this size can be relaxed if more than one sample per cuboid is considered. On the other hand, the vertical cell size t enables some tolerance so that it relaxes the operator movement and it is usually chosen up to $\lambda/2$ to avoid electrically large gaps between adjacent samples. It should be pointed out that when more than one acquisition per cell is performed, i.e. $P > 1$, the effective sampling step in the vertical dimension would be smaller than the value of the tolerance, t, and, thus, the requirement of $t < \lambda/2$ can be relaxed. Since samples outside those cells are discarded, a visual aid is included in the interface so that the operator knows the distance to the cells bottom and top in order to move the probe to the corresponding area. In addition, the density of samples per cell is shown by means of the aforementioned heatmap.

An example of the use of cells is shown in Fig. 3. In this example, only a few cuboids are shown to ease the visualization of the trajectory of the probe and the acquired samples, but a plane through the center of the cells is shown to help in illustrating the process. In this example, a maximum of two samples per cell (i.e., $P = 2$) is considered. Thus, the sample corresponding to the orange empty circle marker is discarded since two samples are already available. In addition, the sample corresponding to the orange empty square marker is also discarded because the vertical tolerance is exceeded.

In addition to mitigate the effect of non-equally spaced samples, it is important to note that there are some environmental agents that can distort the measurement. In particular, these agents are: a) coupling between the AUT and the probe as well as between the probe and the operator holding the antenna; b) reflections due to the non-anechoic environment.

The reactive coupling between the AUT and the probe follows the same rules as in conventional planar measurements and therefore it is considered that the near-field acquisition can be successfully performed as long as a distance of a few wavelengths is considered [34]. It is relevant to consider that, as in conventional planar range measurements, the distance between the AUT and the acquisition plane (i.e., the reference surface) also has an impact on the plane truncation error [34].

Regarding the coupling between the probe and the person who is holding it (i.e., touching the probe antenna), a coupling similar to the supporting structures such as the ones in conventional facilities (e.g., an anechoic chamber) is expected. In this regard, the use of electrically long open-ended waveguides (OEWG) is recommended in order to reduce reactive coupling.

Finally, the reflections due to the non-anechoic environment (including the operator) are also expected to have an impact in the accuracy of the system. These reflections are inherent to any *in situ* measurements. However, the impact of these reflections is expected to be significantly alleviated at high frequencies due to the propagation losses. As it will be experimentally shown, a good quality is found at mm-wave frequencies, whereas the system still shows a fair quality at a few GHz (12 GHz).

III. Validation of the System

The performance of the proposed system was assessed through several measurements conducted at the research facilities of the Signal Theory and Communications group of the University of Oviedo (TSC-UniOvi). A general overview of the setup is depicted in Fig. 4. The first set of tests consisted of different measurements of a two horn antenna array at Ka band and using the laboratory VNA (Keysight PNA-X) to measure the radiated signal. During the second set of tests a leaky wave antenna at 12 GHz was characterized using both the aforementioned VNA and a portable VNA (Keysight Fieldfox N9950A). The sweep time of the PNA-X, which was configured to measure 201 frequency points in all of the measurements, was 1.45 ms and that of the Fieldfox, which was configured to measure 11 frequency points, was 24 ms. The reference results of each set of measurements are compared with the ones obtained with a planar range of the University of Oviedo.

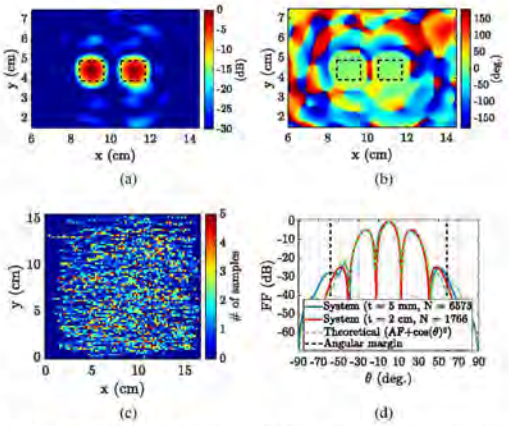

Fig. 6. Magnitude (a) and phase (b) of the equivalent currents distribution retrieved from the NF measurements, which were acquired at the positions depicted in the heatmap (c). The H-plane cut of the far-field pattern computed through a NF-FF transformation is shown in (d).

A. Two horn antenna array

First, a two horn antenna array at Ka band with the antennas separated 2.1 cm (Fig. 5) was measured. Four markers were attached by means of a 3D printed support structure to the

V

probe antenna, which was an open-ended waveguide WR28, so that it could be tracked by the motion capture system.

A total of 6573 measurements were taken at an average distance of 3.5 cm from the AUT and the size of the cuboids used to balance the sampling was given by $d = 2$ mm and $t = 5$ mm. The total acquisition time was 892 s. The magnitude and the phase of the computed equivalent currents distribution at 32 GHz are shown in Figs. 6a and 6b, respectively. As it can be seen, two similar sources both in phase and magnitude, corresponding to the two horn antennas of the array, can be clearly identified (the area corresponding to the aperture of each horn is enclosed by a black dashed line). The maximum of both sources differ only in 0.58 dB in magnitude and 1.2° in phase (which may result from small imperfections in the setup of the array), and the separation between sources matches the physical space between both horns. The phase variation across the aperture of the horns is 27.9°. The heatmap, depicting where measurements were taken, is shown in Fig. 6c. Finally, the H-plane of the far-field pattern obtained from the equivalent currents distribution after performing a NF-FF transformation is shown in blue in Fig. 6d. The theoretical pattern, depicted in red, was obtained considering an array of two elements separated the same distance as the actual horn-array, fed with equal magnitude and phase and considering an element radiation pattern of $\cos^5(\theta)$. The side lobes of the H-plane cut of both patterns are at $\pm 22°$, being the correspondence between the theoretical model and the pattern obtained from the measurements very good within the angular margin of validity of the measurements.

V

In addition, the same AUT was measured using the proposed system but increasing the height of the cuboids (i.e. its dimension in the measurement direction) used to control the sampling to $t = 2$ cm. In this case measurements were acquired at an average distance of 6.1 cm from the AUT. The computed H-plane of the far-field pattern is depicted in dashed-green line in Fig. 6d. As it can be seen, although the obtained pattern is slightly different, the accuracy is still sufficient for a fast diagnostic and characterization of an AUT outside a laboratory facility such as an anechoic chamber. In addition, relaxing the control of the sampling allows for a much faster diagnostic of antennas (the total scanning time for $t = 2$ cm was reduced to only 223 s).

The same array was deployed inside a conventional planar range at the University of Oviedo [35] and it was measured using both the planar range and the proposed system to compare the obtained results with the reference ones retrieved using conventional techniques. Nevertheless, some cables were replaced resulting in slightly different phase shifts and, consequently, radiation patterns. The measurement setup is depicted in Fig. 7, where it is possible to observe the two-horn antenna array inside the planar range and the cameras of the motion capture system. During the freehand scan, a total of 4091 samples were acquired in an area of 19.6×23.3 cm at 7.1 cm from the AUT in 984 s. Using the planar range, a total of 3135 acquisitions were performed in a regular grid of 24.3×25.2 cm at 10 cm from the AUT. The step between consecutive samples was $\lambda/2$ at 32 GHz and the total acquisition time was 6173 s.

Fig. 7. Measurement setup in the planar range.

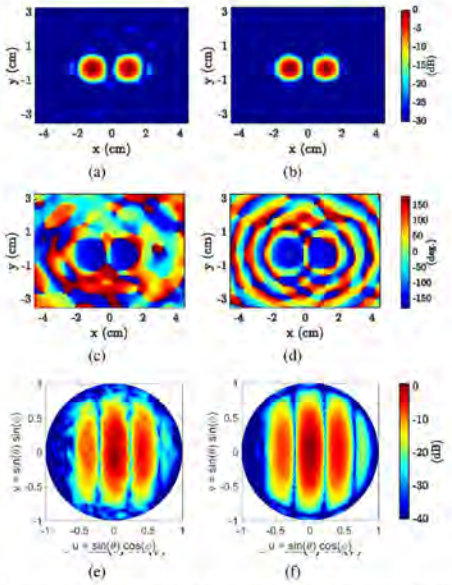

Fig. 8. Amplitude and phase of the computed equivalent currents distribution obtained using the proposed system (a) and (b), respectively, and employing a standard planar range (c) and (d), respectively. UV representation of the retrieved antenna radiation pattern obtained using the proposed system (e) and employing a standard planar range (f).

The amplitude of the reconstructed equivalent currents distribution at 32 GHz is depicted in Fig. 8a and Fig. 8b using the measurements obtained with the proposed system and with the standard planar range, respectively. As it can be seen, although small artifacts below -20 dB appear when using the proposed system, the results are similar. The same holds for the phase of the reconstructed equivalent currents distribution, which is shown in Fig. 8c and Fig. 8d using the proposed system and the planar range, respectively. The radiation pattern computed

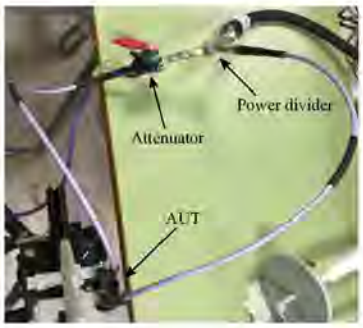

Fig. 9. Measurement setup using an attenuator connected to one of the horns of the two antenna array.

from the equivalent currents distribution estimated using the proposed system and the planar range is depicted in Fig. 8e and Fig. 8f, respectively. As it can be observed, although the pattern obtained with the proposed system is noisier than the one measured with the planar range, the main and the secondary lobes are well-reconstructed, which demonstrates the accuracy of the proposed system.

B. Two horn antenna array with an attenuator

For the next test a variable attenuator was added to one element of the previous two horn antenna array (Fig. 9). In this case the VNA was configured to acquire 201 frequency points between 24 and 32 GHz and the same probe antenna as in the former experiment was used. During the scan a total of 7271 acquisitions were performed at an average distance of 3.6 cm from the AUT and the size of the cuboids used to balance the sampling were given by $d = 2$ mm and $t = 5$ mm.

Results for $f = 32$ GHz are shown in Fig. 10. At this frequency, the attenuator level, previously measured using the VNA, is 4.6 dB. This level matches the difference existing between the amplitude values of the reconstructed equivalent currents on each horn antenna aperture (Fig. 10a), which results in 4.5 dB. In addition, the phase shift between the reconstructed currents on each aperture is 55° (Fig. 10b), in agreement with the extra phase shift of the attenuator branch measured with the VNA. The heatmap depicting where measurements were taken is shown in Fig. 10c and the H-plane cut of the far-field pattern computed through a NF-FF transformation is shown in blue in Fig. 10d, where a good correspondence in the main and side lobes with a theoretical model can be observed; higher differences appear for values of other secondary lobes of the pattern below −20 dB.

The difference in both magnitude and phase of the maximum of the equivalent currents distribution between both horn antennas is depicted for all the measured frequencies in Figs. 11a and 11b, respectively. In addition, the same difference, depicted in red, was characterized using the VNA measuring directly the S_{21} parameter between the end ports of the array feeding network. As it can be seen in Fig. 11a, the difference in magnitude obtained with the diagnosis system and from

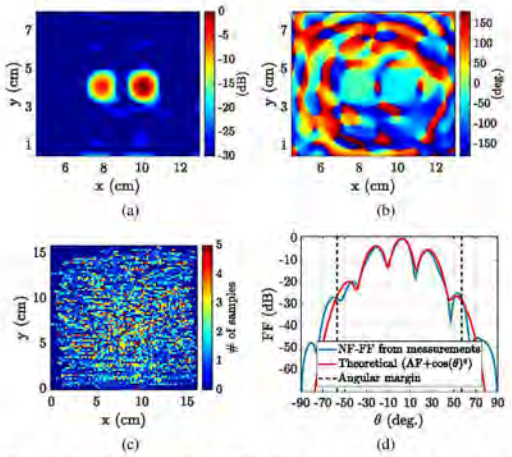

Fig. 10. Magnitude (a) and phase (b) of the equivalent currents distribution retrieved from the NF measurements that were acquired at the positions depicted in the heatmap (c). The H-plane cut of the far-field pattern computed through a NF-FF transformation is shown in (d).

the feeding network measurement are very similar with errors below 1 dB. The curve obtained with the proposed antenna measurement system presents a higher ripple, probably due to the presence of reflections in the near environment. The phase difference retrieved using the system is very similar to that obtained using the VNA across the whole measured frequency range as can be observed in Fig. 11b. As it can be seen, in 97% of the cases the error is below 5°, being the maximum error 7.8°.

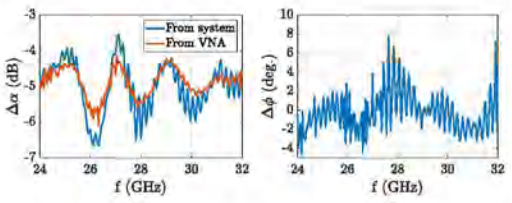

Fig. 11. Difference in magnitude between the maximum of the equivalent currents distribution corresponding to each horn of the array (a). The value retrieved using the proposed system is depicted in blue and the difference obtained using the VNA is depicted in red. The error between the phase values of that same difference obtained using the VNA and the proposed system is depicted in b).

C. Leaky-wave antenna

Finally, the leaky-wave antenna depicted in Fig. III-C was diagnosed at 12 GHz with the proposed system, using both the PNA-X and the Fieldfox portable VNA. In addition, this antenna was also measured in a conventional planar range [35] in order to have a reference result. The probe antenna was an open-ended waveguide WR90.

V

Using the proposed system and the PNA-X a total of 937 NF samples were acquired. Measurements were taken at an average distance of 11 cm from the AUT, covering an area of 27×33 cm, and the size of the cuboids used to balance the sampling were given by $d = 1$ cm and $t = 1$ cm.

Fig. 12. Measured leaky-wave antenna.

Concerning the measurements using the planar range with the setup depicted in Fig. 13, a total of 10201 NF samples were acquired in a planar domain of 1×1 m, with a sampling step of 1 cm in the x- and y- axes.

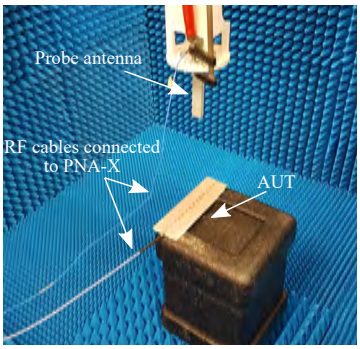

Fig. 13. Measurement setup in the planar range.

The magnitude of the equivalent currents distribution obtained using the proposed system and the planar range are depicted in Figs. 14a and 14b, respectively. As it can be seen, the shape and magnitude of the currents are in good agreement. In addition, in order to show the influence of the value of d, the NF samples acquired with the proposed system were post-processed using $d = 2$ cm (0.8λ). The computed equivalent currents distribution are also depicted in Fig. 14c, where it can be noticed how the reconstructed equivalent currents distribution exhibits more artifacts.

The phase of the equivalent currents distribution retrieved with the proposed system and with the planar range are depicted in Figs. 15a and 15b, respectively. For a better comparison, only the phase where the magnitude of the equivalent currents distribution is above -15 dB is plotted. As it can be observed, both phase profiles are in good agreement.

Finally, the far-field pattern was computed from the equivalent currents distribution by means of a NF-FF transformation. In particular, the results of the E-plane cut obtained using the proposed system with the PNA-X, the proposed system with the Fieldfox portable VNA as well as using the planar range are depicted in Fig. 16. Using the Fieldfox portable VNA a total of 764 samples were acquired at an average distance of 10.3 cm, covering an area of 26×31cm. In this example, it can be noticed that the proposed system, using both hardware configurations, is able to correctly compute the position of the maximum of the field pattern at $\theta = -22°$. In addition, the -15 dB sidelobe at $\theta = 20°$ is also predicted and the rest of radiation pattern in the angular margin of validity (denoted with vertical dashed lines in Fig. 16) is in a fair agreement with the planar range results despite the freehand measurements not being accomplished in an anechoic environment.

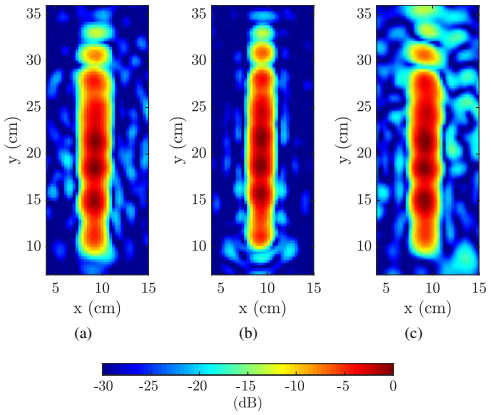

Fig. 14. Magnitude of the computed equivalent currents distribution obtained using the proposed system and $d = 1$ cm (a), using a planar range (b) and employing the proposed system and $d = 2$ cm (c).

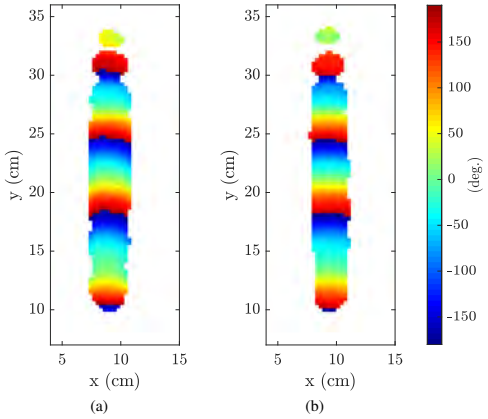

Fig. 15. Phase of the equivalent currents distribution retrieved from the NF measurements obtained using the proposed system (a) and using a planar range (b). Only the phase where the magnitude of the equivalent currents distribution is above -15 dB is plotted.

IV. Conclusions

A system to perform freehand scanning of antennas providing fast diagnosis without the need of a typical antenna measurement range has been presented. The system comprises

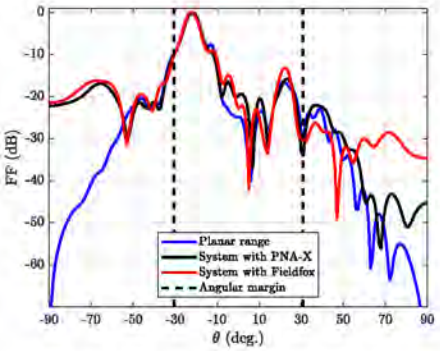

Fig. 16. Measured E-plane cut of the radiation-pattern of the leaky-wave antenna.

a handheld probe antenna, which is moved in front of the AUT aperture, a VNA, which is connected to both the probe antenna and the AUT, a motion capture system to retrieve the position of the probe antenna, and a conventional laptop in charge of controlling the field and position samples and of processing the acquired data. During the scan, field and position acquisitions are triggered as the operator moves the antenna in front of the AUT and the SRM is applied to the obtained data to provide a real-time estimation of an equivalent currents distribution on the aperture of the AUT and its radiation pattern after a NF-FF transformation is performed. In addition, several strategies to cope with non regular hand movements of the probe antenna, which result in an uneven distribution of field samples, are discussed.

The proposed system was validated through several sets of measurements in Ku and Ka bands. The results show that a fast and rough diagnosis of the status of radiating elements can be obtained in a few seconds while a full and more accurate characterization of antennas can be achieved in only a few minutes for low to medium size antennas. Although the accuracy is not expected to be as high as the one obtained in typical anechoic antenna measurement ranges, the results obtained with the presented system exhibit very good accuracy at mm-wave frequencies.

In addition, the presented system can be deployed in a matter of minutes and it can be easily implemented with portable components, paving the way to a new approach to perform fast, *in situ* diagnosis. Future work will focus on modifying the system to include phaseless algorithms to avoid the need of a connection to the antenna under test as well as to reduce the overall cost.

REFERENCES

[1] O. M. Bucci, A. Capozzoli, and G. D'Elia, "Diagnosis of array faults from far-field amplitude-only data," *IEEE Transactions on Antennas and Propagation*, vol. 48, no. 5, pp. 647–652, May 2000.

[2] J. A. Rodriguez-Gonzalez, F. Ares-Pena, M. Fernandez-Delgado, R. Iglesias, and S. Barro, "Rapid method for finding faulty elements in antenna arrays using far field pattern samples," *IEEE Transactions on Antennas and Propagation*, vol. 57, no. 6, pp. 1679–1683, June 2009.

[3] G. Oliveri, P. Rocca, and A. Massa, "Reliable diagnosis of large linear arrays—a bayesian compressive sensing approach," *IEEE Transactions on Antennas and Propagation*, vol. 60, no. 10, pp. 4627–4636, Oct 2012.

[4] M. D. Migliore, "A compressed sensing approach for array diagnosis from a small set of near-field measurements," *IEEE Transactions on Antennas and Propagation*, vol. 59, no. 6, pp. 2127–2133, June 2011.

[5] Y. Alvarez, F. Las-Heras, and M. R. Pino, "Reconstruction of equivalent currents distribution over arbitrary three-dimensional surfaces based on integral equation algorithms," *IEEE Transactions on Antennas and Propagation*, vol. 55, no. 12, pp. 3460–3468, Dec 2007.

[6] J. Araque and G. Vecchi, "Field And Source Equivalence In Source Reconstruction On 3D Surfaces," *Progress In Electromagnetics Research*, vol. 103, pp. 67–100, 2010.

[7] K. Persson and M. Gustafsson, "Reconstruction of equivalent currents using a near-field data transformation with radome applications," *Progress In Electromagnetics Research*, vol. 54, pp. 179–198, 2005.

[8] F. Las-Heras and T. K. Sarkar, "A direct optimization approach for source reconstruction and nf-ff transformation using amplitude-only data," *IEEE Transactions on Antennas and Propagation*, vol. 50, no. 4, pp. 500–510, April 2002.

[9] E. Cano, M. Sierra-Castañer, S. Burgos, and J. L. Besada, "Applications of sources reconstruction techniques: Theory and practical results," in *Proceedings of the Fourth European Conference on Antennas and Propagation*, April 2010, pp. 1–5.

[10] J. Araque and G. Vecchi, "Removal of unwanted structural interactions from antenna measurements," in *2009 IEEE Antennas and Propagation Society International Symposium*, June 2009, pp. 1–4.

[11] L. J. Foged, L. Scialacqua, F. Saccardi, J. L. A. Quijano, G. Vecchi, and M. Sabbadini, "Practical application of the equivalent source method as an antenna diagnostics tool [amta corner]," *IEEE Antennas and Propagation Magazine*, vol. 54, no. 5, pp. 243–249, Oct 2012.

[12] Y. Alvarez, F. Las-Heras, M. R. Pino, and J. A. Lopez, "Acceleration of the sources reconstruction method via the fast multipole method," in *2008 IEEE Antennas and Propagation Society International Symposium*, July 2008, pp. 1–4.

[13] T. F. Eibert and C. H. Schmidt, "Multilevel fast multipole accelerated inverse equivalent current method employing rao–wilton–glisson discretization of electric and magnetic surface currents," *IEEE Transactions on Antennas and Propagation*, vol. 57, no. 4, pp. 1178–1185, April 2009.

[14] Y. Alvarez, F. Las-Heras, and M. R. Pino, "Application of the adaptive cross approximation algorithm to the sources reconstruction method," in *2009 3rd European Conference on Antennas and Propagation*, March 2009, pp. 761–765.

[15] J. A. Lopez-Fernandez, M. Lopez-Portugues, Y. Alvarez-Lopez, C. Garcia-Gonzalez, D. Martinez, and F. Las-Heras, "Fast Antenna Characterization Using the Sources Reconstruction Method on Graphics Processors," *Progress In Electromagnetics Research*, vol. 126, pp. 185–201, 2012.

[16] H. He, "The development of near field probing systems for EMC near field visualization and EMI source localization," Master's thesis, Missouri University of Science and Technology, 2015. [Online]. Available: https://scholarsmine.mst.edu/masters_theses/7435

[17] H. He, P. Maheshwari, and D. J. Pommerenke, "The Development of an EM-Field Probing System for Manual Near-Field Scanning," *IEEE Transactions on Electromagnetic Compatibility*, vol. 58, no. 2, pp. 356–363, April 2016.

[18] H. He, V. Khilkevich, and D. Pommerenke, "2D imaging system with optical tracking for EMI source localization," in *2015 IEEE Symposium on Electromagnetic Compatibility and Signal Integrity*, March 2015, pp. 107–110.

[19] G. Álvarez-Narciandi, M. López-Portugués, F. Las-Heras, and J. Laviada, "Freehand, agile, and high-resolution imaging with compact mm-wave radar," *IEEE Access*, vol. 7, pp. 95 516–95 526, 2019.

[20] P. Petre and T. K. Sarkar, "Planar near-field to far-field transformation using an equivalent magnetic current approach," *IEEE Transactions on Antennas and Propagation*, vol. 40, no. 11, pp. 1348–1356, Nov 1992.

[21] Y. Alvarez Lopez, F. Las-Heras Andres, M. R. Pino, and T. K. Sarkar, "An improved super-resolution source reconstruction method," *IEEE Transactions on Instrumentation and Measurement*, vol. 58, no. 11, pp. 3855–3866, Nov 2009.

[22] C. H. Schmidt and T. F. Eibert, "Assessment of irregular sampling near-field far-field transformation employing plane-wave field representation," *IEEE Antennas and Propagation Magazine*, vol. 53, no. 3, pp. 213–219, June 2011.

[23] M. Farouq, M. Serhir, and D. Picard, "Matrix method for far-field calculation using irregular near-field samples for cylindrical and spherical

V

scanning surfaces," *Progress In Electromagnetics Research B*, vol. 63, pp. 35–48, 2015.
[24] ——, "Matrix method for antenna plane wave spectrum calculation using irregularly distributed near-field data: Application to far-field assessment," *Progress In Electromagnetics Research M*, vol. 42, pp. 71–83, 2015.
[25] Y. Alvarez, F. Las-Heras, and M. R. Pino, "On the comparison between the spherical wave expansion and the sources reconstruction method," *IEEE Transactions on Antennas and Propagation*, vol. 56, no. 10, pp. 3337–3341, Oct 2008.
[26] A. Geise, O. Neitz, J. Migl, H. Steiner, T. Fritzel, C. Hunscher, and T. F. Eibert, "A crane based portable antenna measurement system — system description and validation," *to appear in IEEE Transactions on Antennas and Propagation*, pp. 1–1, 2019.
[27] M. García-Fernández, Y. Álvarez López, A. Arboleya, B. González-Valdés, Y. Rodríguez-Vaqueiro, M. E. De Cos Gómez, and F. Las-Heras Andrés, "Antenna diagnostics and characterization using unmanned aerial vehicles," *IEEE Access*, vol. 5, pp. 23 563–23 575, 2017.
[28] G. Virone, A. M. Lingua, M. Piras, A. Cina, F. Perini, J. Monari, F. Paonessa, O. A. Peverini, G. Addamo, and R. Tascone, "Antenna pattern verification system based on a micro unmanned aerial vehicle (uav)," *IEEE Antennas and Wireless Propagation Letters*, vol. 13, pp. 169–172, 2014.
[29] G. Álvarez-Narciandi, J. Laviada, Y. Álvarez-López, and F. Las-Heras, "Rapidly Deployable Portable System for Real-Time Antenna Diagnostics and Characterization," in *2019 IEEE International Symposium on Antennas and Propagation and USNC-URSI Radio Science Meeting*, July 2019, pp. 1689–1690.
[30] OptiTrack. (2019, May) Optitrack motion capture system. [Online]. Available: http://www.optitrack.com
[31] "IEEE Recommended Practice for Near-Field Antenna Measurements," *IEEE Std 1720-2012*, pp. 1–102, Dec 2012.
[32] "IEEE Standard Test Procedures for Antennas," *ANSI/IEEE Std 149-1979*, 1979.
[33] C. A. Balanis, *Advanced Engineering Electromagnetics*. Wiley, 2010.
[34] S. Gregson, *Principles of Planar Near-Field Antenna Measurements*, ser. Electromagnetic Waves. Institution of Engineering and Technology, 2007. [Online]. Available: https://digital-library.theiet.org/content/books/ew/pbew053e
[35] A. Arboleya, Y. Álvarez, and F. Las-Heras, "Millimeter and submillimeter planar measurement setup," in *2013 IEEE Antennas and Propagation Society International Symposium (APSURSI)*, July 2013, pp. 1–2.

V

Guillermo Alvarez-Narciandi Guillermo Álvarez-Narciandi received the M.Sc. degree in Telecommunication Engineering from the University of Oviedo, Gijón, Spain, in 2016, where he is currently working towards the Ph.D. degree (with the support of a FPU grant from the Spanish Government). He was a Visiting Student at Stanford University, CA, USA, in 2014, and a visiting scholar at the University of Pisa (Italy) in 2018 and at the Institute of Electronics, Microelectronics and Nanotechnology (IEMN), University of Lille (France) in 2019. He received the AMTA 2019 Student Paper Award (second place) and the Special Award to the Best Entrepreneurship Initiative in the XV Arquímedes national contest in 2017 for the development of a RFID-based location system. His main research interests are radar systems and imaging techniques, antenna diagnosis and characterization systems, localization and attitude estimation systems and RFID technology.

Jaime Laviada Jaime Laviada was born in Gijón, Spain. He received the M.S. degree in telecommunication engineering and the Ph.D. degree from the Universidad de Oviedo, Spain (http://www.uniovi.es), in 2005 and 2010, respectively. In 2006, he joined the research group Signal Theory and Communications of the Universidad de Oviedo, where he has been involved in multiple national and European projects as well as contracts with several companies. In 2015, he moved to the Antennas Group of the Universidad Pública de Navarra with a national postdoctoral fellowship collaborating in several applied research projects. Finally, he moved back to the Universidad de Oviedo where he currently holds a position of associate professor. In addition, he has been a Visiting Scholar in the Electromagnetics and Communications Lab, Pennsylvania State University, during 2007 and 2008 as well as in the Applied Microwave NonDestructive Testing Laboratory, Missouri S&T, during 2017. His research interests include numerical techniques applied to EM imaging, antenna measurements, method of moments, and antenna pattern synthesis.

Yuri Alvarez-López Yuri Álvarez López (S'06–M'09–SM'15) was born in Langreo, Spain, in 1983. He received the M.S. and Ph.D. degrees in telecommunication engineering from the Universidad de Oviedo, Gijón, Spain, in 2006 and 2009, respectively. He was a Visiting Scholar with the Department of Electrical Engineering and Computer Science, Syracuse University, Syracuse, NY, USA, in 2006 and 2008, respectively, held a visiting post-doctoral position at the Gordon Center for Subsurface Sensing and Imaging Systems Awareness and Localization of Explosive Related Threats Center of Excellence, Northeastern University, Boston, MA, USA, from 2011 to 2014, and held a visiting post-doctoral position at the ELEDIA Research Center, Trento, Italy, in 2015. He is currently a Professor with the Signal Theory and Communications, Universidad de Oviedo. His research interests include antenna diagnostics, antenna measurement techniques, RF techniques for indoor location, inverse scattering and imaging techniques, and phaseless methods for antenna diagnostics and imaging. He was a recipient of the 2011 Regional and National Awards to the Best Ph.D. Thesis on Telecommunication Engineering (category: security and defense).

Fernando Las-Heras Fernando Las-Heras received the M.S. in 1987 and the Ph.D. in 1990, both in Telecommunication Engineering, from the Technical University of Madrid (UPM). He was a National Graduate Research Fellow (1988-1990) and he held a position of Associate Professor at the Dept. of Signal, Systems and Radiocommunications of the UPM (1991-2000). From 2003 he holds a Full-Professor position at the University of Oviedo where he was the Vice-dean for Telecommunication Engineering at the Technical School of Engineering at Gijón (2004-2008). As of 2001 he heads the research group Signal Theory and Communications TSC-UNIOVI at the Dept. of Electrical Engineering of the University of Oviedo. He was a Visiting Lecturer at the National University of Engineering in Peru in 1996, a Visiting Researcher at Syracuse University, New York, in 2000, and a short-term Visiting Lecturer at ESIGELEC in France from 2005 to 2011. He held the Telefónica Chair on "RF Technologies", "ICTs applied to Environment" and "ICTs and Smart cities" at the University of Oviedo (2005-2015). Member of the board of directors of the IEEE Spain Section (2012-2015), member of the board IEEE Microwaves & Antennas Propagation Chapter (AP03/MTT17) (2016-2017), member of the Science, Technology and Innovation Council of Asturias (2010-12), and president of the professional association of Telecommunication Engineers at Asturias. He has authored scientific papers in the areas of antennas, EM scattering, metamaterials and inverse problems with application to antenna measurement (NF-FF, diagnostics and holography), electromagnetic imaging (security and NDT) and localization, developing computational electromagnetics algorithms and technology on microwaves, millimeter wave and THz frequency bands.